THÈSE DE DOCTORAT

Soutenue à Aix-Marseille Université
le 14 Octobre 2021 par

Sanjeev KUMAR

Numerical and experimental studies of thermo-convective instabilities in sessile drop in the course of evaporation

Discipline
Sciences pour l'ingénieur

Spécialité
spécialité Mécanique
et Physique des Fluides

École doctorale
ED 353 – SCIENCES POUR L'INGENIEUR :
Mécanique, Physique, Micro et Nanoélectronique

Laboratoire/Partenaires de recherche
UMR 7343 - IUSTI - Institut Universitaire Des
Systemes Thermiques Industriels

Composition du jury

Prof. Prashant VALLURI University of Edinburgh, United Kingdom	Rapporteur
DR. Elise LORENCEAU LIPhy CNRS / Université Grenoble Alpes, France	Rapporteure
Prof. Muriel CARIN Université de Bretagne-Sud, France	Examinatrice
Dr. Carlo Saverio IORIO Université Libre de Bruxelles, Belgium	Examinateur
Dr. Christophe DELAROCHE Center National d'Etudes Spatiale, France	Invité
Prof. David BRUTIN Aix Marseille Université, France	Co-Directeur de thèse
Prof. Marc MEDALE Aix Marseille Université, France	Directeur de thèse

I, undersigned, Sanjeev Kumar, hereby declare that the work presented in this manuscript is my own work, carried out under the scientific direction of Marc Médale and David Brutin, in accordance with the principles of honesty, integrity and responsibility inherent to the research mission. The research work and the writing of this manuscript have been carried out in compliance with both the french national charter for Research Integrity and the Aix-Marseille University charter on the fight against plagiarism.

This work has not been submitted previously either in this country or in aother country in the same or in a similar version to any other examination body.

Marseille 14 October 2021

SESSILE DROP EVAPOARATION

SANJEEV KUMAR

Aix-marseille University

आ नो भद्राः क्रतवो यन्तु विश्वतः।

"Let noble thoughts come to us from all directions."

— ऋग्वेद १-८९-१ (Rig Veda 1.89.1), 1500–1000 BCE

ACKNOWLEDGMENTS

This document was typeset using the typographical look and feel classic thesis developed by André Miede. Using his template has avoid me to go berserk with the formatting of my work and to just focus on content instead. The style was inspired by Robert Bringhurst's seminal book on typography **"The Elements of Typographic Style"**. Classic thesis template is available for both LaTeX and LyX:

https://bitbucket.org/amiede/classicthesis/wiki/Home

ABSTRACT

Drops have been fascinating researchers since centuries. Some of the topics of interest include water falling onto a hot cooking plate, which is a typical example of Leidenfrost drops, the evaporation of sessile drops with nanoparticle deposition in coffee rings, inkjet printing, pesticides sprayed onto leaves, and blood analysis. The evaporation of sessile drops of various volatile and non-volatile liquids, and their internal flow patterns with or without instabilities have been the subject of many investigations. Despite the simple geometry of sessile drops, the physics involved in the evaporation process is complex due to the numerous intricate interactions and the fluid nature of the sessile drop. An accurate quantitative model of the evaporation process can lead to a greater understanding and control over it. This knowledge can further enhance the efficiency of several applications.

To advance and quantify the effect of numerous intricate interactions involved, we explored the dynamic of the sessile drop on heated substrate under microgravity with parabolic flights and sounding rocket experiments. Microgravity helped us to quantify and distinguish the influence of the atmospheric natural convection via vapor on the evaporation rate. The results from the ground and sounding rocket experiments concrete that convection in vapor play an important role in evaporation under gravity. It also demonstrates the role of gravity on the shape of the sessile drop interface and its influence on the de-pinning of sessile drops.

The numerical model is developed for sessile drop evaporation on a heated substrate under microgravity, based on the rocket and parabolic experiments understanding to gauge the drop's internal dynamics. The quantitative validation of our model is performed via comparison with experiments. Then, we suggested a correlation for the evaporation rate of Ethanol sessile drop. Simultaneously, we are going to broaden our analysis on flow motion with 3D DNS computations for the whole lifetime of evaporating sessile drop. This provides an insight of the Marangoni effect in the dynamics of evaporation process and the occurrence of secondary instabilities. We capture the fine influences of the secondary instabilities appearance on the evaporation rate. Concurrently, we define the instabilities threshold for the transition from primary to secondary Marangoni instabilities via thermal Marangoni number and geometrical aspect ratio.

Keywords: Sessile Drop, Instabilities, Evaporation, Numerical, Experimental, Heat Transfer, Fluid Dynamics, Microgravity.

RÉSUMÉ

Les gouttes fascinent les chercheurs depuis des siècles. Parmi les sujets d'intérêt, citons l'eau tombant sur une plaque de cuisson chaude, qui est un exemple typique de gouttes de Leidenfrost, l'évaporation de gouttes sessile avec dépôt de nanoparticules dans des anneaux de café, l'impression à jet d'encre, les pesticides pulvérisés sur des feuilles et l'analyse du sang. L'évaporation de gouttes sessiles de divers liquides volatils et non volatils, et leurs modèles d'écoulement interne avec ou sans instabilité ont fait l'objet de nombreuses recherches. Malgré la géométrie simple des gouttes sessiles, la physique impliquée dans le processus d'évaporation est complexe en raison des nombreuses interactions complexes et de la nature fluide de la goutte sessile. Un modèle quantitatif précis du processus d'évaporation peut permettre de mieux le comprendre et de le contrôler. Ces connaissances peuvent améliorer l'efficacité de plusieurs applications.

Pour avancer et quantifier l'effet des nombreuses interactions complexes impliquées, nous avons exploré la dynamique de la goutte sessile sur un substrat chauffé en microgravité avec des vols paraboliques et des expériences de fusées sondes. La microgravité nous a permis de quantifier et de distinguer l'influence de la convection naturelle atmosphérique via la vapeur sur le taux d'évaporation. Les résultats des expériences au sol et en fusée-sonde concrétisent le fait que la convection dans la vapeur joue un rôle important dans l'évaporation en gravité. Ils démontrent également le rôle de la gravité sur la forme de l'interface de la goutte sessile et son influence sur le dérapage des gouttes sessiles.

Le modèle numérique est développé pour l'évaporation de gouttes sessiles sur un substrat chauffé en microgravité, en se basant sur la compréhension des expériences de fusée et de parabole pour évaluer la dynamique interne de la goutte. La validation quantitative de notre modèle est effectuée par comparaison avec les expériences. Ensuite, nous avons proposé une corrélation pour le taux d'évaporation de la goutte sessile d'éthanol. Simultanément, nous allons élargir notre analyse du mouvement de l'écoulement avec des calculs DNS 3D pour toute la durée de vie de la goutte sessile qui s'évapore. Cela permet de comprendre l'effet Marangoni dans la dynamique du processus d'évaporation et l'apparition d'instabilités secondaires. Nous saisissons les influences fines de l'apparition des instabilités secondaires sur le taux d'évaporation. Parallèlement, nous définissons le seuil d'instabilité pour la transition entre les instabilités de Marangoni primaires et secondaires via le nombre de Marangoni thermique et le rapport d'aspect géométrique.

CONTENTS

ACRONYMS

ESA   The European Space Agency

CNES   The National Centre for Space Studies

DLR   German Center for Aviation and Space Flight

CMOS   Complementary Metal Oxide Semiconductor

SSC   Swedish Space Corporation

ISS   International Space Station

FHDM   Fluid flow and Heat transfer Diffusion Model

HDM   Heat transfer Diffusion Model

HFE7100 Hydrofluoroethers

FEM   Finite element method

PID   Proportional integral derivative

ATEX   An integrated explosion safety

IR   Infrared

CR   Constant base radius mode

ALE   Arbitrary Lagrangian Eulerian

VD   Element in the vertical direction of sessile drop

CD   Circumferential direction

RD   Radial direction

BDF   Backward differentiation formula

PARDISO Parallel sparse direct solver

PDEs   Partial differential equations

DNS   Direct numerical simulation

DOF   Degrees of freedom

NOMENCLATURE

1g   Terrestrial gravity, $m \cdot s^{-2}$

ΔT Evaporative cooling / sub cooling, $T_{apex} - T_{sub}$, K

Δt Time step, s

ΔT_{inst} Temperature difference front and center of instability cell, K

$\frac{dm}{dt}$ Average evaporation flux rate, $kg \cdot s^{-1}$

$\frac{d\gamma}{dT}$ Temperature coefficient of surface tension, $N \cdot (K \cdot m)^{-1}$

Γ Moving interface of the sessile drop

γ Liquid-gas interfacial tension, $N \cdot s^{-1}$

u   Velocity vector, $m \cdot s^{-1}$

AR_{crit} Critical geometrical aspect ratio

AR   Geometrical aspect ratio

L_c Capillary length, m

Ma_{SD} Sessile drop Marangoni number

Ma_T Thermal Marangoni number

P   Pressure, Pa

μ Dynamic viscosity, $Pa \cdot s$

$\rho(T)$ Temperature dependent density, $kg \cdot m^{-3}$

n   Normal vector

θ Contact angle of sessile drop, Deg.

θ_{crit} Critical contact angle, Deg.

μg Microgravity, $m \cdot s^{-2}$

ε^* IR camera correction

$c_p(T)$ Specific heat capacity at constant pressure, $J \cdot (kg \cdot K)^{-1}$

C_{sat} Saturated vapour concentration, $kg \cdot m^{-3}$

D_{coeff} Diffusion coefficient of liquid drop in ambient environment, $m^2 \cdot s^{-1}$

$E_{vw,exp}$ Experimental evaporation rate of water, $\mu L \cdot s^{-1}$

$E_{vw,num}$ Numerical evaporation rate of water, $\mu L \cdot s^{-1}$

E_v Evaporation rate independent of base radius, $-\frac{1}{R} \cdot \frac{dm}{dt}$, $kg \cdot (m \cdot s)^{-1}$

g Level of gravity, $m \cdot s^{-2}$

H_{evap} Latent heat of evaporation, $kJ \cdot kg^{-1}$

H_t Maximum height of the interface from the substrate, m

J_{Γ}^{evap} Local evaporation rate, $kg \cdot s^{-1}$

$k(T)$ Thermal conductivity, $W \cdot (m \cdot K)^{-1}$

k_{SW} Absorption coefficient, mm^{-1}

M_a Molecular weights of the ambient fluid, $g \cdot mol^{-1}$

M_l Molecular weights of liquid of sessile drop, $g \cdot mol^{-1}$

$Ma_{SD,crit}$ Critical sessile drop Marangoni number

$Ma_{T,crit}$ Critical thermal Marangoni number

N_{inst} Number of the instability cells

p_{atm} Atmospheric pressure, Pa

$P_{l,sat}^{ref}$ Reference saturation vapour pressure, Pa

P_{sat} Saturation vapour pressure, Pa

Q Heat flux density, $W \cdot m^{-2}$

$R)$ Drop base radius, m

R_{gas} Universal gas constant, $8.314 \, kg \cdot m^2 \cdot s^{-2} \cdot K^{-1} \cdot mol^{-1}$

R_{sc} Radius of sub cooled region at the center of sessile drop, m

s Sessile drop interface surface area, m^2

T Temperature field, K

t Time, s

$T_{avg,\Gamma}$ Interface average temperature, K

t_F Total evaporation time, s

t_h Ratio of heat equilibrium time in a drop

$T_{IR,num}$ IR numerical temperature, K

$T_{l,\Gamma}$ Interface temperature at the mesh node, K

T_{sat}^{ref} Reference saturation temperature, K

T_{sub} Substrate temperature, K

u $x-$component velocity field, $\mathrm{m \cdot s^{-1}}$

u_Γ Interface (Γ) velocity

v $y-$component velocity field, $\mathrm{m \cdot s^{-1}}$

v_a Atomic diffusion volumes of ambient

v_l Atomic diffusion volumes of liquid

V_t Drop volume, µL

w $z-$component velocity field, $\mathrm{m \cdot s^{-1}}$

$\boldsymbol{\nabla}_\Gamma T$ Surface gradient of temperature at the interface Γ

$\mathbf{u}_m$ Mesh velocity $\mathrm{m \cdot s^{-1}}$

$\mathbf{q}$ Conductive heat flux, $\mathrm{W \cdot m^{-2}}$

f(θ)   Geometrical parameter

f(x, y) Local drop thickness, m

Pr   Prandtl number

Re   Reynolds number

Sr   Strouhal number

INTRODUCTION

Drops have been fascinating researchers for centuries [1–3]. Some of the topics of interest include water falling onto a hot cooking plate, which is a typical example of Leidenfrost drops [1], the evaporation of sessile drops with nanoparticle deposition in coffee rings [4], inkjet printing [5, 6], pesticides sprayed onto leaves [7], and blood analysis [8, 9]. Although sessile drops are simple in geometry, the physics involved in the evaporation process is complex due to the numerous intricate interactions with the substrate and ambient environment and the fluid nature of the sessile drop itself. An accurate quantitative model of the evaporation process can lead to a greater understanding of the evaporation rate and control over the pattern formation or the deposition of particles after the evaporation of a sessile drop. This knowledge can then enhance the efficiency of several applications. Physically rich and complex evaporation of sessile drops is thus an area of interest to both the academic and industry communities.

The evaporation of sessile drops of various volatile and non-volatile liquids, and their internal flow patterns with or without secondary instability cells have been the subject of many investigations done previously. The documented history of the previous investigation or interest in drops takes us back as early as two centuries back. The J.G. Leidenfrost, wrote about the "Tract About Some Qualities of Common Water" in the 1756 [1]. Thomas Young in 1805 and Pierre Simon-Laplace in 1806, are among the few who conducted the first investigations on the wetting of drop. They examined the wetting issues, the role of contact angle and the liquid/solid coupling nature driving the drop problems Whereas starting of formulation and explanation of evaporation of sessile drop started with Maxwell in, 1877. The Maxwell model considers droplet evaporation as quasi-steady and controlled by the vapor diffusion in the gas phase. It also implies the isothermia of the system. Similarly, Langmuir in 1918 solved the problem with different approaches using an analogy with heat conduction in contrast to an analogy with electrostatics used by Maxwell. The result which, as Langmuir showed, follows directly from Stephan's theory of diffusion as small spheres of the liquid evaporates in the air in such a manner that the rate of change of surface with time is constant and can be expressed as

$$-ds/dt = 8\pi D_{coeff} M_l C_{sat}/\rho \qquad (1.1)$$

where s sessile drop interface surface area, t time, D_{coeff} diffusion coefficient, C_{sat} concentration in the saturated vapour, M_l mass of a

diffusing molecule, and ρ density of the liquid. It has been verified experimentally for droplets varying in radius from a few millimetres to about $0 \cdot 1$ mm, and tested for a number of liquids of varying vapour pressure. It has also been tested, though less rigorously, on much smaller droplets in the size range 2×10^{-4} to 5×10^{-5} cm by observing their rates of fall through air at atmospheric pressure [10].

Later, Fuchs [3] has quoted the example of a hemispherical drop on an infinite plane where, by symmetry, evaporation rate is seen to be half of that of a spherical drop of the same radius. Fuchs also gave an explanation for the observation that, for a drop on a surface, the evaporation rate could in some cases be proportional to the radius of curvature of liquid-air interface.

Lebedev [11], and later Picknett and Bexon [12], independently, used the analogy between diffusive concentration fields and electrostatic potential fields to the problem of evaporation of a sessile droplet. For diffusion-controlled evaporation, vapor concentration field is equivalent to electrostatic potential field around the top half of an equiconvex lens. These theoretical results should be valid as long as the sessile droplet remains in the shape of a spherical cap. Bourges and Shanahan [13] proposed an evaporation model for sessile droplet by taking the concentration gradient to be that for a hemispherical droplet of the same radius as that of sessile droplet. This approximation is not accurate for a flat droplet because the distribution of evaporation flux along a sessile droplet surface is not uniform as it would be for a hemispherical droplet. Rowan et al. [14] analyzed the problem theoretically using a vapor-phase diffusion model suggested by Birdi et al. [15] and derived an approximate analytic equation for evaporation rate. Their model fits experimental results very well for droplets with large initial contact angles. Erbil et al. [16] modelled the droplet as an ellipsoidal cap, defined by three parameters. By adjusting these parameters, they obtained good agreement with experiments. Meric and Erbil [12] reported another model considering a "pseudo - spherical - cap" geometry (for which the droplet height is given by $h_0 = \alpha R \tan \theta / 2$, where R is the droplet radius and α is an adjustable flatness parameter, with $\alpha = 1$ for a spherical cap), which they argued provided much better fits to experimental results. Deegan et al. [4] presented an analytical solution for a droplet with the shape of a spherical cap. Although authors neglected the evaporation flux distribution along the droplet surface, Deegan et al.[4] used the exact analytic expression for the evaporation flux distribution derived by Lebedev. [11], However, Deegan et al. [4] did not study the relationship between the evaporation rate or flux distribution and the contact angle.

Till the end of the 20th century, researchers' investigations presented an analytical solution applied to sessile drop in the range of "droplets"

and same temperature for drop liquid, substrate and ambient atmosphere. The analytical solution considers mostly geometrical aspects and later included concentration gradient around sessile drop (i.e vapor-phase diffusion model). The experimental results started deviating for medium size sessile drop from diffusion models even at ambient temperature [17, 18] this led to focus also on to add investigation on physical mechanisms (i.e Hydrodynamics) inside liquid domains and vapour phase that consider internal flow motion or vapor flow behavior around the evaporating drop.

Before jumping into the complexity and quite vastness of physics involved in sessile drop, let's go through a brief introduction of sessile drop mechanism. Then, we would return to evaporation's state of the art. The domains of sessile drop are quite vast so we will focus only on the pinned sessile drops (the Latin root of the word sessile means "on which one can sit") of pure fluid. An enormous amount of work has already been produced on the subject of physics involved in droplets, so a full theoretical treatment of all phenomenons involving droplets will not be reproduced here. This section will only describe fundamental notions that have been directly used throughout this thesis. The book Physical Hydrodynamics [19] has been a tremendous help, and the next section is partly based on that text and other references [20–23].

1.1 SESSILE DROP EVAPORATION DYNAMICS

Spherical cap shape drop of pure liquid sitting on an atomically smooth and flat surface, evaporating in an inert gas under gravity conditions (as shown in figure 1.1) can be one of the simplest cases of sessile drop evaporation for investigation by experimentally but the rarest to be found naturally. Natural or industrial environment sessile drop evaporation processes are far more complex and dynamic in nature. Let's discuss the sessile drop in its simplest form as shown in figure 1.1, but it still has multiphysics in its nature and has multi cross-link effect in real-time on evaporation of sessile drop. Sessile drop evaporation of pure liquid at ambient temperature under gravity conditions can be divided into two domains, the liquid domain from the substrate to interface and interface to ambient.

The evaporation is, in essence, an endothermic process, as molecules leave the liquid domain, evaporative cooling of free surface produces a temperature gradient along free surface causing a Marangoni or convective flow depending on the size of the drop. Evaporation can by itself induce the formation of an apparent finite contact angle even for perfectly wetting liquids, the internal flow motion or vapour flow behaviour around an evaporating drop. Mechanisms drive fluid flow in this process under earth conditions: (i) drainage in the drop; (ii)
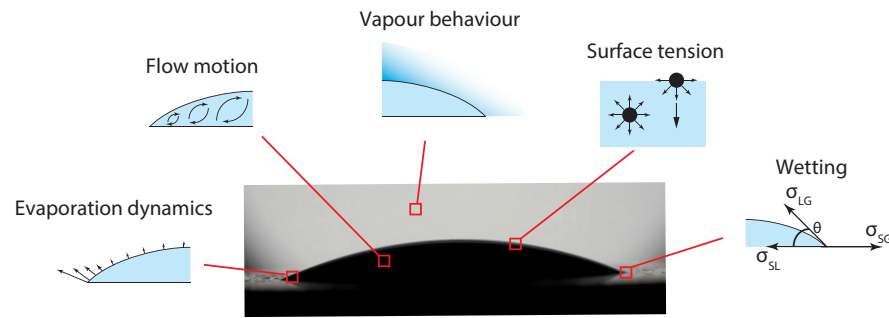
Figure 1.1: Various aspects of physics involved in a sessile drop. Figure credit [24].

buoyancy during liquid and vapour phases; and (iii) thermo-capillary forces, which may induce a fluid flow in liquid or vapour phase, or in both phases. Outside the drop, vapour diffusion towards surrounding air unavoidably induces gradients in vapour concentration, which under gravity conditions results in solutal buoyancy in vapour phase. The temperature of an evaporating drop is different from ambient temperature and almost constant in the course of the evaporation [25] for non-heated substrate whereas for the heated substrate; local heat and mass transfer close to moving three-phase contact line a considerable part of total heat transfer occurs within the direct vicinity of the three-phase contact line. The prevailing driving mechanism under microgravity conditions is surface-tension gradients (also called Marangoni stresses) induced to flow along with the liquid-vapour interface. The effect of this flow depends upon the thermal Marangoni number. As drop volume decreases, the thermal gradient becomes smaller, Marangoni flow becomes negligible, and circular evaporation-induced flow transforms into an outward flow.

The vapour distribution around a sessile droplet was recently studied using experimental [26] and numerical [27, 28] approaches for purely diffusive evaporation. Kelly-Zion et al. [26] have recently shown using infrared spectroscopy and computed tomography that vapour emitted by sessile drops at room temperature behaves differently compared to the commonly accepted diffusion-limited model. Models taking into account convection have been developed to predict evaporation time and obtain the best reagent concentration for combustion [29–33]. The most commonly used model, the Spalding evaporation model, takes into account convection using the calculation of mass and heat balance. This evaporation could be more complicated in presence of external forces such as electric field and force convection [32, 34, 35]. Clearly, all cases mentioned above do not favour producing a neat and reliable benchmark case, and therefore, in ambient, however, complexity can be reduced by removing the gravity component under microgravity experiment. A microgravity experiment not only

helps to classify the effect of natural convection but also the absence of gravity typically decreases the computation times by an order of magnitude, which can be made possible to compare with expensive 3D computations and parametric studies at a reasonable cost.

1.1.1 *Diffusion models*

As described by Ronald G. Larson [36] droplet evaporates slowly enough into stagnant air that mass transfer is vapor-phase diffusion-limited, flow within droplet is of low Reynolds number, and heat, mass, and momentum transport processes are all at quasi-steady state, the problem reduces to solving only quasi-steady-state vapor concentration field, which is controlled by vapor diffusion, and quasi-steady-state droplet velocity field, which is controlled by evaporative mass loss and viscous drag. For spherical cap, these two problems reduce to a Laplace equation for vapor field above the drop, and a Stokes flow problem within the droplet. The coupling between these problems is one-way. The dimensionless heat equilibrium time criterion for the attainment of a quasi-steady state is defined as [36]:

$$t_{\text{heat}} / t_f = \frac{RePr}{Sr} \frac{h_0}{R} \sim 5 \frac{D_{vaq}}{\alpha_L} \frac{h_0}{R} \frac{\rho_{vap}}{\rho_L} < 0.1 \tag{1.2}$$

In figure 1.2 dimensionless heat equilibrium time is plotted for water, ethanol, methanol and isopropanol at different substrate temperatures [37] as a function of the average temperature of the droplet.

In figure 1.3 shown the steady-state diffusion model under predicting evaporation rate of pure ethanol drop of initial volume $5\,\mu L$ at $T_s = 60°C$ with lifetime $12 \pm 1\,s$ [38]), whereas Gurrala et al, 2019 [38] reported that even though steady state diffusion model remains satisfactory for evaporation of water droplet of lifetime $190 \pm 5\,s$ with same initial volume and substrate temperature. Interestingly, Josyula et al, 2021 [39] reported that water drop evaporation time with an initial volume of $5.6 \pm 0.2\,\mu L$ on a hydrophilic substrate with initial contact angle of $67°$ maintained at $50°C$ is over predicted by diffusion model (see fig. 1.3b).

The under prediction by diffusion model at substrate $T_s = 60°C$ for pure ethanol for the experiment performed by [38] can be understood by dimensionless heat equilibrium time (see fig. 1.2) however, for the water with an initial volume of $5.6 \pm 0.2\,\mu L$ with substrate temperature $50°C$ enough though it is still under limit of the assumption of quasi-steady evaporation i.e $t_h/t_F < 0.1$, the higher evaporation rate is the effect of natural convection under gravity conditions that are mostly not accounted in diffusion model [34, 40, 41].
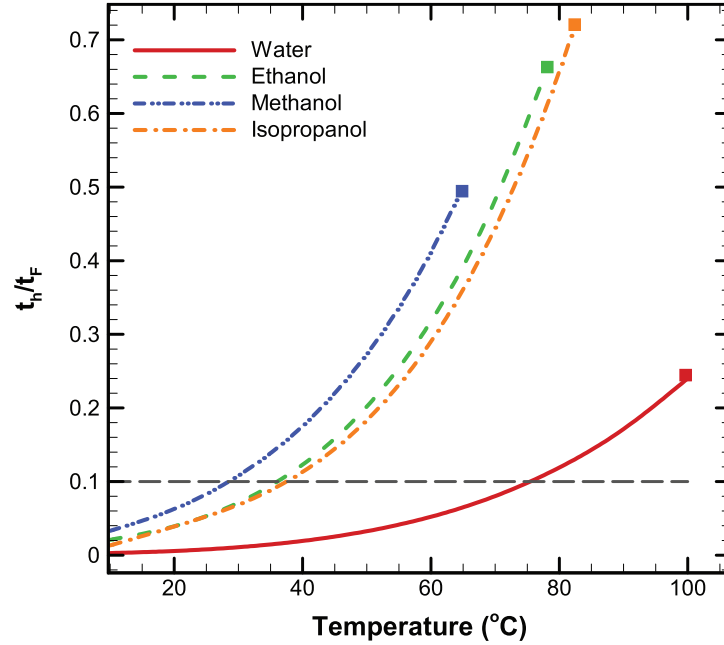
Figure 1.2: Ratio of heat equilibrium time in a droplet (t_h) and its total evaporation time (t_F) as a function of average temperature of the droplet. A filled square on each curve represents boiling point of the respective liquid. A horizontal dashed line represents $t_h/t_F = 0.1$, and assumption of quasi-steady evaporation is valid for $t_h/t_F < 0.1$, as suggested by Larson [36]. Figure credit to [37].

The non-isothermal models which are recently developed such as Nguyen et al, 2018, [42] analytical Model for diffusive evaporation of sessile drops coupled with interfacial cooling effect with the two-way coupling model of quasi-steady thermal diffusion within the droplet and quasi-steady diffusion-controlled droplet evaporation. This coupled problem of diffusive vapor and heat conduction also has been solved numerically by Xu and Ma [43], and Dunn et al. [18]. Pan et al. [27] also carried out numerical modelling to study the competing effects of external natural convection and evaporative cooling. It needs to be considered that the above models are still not applicable for heated substrate.

In another attempt to explain the discrepancy between experimental and theoretical results, Gleason and Putnam [44] used an analytical solution to study "nanolitre" size droplet with isothermal model by replacing vapor concentration along with air-liquid interface by a function of temperature.

The deviations from the diffusion model become noticeable if droplet size is less than 10^{-6} m. These deviations are caused by an increasing influence of kinetic effects at the liquid-gas interface (Hertz – Knudsen – Langmuir equation), and this theory should be applied
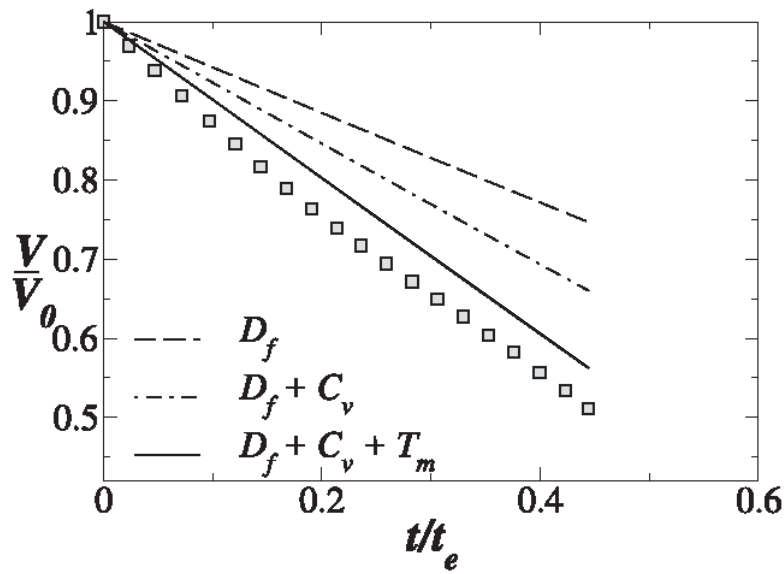
(a)
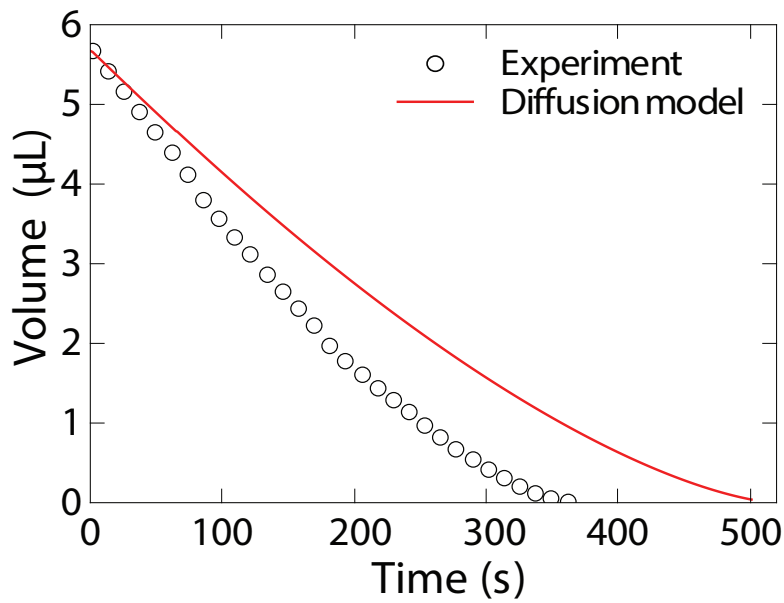
(b)

Figure 1.3: **(a)** Comparison of the experimental and theoretically obtained (V/Vo) versus t/t_e at $T_s = 60°C$ for pure ethanol calculated using diffusion $\left(D_f\right)$, diffusion + convection $\left(D_f + C_D\right)$ and diffusion + convection + transport $\left(D_f + C_o + T_m\right)$ models (fig. credit [38]) **(b)** The drop evaporation with an initial volume of $5.6 \pm 0.2\,\mu L$ on a hydrophilic substrate with initial contact angle of $67°$ maintained at $50°C$. The ambient temperature and relative humidity are $26 \pm 2°C$ and $50 \pm 3\%$, respectively (fig credit [39]).

along with the diffusion equation of vapour in the air if droplet size is less than 10^{-6} m [45] (see fig 1.4a), However, in some cases deviation also becomes noticeable in diffusion model even at room temperature with drop size more than 10^{-3} m. Kelly-Zion et al, 2011 [41], investigated 3-methylpentane (3MP), hexane, cyclohexane, and heptane at ambient temperature $23.2 \pm 0.7°$ C and pressure 1 atm, drops radius from 1 mm to 22 mm during the constant contact line phase only. It is found that diffusion-controlled evaporation model under predicts evaporation rate from 36% to 80% depending on the drop size (see fig. 1.4b). The increase in evaporation rate was attributed to a second transport mechanism, the natural convection of vapors.

1.1.2 *Consideration of hydrodynamics of sessile drop evaporation*

During the evaporation, hydrodynamics within in the liquid domain and ambient of sessile drop play pivotal role in the process. Several experimental and numerical investigated have been conducted in the literature to characterize the internal flow for pure drop [39, 46–48] and natural convection under gravity conditions [33, 34, 40, 41].

Similarly, as we increase the substrate temperature, the coexistence of tangential temperature gradient at the gas-liquid interface and the normal temperature gradient inside the drop will induce various thermal convections, such as, thermocapillary flow and buoyancy convection. The intense and flow direction of thermal convections are influenced by liquid properties [49, 50], drop geometry [39, 51], and other factors such as natural convection in the ambient. The heated substrate also changes the energy transfer during evaporation thus the evaporation rate [52, 53].

Recently, Ye et al [47] experimentally investigated evaporation dynamics of sessile ethanol drops on a heated substrate with contact radius of the drop on substrate is fixed at 2.5 mm and the droplet height varies from 0.4 to 1.2 mm. The experiment indicates that with the decrease of the drop height, the temperature distribution near the drop centre becomes non-uniform, evaporation rate first decreases, and then increases with the decrease of drop height. Kadhim et al [54] performed the experimental and theoretical investigation of water drop on heated hydrophilic and hydrophobic surfaces covering a range of shapes dominated by surface tension or gravity and over a range of temperatures between 40 and 60°C. A significant deviation is observed for hydrophilic substrate due to combined effects of the droplet surface cooling due to evaporation and buoyancy effects that are not included in the model. Kabov et al [55] experimental and numerical studies of evaporation of a sessile water drop on a heated conductive substrate concluded that evaporation of sessile drops on
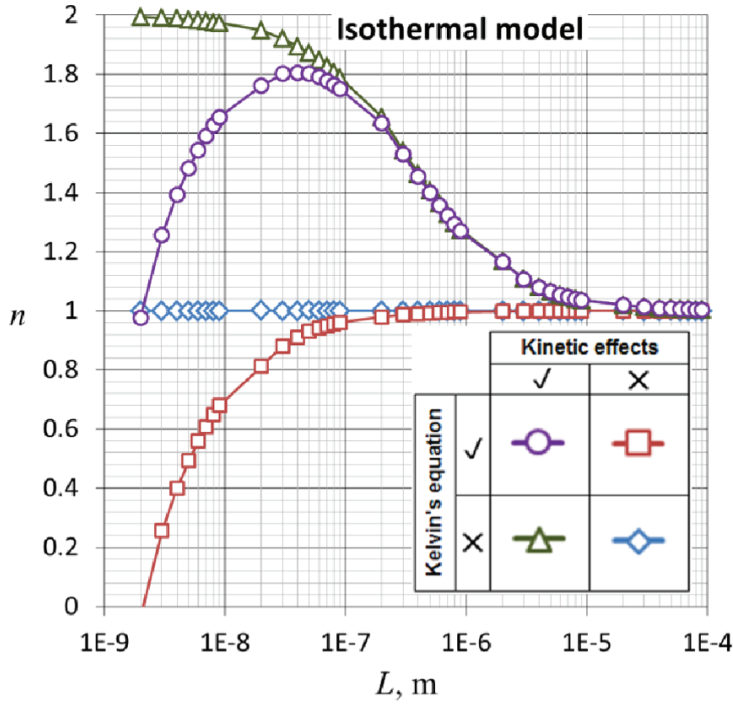
(a)
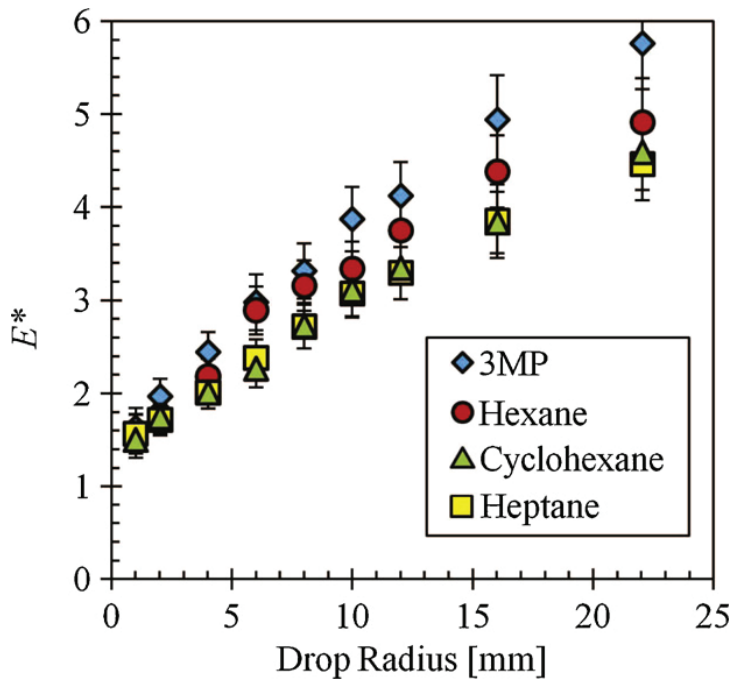
(b)

Figure 1.4: Diffusion limited evaporation drop size limitations. **(a)** Exponent
n for the dependence $J_{c,i} = A(\theta) \cdot L^n$ for the isothermal model
of evaporation. Parameters used: $\alpha_m = 0.5$, $\theta = 90°$, relative air
humidity is 70 %. Results for $L < 10^{-7}$ m do not have physical
meaning, as surface forces action must be included into the model
here. These points are shown to demonstrate the trends of curves
[45]. **(b)** Plot of dimensionless evaporation rate as a function of
drop radius. E^* equal to 1 would indicate agreement between
the measured evaporation rate and that predicted by a diffusion-
controlled model [41]. Figure 1.4a and 1.4b credit to [45] and [41]
respectively.

different surfaces shows much faster evaporation than on more conductive surfaces. The temperature of the substrate is found to play an important role in evaporation intensity and sessile drop lifetime and it is also noted that the sessile drops evaporate significantly faster on a steel substrate than on a glass with Teflon coating. This is explained by the fact that higher the thermal conductivity of a material implies that the temperature of a solid surface under the droplet, including the contact line region, leads to higher evaporation rates.

Gurrala et al. [38] study the evaporation of ethanol-water sessile drop of different compositions at an elevated substrate temperature. Previously, similar studies were conducted by Sefiane et al. [56] on a polytetrafluoroethylene (PTFE) substrate at room temperature, Sáenz et al. [57, 58] investigated the evaporation of non-spherical drops via numerical simulations and experiments. They demonstrated a universal scaling law for evaporation. Also, Innocenzi et al. [59] investigated complex-shaped drops consisting of ethanol-water binary mixtures by conducting theoretical modelling and infrared thermography at different substrate temperatures and concentrations. However, most of the results presented in their studies are at room temperature only.

In parallel, Sefiane et al. [49] reported secondary instability in sessile drop evaporating under ambient conditions and later Brutin et al. [60] presented a series of experiments on heated droplets exhibiting similar patterns. Multiple researcher reported similar instability under various conditions experimentally [53, 61–63] and numerical simulation are performed to resolved the secondary instability [21, 64–66].

However, Karapetsas et al. [67] First to attempt numerically to demonstrate the physical mechanisms that drive instability and pattern formation with "one-sided" two-dimensional (2D) numerical (Finite element method (FEM)) model and using linear stability analysis. Another closely related "one-sided" 3D numerical modeling study conducted by Semenov et al. [64] to observed the flow in drops. Semenov et al. [64] with "one-sided" 3D numerical model provide no direct comparison of the sessile drop evaporation rate, but only insufficient qualitative comparison with the top view of experiment drop. Semenov et al. concluded with the model don't use any fitting parameters, however, equation 9 certainly use fitting parameter namely B and Δh that were previously introduced [68] and required 2D simulation to acquired the values. Semenov et al. [64] "one-sided" 3D numerical model due to fitting and some other inconsistent is restricted to achieve its objective. However Karapetsas et al. [67] and Semenov et al. [64] model remains fundamental and inspiring numerical model. In chapter 3, presented the our model for sessile drop evaporation on heated substrate under microgravity conditions later validation, results and discussion in chapter 4.

The complexity arose with drop evaporation on heated substrate under gravity but this could be reduced by removing gravity. Microgravity not only helps us to understand and quantify the effect of heated substrate on drop hydro thermal dynamic on evaporation but also classified the effect of natural convection under gravity.

In this direction, previously multiple experiments have been performed under various parabolic flight campaigns. The use of parabolic flights has enabled [69] and supported the observation of previous experiments on the effect of natural convection on sessile drop evaporation [34, 40, 70], but parabolic flight are still insufficient in terms of duration and conducting quantifiable measurement. We would discuss parabolic flight experiments later in chapter 2 with details. A better level of microgravity and a longer duration of evaporation is needed. A sounding rocket experiment ARLES (**Advanced Research on Liquid Evaporation in Space**) was conducted on June 24, 2019, from the Esrange Space Center in northern Sweden under the collaboration of the The European Space Agency (ESA) and Swedish Space Corporation (SSC) (Swedish Space Corporation) to support the investigation of evaporation process in a controlled environment of microgravity. The results and discussions are presented in chapter 2.

1.2 EVAPORATION OF SESSILE DROP IN MICROGRAVITY

In chapter 2, 3 and 4 we have presented in detail our analysis on evaporation of sessile drop in microgravity and also its comparison with gravity. So, in this section, we present a brief analysis of evaporation of sessile drop in microgravity. The evaporation under microgravity conditions without heated substrate is primarily quasi-steady diffusive in nature [69]. Evaporation of sessile drop in microgravity is assumed under saturated vapour pressure as evaporation only takes place on the surface of the liquid, and the surface of the liquid is under saturated vapour density due to the collection of vapour around the sessile drop in the absence of gravity as shown in the figure 1.5. So the liquid interface is saturated with vapour particles, equilibrium occurs on the surface of the liquid.

However, due to heated substrate the forward change (liquid to vapour) that is endothermic can be sustained and heat needed to convert the liquid into the vapour is available at the interface. The average energy of the particles leaving from liquid interface is governed by the interface temperature that is sustained by the Marangoni convection.

The validity of the evaporation of sessile drop under saturated vapour pressure in microgravity can put under question, the assumptions of various diffusion models for evaporation of sessile drop in gravity as some diffusion models (mostly one-way coupled [18, 38, 43,
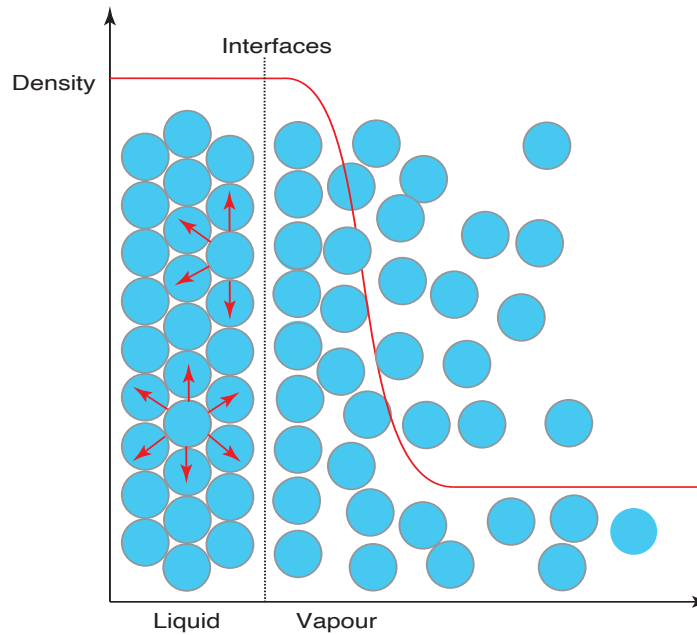
Figure 1.5: Schematic of liquid-vapour near sessile drop interface.

51, 71–75]) also considered evaporation of sessile drop under saturated vapour pressure with gravity but under same conditions (i.e under saturated vapour pressure) the sessile drop evaporation under gravity have higher evaporation rate compared to microgravity [69, 76]. In gravity, natural convection influence (reduces) the vapour pressure, so it should be lower than saturated vapour pressure.

In figure 1.6 partial mind map of research axes of sessile drop are presented. Research axes in bold are investigated in this thesis during the study of sessile drop evaporation under microgravity (for a complete map please refer [24]). Each branch is cross-linked because the physics involved are strongly coupled. The axis that we are going to touch will help us to understand the role of localized saturated vapour density (or pressure), and natural convection on the liquid-vapour phase of sessile drop evaporation, the diffusive evaporation in microgravity, understanding of the thermo hydro dynamic inside liquid domain on the heated substrate, and role of Marangoni convection/instabilities on the pinned sessile drop evaporation rate.

Also, through the above axes, with careful investigation, we can assess the impact of vapour phase on temperature distribution and evaporation rate, the thermal transport in the liquid domain, and temperature difference between a heated substrate and average interface temperature. Thus, we can move more towards not only the formulation of analytical solution for the sessile drop evaporation under microgravity on the heated substrate but also closer to the analytical
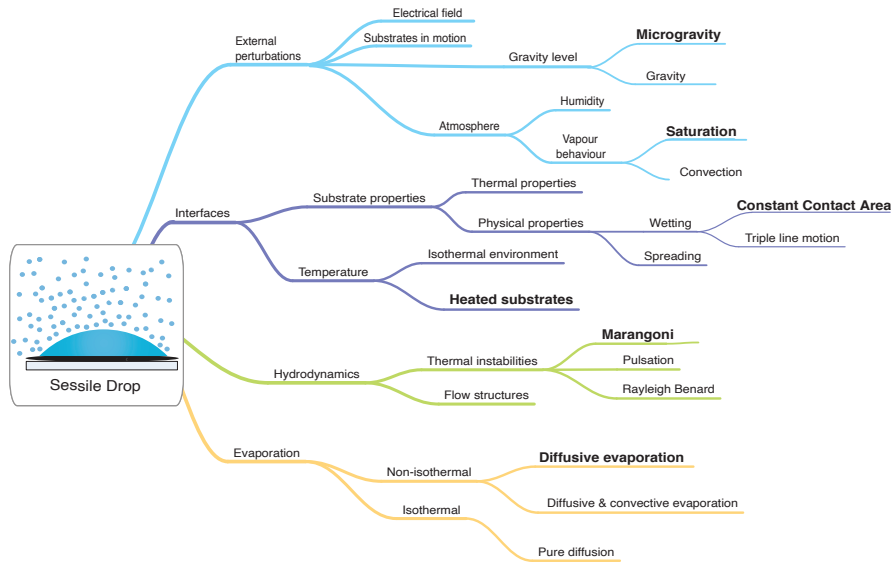
Figure 1.6: Research axes of sessile drop in bold are investigated in this thesis during the study of sessile drop evaporation under microgravity. Modified from figure 1 from [24].

solution for the sessile drop evaporation under gravity on heated substrate.

1.3 IMPORTANT PARAMETERS AND DEFINITION

In chapter 3 and 4 we proposed our numerical model for microgravity conditions and validated it with experiment data from the sounding rocket and parabolic flight [69, 76]. However, in our work we have the multiple physical and geometrical parameters such as P_{sat} is the saturated vapour pressure (used Kelvin equation), and D_{coeff} is the diffusion coefficient of liquid drop in ambient environment (Fuller - Schettler - Giddings equation [77]) and f(θ) is geometrical parameter dependent on the contact angle of sessile drop with substrate. The accuracy of the parameters can influence the overall results. So, we briefly go through the definition, limitation and accuracy of some parameters in state of art. We also go through the state of art for "Stefan Flow" and its applicability for sessile drop evaporation.

1.3.1 *Diffusion coefficients*

The diffusion coefficient D_{coeff} is defined as the ratio between the mass (or molar) flux of a component in a gaseous mixture and its concentration gradient, in absence of mechanical or convective forces [78]. Comparison of the diffusion coefficients vs temperature for ethanol-air mixtures from different equations is present in fig. 1.7. The Fuller - Schettler - Giddings equation that we are going to use in our model
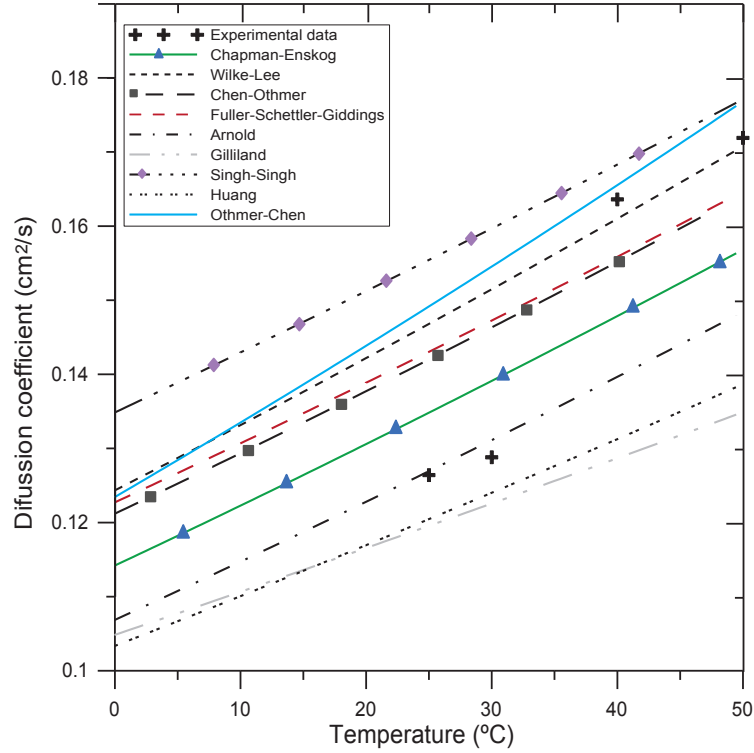
Figure 1.7: **Comparison of the Diffusion coefficients.** Diffusion coefficients vs temperature for ethanol-air mixtures from different equations [78].

assumes: a) the hypothesis of rigid spheres ($\Omega_D = 1$); b) that the collision diameters are proportional to the cubic root of the molecular volumes; and c) the additivity of atomic volumes, v^*, which allows to estimate the molecular volumes from atomic volumes of the elements composing the diffusing molecules [79, 80], both molecular and atomic volumes being quantified in litre per kmol. These hypotheses lead to the following expression [77, 81]:

$$D_{A-B} = \frac{0.0001 T^{1.75} \left(\frac{1}{W_A} + \frac{1}{W_B} \right)^{0.5}}{p \left[\left(\sum v_A^* \right)^{1/3} + \left(\sum v_B^* \right)^{1/3} \right]^2} \tag{1.3}$$

Lapuerta et al. [78] tested the nine different equations among those proposed in the literature to estimate the diffusion coefficient for ethanol-air mixtures (see fig. 1.7). The experimental values were measured at 86 kPa and concluded that there is not a unique optimal formula for all alcohols. The lowest standard deviation for methanol was obtained with the Fuller - Schettler - Giddings equation ($0.0116 \, \text{cm}^2 \cdot \text{s}^{-1}$), for ethanol with the Chapman-Enskog equation ($0.0128 \, \text{cm}^2 \cdot \text{s}^{-1}$), the best fit for all alcohols was obtained with the Arnold equation ($0.0247 \, \text{cm}^2 \cdot \text{s}^{-1}$). However, in our observation Fuller-Schettler-Giddings equation is the most common equation used in

Sources	$f(\theta)$	
Picknett and Bexon [12]	$(0.6366\theta + 0.09591\theta^2 - 0.0144\theta^3) / \sin\theta,\ \theta < 0.175$	Closed, complicated
	$\begin{cases} 0.00008957 + 0.6366\theta + 0.1161\theta^2 \\ -0.08878\theta^3 + 0.01033\theta^4) / \sin\theta,\ 0.175 < \theta < \pi \end{cases}$	
Bourges-Monnier & Shanahan [13]	$-1/\tan\theta\ln(1-\cos\theta)$	Closed, simple
Hu and Larson [17]	$(0.27\theta^2 + 1.30)/2$	Closed, simple
Dinghua Hu et al. [75]	$1/\sqrt{1+\cos\theta}$	Closed, simple
Popov [82]	$\frac{1}{2}\left(\frac{\sin\theta}{(1+\cos\theta)} + 4\int_0^\infty \left(\frac{(1+\cosh 2\theta\tau)}{\sinh 2\pi\tau}\tanh[(\pi-\theta)\tau]d\tau\right)\right)$	Non-closed, complicated

Table 1.1: Expressions of geometrical parameter.

predicting binary gas diffusivities. It can be used considering all the aspects such as pressure, temperature, diffusivities in gas or air with the least deviation.

The deviation in theoretical diffusion coefficient value from the experiment can deviate the comparison significantly of numerical simulation of sessile drop with experiment as the diffusion coefficient effect the evaporation rate, thus the liquid-vapour interface temperature which in return can influence the diffusion coefficient that could affect the numerical overall evaporation rate over the time.

1.3.2 *Geometrical parameter*

The geometrical parameter f(θ) is the function of sessile contact angle that also indirectly connect the evaporation rate with the surface area of the spherical shape sessile drops. In table 1.1, different expressions of f(θ) in the literature and their comparisons are presented in figure 1.8. Among all the expressions, expressions proposed by Picknett and Bexon [12] and Popov [82] are the two exact solutions of f(θ) in different forms with a full application range of $0 < \theta < \pi$, and they are identical (see in fig. 1.8a). The expressions of Dinghua Hu et al. [75], Bourges-Monnier and Shanahan [13] and Hu and Larson [17] are the approximate solutions of f(θ).

Dinghua Hu et al. [75] compared the expression with respect to contact angle and deviation in the expressions with respect to Picknett and Bexon [12] analytical solution (see fig. 1.8). Bourges-Monnier and Shanahan [13] expression is simple, and has a good consistence with the exact solution of Picknett and Bexon [12] with the relative difference less than 5% for $0.294\pi < \theta < \pi\,(53° - 180°)$. However, for $\theta < 0.239\pi\,(43°)$, the deviation of this approximation expression is greater than 10%. The approximate expression of $f(\theta)$ proposed by Hu and Larson [17] was obtained from the numerical analysis on the drops with initial contact angle $\theta < \pi/2$. This expression is much

simpler and easier to be used, however it works well only in their recommended range of $0 < \theta < \pi/2$, and deviates greatly from the exact solution of Picknett and Bexon [12] when $\theta > \pi/2$. Dinghua Hu et al. [75] proposed expression is simple and also agrees well with the exact solution of Picknett and Bexon [12] in a wide range of $0 < \theta < \pi$ with relative difference between Dinghua Hu et al. [75] and exact solution is less than 5% for $0.139\pi < \theta < \pi \, (25° - 180°)$, and less than 10% for $0 < \theta < 0.139\pi \, (0 - 25°)$. The average relative difference in the whole range of $0 < \theta < \pi$ is about 2.2%.

Even though Picknett and Bexon [12] expressions for f(θ) is complicated but it is close and the most accurate and exact solutions of f(θ). Thus, we have used Picknett and Bexon [12] expression in our analysis.

1.3.3 *Stefan flow in vapour phase*

The tangential velocity is continuous at the interface of sessile drop, the fast Marangoni flow will also be present in gas phase. Furthermore, the density difference of liquid and vapour leads to a discontinuous jump in the normal velocity component, which constitutes the so-called Stefan flow. Diddens et al. [83] investigated the influence of these effects, the contribution of Stefan flow, i.e. the normal velocity jump, is barely visible. So, Diddens et al. [83] conclude that any noticeable influence of Marangoni flow and Stefan flow in gas phase on evaporation has been ruled out for pure water drop and binary water-ethanol drop at ambient temperature.

A similar investigation is also performed by S. Y. Misyura [84] on evaporation of water drops with larger drop volume $V_0 = 250\,\mu L$ and substrate temperature $T_{sub} = 75°C$ and estimate that Stefan flow contributes to nearly 3% of the total evaporation whereas for the same waterdrop volume in the presence of intensive nucleate boiling substrate temperature $T_{sub} = 115°C$, evaporation corresponding to Stefan flow is nearly 4% (see fig 3 and 4 of [84]).

In order to distinguish the contribution of Stefan flow from the purely diffusive one on the evaporation Carle et al [69, 85] remove all convection induced by gravity. To achieve this, experiments were performed on weightlessness. With experiments, it is confirmed that in the absence of gravity effects, evaporation can then be correctly assumed to be a quasi-steady, diffusion-controlled process, regardless of substrate temperature and isothermal temperature of the drop. Indeed, the thermal gradient that develops inside an evaporating droplet driven by the latent heat of vaporization appears to be negligible when the droplet is sufficiently thin and when it is evaporated on a highly thermally conductive substrate [86–88]. Thus model does not need
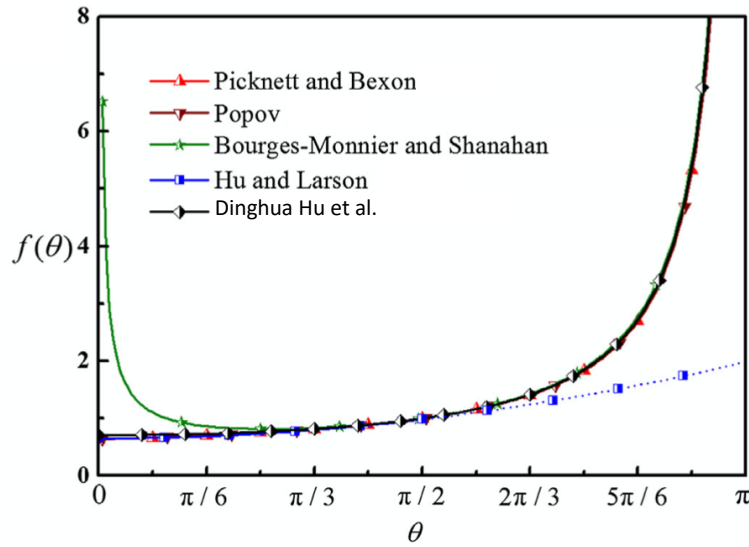
(a)
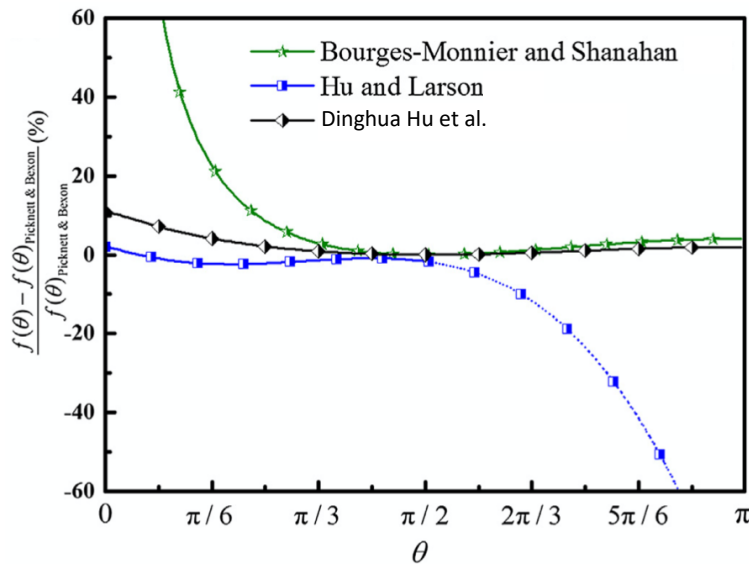
(b)

Figure 1.8: Comparisons of the available expressions of $f(\theta)$ in literature [12, 13, 17, 75, 82] (Please note that the solid lines represent the application range recommended by the researchers, and the dot line represents the extension range of the expression of Hu and Larson [17]). Figure credit [75]

to include Stefan flow for evaporation of sessile under microgravity conditions.

1.3.4 *Primary instability & Secondary instability phase*

Internal flow structure of the evaporating sessile drop for the sufficiently large initial contact angle sessile drop can be divided into two

phases namely Primary instability and Secondary instability, and can be categorised as follows:

Primary instability phase: Evaporation starts with a Marangoni convection that results in an unsteady axisymmetric torus roll, with the lowest temperature and accordingly the lowest evaporation rate around the apex, which increases along with the radial position towards the contact line. The velocity magnitude is the highest along with the free surface surrounding the apex and then the flow dives towards the substrate closer to the symmetry axis. This torus roll appears as soon as it exists temperature gradient over the liquid drop surface.

Secondary instability phase: The axis-symmetric torus roll of the primary instability breaks into cells, core cells get too bigger, and split in turn. The axisymmetric torus roll breaking is triggered by competition between viscosity dissipation and thermo-capillary force that leads to the emergence of a fully H3D unsteady fluid flow of dynamic multicellular thermo-convective non-axis-symmetric flower-like pattern.

1.4   GUIDE THROUGH THESIS

This thesis aims to investigate the Thermo hydrodynamics of sessile drop evaporation by focusing on evaporation dynamics of the drops on heated substrates, the flow motion inside volatile drops, and the effect of secondary Marangoni instability by leveraging microgravity conditions.

This first chapter has been dedicated to the introduction of physics involved in drop evaporation and state of art. Then with thesis chapter 2 we move progressively deeper to understand evaporation of a drop under reduced gravity conditions with sounding rocket and parabolic flight. The chapter 2 contains an introduction on microgravity methods, experiment setups, all the technical data and results from the experiments that are used in the chapters 4 for the comparison with the numerical model. We also, discuss the advantages and difficulties of microgravity experiments. The chapter 3 is about the foundation for the formulation of a numerical model with theoretical concepts and assumptions for sessile drop evaporation on the heated substrate under microgravity. We also look into the methodology used for numerical simulation in COMSOL Multiphysics software along with our numerical model implementation in it. Also, into the optimization method in capturing the H3D instabilities and at the same time reducing the computational time heavily as accurate computations of the entire instability cells dynamics of sessile drop evaporation are quite expensive.

The chapter 4 starts with validation of our numerical model for microgravity conditions. After the validation, we propose the analytical model for the pinned sessile drop of ethanol on a heated substrate under microgravity conditions. Then we are going to focus on the study role of the Marangoni effect that influences evaporation rate and dynamics inside the domain via Marangoni convection/Marangoni instabilities. In parallel, we study the effect of different substrate temperature T_{sub}, contact radius R and ambient pressure P on the evaporation rate, interface temperature, velocity field, instabilities pattern. Then with the above cases, we define the relation for critical Marangoni number for the transition from primary Marangoni instability to secondary Marangoni instability through critical aspect ratio. Next, we use our model for HFE7100 sessile drop evaporation under microgravity to find the critical thermal Marangoni (and critical height) for the transition from primary Marangoni instability to secondary Marangoni instability to help future rocket experiments.

MICROGRAVITY PLATFORMS, EXPERIMENTAL SETUPS & RESULTS

Drop formation is an ongoing process, the phenomenon may be natural like rain, condensation or it can be due to human activities like spraying, and ink printing. It is a matter of investigation to understand the creation of a drop under reduced gravity conditions. It is quite interesting to enquire what makes the drop to be deposited onto the substrate, while the fluid and the scientists float in the test cell and around the experimental setup, respectively.

In this chapter, we will discuss how to employ the advantages of microgravity and dodge the disadvantages of weightlessness. It describes the space projects with a special focus on the parabolic flights and sounding rocket experiment performed during the last three years of research. This chapter contains an introduction on microgravity methods, experiment setups, all the technical data and results from the experiments that are used in the upcoming chapters for comparison with numerical model.

2.1 WHAT MAKES MICROGRAVITY INTERESTING?

The high cost involved in the microgravity experiments has been a subject of argument for the critics of microgravity science, but microgravity experiments are a distinctive means to learn about the phenomena that cannot be seen normally under standard gravity conditions. Micro-gravity environments are well-suited for space applications like astronaut training, antenna deployment, long space program or ISS experiments, hence, making it vital to inspect and validate all the technical solutions before launching the experiments on satellites or on space stations.

Microgravity experiments not only have direct applications like satellite navigation systems, communication and data transmission [89], optics and ophthalmology but also the skills and expertise developed during space conquest can be used for applications on Earth, like, hybrid complementary metal oxide semiconductor (Complementary Metal Oxide Semiconductor (CMOS)), UV protections for sunglasses, and making nutritional supplements for infant formulas.

Biomedical experiments are substantiated by the experiments done by the astronauts and researchers examine different subjects to explore
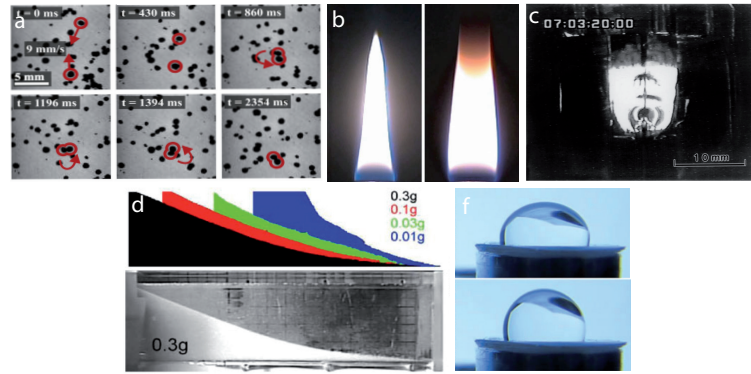
Figure 2.1: Fluid mechanics experiments under micro gravity: **a)** Collision between two dust aggregates [91]; **b)** Heptane flame under normal (left) and reduced gravity (right) [92]; **c)** Marangoni flow in molten-silicon bridge [93], **d)** Glass grains avalanches at various gravity levels [94]; **e)** Contact angle of water drop under normal (top) and reduced gravity (bottom) [95]. Figure credit to F. carle thesis [24].

the effects of microgravity on the various parameters like concentration and reaction time, blood flow, vision, displacement, and orientation as top and bottom concepts are not pertinent under reduced gravity levels, hence, making all this is indeed a great method to conduct high-quality fundamental research that cannot be done on Earth. All these experiments help us to understand the human body and its mechanisms of adaptations in a better way, therefore facilitating the development of techniques and medications for the common people [90].

As microgravity instantly suppresses the buoyancy forces that are in predominance in fluids, this results in the emergence of spectacular fluids driven only by capillary forces (see figure 2.1). We can see that bubbles become spherical, convection is suppressed, particles are floating around, and the widespread liquid films are stable. Hence, we can say that fluid mechanics studies are the most visual experiments.

Microgravity greatly influences the flux rate and the flow motion of drops. Natural convection is reduced to a great extent by suppressing buoyancy forces. Residual gravity can be said as the convection remained to be as negligible and not being totally suppressed. As the drop vapour does not move far from the drop and diffuses along the concentration gradient, so it greatly reduces the evaporation. In the absence of convection in vapour therefore it becomes possible to study purely diffusive evaporation of sessile drop comprehensively.

2.2 MICROGRAVITY PLATFORMS

It is a prolonged and expensive process to launch an experiment in the International Space Station (ISS). The designing and procurement of an experiment can take more than three years. Scientific satellites yield a microgravity environment that is nearly as in the space station, under the same constraints, for a period of ten to fifteen days. Although there are not many opportunities to get an access to the satellites so easily, but it is fortunate that we have other ways to access microgravity on Earth (see fig. 2.2).
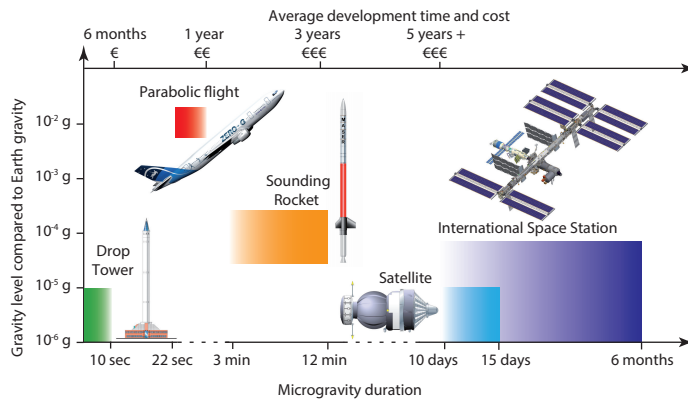
Figure 2.2: Access to reduced gravity levels through various platforms. The axis shows the duration and the gravity level as well as the development time needed from design to performing the experiment. Figure credit to F.carle [24] and ESA website [96].

A microgravity environment can be created on the Earth by using a drop tower. The experiment which is set up in a drag shield is dropped from the top of the tower. The height of the tower h is directly linked to duration t of the microgravity phase i.e $t_{\mu g} = \sqrt{2\,h/g}$. Brisbane drop tower of 20 m gives about 2 s, ZARM vacuum drop tower of height 146 meter in Bremen in free fall allows a duration up to 5.3 s and a duration of 9.3 s with a catapult phase before the drop. These facilities have gravity levels 10^{-5} g which is the lowest and shortest conception time. To benefit from the microgravity phase, the phenomena that are studied must have very short transition phases. During landing, the deceleration involve an air bag, electromagnetic brakes, or fine polystyrene pellets, making them strong, and therefore the experiment requires resistance up to 30 g for the catapulted experiments.

Sounding rockets are launched from underpopulated areas, halfway to space, and they generate microgravity in low orbits-below 200 km, for about three to twelve minutes, before re-entering into the atmosphere and landing using a parachute for recovery. Due to the initial speed, the sounding rockets follow strongly the elliptical orbits,

which are small portions, with conjugal diameter, may be less than 80 km. The experiments run in the payload, which are in constant link with the researchers. They continuously monitor the experiments and collect data, to avoid any loss of data, in case of a mis-happening like a crash during the return to Earth. More about sounding experiment is discussed in section 2.5.

The another popular method to perform microgravity experiments are the Parabolic fights. Parabolic flight technique and weightlessness is discussed in the next section 2.3 in the details with the experiments results from the parabolic flight campaign VP139 and VP140.

2.3   PARABOLIC FLIGHTS EXPERIMENTS: VP139 AND VP140
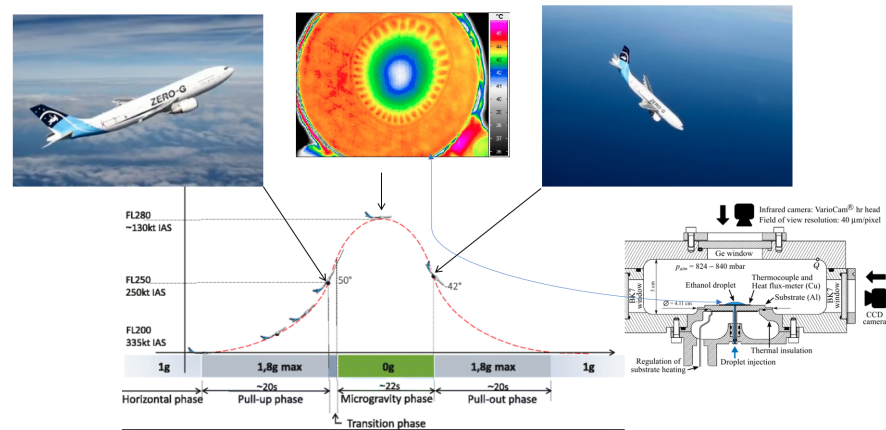
Figure 2.3: Different phase of the parabola performed by Novespace A310-ZeroG aircraft with varying gravity. Also showing the Novespace A300-ZeroG aircraft angle, speed and altitude, and time duration of the each phase. Top center images is the IR view of the ethanol sessile drop evaporation under the microgravity inside the test cell (right bottom) from parabolic flight VP140.

2.3.1   *Parabolic flights*

The experiments performed in the parabolic flight, have been presented in this section. Parabolic flight is a free-fall technique, has been used to create apparent weightlessness. In figure 2.4, we can see the typical path followed by the Novespace $A310 - ZeroG$ aircraft, which is a flying laboratory situated in Bordeaux, France. This plane has been exclusively reserved for scientific experiments under microgravity conditions and performs two flight campaigns for each space agency: The National Centre for Space Studies (CNES), German Center for Aviation and Space Flight (DLR) and ESA, performing a total of six flight campaigns per year. Each campaign comprises of three flights, which
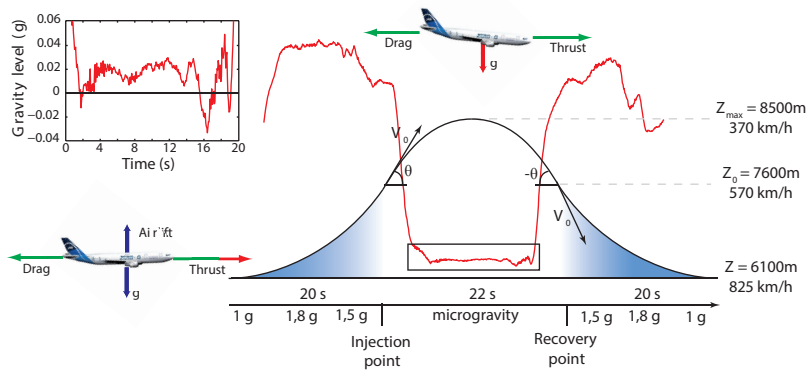
Figure 2.4: Typical parabola performed by Novespace A310-ZeroG aircraft. The trajectory speed and altitude is indicated in black, while the gravity level during the parabola is indicated in red, with a zoom during the microgravity phase in the inset [24].

altogether make microgravity of more than half an hour. Although the level of microgravity is considerably higher than all the other ways of accessing microgravity 10^{-2} g but the access conditions are easy as it takes about 6 months from design to the conduction of the flight, also there are greater chances of the experiments to be selected, because there are approximately 12 experiments, about 40 scientists and the aircraft crew to perform. The campaign is performed in the $100\,m^2$ test area located in the middle of the plane. The designing of the experiments is done in a way that they fit in the seat fixations and can resist emergency landing at 9 g, which is less than the recovery in a drop tower.

The cruise flight is followed by a horizontal trajectory at a constant speed. The plane is like any other commercial aircraft, but it has exceptional flight qualifications and is subjected to several forces. The air drag is overcome by the thrust coming from the motors to apply the horizontal component of speed. The plane's airlift compensates for the Earth's attraction field.

The motor thrust is reduced equivalent to the air drag, the inclination of aircraft is reduced by 4 to suppress any lift, for making the plane enter free fall. At this point, the aircraft is subjected only to Earth's gravity and is made to fall towards the ground. The aircraft is made to follow a parabolic path for obtaining longer times for microgravity and just falling towards the Earth's surface.

2.3.2 *Experiment overview*

The experiment is performed in the frame of the "Drop Evaporation" space experiment engaged with CNES and ESA that intend to study evaporating sessile drops of pure fluids as well as binary mixtures
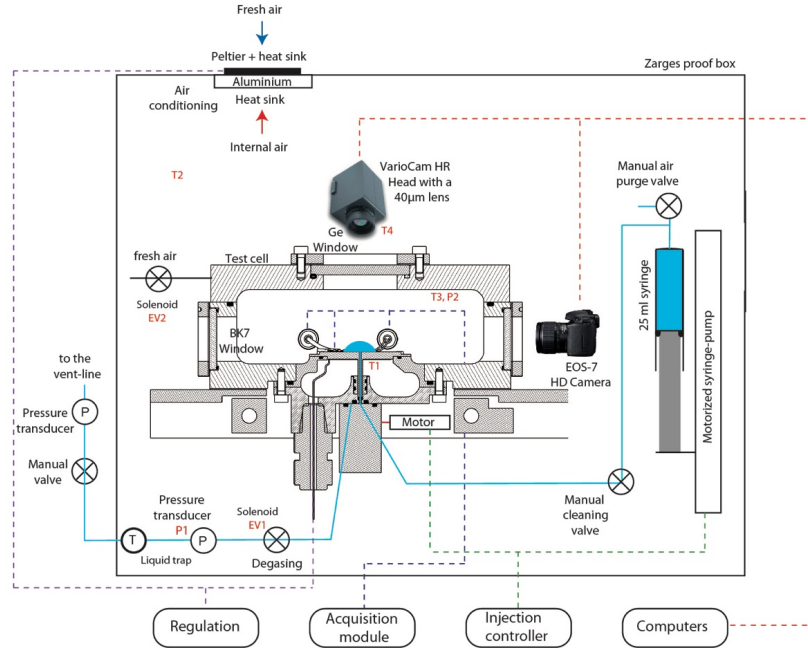
Figure 2.5: Principle of the experiments and material that is used inside the confinement box. Please also see table 2.1. Figure Credit [24].

with or without an electrical field. The scientific objectives are to measure under precisely defined conditions the local and global heat and mass transfer, the flow and instabilities occurring in the drop. Microgravity will in this case be instrumental in creating a well-controlled environment, where, in the absence of far-reaching gravity currents, the principal effects are localized in the vicinity of the drop, thus reducing the dependency on less controlled external factors. The existence of thermo-capillary instabilities occurring under evaporation in pure liquid drop of ethanol in reduced gravity environment has been already evidenced and published [97]. Thus, these parabolic flights campaign aims at mainly improving the preparation of the "Drop Evaporation" experiments.

Name	Device use dot measure	What is measured?	Type of measurement	Control or measure	Range	Power supply	Signal
T_1	Thermocpt. (Tm1)	Heating substrate	Temperature	Control	20 to 55°C	-	T
	Thermocpt. (Tm2)			Measure	20 to 55°C	-	T
T_2	Thermocouple	Zarges box	Temperature	Measure	20 to 40°C	-	T
T_3	Thermocpt. (Tm3)	Exp. test cell	Temperature	Measure	20 to 50°C	-	T
T_4	IR camera	Heating substrate	Temperature	Safety	20 to 50°C	220V	FireWire
P_1	KULITE pressure sensor	Exp. cell	Pressure	Measure	835 mbar	12 V	0-10 mV
Q_{m1}	Injection device	Injection mass flow rate	Motion of the syringe	Measure	0 to 200 μL/min	220V	-
V_g	Injection device	Drop volumes	Motion of the syringe	Control	0 to 50 μL	220V	-

Table 2.1: Measured and/or controlled values (see fig. 2.5).

2.3.3   *Experimental setup*

The principle of the experiment stays the same that during VP100 performed in December 2012 during the F. Carle PhD [24]. During the parabolic flight campaign VP139, October 2018, the new rack but same experiment cell with few up-gradation was used. The refurbished rack was used a few years ago to fit the Novespace rules onboard the A310. There is no change between the VP139 to VP140 that were performed in November 2018. In figure 2.5 and 2.6 provide schematics of the test cells that were used. For VP139/VP140, all the fluid loop is located inside a Zarges Box (K470 − 750x550x580 - ONU). All the fluid loop is at the room pressure (plane cabin pressure during the flights). An integrated explosion safety (ATEX) electro-valves are used not only to enable the pressure equilibrium but also to enable the drop injection and vapour venting. The fluid injection in the test cell is ensured using a syringe pump already used during VP100. The evaporation of alcohol drops presents various dangers, such as leaks, runaways and explosions, that must be reduced to an acceptable level of safety. A large part of the experimental setup was to ensure that the experiments could be carried out safely in the aircraft while the test cell of the experiment (Fig. 2.5), is comparatively simple.

The heated substrate inside the test cell is of 15 mm diameter spherical substrate, is composed of 3 mm aluminium support that is heated by a polyimide thermofoil heater, which is regulated by a PT-100 sensor with a Proportional integral derivative (PID) regulator at $\pm 0.1°$C. A heat-flux meter made of 6 − mm thick copper is used. A number of thermo-couples are installed to measure the local temperature and deliver an electrical signal that is proportional to the heat flux (see figure 2.5 and table 2.1). The heated substrate is larger than the heat flux meter, which is where the drops sit, in order to avoid boundary effects in measurement. Finally, the heat flux meter is coated with 0.9 mm of Nuflon GB, a derivative of Teflon that is composed of fluorinated loads dispersed into a thermoplastic resin. This coating enables drops to maintain contact angles of less than 40° and a surface energy of 18.5 mJ/m^2. A 1.74 μm roughness allows the substrate to maintain the drop and to pin the contact line during the major part of evaporation process.

The fluid is injected through a thin 0.7 mm pipe drilled at centre of the substrate, which is approximately 2% of the surface, and the drop is allowed to evaporate in air. If flow is too large, the liquid forms a jet that creates drops floating around in the test cell far from the observable scene. However, a slow injection rate will make the drop creation time too long relative to the allocated microgravity state duration. This configuration sometimes can lead to unwanted injection or suction during evaporation.
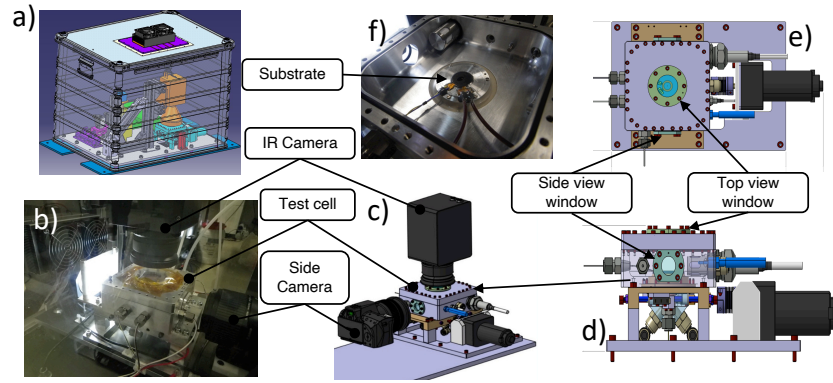
Figure 2.6: **(a)** Zarges box is transparent with the location of all equipment fitting in the box. Also represented the two Peltier modules which enable to thermal control the box temperature on the top of the box (Rack 1); **(b)** Test cell inside the confinement box; **(c)** Schematics of test cell with IR and Side view camera; **(d)** & **(e)** Side view and top view of the test cell respectively; **(f)** Picture of the test cell inner part and substrate.

For each parabola, a sessile drop is created on a substrate at a constant temperature and allowed to evaporate. The test cell is air-tight to prevent potential external perturbations and has a volume of 2.94×10^{-4} mm^3 which is large enough to ensure a constant vapour concentration far from the drop so that it is always below saturation. The air inside the test cell is renewed before each evaporation to ensure that previous evaporation does not affect the later tests. After the microgravity phase, the cell is connected via injection carriage below the test cell and moved by a motor to the plane vent-line to flush the vapour. Once the pressure drop has vacuumed the remaining liquid, vapour-free air at room temperature is injected into the cell to start a new experiment.

For more details on the experiment test cell and experiment design, please refer to the [24, 98].

2.3.3.1 *Video acquisition system*

The visible video acquisition system is composed of a Canon EOS 7D digital camera remotely controlled by a computer. We use a macro lens between $\times 2$ and $\times 3$ in order to magnify the sessile drop and record the movie almost in full field of view. The Infrared video acquisition system is composed of Variocam HR Head infrared camera remotely controlled by another computer. Compared to VP100, we used a macro lens $\times 1$ instead of a $\times 0 \cdot 6$. The aim of using the macro lens was to have an infrared pixel at 25 microns instead of 41 microns. This would also allow us to clearly see the thermocapillary instability cells (see figure 2.10) inside the sessile drop.

Figure 2.7: Experiment running under microgravity conditions. ESA parabolic flight VP140, November 2018).

2.4 PARABOLIC FLIGHT RESULTS AND DISCUSSION

Figure 2.8 shows the IR view (Top view) of sessile drop of pure ethanol on the heated substrate under the microgravity conditions from the parabolic flight experiment (VP140 − PF12). The new microlens allows us to clearly visualise instability cell. For the sessile drop of ethanol liquid drop at the imposed isothermal substrate temperature $T_{sub} = 40.3°C$, with a base diameter (2R) 7.3 mm, and interface height Γ from substrate 0.7 mm, there are approx 27 ± 1 number of instability cell.

We can also see sessile drop eye at the centre that is the sub-cooled region at the centre of the sessile drop and its temperature is approx $2°C$ lower than the substrate temperature with Radius R_{sc} around 1.2 mm.
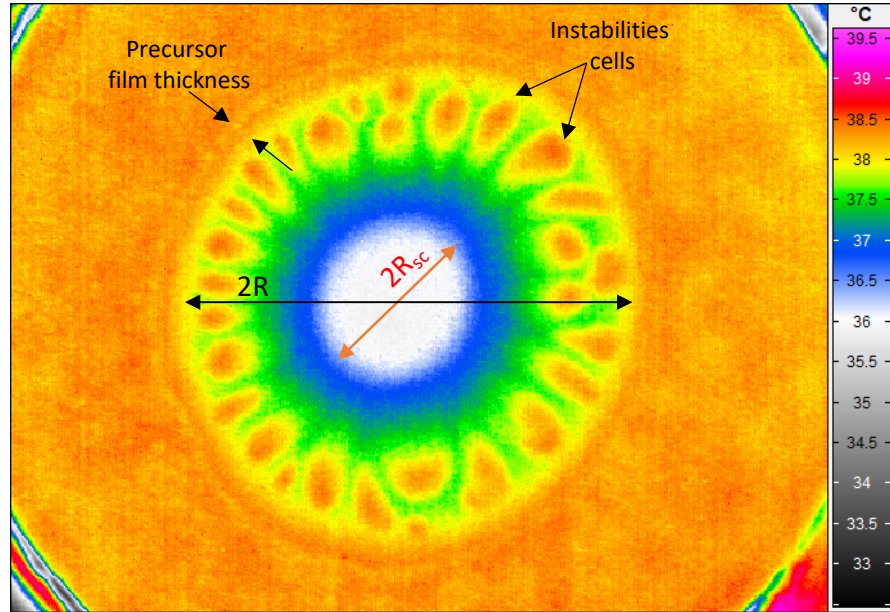
Figure 2.8: Infrared (top view) visualisation of the sessile drop of ethanol liquid drop at the imposed isothermal substrate temperature $T_{sub} = 40.3°C$, from experiment VP140PF12.

As it can be seen in the movie of figure 2.9 at 1.5 s only there is a constant contact diameter, after that sessile drop is sliding and spreading over the heated substrate that leads to an increase in the diameter of sessile drop and width of the precursor film. Due to this, we got only a few seconds of the constant area mode evaporation so it is difficult to compare the evaporation rate for the complete life cycle with numerical simulation from the parabolic flight experiment and unfortunately also, not a single drop evaporated completely. However, we can do a quantitative comparison of experimental results with sessile drop on the heated substrate at a given time (t) to compare the number of instability cells and temperature difference between the sub-cooled region and substrate.

In the each sessile drop evaporation experiment on the heat substrate we see precursor films around the sessile drop apex. Precursor film effect on the evaporation process can be interesting [99]. However, numerically we don't consider precursor films around the sessile drop during the evaporation. The instability cells doesn't travel in precursor film, however it disappears at the beginning of the precursor film. For the complete movie please ▶ play or scan QR..

Movie for Fig. 2.8 & 2.9.

Figure 2.9, shows the time series of the sessile drop from the parabolic flight VP140PF12. At $t = 2.2$ s is shown the injection phase of the sessile drop, then evaporation of ethanol sessile drop between time duration 3.96 s to 5.4 s in constant contact area mode, after $t = 5.4$ s sessile drop starts spreading and sliding towards the south-west cor-

| $t = 2.2$ s | $t = 3.96$ s | $t = 5.4$ s | $t = 8.8$ s |
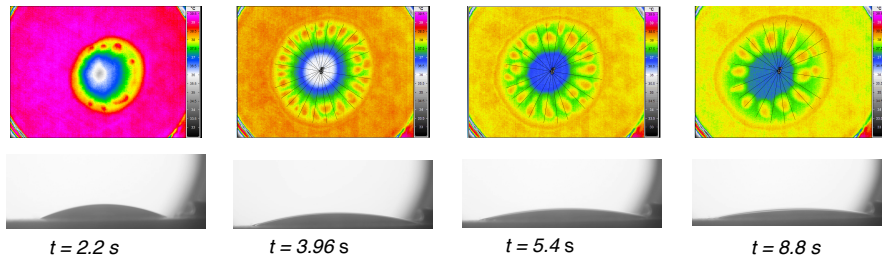
Figure 2.9: Time series of sessile drop from parabolic flight VP140, Parabola no. 12. IR visualisation (top) and drop shape (side view). Please also refer movies ▶ play or Scan QR.

| PF12, Tsub: 40.3 °C, Vol: 18 μL | PF13, Tsub: 45 °C, Vol: 10 μL | PF16, Tsub:50 °C, Vol: 21 μL |
| PF17, Tsub:50 °C, Vol: 21 μL | PF19, Tsub: 50 °C, Vol: 18 μL | PF22, Tsub:55 °C, Vol: 22 μL |
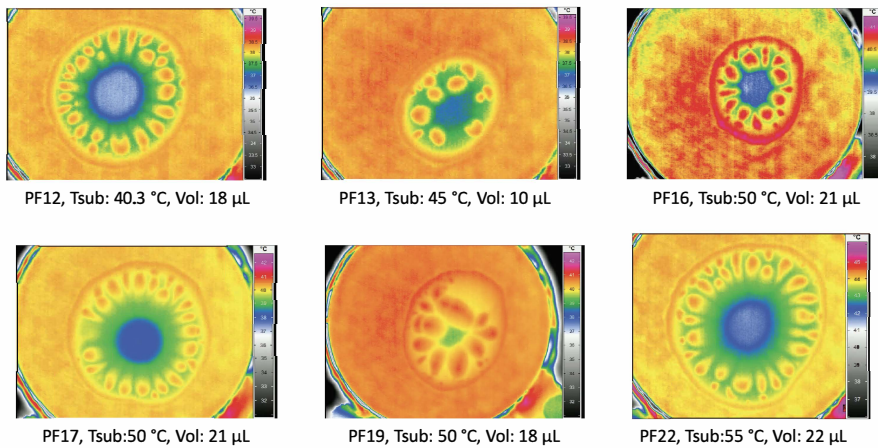
Figure 2.10: Infrared (top view) visualisation of the sessile drop of ethanol liquid at the different substrate temperatures and drop volumes under microgravity condition. ▶ play or Scan QR.

ner of the substrate, a marker is marked at the drop ($t = 3.96s$ s) which can be used in the IR images to follow the change in the diameter during the lifetime of sessile drop. The side view of the sessile drop (bottom) has been used to calculate the interface height only however shadow of the back wall on the right-hand side covers the corner of the drop which makes it difficult to mark the bottom of the drop thus resulting in low accuracy in the calculation of the interface height from the substrate.

Figure 2.10 and movies show the comparison of the sessile drop at the different volume and substrate temperature. During the parabolic flight experiment PF12, PF17 and PF22, we can see stable and clear instability cells for a few seconds of the experiments that would later also be used to compare with the numerical simulation. It can also be noted that all sessile drops in the movies start spreading and sliding towards the southwest corner of the substrate.

Parabolic experiments for sessile drop evaporation under microgravity conditions are complex and difficult to control the re - producibility

Movie for Fig. 2.10.

of the volume of the sessile drop, this issue comes from injection system, we can see similar behaviour in the sounding rocket [76], that still needs to be understood and mastered. Apart from the above problem, vibration and transition from 1.8 g to 0 g are the inherited effects that cannot be solved. If we get correct volume of sessile drop at the beginning of the microgravity phase of parabolic flight, sessile drop spreading and sliding can be controlled by using the groove on the substrate, and similar issues from the side view camera can be resolved by using broader backlight.

Even though we have high qualitative Infrared (IR) images from the parabolic flight VP139 and VP140, however, it would be difficult to follow sessile drops interface from the side view camera calculate the interface height that leads to calculate the evaporation rate. Also, it has been pointed out by F. Carle in his thesis [24] that the injection through a pipe drilled at the centre of the substrate presents a drawback. With the aircraft vibrations and g-jitter, this configuration can lead to unwanted injection or suction during evaporation. This phenomenon is particularly visible in the infrared visualisation and affects the thermal motion inside the drop as well as measurement of evaporation flux rate. In our experiment, it is also noticed that with spreading and sliding, the drop height is increased in the middle of sessile drop evaporation experiment.

Due to the various constraints instead of the re-fly with modification (in the side view camera), we decided to use previous experiment results particularly under microgravity conditions [24, 69, 98] to validate and perform the parametric study of sessile drop of ethanol liquid with our new numerical model for microgravity conditions. It would come with a drawback that we can not compare sessile drop instabilities quantitatively from the experiment with full numerical simulation.

2.4.1 *Experimental results for ethanol sessile drops under microgravity*

In this section, the experiment results from the CNES and ESA parabolic campaigns - VP88 VP95 VP98 and VP100 that were performed during PhD of Dr Florian CARLE [20, 24, 69, 98] have been re-visited. This section mainly focuses on the results of ethanol sessile drop evaporation rate under microgravity conditions and that will further be used for the comparison with numerical simulation in the chapter 4.

As mentioned by Carle et al, 2013 [69], two experiments were conducted with similar setups under terrestrial (1 g) and reduced gravity (μg) conditions (performed with parabolic flights). The results from experiments are shown in the figure 2.11. The experiment conditions and other details are as follows:
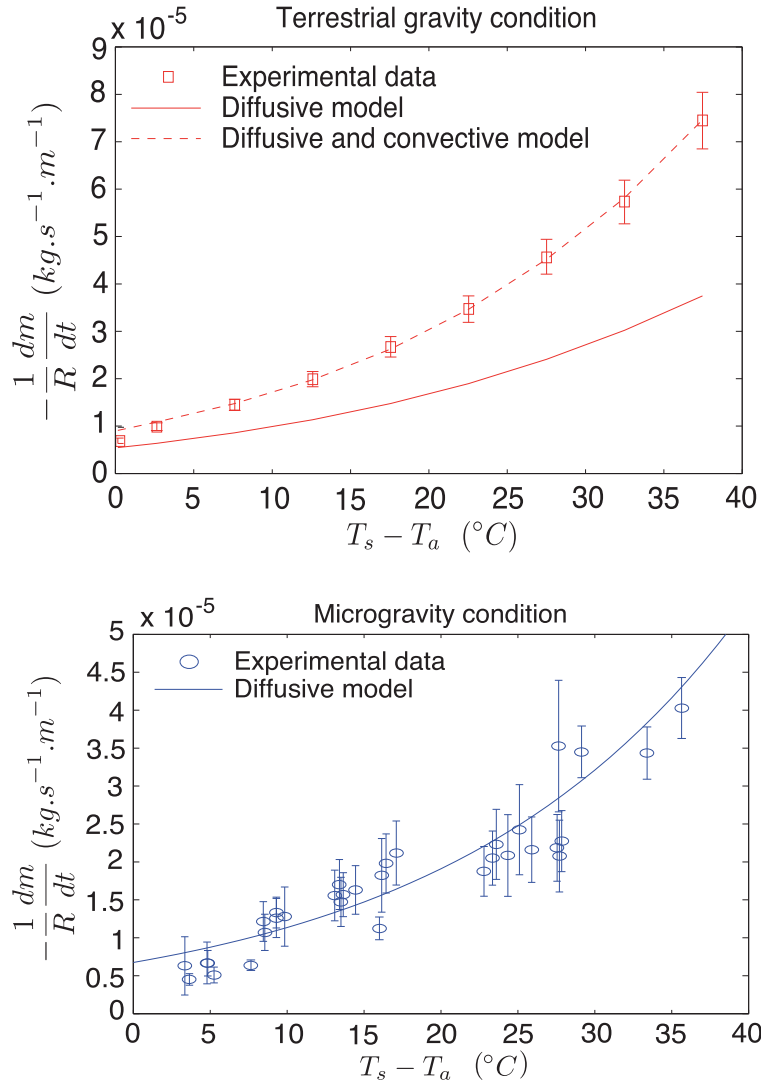
Figure 2.11: Evaporation rate by unit length radius of an ethanol sessile drop as a function of the temperature difference between substrate and ambient air for 1 g (top) and μg conditions (bottom). Figure credit [69]).

Ethanol drops were evaporated in air at the temperature of 25°C onto a cylindrical heated aluminum substrate ($10\,\text{mm} \times 10\,\text{mm}$) coated with a Nuflon layer, inside a cell that was large enough to ensure a constant vapor concentration far from the drop and below saturation to prevent potential external perturbations. The substrate was instrumented by a heat-flux meter that enabled the determination of evaporation rate $\left(-dm/dt = Q \cdot S/H_{evap}\right.$, where Q is the heat-flux absorbed by the drop on the substrate to evaporate, S is the area of wetting surface, and H_{evap} is the latent heat of vaporization). A high-definition camera was used to laterally visualize and measure geometrical parameters of the drops, i.e., base radius R, height H_t, and contact angle θ_t. The encountered base radius was always below the

capillary length ($l_c = 1.69$ mm in 1 g and $l_c = 7.46$ mm in µg); therefore, the drops had a spherical cap shape. They evaporated in a wetting situation ($\theta_i = 30°$ in 1 g and $\theta_i = 23°$ in µg), and the contact line was pinned nearly throughout the entire duration of evaporation due to the relative importance of the surface roughness ($r_{RMS} = 1.75$ µm). More information about the experimental set-up can be found in ref. [24, 69, 97].

Almost all the drops created have a diameter smaller than 8 mm, and therefore let the most of heat-flux meter dry at the least 46%. For the most disadvantageous case - smallest drop: 6 mm and the highest substrate temperature: 55°C - the radiation exchange with this region represents almost 23% of the measured heat flux. Therefore, it is important to subtract from the heat-flux meter signal the radioactive part and to only consider the energy needed to evaporate the drop. Moreover, under microgravity, because the buoyancy forces are null, the heat flux measured by the heat flux-meter is the energy transferred to the drop without any need for correction to account for the natural convection on the dry regions of the substrate. The heat flux applied to the drop is constant over time [24].

In the absence of gravity effects, the evaporation can then be correctly assumed to be a quasi-steady, diffusion-controlled process, regardless of the substrate temperature and isothermal temperature of drop [20, 69]. Indeed, the thermal gradient that develops inside an evaporating drop driven by the latent heat of vaporisation appears to be negligible when the drop is sufficiently thin and when it is evaporated on a highly thermally conductive substrate [86–88].

In figure 2.12 is shown the global evaporation rate of ethanol drops under various gravity levels i.e Earth (1g), Mars (0.38g), Moon (0.16g) and microgravity (10^{-2}g) as a function of the temperature difference between substrate and ambient air (20°C) [98]. Please refer Carle et al, 2016 [69] for more on the Spalding model, diffusive model and empirical diffusive and convective model equations used for the comparison in the plot.

We extract only microgravity results from the above result (from figure 2.11 and 2.12) and compared them. In figure 2.13 is shown the evaporation rate with respect to the substrate temperature. As we can neglect the effect of ambient temperature under microgravity due to the absence of convection in air and conduction due to low thermal conductivity of vapour and air.

In figure 2.13, the evaporation rate difference shown can either be from the heat-flux method for the calculation of evaporation rate or hysteresis from parabolic fight and it can also be both. However, we can use the analytical diffusion model to mark the correct evaporation
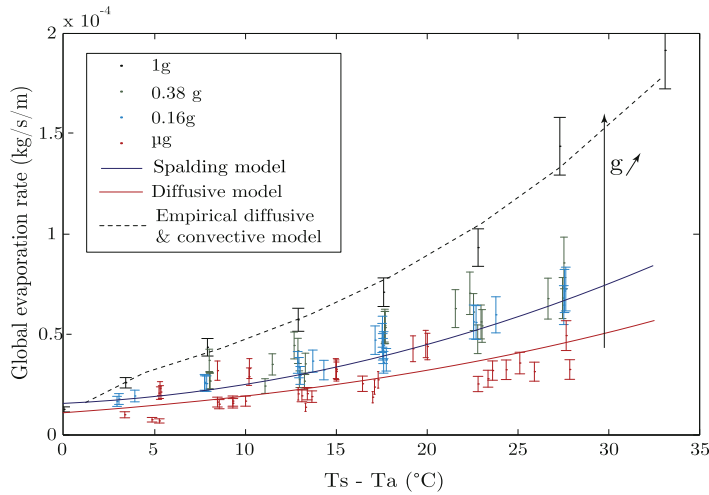
Figure 2.12: Global evaporation rate of ethanol drops under various gravity levels: Earth (1g), Mars (0.38g), Moon (0.16g) and micro (10^{-2}g) gravity as a function of the temperature difference between substrate and ambiant air (20°C). Coloured dots are experimental data with their error bars, and lines are the Spalding model, diffusive model and empirical diffusive and convective model). (For interpretation of the references to colour in this figure legend, the reader is referred to the web version of this article.) Figure credit [98].
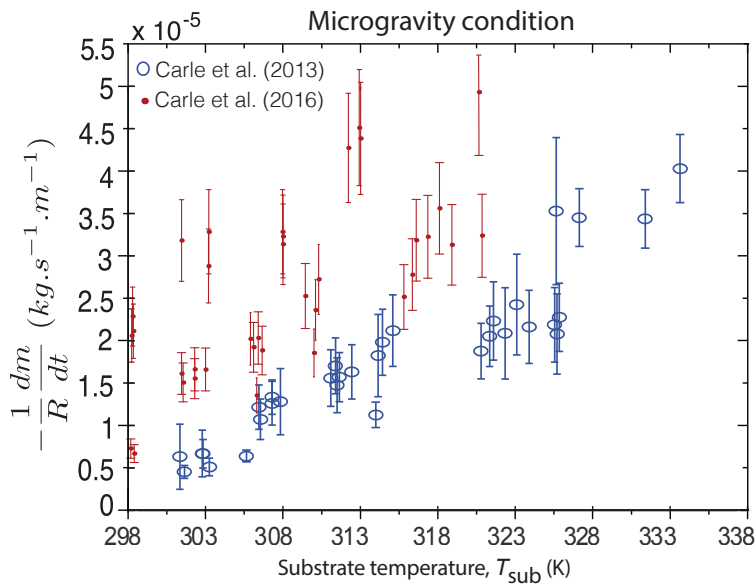
Figure 2.13: Comparison of the evaporation rate with respect to substrate temperature of the ethanol sessile drop under microgravity [69, 98].

rate. Picknett & Bexon is a well known analytical diffusion model that can be used to calculate sessile drop evaporation rate at ambient conditions (Non-heat substrate) [12]. Then results can be extrapolated by using temperature inside the Picknett & Bexon equation equivalent to substrate temperature (surely it would over predict the evaporation rate as Picknett & Bexon is not meant for the heated substrate). In figure 4.6, legend with blue circle shows that experimental results from Carle et al. 2013, (see fig. 2.13 & 2.11 blue circles) is relatively closure to the analytical diffusion model of Picknett & Bexon.

In conclusion, the heat flux method used to calculate the evaporation rate is prone to higher error in the calculation of the evaporation rate as it needs to calculate three different independent parameters correctly i.e contact area of the sessile drop with the substrate and heat flux from the sensor. Thirdly, in the heat flux method, we also need to account for the radiation exchange that will change with substrate temperature. It needs prier (over or under) knowing and then subtracting the radiative part from the heat-flux meter signal to only consider the energy in the evaporation of sessile drop.

As shown by the experiments under microgravity, evaporation can then be correctly assumed to be a quasi-steady, diffusion-controlled process. So, we can neglect Stefan flow in our diffusion model for microgravity conditions [20, 69].

Parabolic flight are not the best suitable means for sessile drop evaporation experiment due to vibration but most importantly due to hysteresis effect comes from the gravity levels (sudden transition from the 1.8g to μg, see figure 2.4) on the ambient inside the test cell. This hysteresis effect can influence the vapour around the sessile drop during the microgravity phase of the experiment. This influence on the vapour would increase the evaporation rate but in microgravity conditions, it should be the lowest in all the cases. Along with it unwanted injection or suction, spreading and sliding of sessile drop during evaporation made it complex and difficult to control the reproducibility.

In the next section, we follow the sounding rocket experiment that has higher advantages over parabolic flights for the microgravity experiment because of the absence of vibration, hysteresis effect and longer duration of the microgravity time duration. However, it is costly and requires sophisticated technology and specialized skills.

2.5 SOUNDING ROCKETS EXPERIMENT (ARLES)

This section is the article published in njp microgravity, Dec 2020 [1] "Kumar, S., Medale, M., Marco, P.D. et al. Sessile volatile drop evapo-

---

ration under microgravity. npj Microgravity 6, 37 (2020)" [76]. For the article please refer to appendix A.

NUMERICAL SIMULATIONS AND MODELING

3.1 INTRODUCTION

In this chapter, we shall be discussing the foundation of the numerical model for sessile drop evaporation on a heated substrate under microgravity. Based on the rocket and parabolic experiments that were discussed in the chapter 2.5 we are going to put forward the theoretical concept and assumptions for our numerical model. Then we look into the equations for drop liquid domain and surface boundary conditions with it to formulate the equation for local evaporation rate for sessile drop evaporation under microgravity conditions. We also look into the methodology used for numerical simulations in the COMSOL Multiphysics software along with our numerical model implementation in it. Also, into the optimization method in capturing the 3D instabilities and at the same time reducing the computational time heavily as accurate computations of the entire instability dynamics of sessile drop evaporation are quite expensive. Then the methods of time and space discretization are described. Finally, strategies for the initiation of the numerical simulation with ramping and other tweaks to avoid the thermal oscillations in domain during the Marangoni convection phase will be discussed.

3.2 THEORETICAL CONCEPT AND ASSUMPTION

We are considering sessile drop evaporation under microgravity conditions. The sessile drop is a spherical cap with a constant contact area with substrate (pinned mode). During the evaporation process, sessile drop evaporation rate is mainly controlled by the vapour diffusion in the surrounding atmosphere. The energy transfer from substrate to the interface of sessile drop under microgravity conditions is considered mainly due to Marangoni convection [76]. Marangoni convection occurs inside the sessile drop as an effect of surface tension gradient due to its temperature dependency. We neglected the energy transfer into gas phase via radiative and conductive mode. Due to the absence of gravity in space, there is no convection in vapour phase that plays an important role in vapor for mass and energy transport that leads to higher evaporation rate on the Earth conditions [69, 76] and we can also neglect the Stefan flow in microgravity conditions [20, 69]. So, most importantly, we assume in microgravity conditions, sessile drop is evaporating under fully saturated vapour pressure condition based on local interface temperature, i.e interface of the sessile drop is fully

covered with vapour. In summary, we consider the fully coupled fluid flow-heat transfer problem inside the domains and at the interface we successfully managed to accommodate the effect of vapor (ambient conditions) via our surface boundary conditions. Surface boundary conditions are only valid in the absence of external forces such as an external electric field that could affect the vapour transportation around the sessile drop interface thus the evaporation rate [76, 100]. For surface boundary conditions we are going to take help from Pickentt & Bexon's analytical equation [12] which is mainly used for the diffusion base evaporation at the ambient temperature for capillary length $L_c < \sqrt{\sigma/(\rho g)}$, to translate into the local evaporation rate at the sessile drop interface. The local evaporation rate would later be used to calculate and define the global evaporation rate (E_v) for the sessile drop on the heated substrate under microgravity conditions.
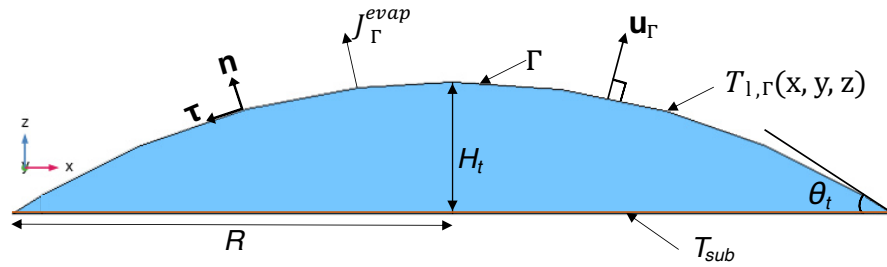
3.3   GEOMETRY AND ENVIRONMENT CONDITIONS

Figure 3.1: **Schematic of the sessile drop.** R is the base radius of the pinned sessile drop, T_{sub} is the substrate temperature, θ_t is the contact of sessile drop, H_t maximum height of the interface from the substrate, Γ is the interface of the sessile drop, $T_{l,\Gamma}(x,y,z)$ is the temperature at the mesh node, u_Γ is the interface Γ velocity due to evaporation, and J_Γ^{evap} is the local evaporation rate.

The model considers sessile drop as a three - dimensional spherical cap with a constant base radius, ($R = constant$) (i.e Constant base radius mode (CR) mode) which is also known as the pinned sessile drop, and moving interface (Γ) with substrate over time as volume changes during the evaporation process. Figure 3.1 shows the details for sessile drop geometries. This is valid for the 90% of the drop lifetime of the evaporation process. Substrate is considered isothermal (heated substrate) with constant substrate temperature (T_{sub}).

3.4   NUMERICAL MODEL FORMULATION

The model solves the in-compressible Navier-Stokes equations for conservation of momentum and continuity equations for conservation of mass in the drop liquid domain along with heat transfer equations for single-phase fluid flow which in their most general form are:

$$\rho \left(\left. \frac{\partial \mathbf{u}}{\partial t} \right|_f + [(\mathbf{u} - \mathbf{u}_m) \cdot \boldsymbol{\nabla}] \, \mathbf{u} \right) = \boldsymbol{\nabla} \cdot \boldsymbol{\sigma}, \qquad (3.1)$$

$$\boldsymbol{\nabla} \cdot \mathbf{u} = 0, \qquad (3.2)$$

$$\rho c_p \left(\left. \frac{\partial T}{\partial t} \right|_f + (\mathbf{u} - \mathbf{u}_m) \cdot \boldsymbol{\nabla} T \right) + \boldsymbol{\nabla} \cdot \mathbf{q} = 0, \qquad (3.3)$$

$$\mathbf{q} = -k\nabla T \qquad (3.4)$$

Here, $\mathbf{u}$ is the velocity vector $(\text{m} \cdot \text{s}^{-1})$, $\mathbf{u}_m$ mesh velocity $(\text{m} \cdot \text{s}^{-1})$, T is the temperature field (K), and $\rho(T)$, $c_p(T)$ and $k(T)$ are temperature dependent density $(\text{kg} \cdot \text{m}^{-3})$, specific heat capacity at constant pressure $(\text{J} \cdot (\text{kg} \cdot \text{K})^{-1})$ and thermal conductivity $(\text{W} \cdot (\text{m} \cdot \text{K})^{-1})$ of the drop respectively, subscript f means that time derivative is taken at a fixed mesh node (fixed mesh coordinates), total stress tensor is $\boldsymbol{\sigma} = -p\mathbf{I} + \boldsymbol{\pi}$ where p is hydrodynamic pressure (Pa), $\mathbf{I}$ is the identity matrix and $\boldsymbol{\pi} = \mu \left(\boldsymbol{\nabla}\mathbf{u} + (\boldsymbol{\nabla}\mathbf{u})^{\mathsf{T}} \right)$ is viscous stress tensor (Pa), μ dynamic viscosity, $(\text{Pa} \cdot \text{s})$, $\mathbf{q}$ is conductive heat flux, that satisfies the Fourier's law of heat conduction. k is the thermal conductivity $(\text{W} \cdot (\text{m} \cdot \text{K})^{-1})$.

3.5 INITIAL CONDITIONS

Since, the physical problem of sessile drop that we are solving is an unsteady, non-isothermal evaporation of pinned sessile drop, so, the initial conditions are as follows: at time $t = 0$, the drop is a spherical cap of contact angle $\theta_t = \theta_0$ with substrate and base radius R; sessile drop initial temperature $T|_{t=0} = T_{sub}$, the fluid flow inside sessile drop is at rest $(\mathbf{u}|_{t=0} = 0)$. The initial pressure filed within the drop is set to the Laplace pressure (Δp) plus the atmospheric pressure $(P_{atm} = P)$, i.e $p|_{t=0} = P_{atm} + 2\gamma \sin\theta_0 / R$, where γ is the liquid-gas interfacial tension and θ_0 is initial contact angle. The initial temperature in the whole domain is set to the substrate temperature (T_{sub}).

3.6 BOUNDARY CONDITIONS

The above governing equations are subject to boundary conditions along liquid-gas interface and the substrate. So, now we layout details about the constraints applied to the sessile drop along liquid-gas interface and the substrate. In our work, the substrate is considered isothermal at T_{sub}. The fluid flow boundary condition at the substrate is no slip.

Now, let us consider the interface (Free-surface boundary) conditions Γ at the sessile drop moving interface. To begin with, the

temperature at the interface is non-uniform based on the latent heat of evaporation, provided that local evaporation rate is known (see eq. 3.8), one can define the boundary conditions at Γ as follows:

$$-k\nabla T \cdot \mathbf{n} = \frac{J_\Gamma^{evap} H_{evap}}{\pi(R^2 + H_t^2)}, \tag{3.5}$$

$$\rho\left(\mathbf{u} \cdot \mathbf{n} - u_\Gamma\right) = \frac{J_\Gamma^{evap}}{\pi(R^2 + H_t^2)}, \tag{3.6}$$

In equation 3.5, $\mathbf{n}$ is the unit normal vector, J_Γ^{evap} is local evaporation rate, H_{evap} is latent heat of evaporation, and H_t is the height of sessile drop at time. In equation 3.6 conservation of mass across the interface Γ imposes the velocity for deforming mesh. So, the moving interface Γ is considered as a boundary, moving along normal vector $\mathbf{n}$ with velocity u_Γ. Local interface velocity u_Γ and local evaporation rate J_Γ^{evap} are defined later.

Similarly, the stress balance at the moving liquid interface Γ is as follows:

$$\underbrace{\boldsymbol{\sigma} \cdot \mathbf{n}}_{\text{Total stress}} = \underbrace{-\gamma\left(\nabla \cdot \mathbf{n}\right)_\Gamma \mathbf{n}}_{\text{Normal stress}} + \underbrace{\frac{d\gamma}{dT}\nabla_\Gamma T}_{\text{Tangential stress}}, \tag{3.7}$$

The normal and tangential stresses at the liquid boundary should be balanced across and along the interface, where $\left(\nabla \cdot \mathbf{n}\right)_\Gamma$ is the divergence of vector $\mathbf{n}$ at Γ, that is curvature of Γ, which is equal to $2\sin\theta/R$, $\nabla_\Gamma T$ is the surface gradient of temperature at the interface Γ and $\frac{d\gamma}{dT}$ is temperature coefficient of surface tension.

3.7   EVAPORATION RATE

In order to compare evaporation rates of sessile drops measured in microgravity experiments, one can refer to the analytical model for evaporation limited by diffusion adapted from Picknett and Bexon [12] for constant contact area (up to de-pinning) and spherical cap shape. However, the analytical model derived by Picknett and Bexon is for the sessile drop in the ambient temperature on the surface (no heating). In order to adapt and to calculate the correct evaporation rate based on the interface temperature, we modified the equation 13 derived by Picknett and Bexon [12]. The modified equation can be read as follows:

$$J_\Gamma^{evap}\left(R, P, T_{l,\Gamma}, \theta_t, x, y, z\right) = 2\pi D_{coeff}(P, T_{l,\Gamma})C_{sat}(T_{l,\Gamma})$$
$$\times RF(\theta(t)) \tag{3.8}$$

where, $J_\Gamma^{evap}(R, P, T_{l,\Gamma}, \theta_t, x, y, z)_\Gamma$ is local evaporation rate on the Γ instead of the total evaporation rate derived by Picknett and Bexon, and x, y and z are the coordinates of computational domain in the direction of the x-axis, y-axis, z-axis respectively, $T_{l,\Gamma}$ is the interface temperature at the mesh node in Kelvin, R is the base radius, C_{sat} is the saturated vapour concentration, and D_{coeff} is the diffusion coefficient of liquid drop in ambient environment. D_{coeff} is calculated according to the Fuller - Schettler - Giddings equation [77] as follows:

$$D_{coeff}(P, T_{l,\Gamma}) = \frac{0.01013 T_{l,\Gamma}^{1.75} \left(\frac{1}{M_a} + \frac{1}{M_l}\right)^{0.5}}{P \left[\left(\sum v_a\right)^{1/3} + \left(\sum v_l\right)^{1/3}\right]^2}, \tag{3.9}$$

where M_a and M_l are the molecular weights of the ambient fluid and liquid of sessile drop in $\text{g} \cdot \text{mol}^{-1}$ respectively; P is the ambient pressure in Pa, and v_a and v_l are the atomic diffusion volumes. For more information on the accuracy and other method of the D_{coeff} please refer to section 1.3.1.

The concentration of vapor at drop interface Γ, C_{sat} can be calculated by assuming it as ideal gas and can be written as:

$$C_{sat}(T_{l,\Gamma}) = \frac{P_{sat} M_l}{R_{gas} T_{l,\Gamma}} \tag{3.10}$$

In equation 3.10, R_{gas} is the universal gas constant, P_{sat} is the saturation vapour pressure based on local temperature $T_{l,\Gamma}$, as, we assume that due to absence of the microgravity there is no convection transport in the vapour, P_{sat} can be determined according to the Clausuis-Clapeyron equation, defined by

$$P_{sat}(T) = P_{l,sat}^{ref} \exp\left[-\frac{(H_{vap} M_l)}{R_{gas}}\left(\frac{1}{T_{l,\Gamma}} - \frac{1}{T_{sat}^{ref}}\right)\right] \tag{3.11}$$

In the Clausuis-Clapeyron equation $P_{l,sat}^{ref}$ is the reference saturation vapour pressure based on the reference saturation temperature T_{sat}^{ref}.

$$F(\theta(t)) = \begin{cases} \left(0.6366\,\theta + 0.09591\,\theta^2 - 0.06144\,\theta^3\right) / \sin\theta \\ \qquad\qquad \text{for} \quad 0 \le \theta < \pi/18, \\ \left(0.00008957 + 0.6333\,\theta + 0.116\,\theta^2 \right. \\ \qquad\quad \left. -0.08878\,\theta^3 + 0.01033\,\theta^4\right) / \sin\theta \\ \qquad\qquad \text{for} \quad \pi/18 \le \theta \le \pi. \end{cases} \tag{3.12}$$

$F(\theta(t))$ is the function of contact angle with substrate derived by Picknett and Bexon [12] using the Snow's series solution [101]. For

more information on the $F(\theta(t))$ please refer chapter 1 section 1.3.2. Finally, the local evaporation rate J_Γ^{evap} at Γ can be derived by using the equation 3.8 along with the equation 3.9 3.10, 3.11 and 3.12 :

$$
\begin{aligned}
J_\Gamma^{evap} & (R, P, T_{l,\Gamma}, \theta_t, t, x, y, z) \\
&= 2\pi R \frac{0.01013 T_{l,\Gamma}^{1.75} \left(\frac{1}{M_a} + \frac{1}{M_l}\right)^{0.5}}{P\left[(\sum v_a)^{1/3} + (\sum v_l)^{1/3}\right]^2} \times \frac{M_l}{R_{gas} T_{l,\Gamma}} \\
&\quad \times P_{l,\text{sat}}^{ref} \exp\left[-\frac{(H_{\text{vap}} M_l)}{R}\left(\frac{1}{T_{l,\Gamma}} - \frac{1}{T_{\text{sat}}^{ref}}\right)\right] \times F(\theta(t))
\end{aligned}
\tag{3.13}
$$

As J_Γ^{evap} is the local evaporation rate at the interface Γ, in other words, is the spatial dependent evaporation rate, however to validate and compare with experiment we define the average evaporation rate of sessile drop at any given θ (or time), that could be defined as:

$$
-\frac{dm}{dt} = J_{avg,\theta}^{evap} = \frac{1}{\int_\Gamma d\Gamma} \int_\Gamma J_\Gamma^{evap}(R, P, T_{l,\Gamma}, \theta_t, t, x, y, z) \, d\Gamma \tag{3.14}
$$

And then finally, the evaporation rate independent of base radius R that we are going to use in our further discussion can be written as:

$$
E_v = -\frac{1}{R} \cdot \frac{dm}{dt} = \frac{J_{avg,\theta}^{evap}}{R} \tag{3.15}
$$

Finally the interface velocity u_Γ at Γ is derived based on average evaporation rate and that can be calculated by using the equation 3.14, $J_{tot} = J_{avg,\theta}^{evap}$; with two assumptions: pinned contact line ($R = const$) and spherical-cap shape of the drop in the course of evaporation [64].

$$
u_\Gamma = -\frac{J_{tot}}{\pi \rho R^3} \frac{(1 + \cos \theta_t)^2}{\sin \theta_t} z. \tag{3.16}
$$

In an effort to obtain observable comparisons between numerical and experimental results, we post-processed the computed temperature field into simplified IR images. Computation is done by summing the IR radiation coming from substrate surface (assumed to be a grey body) with the integral of IR radiation sources distributed across the thickness of a semi-transparent drop [64]. The equation 31 of the [64] is expressed as:

$$
\begin{aligned}
T_{IR,num}^4(x,y) = {} & T_{sub}^4 e^{-k_{SW} f(x,y)} \\
& + \int_0^{f(x,y)} T^4(x,y,z) k_{SW} e^{-k_{SW}(f(x,y)-z)} dz
\end{aligned}
\tag{3.17}
$$

where, $T_{IR,num}$ is IR numerical, k_{SW} (mm^{-1}) absorption coefficient, f(x,y) represents the local drop thickness and T_{sub} is substrate temperature. The equation 31 of [64] is corrected as the ε^* is not the emissivity but it is IR camera correction.

3.8 OVERVIEW AND MODEL IMPLEMENTATION IN COSMOL

The governing equations have been implemented and solved with the commercial COMSOL Multiphysics® software, which is based on the finite element method (FEM). The modeling workflow of COMSOL Multiphysics is straightforward and is defined by the following steps: define the geometry, select the material to be modeled, select the type of heat transfer, define the boundary and initial conditions, define the finite element mesh, select a solver, compute the problem solution and visualize the results. All of these steps are accessed from the COMSOL Desktop. The mesh and solver steps are often automatically included with the default settings, which are tailored to each type of heat transfer interface [102].

3.8.1 *Physics interface and physical properties*

The Laminar flow physics interfaces build on conservation laws for momentum, mass, and energy. These laws are expressed in terms of partial differential equations, which are solved by the module together with the specified initial and boundary conditions. The equations are solved using stabilized finite element formulations for fluid flow, in combination with damped Newton methods and, for time-dependent problems, different time-dependent solver algorithms. Whereas the Heat Transfer in Fluids interface defined in fluid domains corresponds to the convection-diffusion equation that may contain additional contributions like heat sources. The Heat Transfer in Fluids interface accounts for conduction and convection in gases and liquids as the default heat transfer mechanisms. The coupling to the flow field in the convection term may be entered manually in the physics interface, or it may be selected from a list that couples heat transfer to an existing fluid flow interface. Physical properties such as thermal conductivity, heat capacity, density, and emissivity can be obtained from the built-in material library for solids and fluids and from the Material Library add-on in COMSOL Multiphysics® software [102].

To model the sessile drop evaporation process we are using the mixed-order discretization for Laminar Flow, i.e P2 + P1 elements — that is, tri-quadratic interpolations for the velocity fields and piecewise linear interpolation for pressure. Discretization for the temperature field for heat transfer in fluids is tri-quadratic Lagrange. The geometry shape order is using the quadratic shape functions.

3.8.2 *Model implementation in COMSOL*

In figure 3.2 is shown our sessile drop numerical simulation workflow, which describes in detail the entire model building process. We de-
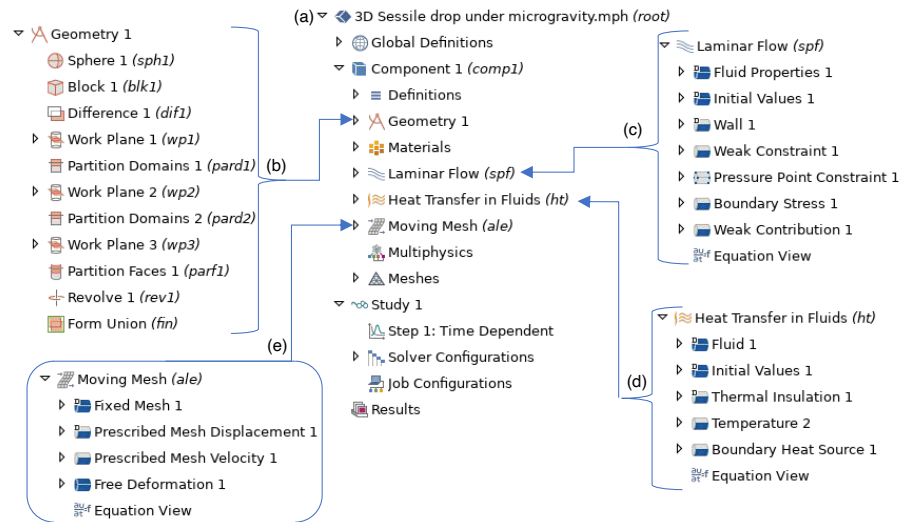
Figure 3.2: **Modelling workflow. (a)** Model Builder with main branches and subbranches; **(b)** This subbranch contains the definition of the model's geometry for sessile drop; **(c)** Laminar flow physics interface with its sub nodes based on the model definition; **(d)** Physics interface of Heat Transfer in fluid; **(e)** Physics interface of the moving mesh.

velop and execute a multiphysics simulation from geometry, physics and finally to results that could be easily used in the optimization and to reproduce the results. In figure 3.2a, showing root containing the main branches:

1. Global Definitions : Define global parameters, global Variables, Functions and Mesh Parts. Which are globally available in all model components.

2. Component : This branch includes the subbranches Definitions (local), Geometry, Materials, physics interfaces, and Mesh.

3. Study : This subbranch is where we set up study steps and solver configurations to solve a model using one or more study types.

4. Results : To present and analyze results.

After the above brief introduction on the workflow, let's drive into the implementation of the model using the weak form. After defining the initial independent variables such as based radius and contact angle of the sessile drop, substrate temperature, ambient pressure, molar masses of the ambient gas and liquid drop, and others in the global definition we generate the sessile drop cap. Geometry is shown in figure 3.2b and the final shape of the sessile drop in the figure 3.5.

Next, the temperature-dependent properties such as density, dynamic viscosity, thermal conductivity, surface tension coefficient and heat capacity at constant pressure are defined in the materials whereas
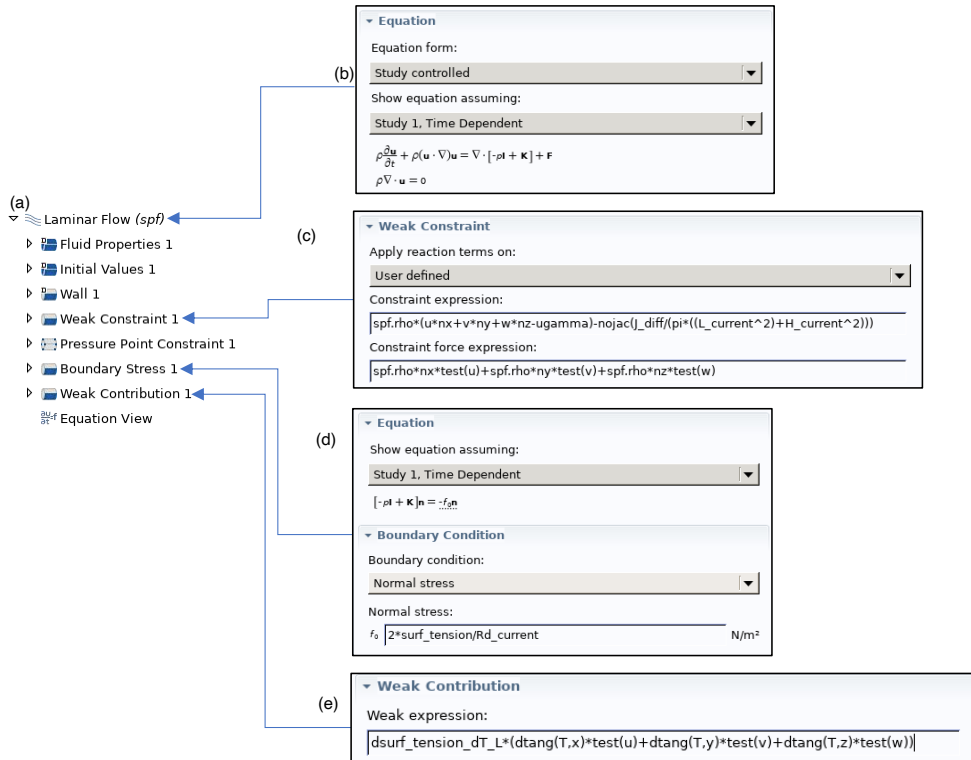
Figure 3.3: **Laminar flow physics interface with implemented boundary conditions. (a)** Laminar flow physics interface with its nodes; **(b)** Laminar flow physics equation (equation 3.1 & 3.2); **(c)** Surface boundary conditions equation 3.6 in weak form; **(d)** & **(e)** Total Stress at the moving liquid interface (equation 3.7).

the equation 3.13, equation 3.17 and equation 3.16 for local evaporation rate, IR numerical and moving mesh velocity respectively are defined in the definition.

Now, to handle the physical problems of the sessile drop evaporation we add the Laminar flow physics interface, heat transfer interface and moving mesh interface as shown in the figure 3.2c, 3.2d and 3.2e. The equations solved by the Laminar Flow interface are the Navier-Stokes equations for conservation of momentum and the continuity equation for conservation of mass (equation 3.1 & 3.2) as shown in the figure 3.3b using the weak form of the equations. Solving Partial differential equations (PDEs) generally means we must take the time to set up the underlying equations, material properties, and boundary conditions for a given problem. COMSOL Multiphysics, however, relieves much of this work. The software provides physics interfaces that consist of nodes and settings that set up the equations and basic initial and boundary conditions of physics as showing in figure 3.3a, but any other boundary conditions must be defined using the weak constraints and contribution (see figure 3.3c and 3.3e), i.e to add an extra term that does not fit into the general or coefficient form used by COMSOL,
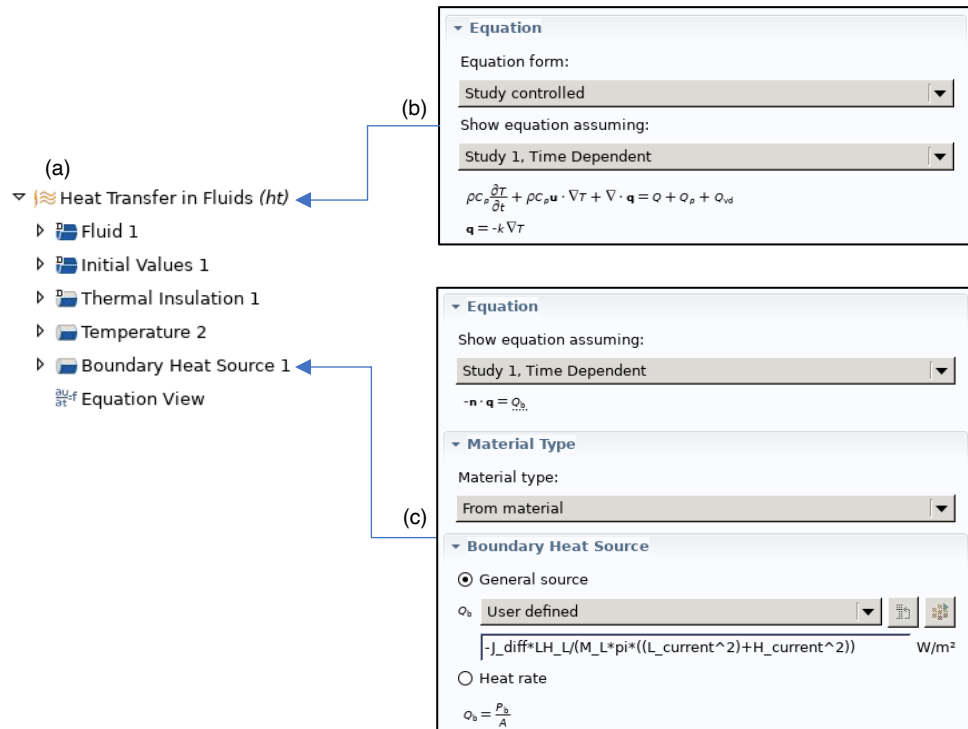
Figure 3.4: **Heat transfer interface with implemented boundary conditions. (a)** Heat transfer in fluids interface with its nodes; **(b)** Heat transfer physics equation (equation 3.3 & 3.4); **(c)** Boundary heat source (Sink) at the Γ (equation 3.5).

the weak form is the most general form to use. The weak constraints should read "constraint added to the weak form of the equation". It might be a constraint added in the domain or boundary or both, more commonly it is simply a Dirichlet-like boundary condition. The usual way to add such a constraint still solving the problem consists of adding a Lagrange multiplier. It leads to a choice to make about which degrees of freedom you allow to be modified so that your problem is still well-posed.

The equation 3.6 along Γ is implemented using the weak constraint as shown in the figure 3.3c, with constraint expressed as

```
spf.rho*(u*nx+v*ny+w*nz-ugamma)
        -nojac(J_diff/(pi*((L_current^2)+H_current^2)))
```

and the constraint force expression is

```
spf.rho*nx*test(u)+spf.rho*ny*test(v)+spf.rho*nz*test(w)
```

The operator nojac(*expr*) used here makes sure that expression

```
J_diff/(pi*((L_current^2)+H_current^2))
```

that it operates on is excluded from the Jacobian computation (it prevents all symbolic differentiation). The use of the nojac operator can then significantly lower the memory requirements by avoiding fill-in of the Jacobian matrix, but its use might also slow down the convergence of the solution but overall it improves performance on CPU time. Concurrently, the equation 3.7 at Γ is implemented in two steps, Boundary stress is used to implement the normal stress component,

```
2*surf_tension/Rd_current
```

where, term

```
Rd_current = R/(1-cos_Theta_current^2)^0.5
```

see figure 3.3d, along with it to add tangential component of the total stress a Weak contribution is used. The Weak Contribution adds a term or contributes in the weak form of the existing boundary equation. So, tangential component of the total stress in Weak form reads,

```
dsurf_tension_dT_L*(dtang(T,x)*test(u)
      +dtang(T,y)*test(v)+dtang(T,z)*test(w))
```

as shown in figure 3.3e. Where, dtang(*expr*) operator to compute components of the gradient of an expression projected onto the plane tangent to the boundary where the evaluation takes place.

We also add the pressure point constraint as Navier Stokes equation involves the pressure only through its derivatives, so in our model, we need to specify the pressure at least at one point. In our case, we use the highest point of interface Γ.

Similarly, the temperature equations 3.3 & 3.4 defined in fluid domains correspond to convection-diffusion equation that may contain additional contributions like heat sources which are defined in Heat transfer for fluids physics interfaces (see figure 3.4a & 3.4b). The default nodes of the interface are Fluid (properties), Thermal Insulation (the default boundary condition), and Initial Values. Then, we add other nodes that implement, for example, temperature (for the constant substrate temperature) and boundary heat sources (sink at the Γ) are added. In figure 3.4c shown the equation 3.5 for the energy balance at the Γ.

3.9 MOVING MESH INTERFACE

To solve for the time-dependent moving interface problem where the sessile drop interface Γ is changing its shape due to evaporation, the Moving Mesh interface based on an Arbitrary Lagrangian-Eulerian (Arbitrary Lagrangian Eulerian (ALE)) formulation is used to control

the spatial frame at Γ. The Moving Mesh (ALE) interface is that which defines the deformation of the material frame relative to the geometry frame, i.e Moving Mesh functionality deforms the spatial frame mesh relative to the material frame mesh. Moreover, as the interface Γ moves in time, the mesh on which it is discretized the governing equations are dynamically fitted on the moving boundary. The location of Γ during evaporation is located based on the drop interface velocity u_Γ which is given by equation 3.16. Therefore, a mesh velocity term $\mathbf{u}_m$ appears in momentum and heat transport equations (equation 3.1 and 3.3). The mesh deforms in such a way to follow the moving interface Γ of the computational domain, and so, it approaches closer and closer to the substrate due to evaporation. In figure 3.2e is shown the Moving Mesh physics interface that handles the removal of the mass at Γ due to evaporation. The equation 3.16 is added to the node Prescribed Mesh Velocity.
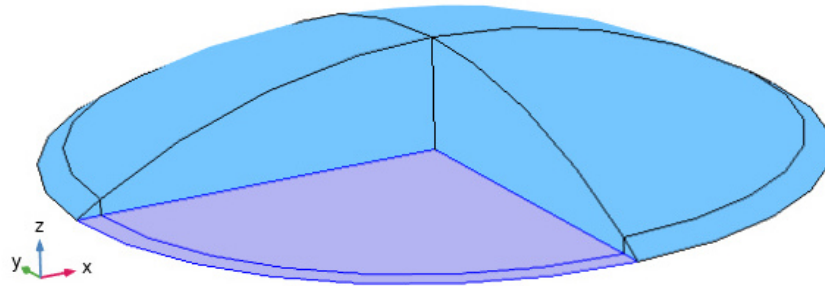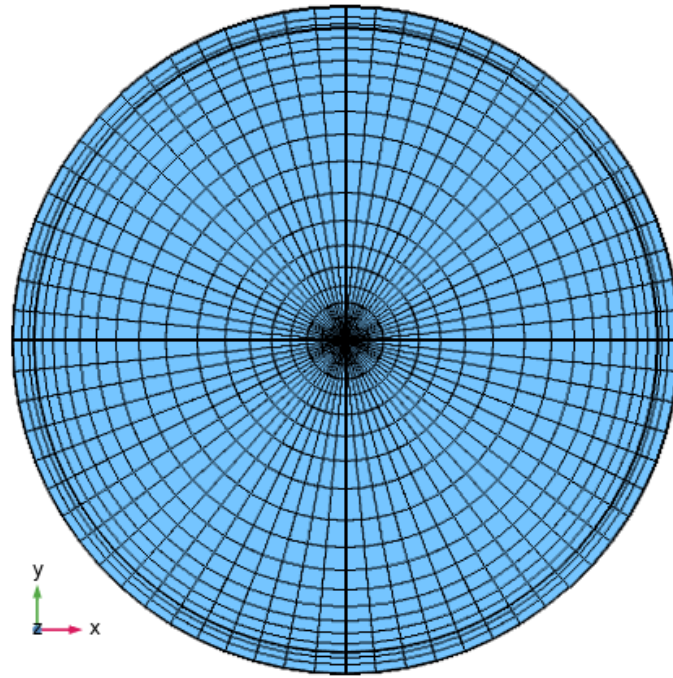
3.10   SPATIAL AND TIME DISCRETIZATIONS

Figure 3.5: **Cut view of the computational domain.** For our numerical simulation of the pure fluid Ethanol at initial contact angle $\theta_0 = 33°$.

Accurate computations of the entire instability dynamics of sessile drop evaporation are quite expensive as the observed flow is essentially three-dimensional [63, 97]. Indeed, owing to huge ratios between time scales (instability dynamics versus total evaporation time) and spatial ones (local fluctuation scales versus total device volume), one has to consider a small time and space discretization parameters simultaneously, while integrating over long evaporation time and sessile drop computational domains.

3.10.1   *Spatial discretization: Meshing*

A simulation campaign was dedicated to determining the appropriate mesh that can provide numerical outputs independent of the mesh used. We tested various types of spatial discretizations, from fully unstructured mesh to mixed with an aim to achieve evaporation and Marangoni instabilities occurrence independent of grid sensitivity. Fig-

(a) **Top View of the mesh.** Radial and circumferential distributions of the mesh elements.
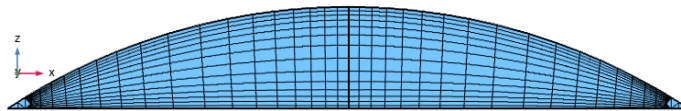
(b) **Cut side view of the mesh in vertical median plane.** Element distribution between the substrate and Interface.

Figure 3.6: Spatial discretization: Meshing of the sessile drop.

ure 3.6 presents the final configuration used for numerical simulations. Figure 3.6a is the top view of the mesh structure. Similarly, figure 3.6b shows structure of the mesh elements in the depth of sessile drop (for the other tested meshes see appendix C). Generated meshes are axisymmetric with the combination of hexahedra, prisms, quads and triangle elements. Mesh elements are controlled by defining the distribution of the elements in vertical, radial and circumferential directions, which are adjusted according to the size of the sessile drop, substrate temperature and fluid properties.

For the sessile drop of the ethanol with initial contact angle $\theta_0 = 33°$, base radius $R = 1.5$ mm, ambient pressure $P = 0.835$ bar, and substrate temperature $T_{sub} = 318.15$ K, for which we used 17 number of elements in the radial direction (RD) with element ratio(ER) 3, 68 number of elements in the circumferential direction (CD) with element ratio (ER) 1 (see fig.3.6a), and 14 number of element in the vertical direction (VD) with ER 4 (see 3.6b), that leads to a total of 17695

mesh elements. Types of the element: 15232 are hexahedra elements, 4488 are quads elements, 2176 are prisms elements and remaining are the triangles, edges elements and vertex elements. Please, refer to appendix section C for details on the mesh convergence results and other type of tested meshes.

3.10.2 *Time discretization*

The coupled Navier-Stokes and energy equations constitute a non-linear equation system. A nonlinear solver must hence be selected to solve the problem. The nonlinear solver iterates to reach the final solution. At every iteration, a linearized version of the nonlinear system is solved using a linear solver. Moreover, in the considered time-dependent case, a time integration is also performed to get relevant transient solutions.
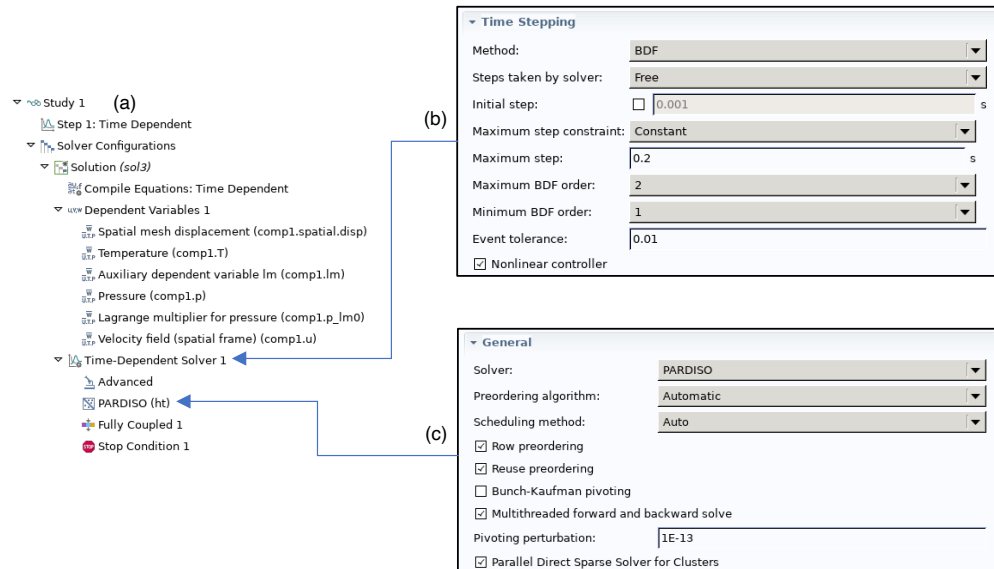

Figure 3.7: **Study setting (a)** Solver sequence and configuration; **(b)** Time stepping; **(c)** Linear solver.

3.10.2.1 *Time integration method:*

To perform the solution of our time-dependent problem we selected the implicit time-stepping method Backward differentiation formula (BDF) at order two for solving the set of partial differential equations. BDF methods have been used for a long time and are known for their stability. The maximum time-step (Δt) is set to 1 s in case of primary Marangoni instability. However, during the secondary instability phase of sessile drop evaporation Δt is between 10^{-2} to 10^{-3} s for Ethanol and in the range of 10^{-3} to 10^{-4} s for HFE7100.

Nonlinear solver: In the time-dependent case, the initial guess for each time step is the previous time step, which is a very initial value for the nonlinear solver, provided the time step is conveniently chosen, as previously indicated. The automatic damping algorithm in the Newton method is used.

Linear solver: To solve linearized systems of equations we follow the fully coupled approach, i.e a single large system of equations that solve for all of the unknowns at once (includes all of the couplings between multiphysics effects), within each iteration. The Parallel sparse direct solver (PARDISO) (parallel sparse direct solver) algorithm is chosen for solving linear systems of equations. PARDISO is selected with a preordering algorithm: nested dissection multithreaded (the default to perform the nested dissection faster when COMSOL Multiphysics runs multi threaded). This approach has the advantage of being the most robust and general. They have the drawback of requiring relatively a lot of memory and computational time, which go up rapidly with an increasing problem size (finer space and time discretizations).

For more details on time discretization in COMSOL Multiphysics ® software please refer to its documentation [103].

3.11 SOLUTION STRATEGIES

At time $t = 0$, the initial conditions are imposed on the computational domain (ref 3.5), the terms J_Γ^{evap} and u_Γ from equations 3.13 and 3.16 are respectively calculated. Computation then proceed to next iteration $t_{i+1} = t_i + \Delta t_i$, with the solution of equations 3.2 3.3 and 3.4 in the domain and equations 3.5, 3.6 and 3.7 at the interface Γ. The unknown variables u, v, w, p, and T are calculated, then accordingly the local evaporation rate (3.13) is calculated in turn to define the interface and mesh velocities. During the solution procedure at every iteration, the local evaporation rate (3.13) depends only on the local temperature $T_{l,\Gamma}$, so to calculate the global evaporation rate we need to perform some post-processing (refer equation 3.14).

In the cases of high substrate temperatures we introduce some ramping for the substrate temperature up to $t = 1\,\text{s}$ that allows to increase substrate temperature in steps and prevent numerical oscillations inside the domain. In some cases, this could even effect the primary instability and secondary instability phase. Similarly in the case of highly volatile fluid (or low ambient pressure) such as HFE7100 we use another strategy that follows in three steps. Firstly, we perform only thermal diffusion for $t = 1\,\text{s}$ to prevent numerical instabilities without moving the mesh. Secondly, the last results from the first step are used to initialize the coupled computations, i.e fluid flow and thermal equation, without moving mesh for 0.1 s that stabilizes the

thermal distribution inside the drop. Finally, results from the latter are used as the initial solution for the standard simulation. With the above strategies, we can reach a stable primary instability phase that otherwise could effect the evaporation rate and subsequent evaporation process.

NUMERICAL MODEL VALIDATIONS, RESULTS AND DISCUSSION

This chapter is dedicated mainly to the validation and quantitative comparison of our model for microgravity conditions via comparison with experiments. Two configurations are considered: Hydrofluoroether (HFE7100) sessile drops in a sounding rocket [76] and Ethanol in parabolic flight experiment [69]. For validation of our numerical model purposes, we are using the experiment data of Hydrofluoroether (HFE7100) sessile drops over 30 s evaporation in a sounding rocket [76]. Then to further extend our understanding we need to switch to Ethanol in parabolic flight experiment [69]. The main reason behind for considering two configurations are that firstly, experiment data of Hydrofluoroether (HFE7100) sessile drops lack the number of experiments sets from the sounding rocket, secondly it is difficult to perform the parametric study with HFE7100 due to its high computational cost (see table C.3), whereas for Ethanol we have the previous studies over the range of substrate temperature and it has a comparative low computational cost for numerical simulation (see table C.2) but lack of data for the complete cycle for ethanol evaporation for validation of evaporation rate with respect to time for the complete cycle, so we need to use experiment data.

By the quantitative comparison with Ethanol parabolic flight results over the range of substrate temperature T_{sub}, we propose an analytical model for the pinned sessile drop of Ethanol on a heated substrate under microgravity conditions. Then we contribute to understanding the Marangoni effect in the dynamics of the evaporation process and the occurrence of secondary instability. Moreover, we study the effect of main problem parameters, substrate temperature T_{sub}, contact radius R and ambient pressure $P_{atm} = P$ on evaporation rate, interface temperature, velocity field and instabilities pattern. Then with the above cases, we define the relation for critical Marangoni number for a transition from primary Marangoni instability to secondary Marangoni instability through critical aspect ratio. Next, we use our model to study HFE7100 evaporation microgravity to find critical thermal Marangoni (and critical height) for a transition from primary to secondary instability to help future rocket experiment. Similarly, we compare the top view of Ethanol sessile drop from parabolic flight experiment VP140PF12 (refer section 2.4) and numerical simulation to compare the number of instability cells.

	HFE7100 [105, 106]	Ethanol [104, 107]
Density, $\rho\ (\text{kg}\cdot\text{m}^{-3})$	1516.15	789
Dynamic viscosity, $\mu(\text{mPa}\cdot\text{s})$	0.69	1.095
Molar mass, $M_l(\text{kg}\cdot\text{mol}^{-1})$	0.25	0.046
Atomic diffusion volume, v_l	224.84	51.77
latent heat of vaporization, $H_{\text{evap}}\left(\text{kJ}\cdot\text{kg}^{-1}\right)$	111.6	923
Specific heat capacity, $C_P\left(\text{J}\cdot\text{kg}^{-1}\cdot\text{K}^{-1}\right)$	1183	2845
Thermal conductivity, $K\left(\text{W}\cdot\text{m}^{-1}\cdot\text{K}^{-1}\right)$	0.069	0.140
Capillary length (1g), $L_c(\text{mm})$	0.95	1.69
Thermal expansion coefficient, $\beta\left(\text{K}^{-1}\right)$	1.8×10^{-3}	1.08×10^{-3}
Surface tension, $\gamma(\text{mN}\cdot\text{m}^{-1})$	13.345	21.97
Surface tension temperature coefficient, γ_T $\left(\text{N}\cdot\text{m}^{-1}\cdot\text{K}^{-1}\right)$	-1.14×10^{-4}	-0.83×10^{-4}
Emissivity, $\varepsilon(-)$	0.922	0.859 [60]
Absorption coefficient, $k_{SW}\ \text{mm}^{-1}$	2.55	1.85 [60]
Boiling point ($^\circ$C)	61	78.0

Table 4.1: Physical properties of pure liquid HFE7100 and Ethanol at 298.15 K and 1 atm.

4.1 PHYSICAL PROPERTIES

The thermo-physical properties considered for HFE7100 and Ethanol are presented in table 4.1 and for results related to Water and Methanol are presented in table B.1. However, full temperature dependency of properties are presented in appendix section B. Universal gas constant R_{gas} is $8.314\,\text{J}\cdot(\text{mol}\cdot\text{K})^{-1}$, molar mass of ambient air is $28.97\,\text{g}\cdot\text{mol}^{-1}$, atomic diffusion volumes of air is 19.7, molar mass of ambient nitrogen $28.014\,\text{g}\cdot\text{mol}^{-1}$ and atomic diffusion volumes nitrogen 18.5 [77]. The reference saturated vapour pressure $P_{l,\text{sat}}^{ref}$ is $26900\,\text{Pa}$, $7833.2\,\text{Pa}$, $3169\,\text{Pa}$, and $16915.1\,\text{Pa}$ for HFE7100, ethanol, water and methanol respectively at reference temperature $T_{\text{sat}}^{ref}=298.15\,\text{K}$ [104].

In figure 4.1 we depict differences in density and dynamic viscosity of liquid HFE7100 depending on root references [105, 106]. For example, at temperature of 303.15 K, the density from the first reference is $1470.23\,\text{kg}\cdot\text{m}^{-3}$ and whereas it is $1503.18\,\text{kg}\cdot\text{m}^{-3}$ for the second one, concerning dynamic viscosity, they are $0.64\,\text{mPa}\cdot\text{s}$ and $0.53\,\text{mPa}\cdot\text{s}$, respectively. The discrepancies in the basic physical properties of fluid need to be taken in consideration while comparing the quantitative results from numerical simulation with experiments.

4.2 NUMERICAL MODEL VALIDATION

The validation of numerical solutions with respect to experiments for microgravity conditions is a challenging task particularly due to lim-
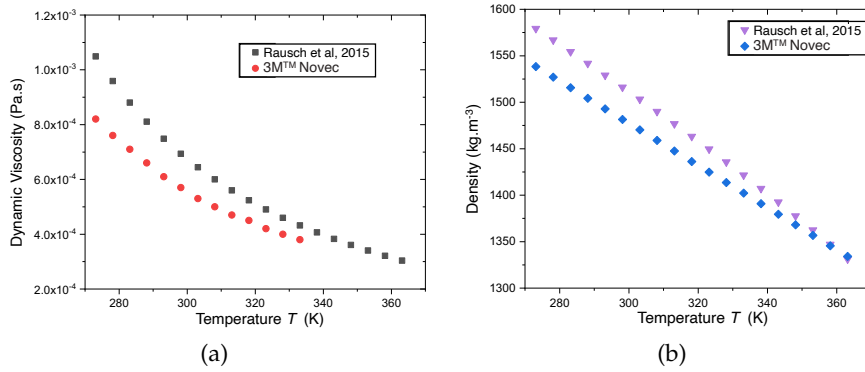
Figure 4.1: Comparison of the HFE7100 density **(a)** and dynamic viscosity **(b)** with respect to the temperature.

ited access to microgravity platform, complexity of the experimental set-up to get desired set of experiment data, along with computational cost linked with solving fully-coupled highly nonlinear PDEs. Moreover, once secondary instability occur, the resulting fields are fully time-dependent and 3D, leading to costly Direct numerical simulation (DNS) computations.

Validation of numerical solution is divided into different stages, first, we start with validation by comparing the numerical results at ambient temperature with well known purely diffusion model of Picknett and Bexon [12], due to the lack of an analytical model for purely diffusion model for non-isothermal heated substrate evaporation under microgravity.

Then, for full validation, we compare numerical results with sounding rocket experiment results for pinned sessile drop of HFE7100 fluid that are discussed in detail under chapter 2 and section 2.5 [76], then we further extend our understanding with comparison of numerical results from parametric studies with parabolic flight experiments. For more details refer chapter 2 and section 2.3 for Ethanol pinned sessile drop [69].

To achieve our objective we used our main model Coupled **F**luid flow and **H**eat transfer **D**iffusion **M**odel for microgravity conditions. In the following discussion we will refer to it as **FHDM**, however in some cases, for comparison, we also use the **HDM** that designates **H**eat transfer (by conduction only in the drop) **D**iffusion **M**odel is just to understand how does **HDM** models perform without accounting the fluid flow for the sessile drop evaporation on the heated substrate with lower computational cost. The main difference between the **FHDM** and **HDM** comes from number of PDEs equation solved, **FHDM** solved the coupled fluid flow and heat transfer inside the sessile domain (equations 3.2, 3.3 and 3.4 inside the domain, equations 3.5,

3.6 and 3.7 at interface) and when in the same model, we switch off the fluid flow module and only solve heat transfer (equation 3.4 inside the domain, equation 3.5 at the interface) from heated substrate to sessile drop interface via conduction (is called **HDM**). Thus these modelling choices strongly affect the computational cost of the solution and accuracy of flow dynamic inside the sessile domain which in turn reflects on global results. However, in some cases, **HDM** method could be advantageous over the **FHDM** with some tolerance in the accuracy. Later, we will also discuss the **HDM** method's limitations and domains of its applicability.

In table 4.2, we have presented the details of numerical simulations performed to achieve our set goals from the current study.

4.2.1 *Numerical validation with purely diffusion model*

In figure 4.2, presented the quantitative comparisons of the Ethanol evaporation rate for different contact angles at substrate temperature $T_{sub} = 298.15$ and 293.15 K with analytical model derived by Picknett and Bexon [12]. The physical properties used are presented in table 4.1, and space discretization with mesh convergence is presented in appendix section C.0.1 and time discretization is same as discussed in the section 3.10.2.

The numerical results are based on our **FHDM** method i.e non-isothermal domain and isothermally heated substrate under micro-gravity conditions. The complete cycle of evaporation for Ethanol is presented in figure C.2.

As previous experimental results from microgravity conditions [20, 69] show that in the absence of gravity, evaporation rate can then be correctly assumed to be a quasi-steady in the pinned mode, which suggests that it is a diffusion-controlled process regardless of substrate temperature. So we use a well-known diffusion model derived by Picknett and Bexon [12] for constant contact area (up to de-pinning) and spherical cap shape. However, this analytical model derived by Picknett and Bexon is for sessile drop at ambient temperature on a non-heating surface. By considering this equation (equation 1 of section A), it is also not possible to define any temperature difference between the ambient and substrate. So for the analytical evaporation rate in our study, we assume isothermal sessile drop at substrate temperature during the whole lifetime of evaporation process which means we have to neglect the evaporating cooling effect of evaporation on sessile drop thus resulting in comparatively higher calculated evaporation rate. However, the analytical model could be comparable at low temperature and low contact angle.

S.No	Liquid	R (m)	T_{sub} (K)	P (bar)	H_t (m)	T_{apex} at θ_{crit}, (K)	$E_v = -\frac{1}{R}\frac{dm}{dt}$, kg·(s·m)$^{-1}$	θ_{crit}, (deg.)	$T_{avg,\Gamma}$ at θ_{crit} (K)	$\Delta T = (T_{sub} - T_{apex})$, (K)	$E_{\Delta J} = -\frac{1}{R}\frac{dm}{dt}\big|_{bi \to ai}$ (%)	$AR_{crit} = H_t/R$	$Ma_{T,crit}$	$Ma_{SD,crit}$
1	HFE7100	2.0E-3	301.15	1.054	3.47E-04	298.09	6.67E-05	19.7	299.94	3.06	1.06	0.173	5195.75	900.59
2	Ethanol	1.5E-3	308.15	0.835	2.03E-04	304.5	1.47E-05	14.9	307.09	3.65	1.59	0.136	829.88	108.69
3	Ethanol	1.5E-3	313.15	0.835	2.29E-04	309.59	1.88E-05	17.3	311.77	3.56	2.09	0.152	1015.21	154.78
4	Ethanol	1.5E-3	318.15	0.835	2.34E-04	313.56	2.38E-05	17.7	316.49	4.59	2.49	0.156	1488.93	231.88
5	Ethanol	1.5E-3	323.15	0.835	2.54E-04	317.31	2.99E-05	19.2	321.07	5.84	2.53	0.169	2279.57	385.62
6	Ethanol	1.5E-3	328.15	0.835	2.78E-04	321.4	3.74E-05	21	325.64	6.75	2.62	0.185	3136.83	580.39
7	Ethanol	2.0E-3	318.15	0.835	3.35E-04	313.53	2.40E-05	19	316.50	4.62	2.25	0.167	2147.69	359.38
8	Ethanol	2.5E-3	318.15	0.835	4.31E-04	313.93	2.41E-05	19.6	316.57	4.22	2.1	0.172	2530.04	436.17
9	Ethanol	3.0E-3	318.15	0.835	5.36E-04	313.84	2.41E-05	20.2	316.58	4.31	1.92	0.179	3211.63	573.32
10	Ethanol	2.0E-3	318.15	0.67	3.46E-04	312.92	2.95E-05	19.7	316.19	5.23	2.57	0.173	2498.71	432.82
11	Ethanol	2.0E-3	318.15	1	3.32E-04	313.96	2.02E-05	18.8	316.72	4.19	1.98	0.166	1940.96	322.05

Table 4.2: Summary of numerical simulations. $E_{\Delta J} = -\frac{1}{R}\frac{dm}{dt}\big|_{bi \to ai}$ is change in evaporation rate after the secondary instability appear.
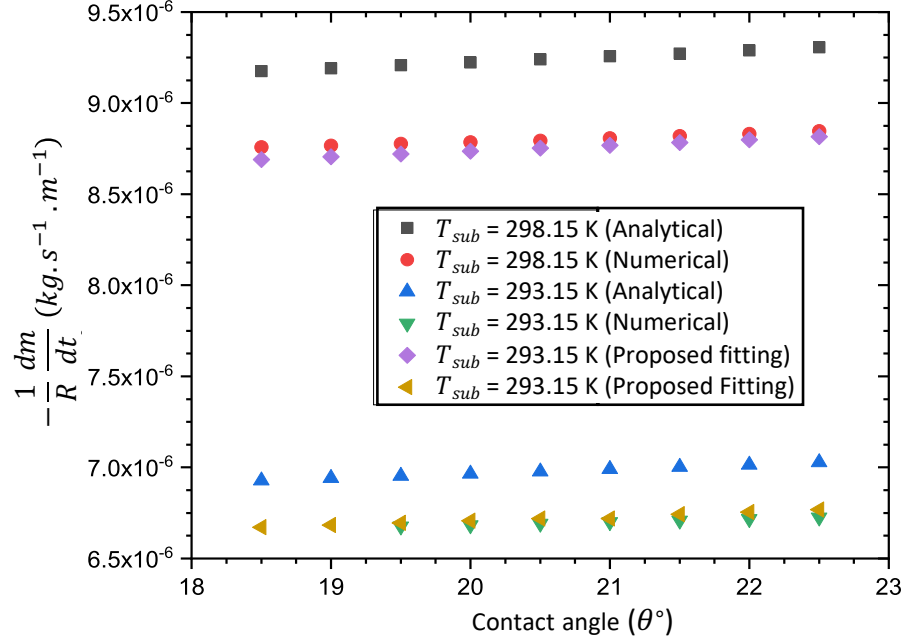
Figure 4.2: Comparisons of numerical evaporation rate (**FHDM**) at T_{sub} = 298.15 and 293.15 K with analytical model derived by Picknett and Bexon [12]. The analytical results from proposed fitting are based on the equation 4.3. For complete cycle numerical results for above figure please refer fig. C.2.

As it can be seen in the figure 4.2 at T_{sub} = 298.15 K, with **FHDM** method evaporation rate is 5% and 4.6% lower to analytical model for Ethanol pinned sessile drop at contact angle $\theta = 22.5°$, and 18.5°, respectively. Similarly, for T_{sub} = 293.15 K, it is 4.3% and 4% at contact angle $\theta = 22.5°$, and 19.5°, respectively. With the above results, we can conclude that our model with **FHDM** method is validated for the low heated substrate temperature and contact angle.

4.2.2 *Numerical validation with HFE7100*

Now, in the second stage, we take a much volatile liquid drop. When compared to Ethanol, liquid HFE7100 has high volatility at the room temperature thus higher is the evaporation rate. The physical properties of the liquid HFE7100 are presented in table 4.1. For simulation, sessile drop's initial geometrical parameter, substrate and ambient conditions corresponding to drop $7DP\mu g$ are from sounding rocket experiment[76], which are as follows: the drop base radius R is 2 mm and initial contact angle (θ_0) is 60°, whereas ambient gas is nitrogen at pressure 105400 Pa and substrate temperature T_{sub} is 301.15 K (refer section A for more on HFE7100 experiment).

The domain is discretized by the hybrid mesh elements (90% elements Hexahedra elements). The discretization of sessile drop domain

(a) Top side view   (b) Top side cut view
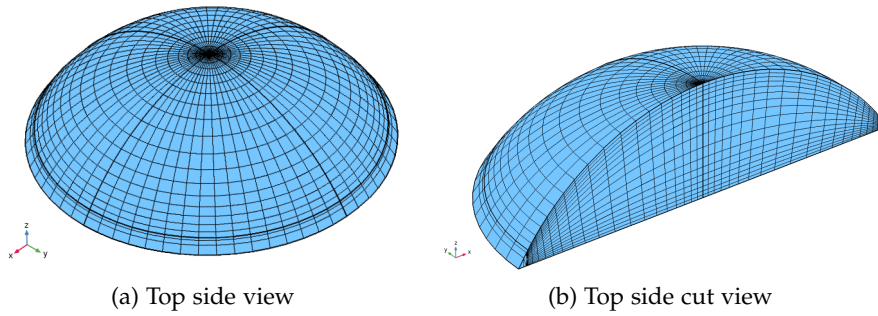
Figure 4.3: Meshed sessile drop of the HFE7100 with initial contact angle $\theta_0 = 60°$ and base radius $R = 2\,\text{mm}$.

consist 18 elements in radial direction (Radial direction (RD)), 17 elements in vertical direction (Element in the vertical direction of sessile drop (VD)) and 64 circumferential elements (Circumferential direction (CD)) (see fig.4.3b and 4.3)that lead to generate total number of 21074 Mesh elements. The Fluid flow and Heat transfer Diffusion Model (FHDM) method uses 1240906 number of degrees of freedom (DOF) with quadratic geometry shape order whereas for the same shape order and mesh Heat transfer Diffusion Model (HDM) method solved 756530 Degrees of freedom (DOF). The time discretization and solution strategies are followed as mentioned in the section 3.10.2 and 3.11.

Types of element: 18496 are hexahedra elements, 4872 are quads element, 2432 are prisms elements and rest are triangles, edges elements and vertex element

In figure 4.4, volume evolution with time compared between numerical simulation and experiment [76]. The experiment data extrapolated further to mark the expected critical volume for the appearance of secondary instability. More on the HFE7100 instabilities is provided later under section 4.5.1. The comparison between experiment and numerical estimated within 4.6% deviation at $t = 30\,\text{s}$ from experiment, that also within the limit of error bar in the experiment (see fig 4.5).

In figure 4.5, we compare evaporation rate from simulations, experiments and analytical model. The evaporation rate under earth conditions is nearly twice as compared to microgravity conditions due to convective transport in ambient and vapour phase [69, 76]. Evaporation rate under microgravity experiments and simulations (both FHDM and HDM) are comparable which validates our assumption (and numerical model) for sessile drop evaporation under microgravity that it is purely diffusive in nature and sessile drop interface is fully under saturated vapour pressure (of HFE7100 vapour). This can be explained due to the absence of gravity and convective transport in vapour, HFE7100 vapour generated during evaporation, saturates ambient nitrogen near the sessile drop interface that results in the reduction of the evaporation rate of sessile drop in microgravity which also validates that gravity dominant effects are actually located in vapor phase (vapour density gradient induces thermal-solutal convec-
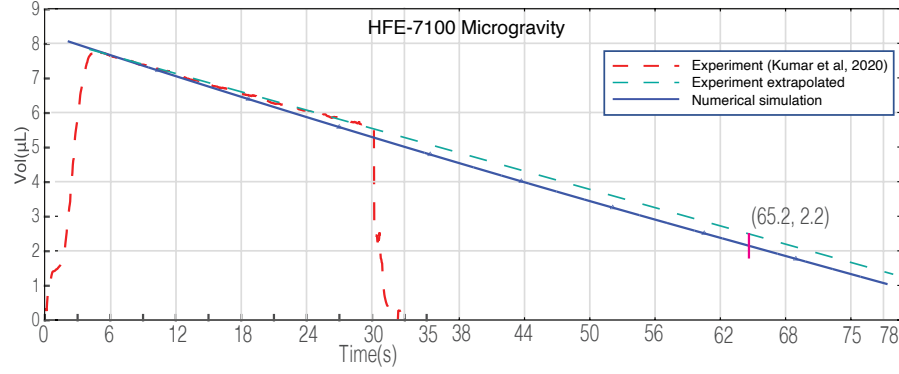
Figure 4.4: **Numerical simulation for** HFE7100 **on heated substrate under microgravity condition.** Comparison of volume evolution with respect to time between numerical simulation and experiment (with experiment [76]). Numerical simulation time shifted according to match with experiment maximum initial volume. The vertical bar on plot at $t = 65.2\,$s and *Vol.* $= 2.2\,\mu$L marks the appearance of secondary instability. For time evolution refer to movie. ▶ play or Scan QR.

tion). So, it necessitates using a 2-sided model for gravity conditions. As expected analytical model predicts higher evaporation rate in comparison to microgravity experiments by considering sessile drop domain as isothermal, at substrate temperature for analytical model. It is also noteworthy that isothermal boundary conditions for substrate temperature T_{sub} could be seen as a strong boundary condition as in experiments, the difference between substrate centre and edge temperatures is in the range of $0.15 - 0.21^\circ$C.

Stop conditions for simulations (both FHDM and HDM) set $\theta_t = 9.45^\circ$ which is expected to be higher than ground experiment (approximately $\theta = 8^\circ$) and lower than ground experiment with electric field (approximately $\theta = 14^\circ$, refer table 1 of section A).

Movie for Fig. 4.4, 4.24, 4.25 & 4.26.

It is worth to mention computational cost of FHDM and HDM simulations for Hydrofluoroethers (HFE7100) sessile drop on a heated substrate. The FHDM simulation with 1240906 DOF, total computational time on 48 cores for $t = 75.3\,$s **is** 70 **days,** 17 **hours!** in comparison with 756530 DOF, HDM method on 32 cores for $t = 86.6\,$s **is** 22 **hours,** 40 **min** only. The cost of simulation with FHDM is very high for resolving secondary instability i.e 57.5 to 75.3 s in 62 days, 19 hours. The computational cost for the FHDM is 73 times of HDM method for HFE7100 sessile drop due to its volatility, in same duration HDM under predicted 15% evaporation to the FHDM (see table C.3 for more computational resources).
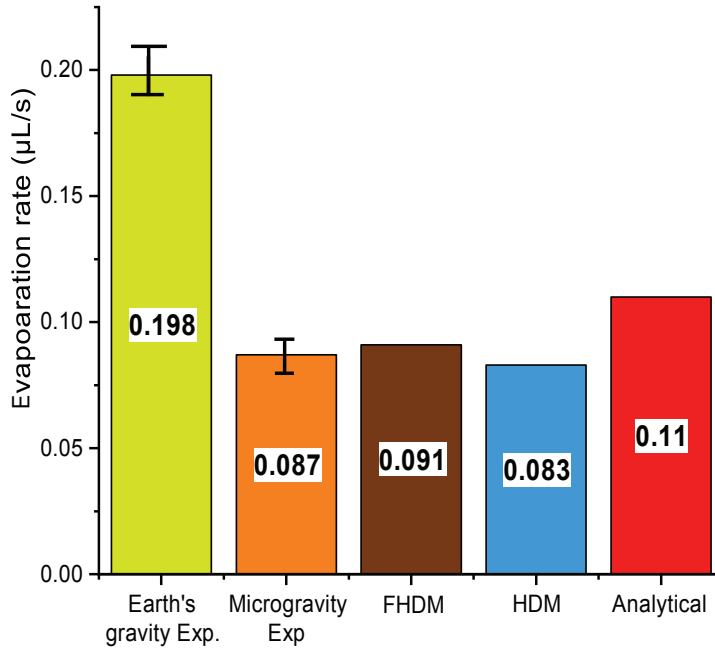
Figure 4.5: **Comparison of** HFE7100 **sessile drop evaporation rate from ex-
periment and numerical simulations. For Earth gravity exp**: av-
erage evaporation rates of sessile drops 1DP1g and 3DP1g, **Micro-
gravity Exp**: evaporation rates of sessile drops $7DP\mu$g [76] (refer
table 1 of section A). The parameters of sessile drop $7DP\mu$g were
used for the numerical simulation FHDM and HDM and also
for the calculation of analytical diffusion-limited evaporation rate
without an electric field [12]. The evaporation rate is calculated
from initial contact angle $\theta_0 = 57°$ to $\theta_0 = 46°$.

4.2.3 *Quantitative comparison with Ethanol*

The physical properties of Ethanol are presented in table 4.1. For
simulation, sessile drop's initial geometrical parameter, substrate and
ambient conditions are corresponding to drop parabolic flight exper-
iment [69] which are as follows: the sessile drop base radius R is of
different range from 1.5 to 3.6 mm, However for most of the com-
parisons the effect of diameter is neutralized by dividing the global
evaporation rate by radius of sessile drop. The ethanol sessile drop
evaporating in ambient air which is at cabin pressure $P = 83500$ Pa,
substrate temperature T_{sub} from 298.15 K to 333.15 K, and at contact
angle $\theta_0 = 23°$. The spatial discretization used in numerical simulation
for the Ethanol sessile drop is discussed in detail in section 3.10.1. In
figure 3.5 and 3.6 is shown the geometry and mesh structure respec-
tively. The mesh structure for all the substrate temperatures remains
the same only the number of elements in radial, vertical and circumfer-
ential direction changes with substrate temperature. For more details
on mesh sensitivity refer appendix section C. The time discretization
remains the same as discussed earlier (For more refer section 3.10.2

& 3.11). The computational cost and resources for the current study presented in appendix table C.2.
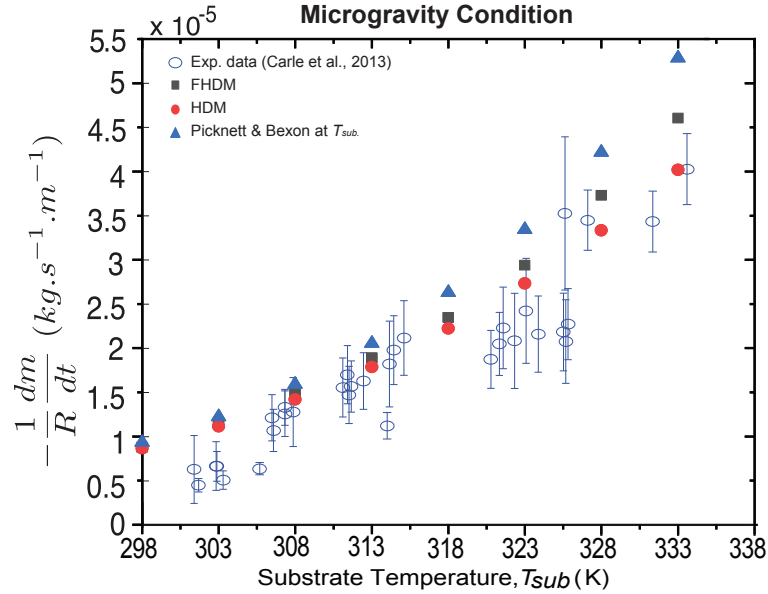
Figure 4.6: **Experimental and numerical simulation comparison at different substrate temperatures.** Numerical simulations of pure Ethanol evaporation rate with microgravity experimental results [69] at contact angle $\theta_0 = 23°$ and cabin pressure ($P = 0.835\,\text{bar}$) for different substrate temperature.

In figure 4.6, we presented quantitative comparison of Ethanol sessile drop evaporation rate (E_v) from numerical simulation with parabolic flight experiments and Pickentt & Bexon analytical equation [12]. For low substrate temperatures (comparable to ambient temperature), numerical results from FHDM, HDM and analytical model are comparable to experiments. As the temperature of substrate increased, evaporation rate increases following a power law and a divergence between analytical, FHDM and HDM evaporation rates emerges clearly. For comparison, values of evaporation rate is 4.61×10^{-5}, 4.02×10^{-5} and $5.29 \times 10^{-5}\,\text{kg} \cdot (\text{s} \cdot \text{m})^{-1}$ for FHDM, HDM and analytical model respectively at the $T_{\text{sub}} = 333.15\,\text{K}$, contact angle $\theta_0 = 23°$ and cabin pressure $P = 0.835\,\text{bar}$. As described by Carle et al, 2013 [69], experimental results have a dispersion of data due to perturbations caused by the aircraft flight, for example, by vibrations. However, in our opinion lower values of experimental evaporation rates to numerical ones also result from the combination of two different factors. The first one is an indirect method (Heat flux method) used by Carle et al, 2013 [69] to evaluate experimental evaporation rate and the second one is numerical modelling one assuming isothermal substrate boundary conditions.
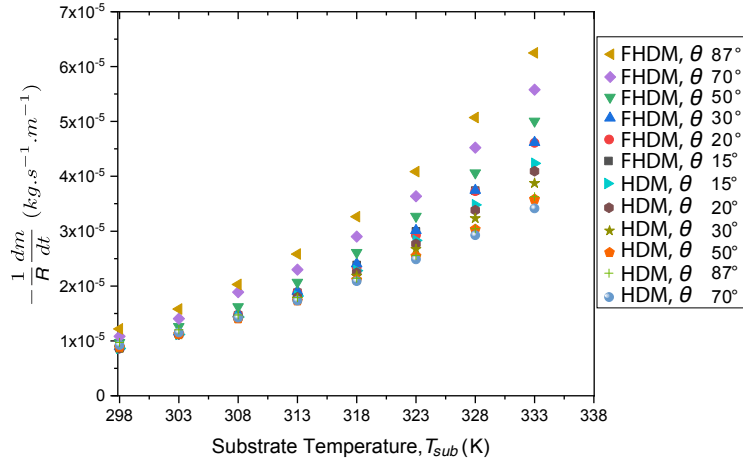
Figure 4.7: **Numerical simulation evaporation rate at different substrate temperature and contact angle.** The pure fluid ethanol sessile drop evaporation rate with FHDM and HDM at $\theta_0 = 87°$ to $\theta_0 = 15°$ and pressure $P = 0.835\,\text{bar}$.

However, as shown in figure 4.7 divergence in evaporation rate is much broader for higher contact angles. For comparison at contact angle $\theta_0 = 87°$, $T_{\text{sub}} = 333.15\,\text{K}$ evaporation rate (E_v) is 6.25×10^{-5}, 3.63×10^{-5} and $7.52 \times 10^{-5}\,\text{kg} \cdot (\text{s} \cdot \text{m})^{-1}$ for FHDM, HDM and analytical model respectively. Evaporation rate for FHDM at initial contact angle $\theta_0 = 87°$ is the highest contrary to HDM where it is the lowest during the lifetime of sessile drop with initial contact angle $\theta_0 = 87°$. The divergence between the two not only reduces with decrease of contact angle with time, but also divergence reduced for low substrate temperature even for higher contact angles. This divergence represents the important role played by the Marangoni convection in transport of energy from substrate to sessile drop interface Γ thus in elevating interface temperature $T_{l,\Gamma}$ and evaporation rate.

Please also refer figure 4.9a and 4.9b, for more clarity and to follow full lifetime of sessile drop evaporation with FHDM and HDM at $T_{\text{sub}} = 318\,\text{K}$ and $323.15\,\text{K}$, and section 4.4.1 for discussion on the role of primary and secondary Marangoni instability.

Figure 4.8 shows the plot of average interface temperatures $T_{avg,\Gamma}$ with respect to substrate temperatures. The $T_{avg,\Gamma}$ from HDM evolves with contact angles meanwhile $T_{avg,\Gamma}$ from FHDM does not (see figure 4.9b) up to secondary instability appear. So, according to the FHDM, $T_{avg,\Gamma}$ is approximately independent of the contact angle and evaporation rate reduced with contact angle due to the reduction of the evaporating surface area Γ or in another words f(θ)). The insert of fig. 4.8) shows the obtained fitting of $T_{avg,\Gamma}$ with respect to T_{sub},
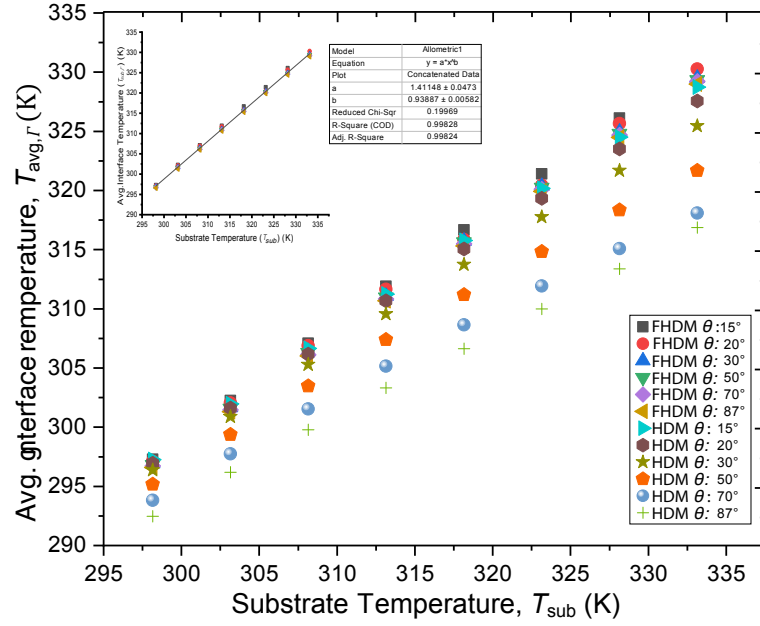
Figure 4.8: **Numerical simulation's average interface temperature ($T_{avg,\Gamma}$)**
vs substrate temperatures. $T_{avg,\Gamma}$ of ethanol sessile drop between
$\theta_0 = 87°$ to $\theta_0 = 15°$ with FHDM and HDM. Insert shows fitting
for the $T_{avg,\Gamma}$ vs T_{sub} only for FHDM. Fitting details (for FHDM):
$T_{avg,\Gamma} = a_E \times T_{sub}^{b_E}$ with $a_E = 1.41148 \pm 0.047$ and $b_E = 0.93887 \pm 0.0058$.

where,

$$T_{avg,\Gamma} = \frac{1}{\Gamma} \int_\Gamma T_{l,\Gamma} d\Gamma \tag{4.1}$$

for the Ethanol sessile drop, from fitting

$$T_{avg,\Gamma} = a_E \times T_{sub}^{b_E} \tag{4.2}$$

with $a_E = 1.41148 \pm 0.047$ and $b_E = 0.93887 \pm 0.0058$. Now we can
replace $T_{l,\Gamma}$ in the equation 3.13 with $T_{avg,\Gamma}$:

$$E_{v,E} = 2\pi \frac{0.01013 T_{avg,\Gamma}^{1.75} \left(\frac{1}{M_a} + \frac{1}{M_l} \right)^{0.5}}{P \left[(\sum v_a)^{1/3} + (\sum v_l)^{1/3} \right]^2} \times \frac{M_l}{R_{gas} T_{avg,\Gamma}}$$

$$\times P_{l,sat}^{ref} \exp \left[-\frac{(H_{vap} M_l)}{R} \left(\frac{1}{T_{avg,\Gamma}} - \frac{1}{T_{sat}^{ref}} \right) \right] \times F(\theta) \tag{4.3}$$

The analytical equation 4.3 is valid for Ethanol pinned sessile drop
of spherical shape under microgravity conditions (under saturation
vapour density on the interface Γ) on a heated substrate for any given
pressure, with neglecting the effect of secondary Marangoni instability
for the lower contact angle.

In the results section, we are going to discuss the role of Marangoni instabilities, and the strength of Marangoni (thermocapillary) convection can be estimated in a liquid layer of uniform thickness thanks to the non-dimensional thermal Marangoni number:

$$\text{Ma}_\text{T} = -\frac{d\gamma}{dT} \times \frac{\Delta T\, H_t}{\mu} \frac{C_p \rho}{K} \tag{4.4}$$

Here, $d\gamma/dT$ is the thermal coefficient of surface tension, ΔT is the temperature difference between substrate and the drop apex at the interface (degree of sub-cooling), H_t is the height of drop at time t considered as characteristic length, ρ, K and μ are density, thermal conductivity and dynamic viscosity of liquid drop, respectively.

However, in the case of sessile drops, the liquid height constantly changes along the drop radius, so the classical Marangoni number can be adapted accordingly for the sessile drop evaporation. So, we also introduce a specific Marangoni number for sessile drops denoted as Ma_SD,

$$\text{Ma}_\text{SD} = -\frac{d\gamma}{dT} \times \frac{\Delta T\, H_t}{\mu} \frac{C_p \rho}{K} \times \tan\left(\frac{\theta_t}{2}\right) \tag{4.5}$$

which is related to the classical one as follows:

$$\text{Ma}_\text{SD} = \text{Ma}_\text{T} \times \tan\left(\frac{\theta_t}{2}\right) \tag{4.6}$$

where subscript SD stand for the **S**essile **D**rop and θ_t is the contact angle at time t.

4.4 RESULTS AND ANALYSIS

In this section, we are going to broaden our analysis to in-depth our understanding of sessile drop evaporation on a heated substrate under microgravity conditions with DNS computations using the FHDM method for the whole lifetime of evaporating sessile drop. This can also provide insight into Marangoni convection and dynamics of instability cell patterns evolution with time. In the meanwhile, they contribute to understanding the Marangoni effect in the dynamics of the evaporation process and the occurrence of secondary Marangoni instability. Moreover, we study the effect of main problem parameters, substrate temperature T_{sub}, contact radius R and ambient pressure P on evaporation rate, interface temperature, velocity field and instabilities pattern. Then with the above cases, we define the relation for critical Marangoni number for the transition from primary Marangoni instability to secondary Marangoni instability through critical aspect ratio.

4.4.1 *Marangoni convection and related secondary instabilities*

To illustrate Marangoni convection influence on dynamics inside the liquid domain and at interface during sessile drop evaporation, we first go through the case study that compares FHDM and HDM. Two substrate temperatures $T_{sub} = 318.15\,\text{K}$ and $323.15\,\text{K}$ are considered for ethanol sessile drop starting with an initial contact angle $\theta_0 = 90°$. Then in the same cases, we analyse secondary Marangoni instability, its role in evaporation and interface temperature. Then we look into the computational cost for resolving Marangoni convection and secondary Marangoni instability based on the volatility of fluid and substrate temperature. To further extend our understanding we undertake parametric studies by using FHDM. The comparisons of different substrate temperatures, contact base radius and pressure would help us to look into evaporation dynamics such as evaporation cooling of interface, velocity profile, surface temperature profile, secondary instability pattern. Next, by using the same set of simulations we define the critical heights for the transition from primary Marangoni instability to secondary Marangoni instability phase of evaporation and formulate the relation between critical Marangoni number and critical aspect ratios.

4.4.1.1 *Evaporation of Ethanol sessile drops for two substrate temperature whole cycle*

In figure 4.9 are plotted the comparison of FHDM and HDM for the two substrate temperatures $T_{sub} = 318.15\,\text{K}$ and $323.15\,\text{K}$ for ethanol sessile drop. Both computations start with an initial contact angle of $\theta_0 = 90°$ and with a uniform initial temperature field (at substrate heating temperature) in the drop and an imposed isothermal heating temperature at the substrate surface.

The liquid domain initial discretization consists hybrid mesh of 21312 elements as shown in the figure C.5. The computational domain consists of 18 elements in the radial direction (RD), 15 elements in the vertical direction (VD) and 64 circumferential elements (CD). The time discretization remains the same as discussed earlier (for more details, refer to sections 3.10.2 & 3.11). The computational cost and resources for the current study are presented in the appendix table C.2.

Types of the element: 16320 are the hexahedra elements, 4600 are the Quads element, 4992 are the prisms elements and rest are the triangles, edges elements and vertex

For FHDM, the current simulation is performed in two stages. In the first stage simulation starting from $\theta = 90°$ to $27°$, then the computational domain is re-meshed. In the second stage simulation started from $\theta = 33°$ to $9.45°$. Then simulations were later merged to get a complete simulation for $\theta = 90°$ to $9.45°$.

For the first stage, FHDM ran with 1250371 DOF on 32 cores, total computational time of the FHDM simulation for substrate temperature

(a)

(b)
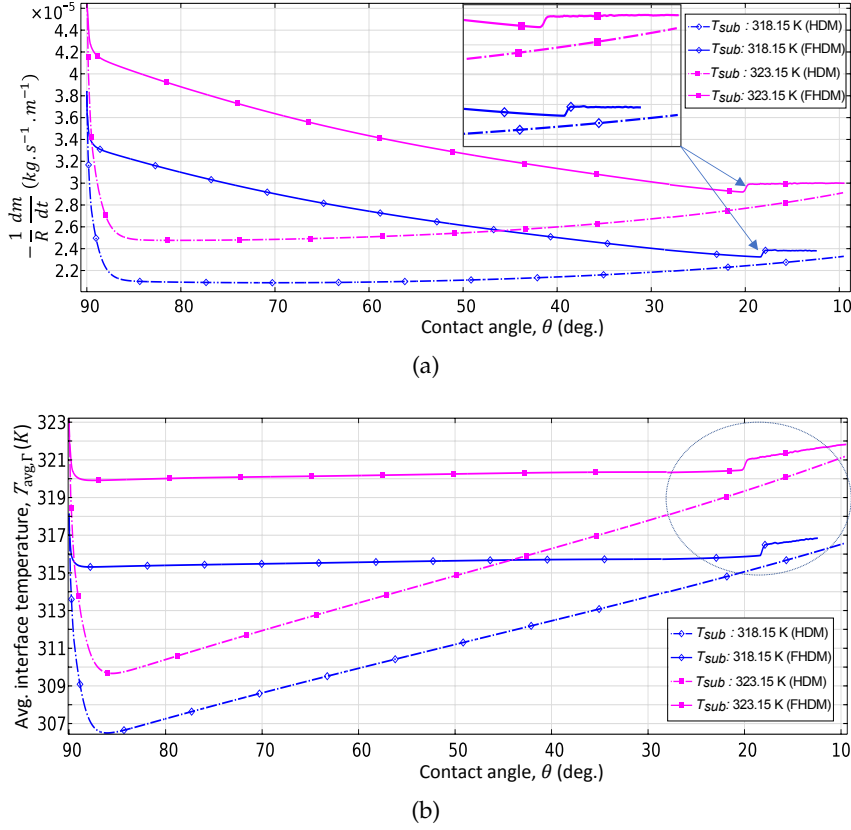
Figure 4.9: Comparison of FHDM and HDM for ethanol sessile drops at $T_{sub} = 318.15$ and $323.15\,\mathrm{K}$ with base radius $R = 1.5\,\mathrm{mm}$ and pressure $P = 0.835\,\mathrm{bar}$. **a)** Evaporation rate; **b)** Average interface temperature.

$T_{sub} = 318.15\,\mathrm{K}$ and $t = 106.8\,\mathrm{s}$ is 1 day, 17 hours. For the Second stage (from $\theta = 33°$ to $9.45°$), FHDM is computed with 1037661 DOF and using 2 nodes with total 64 cores. The FHDM simulation total computational time for $t = 106.8$ to $132.8\,\mathrm{s}$ is 6 days, 11 hours. On the other hand, HDM using 709260 DOF for same mesh and shape order, on 32 cores, and for $t = 143.6\,\mathrm{s}$. The HDM simulation computational time is 4 hours. With maximum time-stepping restricted to 1 s. The stop conditions for simulations (both FHDM and HDM) set $\theta_{tf} = 9.45°$ For other details refer to table C.2.

Similarly, for the $T_{sub} = 323.15\,\mathrm{K}$ with FHDM, for first stage $t = 84.9\,\mathrm{s}$ is 1 day, 23 hours and for second stage from $t = 84.9$ to $105.1\,\mathrm{s}$ it is 8 days, 22 hours whereas with HDM, computational time for $t = 119.6\,\mathrm{s}$ is 3 hours, 22 min (for more details refer to table C.2).

By comparing the first and the second stage for FHDM we can clearly see the high cost for simulation after the appearance of secondary instability which are further costlier for high substrate temperature. However, the computational cost of HDM is far lower than the FHDM method but with its own disadvantages as inaccuracy is high

to medium range contact angle. As we can see for $T_{sub} = 318.15\,\text{K}$, evaporation starting from $\theta = 90°$ to $9.45°$, took $t = 132.8\,\text{s}$ and $143.6\,\text{s}$ for FHDM and HDM respectively. For other numerical parameters and computational resource details refer to table C.2.

In figure 4.9, at $t = 0$, computations start with a uniform initial temperature (at substrate heating temperature) in sessile drop liquid domain and imposed heating temperature at substrate surface. Thus, measured evaporation rate is the highest (equivalent to the analytical model) at $t = 0$, due to latent heat of vaporization, drop cools down from interface; meanwhile, temperature near the contact line remains higher due to heat conduction from the substrate through a thin layer of Ethanol. This creates a vertical temperature gradient in drop bulk and a tangential one along the drop surface near the contact line. These temperature gradients promote the development of tangential stress that lead to development of Marangoni convection, after initial intense unsteady phenomena finished (at about $t = 5$ s), then due to Marangoni convection, the drop reaches thermal equilibrium. The important role of Marangoni convection can be seen clearly in the figure 4.9 by comparing the evaporation rate of FHDM and HDM at contact angle $\theta = 80°$ which is for FHDM, the evaporation rate is $E_v = 3.1 \times 10^{-5}\,\text{kg} \cdot (\text{s} \cdot \text{m})^{-1}$ corresponding average interface temperature is $T_{avg,\Gamma} = 315.40\,\text{K}$, while in comparison, for HDM the evaporation rate and average interface temperature are only $2.1 \times 10^{-5}\,\text{kg} \cdot (\text{s} \cdot \text{m})^{-1}$ and $307.25\,\text{K}$ respectively. Similar trends followed by evaporation at $T_{sub} = 323.15\,\text{K}$ (see fig 4.9), comparison shows that evaporation rate for the HDM is nearly 32% lower than that of FHDM at contact angle $\theta = 80°$.

In figure 4.9a, FHDM has the highest evaporation rate initially, which starts reducing with contact angle, meanwhile, HDM has the lowest initial evaporation rate and then it starts increasing with contact angle. The difference could be understood from figure 4.9b, indeed with FHDM, Marangoni convection increases interface temperature which remains nearly constant until the secondary Marangoni instability appear, while with HDM the energy transfer is only by thermal diffusion in liquid drop, interface temperature increases as time goes on and contact angle reduces, narrowing the substrate to interface distance. The difference between FHDM and HDM evaporation rate reduces as time goes on and contact angle decreases. So, the higher is the interface temperature due to Marangoni convection, the higher is the supplied energy to account for latent heat of vaporisation resulting in higher evaporation rate.

The effect of secondary instability is shown in insert and circle of figure 4.9, where we can see transition from the base primary Marangoni instability (axisymmetric torus) to the secondary Marangoni instability

characterized by fully 3D unsteady fluid flows. After this transition one can observe a dynamic multicellular thermo-convective pattern as shown in figure 4.10. The secondary Marangoni instability cells clearly appear at contact angle $\theta = 17.7°$ and $19.2°$ for $T_{sub} = 318.15\,\text{K}$ and $323.15\,\text{K}$, respectively. The evaporation rate suddenly rises and becomes constant instead of decreasing while interface temperature starts to increase with the decrease in contact angle (see figure 4.9b).

So, the change in evaporation rate due to secondary instability are 2.49% and 2.53% for $T_{sub} = 318.15\,\text{K}$ and $323.15\,\text{K}$, respectively (refer to table 4.2 for more details and other cases). It shows that despite primary Marangoni instability has a strong effect on sessile drop evaporation under microgravity, the secondary Marangoni instability have comparatively a low effect on the evaporation rate of sessile drop. Similar results are seen for HFE7100 experiments, both on the ground as well as in microgravity experiments [76]. Figure 3 of section A shows no change in the slope of the volume vs time plot after the secondary instability appear. They seem to play a minimal role in evaporation of pure liquid sessile drop, meanwhile, it plays important role in particle deposition [108].

The effect of the secondary Marangoni instability on evaporation rate is approximately $2 - 3\%$, but the computational cost is approximately 6 to 8 times higher due to finer mesh and time step requirements. The cost can increase drastically with volatile fluids as in case of HFE7100, for which the computational cost for the same physical time is approximately 30 times higher. As in most of the cases secondary instability appear at low contact angle so it is advisable to use HDM in those latter cases. HDM is a good option for low temperature and low contact angle as in case of ethanol it could be used below $\theta = 20°$ and $T_{sub} = 323\,\text{K}$ (see figure 4.7). For comparison, the evaporation rate at $\theta = 19.2°$ and $T_{sub} = 323\,\text{K}$ is $E_v = 3 \times 10^{-5}\,\text{kg} \cdot (\text{s} \cdot \text{m})^{-1}$ and $2.8 \times 10^{-5}\,\text{kg} \cdot (\text{s} \cdot \text{m})^{-1}$ for FHDM and HDM, respectively. So, HDM has approximately 7% lower evaporation rate compared to FHDM and this difference would reduce with decreasing contact angle. The computational cost for some other cases is provided in the appendix in table C.2.

4.4.2 *Parametric studies for substrate temperature, drop radius, ambient pressure*

Now, to have a broader understanding let us look at a comparative study of the influence of various control parameters such as substrate temperature, drop radius, and pressure on evaporation process of sessile drop of liquid Ethanol through evaporation rate, surface temperature, surface velocity, primary Marangoni instability and secondary Marangoni instability. The space and time discretizations in

the current study remains the same as discussed earlier (for more details refer to sections 3.10.1, 3.10.2 & 3.11). The number of elements in RD, VD, and CD are changed and adapted as per the temperature, diameter and pressure, however, mesh structure remains the same. The details on the DOF, computational cost and other resources for the current study are presented in the appendix table C.2.

4.4.2.1 Influence of substrate temperature

From figure 4.6, we know that evaporation rate increases following a power law with substrate temperature, and a similar trend can be seen in figure 4.15 for the local evaporation rate profile along the radial position of sessile drop.

In figure 4.10 we compare temperature and velocity patterns at the interface (top-view), for substrate temperature T_{sub} from 308.15 to 328.15 K (Top to bottom). The evaporation rate is increased with substrate temperature as seen in the figure 4.6, 4.7 and 4.8. Also, the contact angle at which secondary instability appear increases from $\theta = 14.9°$ to 21° for same drop radius R.

Similarly, the change in evaporation rate due secondary instability also increases from 1.59% to 2.62%, so the critical aspect ratio (AR_{crit}) rises from 0.14 to 0.18, and critical thermal Marangoni number ($Ma_{T,crit}$) accordingly increases from 829.9 to 3136.8 with T_{sub}, for T_{sub} ranging from 308.15 to 328.15 K (see table 4.2 and figure 4.15).

As seen, the AR_{crit} and $Ma_{T,crit}$ values for triggering of the secondary instability also increase with the substrate temperature. Also, in figure 4.10, we can see difference in pattern of the secondary instability where the number of cells and dynamics increase along with surface velocity as substrate temperature increases from 308.15 to 328.15 K. Please refer to video ▶ play or scan QR. and refer to table 4.2 for other details.

Movie for Fig. 4.10

4.4.2.2 Influence of sessile drop radius

The influence of the sessile drop's base diameter passes over in the evaporation rate in equation 3.15 as it is divided by it. So, even though evaporation rate are approximately the same we are going to explore influences of base diameters on the evaporation dynamics. In figure 4.11 and 4.12 we compare sessile drop evaporation cases of base radius $R = 1.5, 2, 2.5$ and 3 mm at constant substrate temperature $T_{sub} = 318.15$ K, initial contact angle $\theta_0 = 33°$ and ambient pressure $P = 0.835$ bar.

Movie for Fig. 4.12.

In figure 4.11a, is shown the evaporation rate versus time for different drop radius. As expected, the evaporation time increases as drop

Surface temperature, T_Γ (K)

Velocity, U (m. s^{-1})
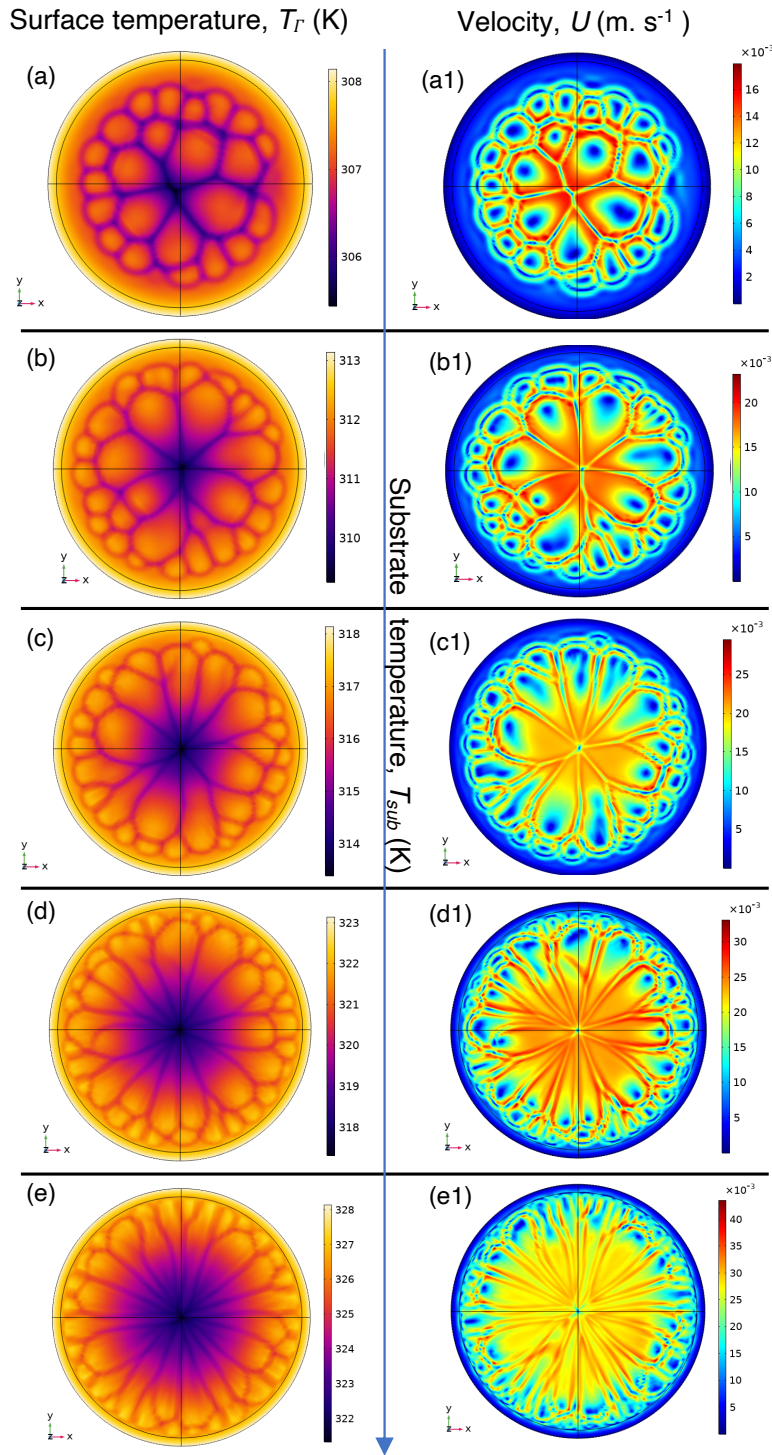
Figure 4.10: **Top view comparison of sessile drop at different substrate temperatures**. **(a-e)**: Surface temperature, **(a1-e1)**: surface velocity for T_{sub} = 308.15, 313.15, 318.15, 323.15, and 328.15 K at contact angle θ = 14.9°, 17.3°, 17.7°, 19.2° and 21°, respectively, with FHDM. For the Movie ▶ play or Scan QR.

(a)

(b)

(c)
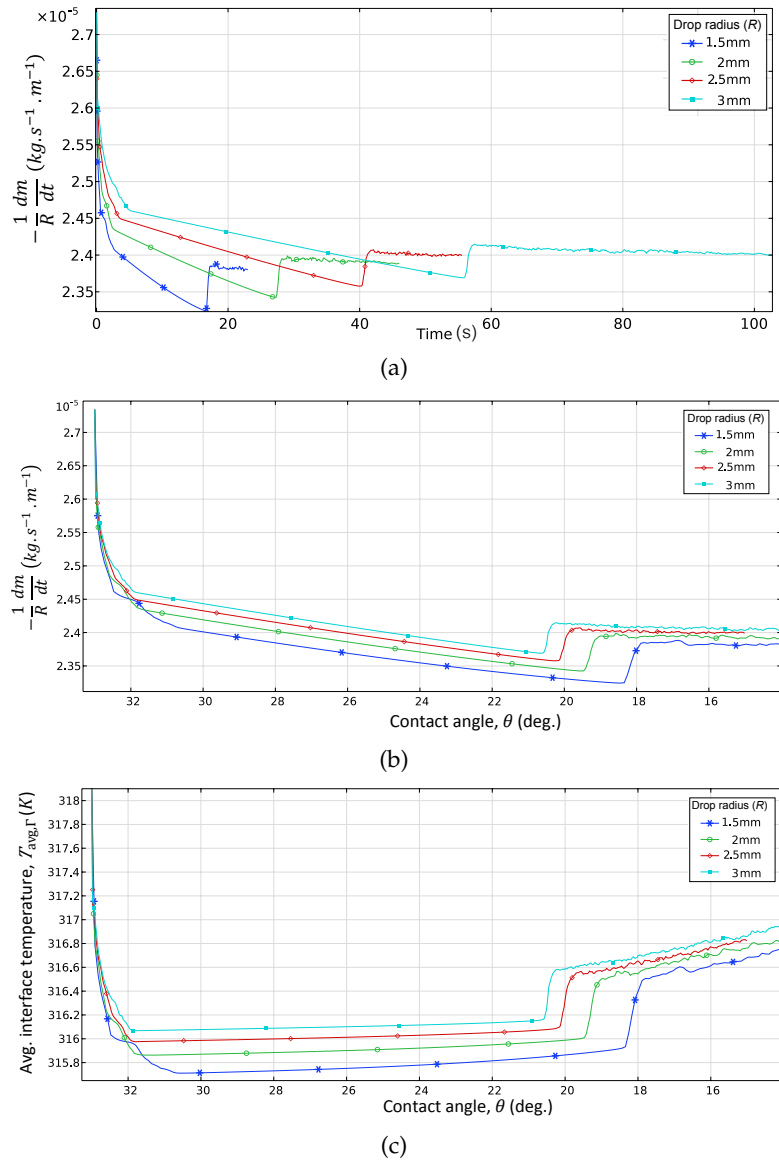
Figure 4.11: **Comparison of ethanol sessile drops of different radius R and substrate temperature $T_{sub} = 318.15$K.**
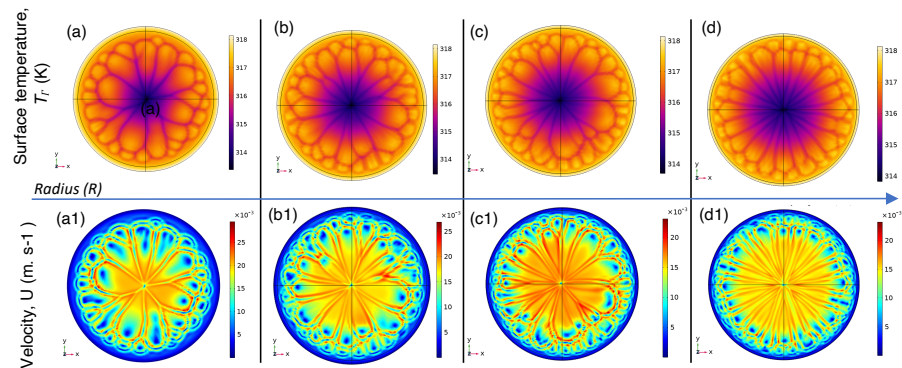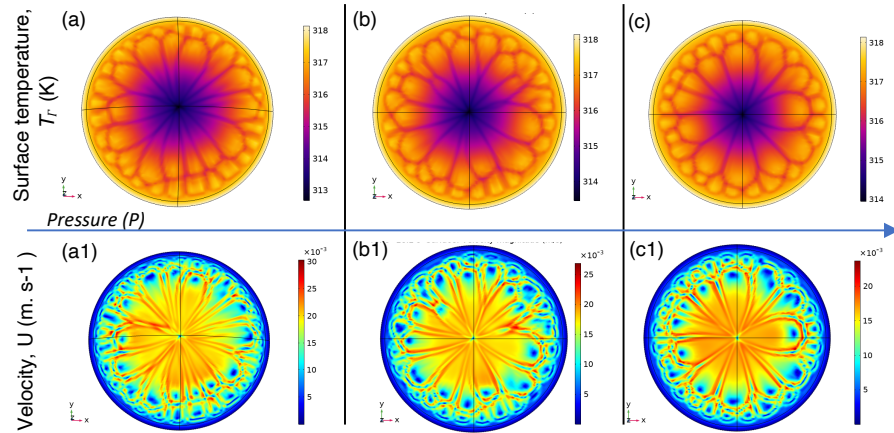

Figure 4.12: **Comparison of ethanol sessile drop surface temperature (top) and surface velocity (bottom) of different radius (R) and substrate temperature $T_{sub} = 318.15$ K (a & a1)**: at contact angle $\theta = 17.7°$ and radius $R = 1.5$ mm; **(b & b1)**: at contact angle $\theta = 19°$ and radius $R = 2$ mm; **(c & c1)**: at contact angle $\theta = 19.6°$ and radius $R = 2.5$ mm; **(d & d1)**: at contact angle $\theta = 20.2°$ and radius $R = 3$ mm. Refer movies ▶ play or Scan QR.

volume increases with base radius for same initial contact angles. The evaporation time from initial contact angle $\theta = 33°$ to final $\theta = 15°$ for sessile drop radius between $R = 1.5$ to $3\,\text{mm}$ ranges from $t = 20.2$ to $79.6\,\text{s}$. For each drop, we have different evaporation rates with respect to time however in figure 4.11b & 4.11c, we can clearly see that with respect to contact angles all the drops evaporation rates are nearly the same. So, it could be mentioned that in the experiments for the calculation of the evaporation rate, instead of reporting the time averaging of evaporation rate it must be based on the contact angles.

As discussed earlier, the evaporation rate reduces with contact angle and interface temperature remains constant due to primary Marangoni instability until the secondary instability appear, then evaporation became constant and interface temperature starts to increase (see fig. 4.11b & 4.11c). During primary Marangoni instability phase for all sessile drops evaporation rate (E_v) remains approximately between $2.45 - 2.30 \times 10^{-5}\,\text{kg} \cdot (\text{s} \cdot \text{m})^{-1}$ and average interface temperature is around $316 \pm 0.2\,\text{K}$. The transition from primary Marangoni instability to the secondary Marangoni instability for the sessile drops happens between $\theta = 17.7°$ and $20.2°$ that corresponds to the heights between $H_t = 2.34 \times 10^{-4}$ and $5.36 \times 10^{-4}\,\text{m}$. As we increase the base radius from $R = 1.5\,\text{mm}$ to $3\,\text{mm}$, critical height also increases nearly by twice, so the critical thermal Marangoni number increases from $\text{Ma}_{\text{T,crit}} = 1488.93$ to 3211.63 with slight increase of critical aspect ratio from $\text{AR}_{\text{crit}} = 0.16$ to 0.18. However, change in the evaporation rate due to appearance of the secondary instability is reduced from 2.49% to 1.92% (see table 4.2). So with that, it can be concluded that lower is the base radius of sessile drop, the lower is the contact angle (or height) for the appearance of secondary Marangoni instability and the higher is the effect of the secondary instability on the evaporation rate. Indeed, larger base radius dilutes the effect of secondary instability on the evaporation rate. An increase in the evaporation rate after the secondary instability is greater in the sessile drop of the small base radius in comparison to larger ones.

In figure 4.12, the evaporating cooling effect is approximately the same irrespective of drop radius as temperature difference across drop height is nearly the same $\Delta T = 4.5\,\text{K}$. However, noticeable difference can be seen in surface temperature distribution, cell shapes and its number, and surface velocity profile. Interestingly, the number of the secondary instability cells is the highest for the largest drop radius but the effect of these instability cells on the change of the evaporation rate after it appears is the lowest.

4.4.2.3   *Influence of ambient pressure on sessile drop evaporation*

Meanwhile, it is well understood that surrounding pressure has an inverse relation with evaporation rate. However, instead of the evap-

(a)

(b)
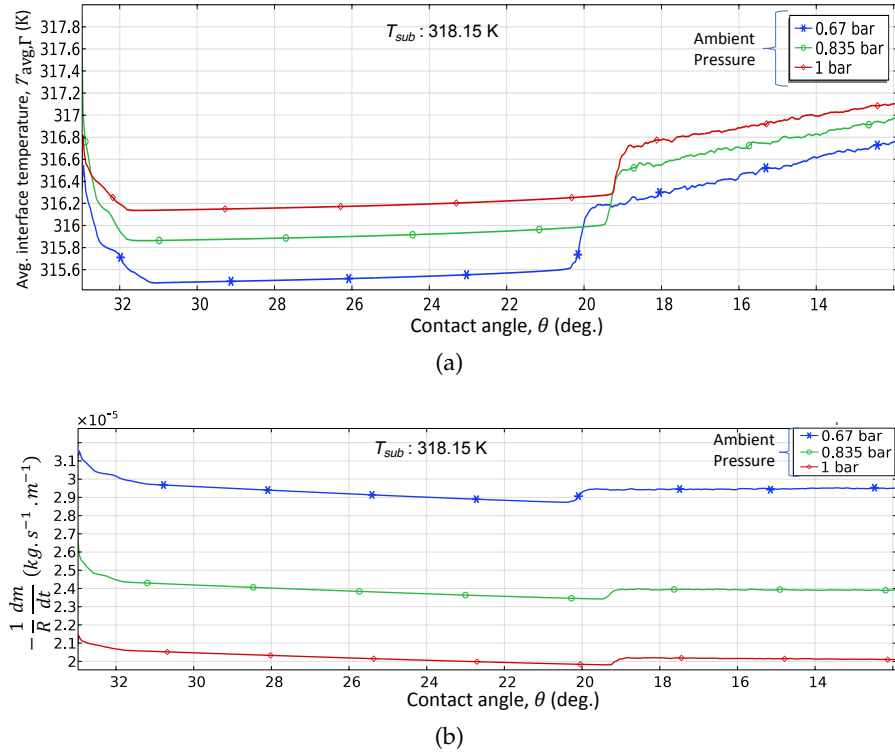
Figure 4.13: **Comparison of ethanol sessile drops of the different ambient pressure (P) at the same substrate temperature $T_{sub} = 318.15$K.**

Figure 4.14: **Comparison of ethanol sessile drop surface temperature (top) and surface velocity (bottom) of different pressure (P) at substrate temperature $T_{sub} = 318.15$K and radius $R = 2$ mm (a & a1)**: at contact angle $\theta = 19.7°$ and pressure $P = 0.67$ bar; **(b & b1)**: at contact angle $\theta = 19°$ and pressure $P = 0.835$ bar; **(c & c1)**: at contact angle $\theta = 19.3°$ and pressure $P = 1$ bar. For movie ▶ play or scan QR.

oration rate, with the current set of the numerical simulation, we are going to mainly explore the pressure effect on the instabilities dynamics.In figure 4.13, we have presented the comparison of the

Ethanol sessile drop evaporation rate and average interface temperature of base radius $R = 2\,\text{mm}$ at constant substrate temperature $T_{sub} = 318.15\,\text{K}$ and different ambient pressure values: $P = 0.67, 0.835$ and $1\,\text{bar}$. Also, in figure 4.14, the comparison of ethanol sessile drop surface temperature (top) and surface velocity (bottom) is presented just after the secondary Marangoni instability appeared.

Movie for Fig. 4.14

With the decrease of the ambient pressure from $P = 1\,\text{bar}$ to $0.67\,\text{bar}$, the evaporation rate of sessile drop is increased from $E_v = 1.98 \times 10^{-5}$ to $2.87 \times 10^{-5}\,\text{kg} \cdot (\text{s} \cdot \text{m})^{-1}$ and concurrently temperature difference increases from $\Delta T = 4.2$ and $5.3\,\text{K}$. The transition from the primary instability to secondary instability happened approximately at contact angle $\theta = 19°$ (height $H_t = 3.4 \times 10^{-4}\,\text{m}$). The change in the evaporation rate due secondary instability increases from 1.98% to 2.57%, so the critical thermal Marangoni number increases from $\text{Ma}_{T,\text{crit}} = 1941$ to 2498.7 where as critical aspect ratio nearly remains the same $\text{AR}_{\text{crit}} = 0.17$.

In conclusion, as expected for the given R and T_{sub}, evaporation rate is the highest under low ambient pressure, that results into higher evaporating cooling thus in comparison lower average interface temperature and greater ΔT (see table refer 4.2). Also, $\text{Ma}_{T,\text{crit}}$ is the highest for the lowest ambient pressure. In figure 4.14, shows surface temperature and velocity profile for different pressure, it shows that for lower pressure, ΔT and surface velocity is higher.

It needs to be noted that secondary instability appears nearly at the same contact angle (or same volume) even though it has a different evaporation rate, evaporative cooling ΔT, average interface temperature and velocities, so the secondary instability cells appearance is much more influenced by geometrical parameters of the sessile drop along with substrate temperature.

4.4.2.4   *Summary of local evaporation rate and global normalized evolution of sessile drops*

In figure 4.15, we have presented the comparison of evaporation rate along the radial position of ethanol sessile drop from parametric study 4.4.2 (refer also to table 4.2). It shows that evaporation rate along the sessile drop interface increases along the drop radius from the apex with the maximum at the contact-line of the drop.

Globally, evaporation rate is minimum for $T_{sub} = 308.15\,\text{K}$ and maximum for $T_{sub} = 323.15\,\text{K}$. The evaporation rate along the interface is equal for all the sessile drop with $T_{sub} = 318.15\,\text{K}$, $P = 0.835\,\text{bar}$ and varying radius R. Higher evaporation rate can be achieved at lower temperature for larger base radius sessile drop by decreasing pressure
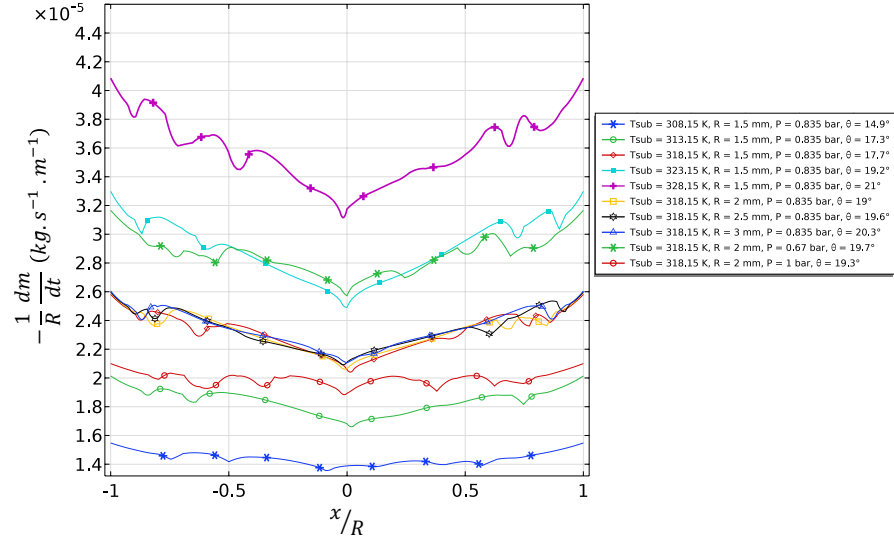
Figure 4.15: **Local evaporation rate J_Γ^{evap} along the radial position of the drop interface.** Evaporation rate profile along the radial position of sessile drop for different substrate temperatures, sessile drop radius and ambient pressure. The sudden fall in the evaporation rate along the radial positions are corresponding to the front of the instability cells.

as seen in the case of sessile drop of parameters $T_{sub} = 318.15\,\text{K}$, $P = 0.67\,\text{bar}$ and $R = 2\,\text{mm}$, and sessile drop with parameters $T_{sub} = 323.15\,\text{K}$, $P = 0.835\,\text{bar}$ and $R = 1.5\,\text{mm}$ are approximately equal. The sudden fall in the evaporation rate along the radial positions are corresponding to the front of the secondary instability cells, the cells of the secondary instability on the drop surface have low temperature at it boundaries compared to the cell's center (see fig 4.14) and it can be noted that magnitude of the sudden change of evaporation rate increases with substrate temperature (or evaporation rate).

Figure 4.16, illustrates the normalized evolution contact angle and volume of Ethanol drop for various values of the substrate temperature, sessile drop contact radius and pressure (see table 4.2). As, expected for pure diffusion, evaporation and pinned sessile drop evolution perfectly follows the linear trend with time as for the water [38]. The concentrate linear fit for normalised contact angle is $\frac{\theta_t}{\theta_{min}} = a_\theta + b_\theta \times \frac{t}{t_{max}}$ where $a_\theta = 3.51 \pm 4.53 \times 10^{-4}$ and $b_\theta = -2.48 \pm 7.83 \times 10^{-4}$, and normalised sessile drop volume concentrate linear fit is $\frac{Vol}{Vol_{t=0}} = a_{vol} + b_{vol} \times \frac{t}{t_{max}}$ where $a_{vol} = 1 \pm 3.08 \times 10^{-5}$ & $b_{vol} = -0.73 \pm 5.34 \times 10^{-5}$. The slope of normalised contact angle follows 3.4% time of the drop's volume during the evaporation.
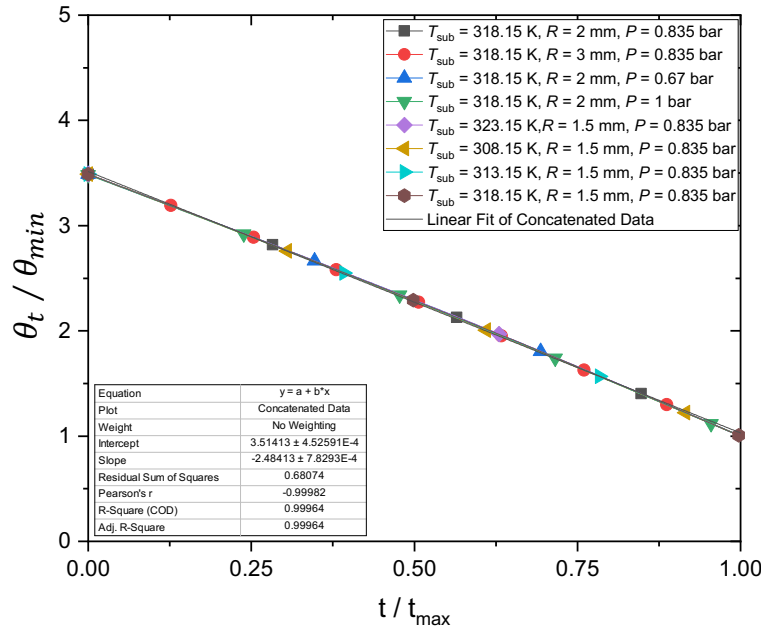
(a)
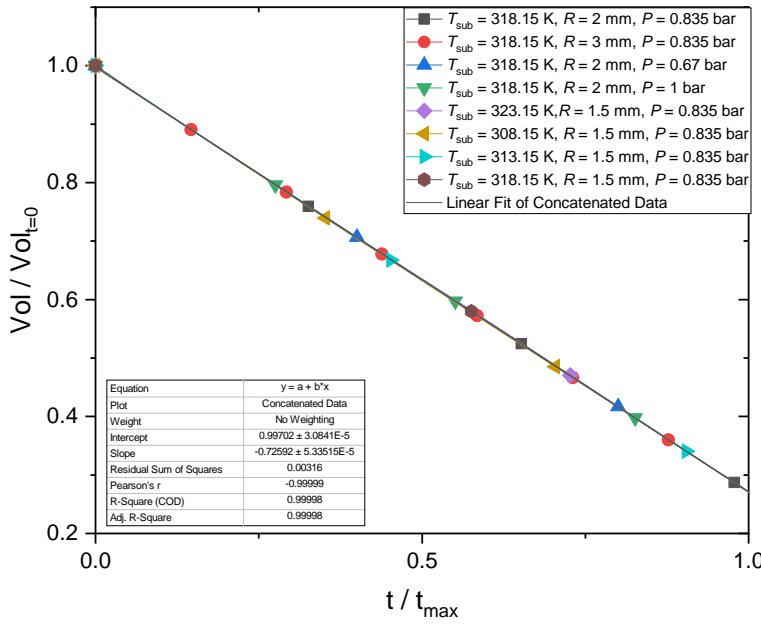
(b)

Figure 4.16: **Normalised numerical values for the time-dependent sessile drops evaporation and the approximate fit to these. (a)** Normalised contact angle with respect to time and concentrate linear fit for all: $\frac{\theta_t}{\theta_{min}} = a_\theta + b_\theta \times \frac{t}{t_{max}}$ where $a_\theta = 3.51 \pm 4.53 \times 10^{-4}$ & $b_\theta = -2.48 \pm 7.83 \times 10^{-4}$; **(b)** Time dependent normalised sessile drop volume and concentrate linear fit for all: $\frac{Vol}{Vol_{t=0}} = a_{vol} + b_{vol} \times \frac{t}{t_{max}}$ where $a_{vol} = 1 \pm 3.08 \times 10^{-5}$ & $b_{vol} = -0.73 \pm 5.34 \times 10^{-5}$. The time is non-dimensionalized with respect to total evaporation time (t_{max}).

4.4.3   *Sessile drop dynamics and cells patterns evolution with time*

After the global parametric study, let's take a case to explore other parameters of sessile drop evaporation that are varying in the different phases of evaporation process. For our analysis, we take a sessile drop of ethanol at substrate temperature T_{sub} = 318.15 K, pressure P = 0.835 bar and radius R = 2 mm as it is common drop between the study for influence of the radius and pressures. In figure 4.11a, the plot of the evaporation rate versus time is shown, and the total time taken for evaporation from initial contact angle θ = 33° up to 15° is t = 35.7 s. The average evaporation rate during the primary instability phase for sessile drop is approximately E_v = 2.4 ± 0.05 × 10^{-5} kg · (s · m)$^{-1}$ and average interface temperature is around $T_{avg,\Gamma}$ = 316 K (please refer to figure 4.11c, 4.11b, 4.13a and 4.13).
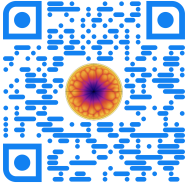
In figure 4.17, the illustration presents the evolution of the sessile drop (top view) with contact angle (left to right in the sequence of the appearance) and interface surface temperature, top view (IR) using equation 3.17, local evaporation rate using equation 3.13, surface velocity and local normal total flux (on the substrate, opposite to isothermal boundary surface layer).

Similarly, figure 4.18a displays streamlines (colored with temperature) with velocity vector (back) in quarter geometry, and in figure 4.18b vector are uniformly distributed over the top surface and cut plane with vector length proportional to the velocity magnitude and colored with temperature. Whereas figure 4.19 is 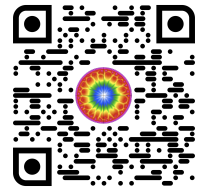top view of the vorticity vector field on the surface of sessile drop and figure 4.20 is temperature (top), velocity vector (middle) and velocity magnitude (bottom) at the cut plane (half), inside the domain of Ethanol sessile drops.

Figure 4.21, shows the Ethanol evaporation rate along the radial position of sessile drop interface in X-Y plane at different contact angles and corresponding temperatures, velocity field, heat flux profile at interface and normal total flux on the substrate are provided in appendix figure D.4, D.6 and D.5a.

The divided illustrations in figure 4.18, 4.19 and 4.20 are representing the four phases of Ethanol sessile drop's evaporation: **(a)** at contact angle θ = 20.6°: primary instability phase; **(b)** at contact angle θ = 19.4°: transition begins from primary to secondary instability; **(c)** at contact angle θ = 19°: complete appearance of secondary instability cells; **(d)** at contact angle θ = 15.4°: fully developed flow with secondary Marangoni instability cells at the low contact angle.

In figure 4.11a, at t = 0 s, the evaporation rate is maximum due to the effect of the initial boundary conditions, i.e initial drop temperature
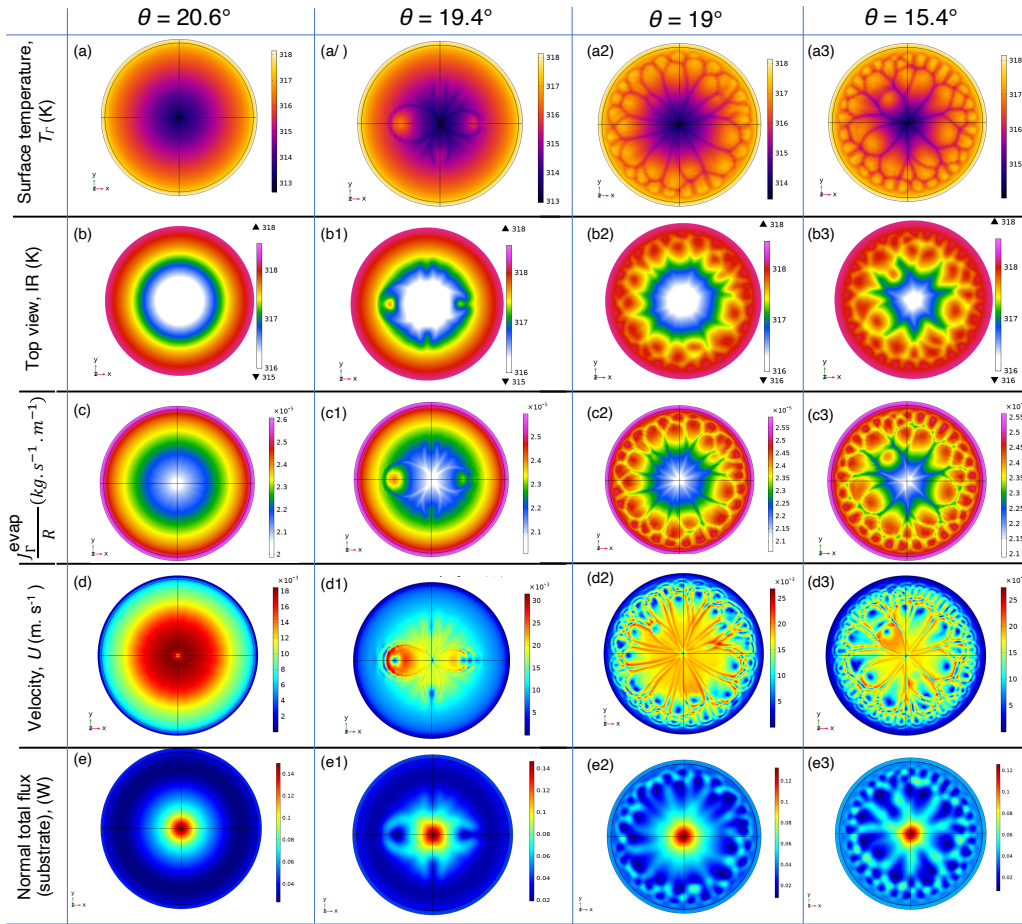
Figure 4.17: **Ethanol sessile drops with surface temperature, IR temperature, local evaporation rate distribution, normal total flux (substrate) and velocity and at the substrate temperature $T_{sub} = 318.15\,\mathrm{K}$, pressure $P = 0.835\,\mathrm{bar}$ and radius $R = 2\,\mathrm{mm}$. (a-e)** at contact angle $\theta = 20.6°$ showing in primary instability phase; **(a1 - e1)** at contact angle $\theta = 19.4°$, starting of the secondary instability cells; **(a2 & e2)** at contact angle $\theta = 19°$ fully developed stage of the secondary instability with flower like pattern; **(a3 & e3)** at contact angle $\theta = 15.4°$ secondary instability core cells are getting bigger. Please refer also figure 4.11 and table 4.2. For movies ▶ play or scan QR.

is equal to the substrate temperature. With time at $t = 2\,\mathrm{s}$ thermal energy is adjusted with fluid flow and thermal distribution in domain according to boundary conditions, and it arrives in equilibrium state. After that, from $t = 2$ to $27.4\,\mathrm{s}$ (from $\theta = 32$ to $19°$) a primary instability is developed having toroidal shape with axis at the center of sessile drop (see fig. 4.18aa & 4.18ba), with the lowest temperature around the apex, accordingly the lowest evaporation rate at the apex that increases along the radial position towards the contact line (see fig. 4.21 & D.4, follow legend $\theta = 20.6°$). Concurrently, while fluid flowing from contact line toward apex at interface, velocity magnitude is the highest near surrounding of the apex and reduces towards the contact line similar pattern followed by normal total flux at substrate (see

Movie for Fig.4.18b

(a)

(b)
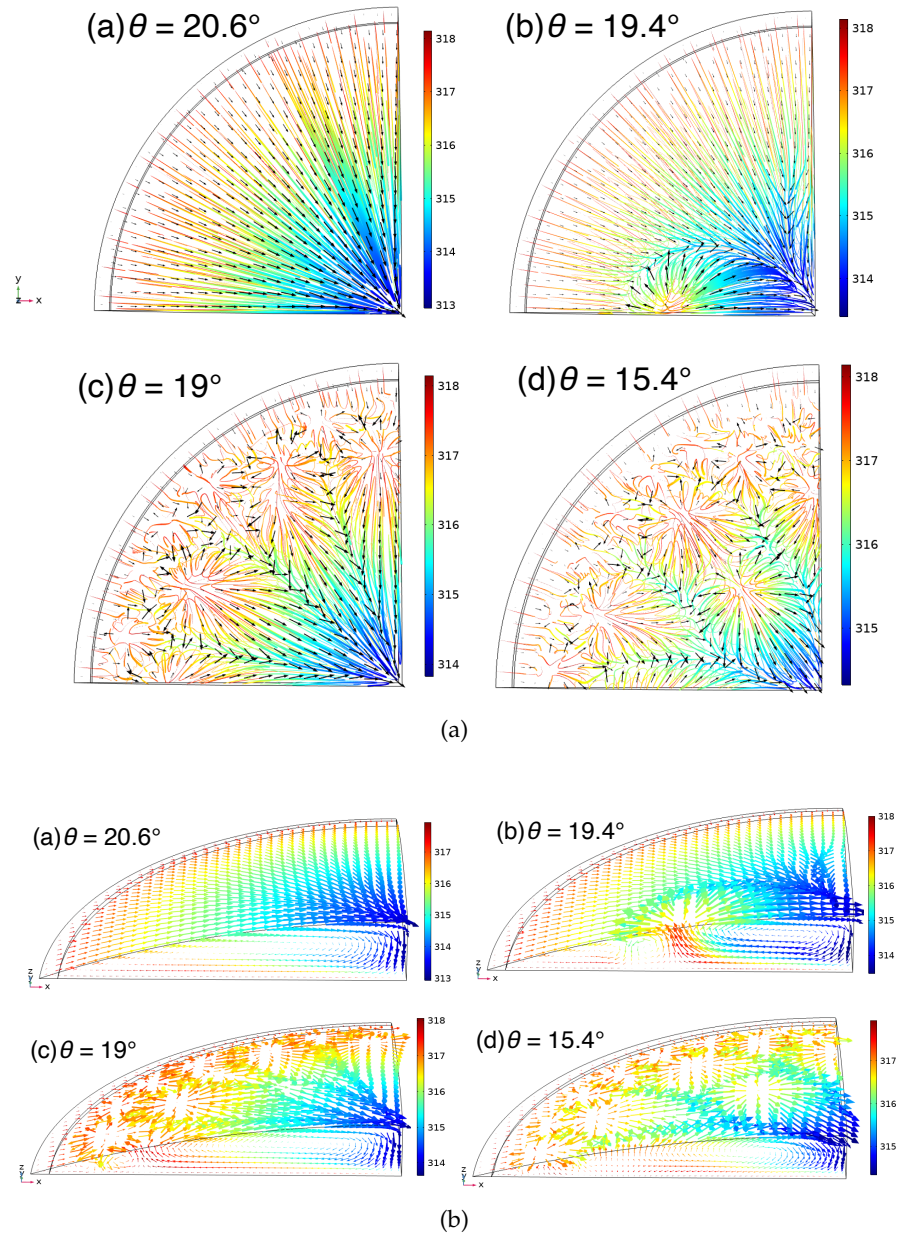
Figure 4.18: **Streamline and velocity vector of ethanol sessile drops at substrate temperature** $T_{sub} = 318.15\,\mathrm{K}$**, pressure** $P = 0.835\,\mathrm{bar}$ **and radius** $R = 2\,\mathrm{mm}$. The subplot of both (4.18a & 4.18b) are as follows: **(a)** at contact angle $\theta = 20.6°$ showing in the primary instability phase; **(b)** at contact angle $\theta = 19.4°$, starting of the secondary secondary instability cells; **(c)** at contact angle $\theta = 19°$ fully developed stage of the secondary instability with flower like pattern; **(d)** at contact angle $\theta = 15.4°$ secondary instability core cells are getting bigger at center. Figure 4.18a is with streamline and velocity vectors (black). Streamline properties are tube types and tube radius is proportional to velocity magnitude and colored with temperature and figure 4.18b velocity vector are uniformly distributed over the top surface and cut plane with vector length proportional to the velocity magnitude and colored with temperature. ▶ play or scan QR.
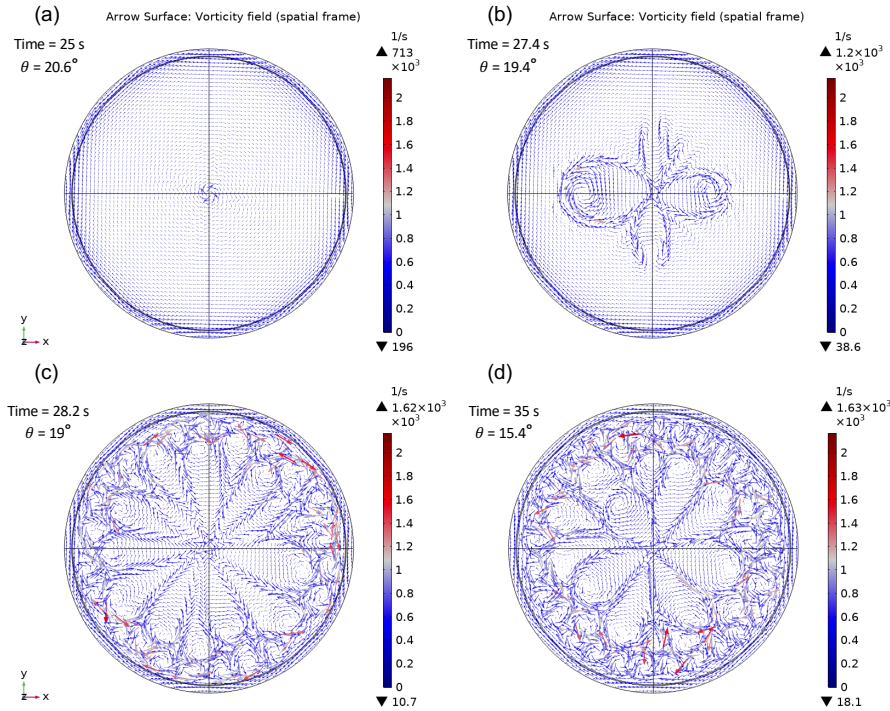
Figure 4.19: **Vorticity field vector on the surface of Ethanol sessile drop on heated substrate. Numerical simulation and subplot conditions are same as fig. 4.18.**

fig. D.6a & D.5). In Figure D.6a, velocity field $x-$component (u), and velocity field $z-$component (w) shows that flow moving toward the apex without any velocity field $y-$component (v) representing no azimuthal velocity in flow which is also affirm by the vorticity fields in figure 4.19a. The cut plane in domain shows temperature and velocity profile corresponding to the primary instability phase (see figure 4.17 a, b, c, d, & e and fig. 4.18aa, 4.18ba and figure 4.20a).

Movie for Fig. 4.20

Movie for fig. 4.19

The occurrence of secondary instability cells begin with the break of axisymmetric torus roll at $t = 27.4\,\mathrm{s}$ ($\theta = 19.4\,^\circ$), instability cells appear near the middle of sessile drop radius. Instability cells can be seen in figure 4.17a1 and 4.18bb in the direction moving from substrate to sessile drop interface while moving towards the contact lines, having approximately 1 K higher temperature than the surrounding liquid (see fig. D.4). Velocity field of sessile drop interface in fig D.6b shows sudden change and fluctuation in the velocity field that corresponds to secondary instability cell. Figure 4.18ab, c & d, also show that cells are moving in the opposite direction of main flow and it is confirmed by the velocity field u and v (see fig. D.6b). Also, figure 4.19b shows increase in the vorticity magnitude. Concurrently, fig. 4.18bb & fig. 4.20b clearly show the dynamics inside the cell in liquid domain with streamlines and vectors around cells, it also shows high temperature fluid moving from substrate to interface and going towards the contact

Figure 4.20: **Temperature (top) and velocity vector (middle) and velocity magnitude (bottom) at the cut plane (half), inside the domain of ethanol sessile drops.** Numerical simulation and subplot conditions are same as fig. 4.18. Velocity vector is color with temperature. For movie ▶ play or scan QR.
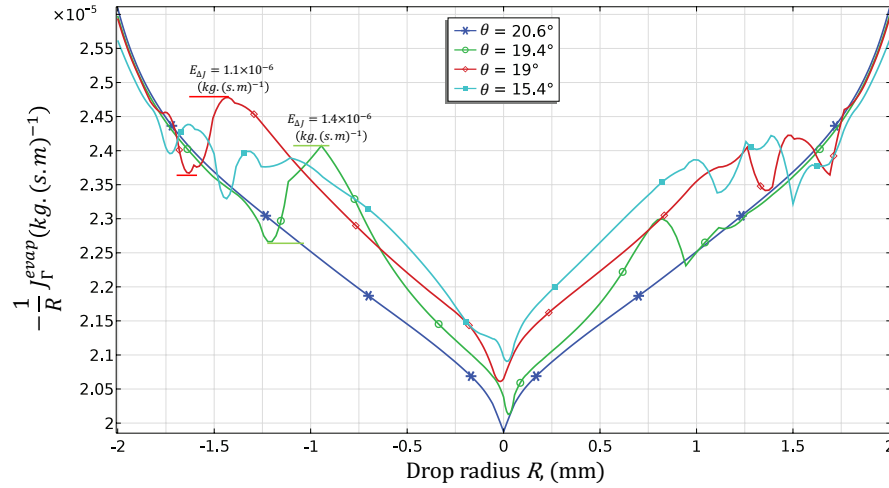
Figure 4.21: **Comparison of Ethanol evaporation rate along the radial position of sessile drop interface at different contact angle and substrate temperature** $T_{sub} = 318.15\,\text{K}$**, pressure** $P = 0.835\,\text{bar}$ **and radius** $R = 2\,\text{mm}$. The smooth profile of evaporation rate at $\theta = 20.6\,^\circ$ corresponding to primary instability phase and rest remaining evaporation rate along the radial position with fluctuation represent the secondary instability (refer to fig. D.4 for corresponding temperature profile). For movie ▶ play or scan QR.
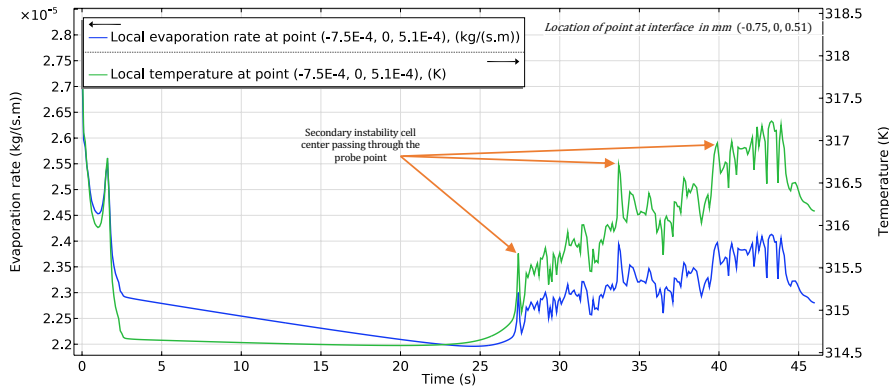
Figure 4.22: **Local evaporation rate and temperature at the probe point at initial location ($x = 0.75\,\text{mm}, y = 0\,\text{mm}, z = 0.51\,\text{mm}$) on the sessile drop interface.** Numerical simulation conditions are same as fig. 4.17. For movie ▶ play or Scan QR.

line. While figures 4.17 a1, b1, c1, d1, & e1 and figure 4.18ab show the top view of sessile drop with appearance of the instability cells.

The non-axis-symmetric flower like pattern is developed corresponding to secondary instability phase at contact angle $\theta_{crit} = 19°$ (at $t = 28.2\,\text{s}$ and height $H_t = 3.35 \times 10^{-4}\,\text{m}$). The change in evaporation rate due to secondary instability is around $E_{\Delta J} = 2.25\%$, at critical thermal Marangoni number $\text{Ma}_{T,crit} = 2147.69$ and critical aspect ratio $\text{AR}_{crit} = 0.17$. With secondary instability development the reducing evaporation rate with contact angle became constant and average interface temperature starts increasing (see fig. 4.11b & 4.11c). In figures 4.18bc and 4.20c is shown local circulation of fluid near contact line that creates low temperature region that influences the local evaporation rate as we can see in figure 4.21 the sudden decrease along the radial position that corresponds to the front of instability cell. For example, for $\theta = 19°$, legend (red) in figure 4.21, the instability cell located with center at $R = -1.44\,\text{mm}$ and front at $R = -1.64\,\text{mm}$, have approximately 4.5% difference between the evaporation rate of front and center of the instability cell (for top-view refer to fig. 4.17a2) and corresponding temperature difference is $\Delta T_{inst} = 0.94\,\text{K}$ (see fig. D.4 and also refer figure D.5 for heat flux variation). In figure 4.22, shown the evaporation rate and temperature plot of probe point at initial location ($x = 0.75\,\text{mm}, y = 0\,\text{mm}, z = 0.51\,\text{mm}$) and moving with interface. As, the secondary instability cell centre passes through the probe point, a clear spikes are registered for the local evaporation rate and temperature (refer to Fig. 4.22 and movie ▶ play or Scan QR).

In general, the velocity magnitude is lower in comparison to initial primary instability phase except around the instability cells (see fig. D.6c). As seen in figures 4.17d2 and 4.18ac, velocity is compar-
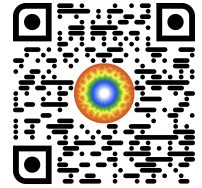
Movie for Fig. 4.21, D.4 & D.6.
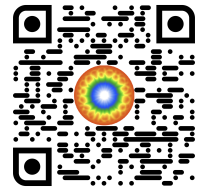
Movie for fig. 4.17, D.7 & 4.22

atively higher around the periphery of the cells. The velocity field $x-$component (u), and velocity field $z-$component (w) along with velocity field $y-$component (v) in figure D.6c shows that flow is moving towards the apex while the secondary instability cells are moving towards the contact line contrary to primary instability phase now velocity field $y-$component (v) is also inducing the azimuthal velocity in the flow which is also affirmed by the vorticity fields in figure 4.19c. Interestingly, vorticity fields in figure 4.19b, c & d shows that the rotation of the flow within the secondary instability cells is higher and opposite to the sessile drop primary flow. As the secondary instability have minimal contribution in the evaporation so is the vorticity however, vorticity could be interesting for the particle transportation and deposition studies.

With time (or reducing contact angle) number of cells increased as we can see in figures 4.18ad and the cells are also developed closer to the center of sessile drop. The secondary instability cells have an intrinsic wavelength that roughly depends on the local liquid thickness along the radial direction of the sessile drop. The secondary instability cells wavelength decreases along with the aspect ratio. The wave number strongly depends on the aspect ratio, substrate temperature and volatility of the fluid. However, evaporation rate nearly remains constant and average interface temperature continues to increase slowly (see fig. 4.11a and 4.11c) whereas, ΔT continues to reduce with the increasing average interface temperature. The local evaporation rate along the radial position of sessile drop interface also elevates from apex to the position approximately at $|R| = 1.7\,\text{mm}$, after that local evaporation rate remains the same as it was in primary instability phase (see fig. 4.21). Globally, we can see in the figure 4.17 that the local distribution pattern of evaporation rate is following the temperature profile where the heat flux from the substrate is following the velocity profile. We can also mention that the density of the number of cells neither heavily influences the evaporation rate nor the velocity of the sessile drop.

Refer to movies of the current section for the understanding of the complete dynamics of sessile drop evaporation.

Every insatiability cell irrespective of the size creates fluctuation on the local evaporation rate.

4.4.4 *Bifurcation from primary to secondary instability in sessile drops*

The thermal Marangoni number (Ma_T) represents the thermal transport via flow (convection) due to a gradient in surface tension, with thermal diffusion. In figure 4.23, the strength of Marangoni convection is presented via thermal Marangoni number (Ma_T) and sessile drop Marangoni number (Ma_{SD} with respect to aspect ratio $AR = \frac{H_t}{R}$ for the complete set of numerical simulations for ethanol sessile drops those are discussed in the previous sections 4.4.2 (see table 4.2). Figures 4.23

(a)

(b)
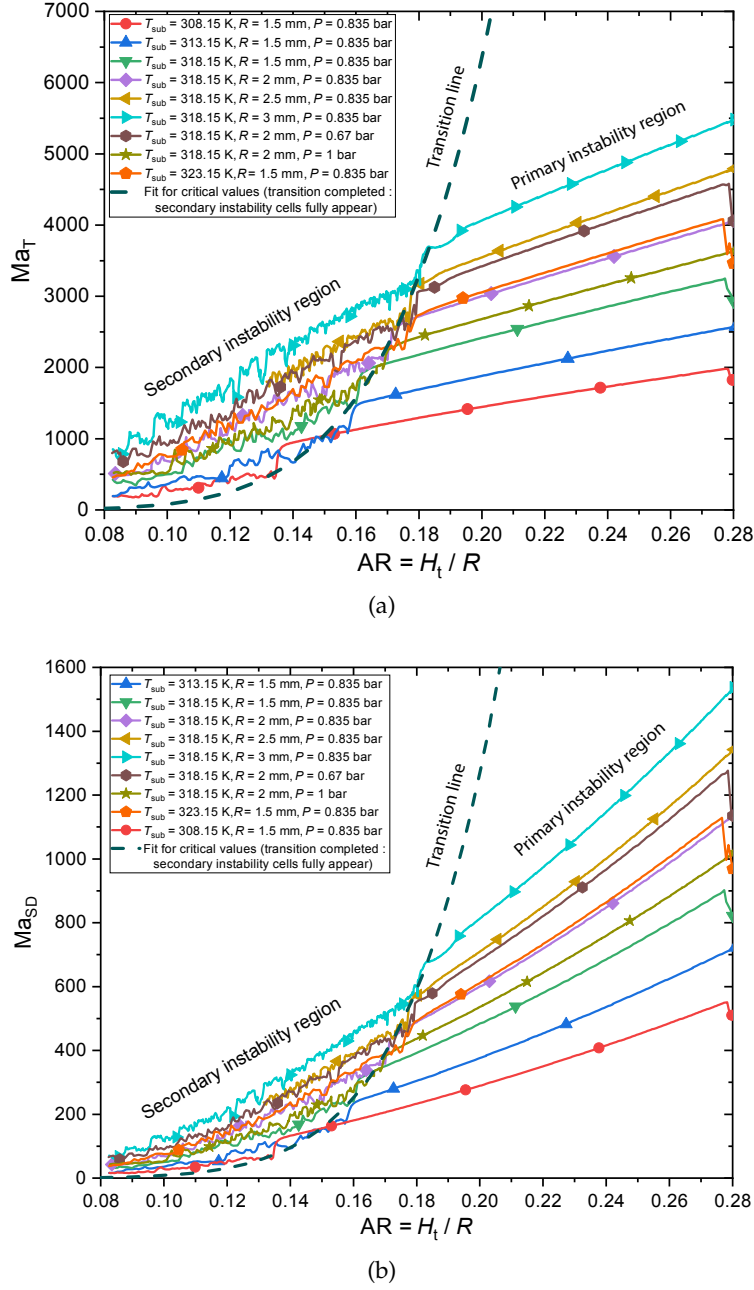
Figure 4.23: **Marangoni number of ethanol sessile drop as a function of aspect ratio** $AR = \frac{H(t)}{R}$. **(a)** Thermal Marangoni number (Ma_T) started with stable Marangoni number with higher aspect ratio then became unstable after secondary instability cells appeared at the critical aspect ratio (AR_{crit}); **(b)** Sessile drop Marangoni number (Ma_{SD}) showing similar trend as (Ma_T) with different slopes. Linear fit for the log-log plot of $Ma_{T,crit}$ and $Ma_{SD,crit}$ as a function of (AR_{crit}). Fitting data as follows: $Ma_{T,crit} = 10^{a_{Ma}} \times (AR_{crit})^{b_{Ma}}$ where $a_{Ma} = 8.1765 \pm 0.29$ & $b_{Ma} = 6.26 \pm 0.26$ and $Ma_{SD,crit} = 10^{a_{SD}} \times (AR_{crit})^{b_{SD}}$ where $a_{SD} = 8.1765 \pm 0.29$ & $b_{SD} = 7.26 \pm 0.36$ (refer to fig. D.2 and D.3, Fig. D.3 is with the fit for the critical values from the starting and completion of the transition).

& 4.23b show that Thermal Marangoni number linearly decreases with the drop aspect ratio during the primary instability phase and starts fluctuating with the occurrence of secondary instability. The values at the point of appearance of the secondary instability cells are referred as critical values, i.e $Ma_{T,crit}$, $Ma_{SD,crit}$ and AR_{crit}. In figure D.2 is shown that log-log plot of $Ma_{T,crit}$ and $Ma_{SD,crit}$ as a function of (AR_{crit}) is a linear fit. So, the power relations of the critical values can be presented by fitting data as follows: $Ma_{T,crit} = 10^{a_{Ma}} \times (AR_{crit})^{b_{Ma}}$ where $a_{Ma} = 8.1765 \pm 0.29$ & $b_{Ma} = 6.26 \pm 0.26$ and $Ma_{SD,crit} = 10^{a_{SD}} \times (AR_{crit})^{b_{SD}}$ where $a_{SD} = 8.1765 \pm 0.29$ & $b_{SD} = 7.26 \pm 0.36$. Finally, it can be concluded that the secondary instability cells appear earlier for the higher Ma_T i.e secondary instability cells appear at larger contact angle for high substrate temperature and larger diameter (see also figure 4.11c and table 4.2). Figure 4.23 shows that the dynamic evolution of sessile drop can be divided into primary and secondary instability phase by fit and it can be used in experiment design or to anticipate the phase of instability.

The comparison of Ma_T and Ma_{SD}, show the same trend, indicating that they are equivalent, up to a magnification factor, but the second relationship explicitly contains contact angle, which seems much more relevant for sessile drops.

4.5   EXPLORATORY NUMERICAL SIMULATION

The following section is exploratory in the essence as the discussions in the coming subsections mainly focus on providing an insight on the sessile drop evaporation under microgravity to facilitate the experiment design based on numerical results. Then, to provide observation on the Ethanol sessile drop secondary instability cells and its structure via comparing it with experiment. However, it is difficult to extend the analysis further due to lack of experimental data. Also, the numerical results for the Water and Methanol are incorporated for future microgravity experiments.

4.5.1   *Computation for the sounding rocket experiment (ARLES)*

As we discussed in chapter 2, the ARLES experiment partly failed owing to over sized sessile drops that would have necessitated much longer evaporation time to see all the dynamics induced by secondary instability. So, the objective is to perform computations for actual sessile drop ($7DP\mu$g drop) from the ARLES experiments until complete evaporation time. The aim of this computation is to extrapolate our understanding to predict the missed dynamics of sessile drop during the sounding rocket experiment in microgravity. As we saw during the ground experiment all drops showed the instability cells, however un-
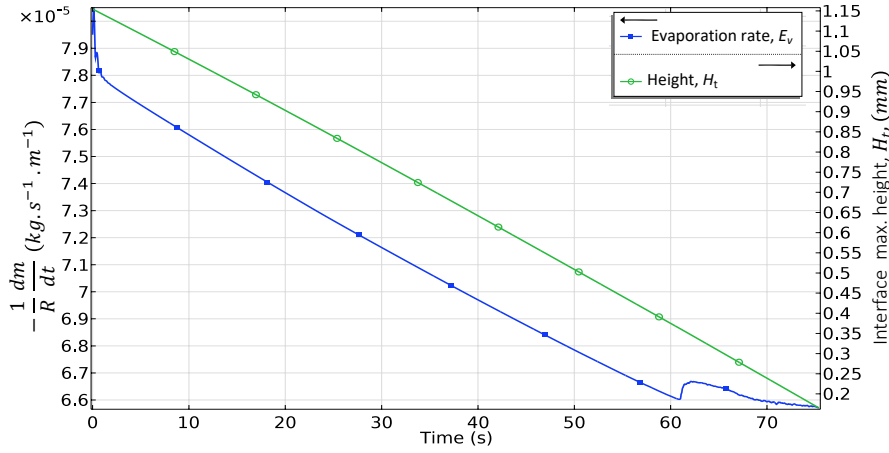
Figure 4.24: **Numerical simulation for** HFE7100 **on heated substrate under microgravity condition.** Evaporation rate and drop height with time at initial contact angle $\theta_0 = 60°$, $T_{sub} = 301.15\,\text{K}$, $P = 105400\,\text{Pa}$ and $R = 2\,\text{mm}$. The initial $\theta_0 = 60°$ nearly corresponds to the microgravity experiment [76].

der microgravity experiment unfortunately we missed the secondary Marangoni instability due to early flushing of the sessile drop. By using our current model now we can compute the critical volume and critical height for transition from primary Marangoni instability to secondary Marangoni instability and supply the next experiment with initial volume for given base radius, pressure and substrate temperature and given duration for each sessile drop evaporation.

In figure 4.24, plot of the evaporation rate and height with respect to time is presented for sessile drop of liquid HFE7100 at substrate temperature $T_{sub} = 301.15\,\text{K}$, pressure $P = 105400\,\text{Pa}$ and radius $R = 2\,\text{mm}$ (from experiment [76], for $7DP\mu g$ drop). The space and time discretizations of the current simulation are already discussed while presenting validation of our model in section 4.2.2. Earlier section was more focused on the validation of our numerical model via comparing the evaporation rate over the time. Now, we are going to focus on the secondary instability phase of the liquid HFE7100 sessile drop. For details on the DOF, computational cost and other resources for the current study are presented in appendix table C.3.

If the initial volume is sufficiently closer to the critical values then instability cells may appear earlier due to the influence of initial dynamics from the injection phase.

The average evaporation rate between $\theta_{t=0} = 60°$ to $\theta_{t=75} = 9.4°$ is $0.09\,\mu\text{L}\cdot\text{s}^{-1}$ (see fig 4.24). From $t = 2$ to $60.9\,\text{s}$ a primary Marangoni instability is developed having toroidal shape with axis at the center of sessile drop, with the lowest temperature around the apex of interface Γ (see figure 4.25 d & c (bottom)). At $t = 60.9\,\text{s}$ ($\theta = 19.4°$), transition begins and secondary instability cells appear. Figure 4.5 shows that instability cells appear at much lower volume as compared to the volume at the point of flushing started for the sessile drop $7DP\mu g$. For the given conditions and $t = 30\,\text{s}$ window for each experiment, the
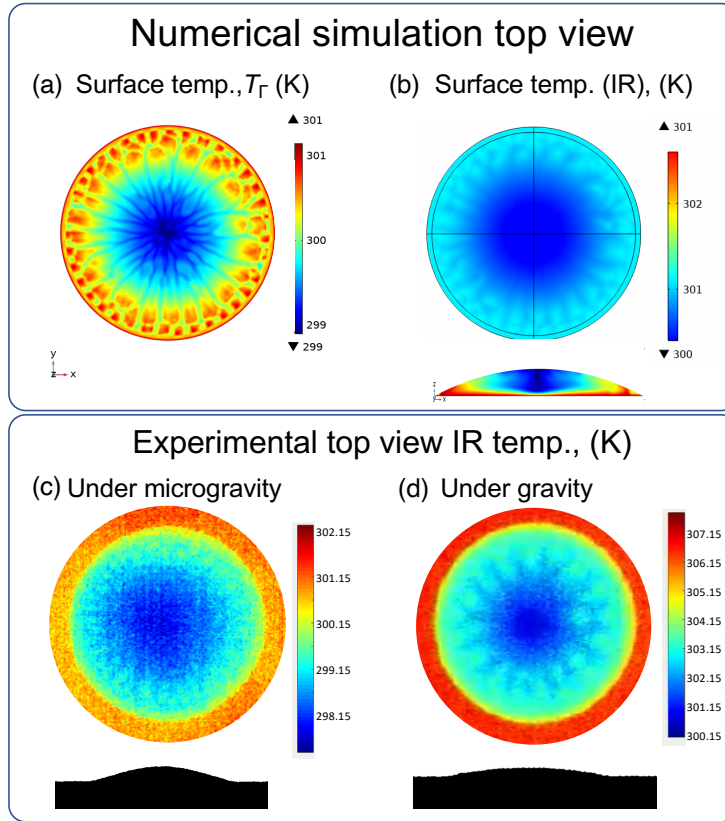
Figure 4.25: **Experiment and numerical comparison during primary Marangoni instability phase of liquid** HFE7100 **sessile drop evaporation under micro gravity conditions. (a)** Top view (IR), experiment drop $5DP$µg at $t = 25$ s at $Vol. = 8.5$ µL; **(b)** Top view (IR), experiment drop $7DP$µg at $t = 25$ s, $Vol. = 6$ µL, $\theta_{t=25} = 48.2°$ and height $H_t = 0.9$ mm; **(c)** Top View (IR) at $t = 20.6$ s, $Vol. = 6$ µL, $\theta_{t=20.6} = 48.2°$ and $H_t = 0.9$ mm, numerical of the HFE700 have same parameter as fig 4.24; **(d)** & **(e)** Top view surface temperature of figure 4.25c.

drop volume should not be more than 3.5 ± 0.5 µL to have efficiently both phases i.e primary Marangoni instability and later secondary Marangoni instability.

Movie for fig. 4.4, 4.24, 4.25 & 4.26.

As we know we missed the possibilities to see clearly the secondary instability cells in the microgravity conditions only due to time limitation for each experiment however we see secondary instability cells under microgravity condition with electric field (see fig. 4.26c) and very clearly for all the case of HFE7100 sessile drop on heated substrate under gravity conditions (for example see fig. 4.26d and fig. 3 of section A). So, let's take that opportunity to have some qualitative comparison of instabilities from top-view between the numerical and experiment irrespective of the gravity conditions. To allow this comparison we need to assume that electric field and gravity doesn't heavily influence the structure of secondary instability cells. Figure 4.26 shows the experiment and numerical comparison during secondary Marangoni

Figure 4.26: **Experiment and numerical comparison during secondary Marangoni instability phase of liquid** HFE7100 **sessile drop evaporation under microgravity conditions. (a) & (b)** Surface temperature (top view) and IR view (top view) respectively at time $t = 62.1\,\text{s}$, $Vol. = 2.2\,\mu\text{L}$, $\theta_{t=62.1} = 19.7°$ and $H_t = 0.35\,\text{mm}$; **(c)** Experiment drop ($6DP\mu\text{gEF}$) under microgravity condition with electric field at $t = 18.32\,\text{s}$, $Vol. = 2.01\,\mu\text{L}$ and maximum sessile drop height is $0.41\,\text{mm}$; **(d)** Experiment drop ($1DP1g$) under gravity condition at $t = 11.25\,\text{s}$, $Vol. = 1.25\,\mu\text{L}$ and maximum sessile drop height $H_t = 0.2\,\text{mm}$. Parameters for numerical simulations are same figure 4.24 and for experiments same as figure 3 of section A. For experiment please refer figure 3 and table 1 of section A. For better understanding please also refer to movie ▶ play or Scan QR.

instability phase of liquid HFE7100 sessile drop evaporation under microgravity conditions. In figure 4.26a & b, top view from numerical simulation at $t = 62.1\,\text{s}$ is show, the non-axis-symmetric flower like pattern is developed corresponding to secondary Marangoni instability at contact angle $\theta = 19.7°$, $Vol. = 2.2\,\mu\text{L}$, and height $H_t = 3.47 \times 10^{-4}\,\text{m}$ with evaporation rate $E_v = 6.67 \times 10^{-5}\,\text{kg} \cdot (\text{s} \cdot \text{m})^{-1}$ and average interface temperature $T_{avg,\Gamma} = 300\,\text{K}$. The change in evaporation rate due secondary instability is 1.06%, the critical aspect ratio $\text{AR}_{\text{crit}} = 0.17$ and critical thermal Marangoni number $\text{Ma}_{\text{T,crit}} = 4270$. Figure 4.26c,

shows secondary instability cells of experiment drop ($6DP\mu$gEF) under microgravity condition with electric field at $t = 18.32$ s, $Vol = 2.01\,\mu$L and maximum sessile drop height is $H_t = 0.41$ mm. Unfortunately, as explained earlier it is the single drop in whole microgravity experiment that reached to the critical volume required for appearance of the secondary Marangoni instability. We are going to use drop $6DP\mu$gEF to mark the experimental critical parameters for the appearance of the secondary Marangoni instability by neglecting the effect of electric field under microgravity condition as it is seen in the ground experiment that electric field doesn't influences heavily the appearance of secondary Marangoni instability but it could influence in microgravity due to cone formation under micro gravity with electric field. Figure 4.26d, shows top view (IR) of the sessile drop (1DP1g) under gravity condition at $t = 11.25$ s, $Vol. = 1.25\,\mu$L and maximum sessile drop height is $H_t = 0.2$ mm with secondary instability cells

Electric field and gravity influence on the structure of instability cells can be itself a subject for investigation and can be interesting for particle deposition.

(please refer also figure 3 of section A). In summary, we can conclude that the appearance of secondary Marangoni instability for liquid HFE7100 sessile drop evaporation under microgravity conditions on heated substrate at critical height is $H_{crit} = 0.35$ mm, which is lower to sessile drop ($6DP\mu gEF$) under microgravity condition with electric field ($H_{crit} = 0.41$ mm), and higher to the sessile drop (1DP1g) under gravity condition ($H_{crit} = 0.2$ mm). So, considering critical height $H_{crit} = 0.35$ mm and given time $t = 30$ s for each cycle we propose maximum initial volume of sessile drops in the range of $3.5 - 4\,\mu$L, and flushing could be started when $Vol. = 1\,\mu$L remains. The total volume of $3\,\mu$L of HFE7100 liquid sessile drop with $R = 2$ mm, $T_{sub} = 301.15$ K and $P = 105400$ Pa could evaporate in 33 s with evaporation rate of $0.09\,\mu\text{L} \cdot \text{s}^{-1}$.

4.5.2   *Comparison of secondary instability for Ethanol sessile drop (from parabolic flight)*

Next, as we discussed in experiment section 2.4), we are going to compare number of instability cells for Ethanol sessile drop. In figure 4.27, we compared the infrared top view numerical with experiment sessile drop VP140PF12 (for experiment, drop top IR view marked $t = 3.96$ s) of liquid ethanol on the heated substrate under microgravity conditions performed during the parabolic flight campaign VP140, in 2018 (for more details please refer section 2.4). The parameter for sessile drops at comparison are: $R = 3.6$ mm, $T_{sub} = 313.45$ K, $P = 83500$ Pa and $H_t = 0.7$ mm. The space & time discretizations is remains same as discussed earlier (for more detail refer to sections 3.10.1, 3.10.2 & 3.11).

In figure 4.27 c, we also presented top view of sessile drop with surface temperature. As explained in section 2.4) of chapter 2.5 that it is difficult to follow volume with time so the evaporation rate in

(a) Numerical sim. (IR)   (b) Experimental (IR)

(c) Surface: Temperature (K)

(Simulation)
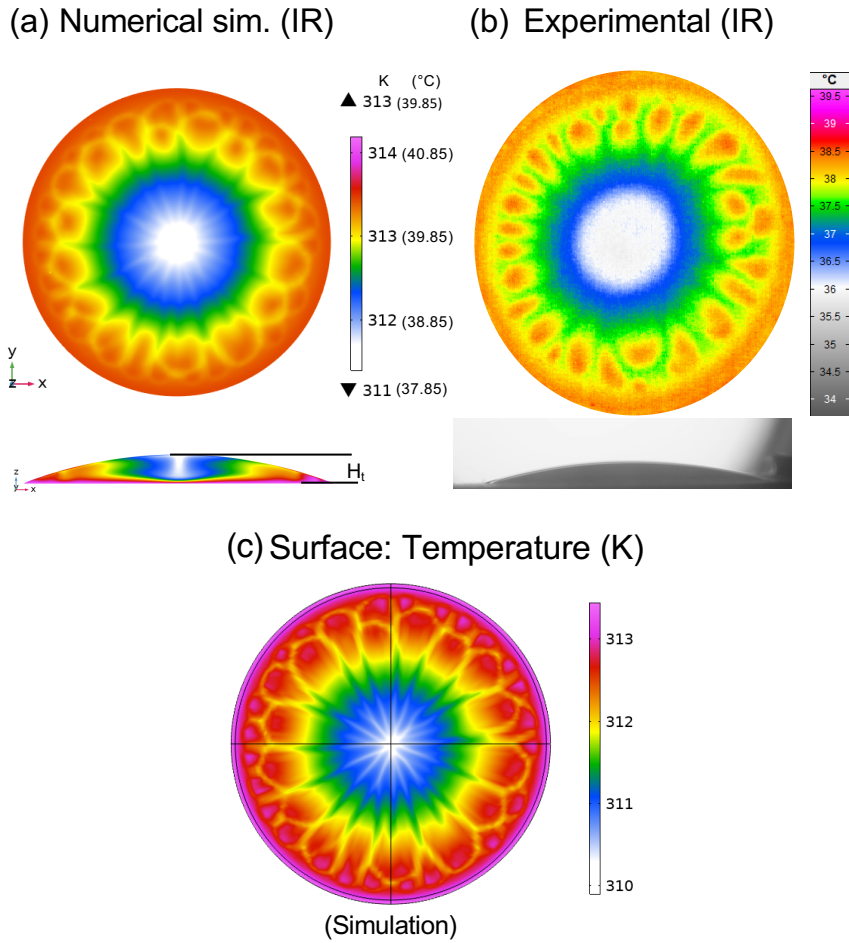
Figure 4.27: **Top view numerical and experiment comparison of the parabolic flight ethanol sessile drop** VP140PF12. **(a)** Infrared top view (numerical); **(b)** Infrared top view (experiment); **(c)** Top view surface temperature (numerical). Parameter for sessile drop at comparison are: $R = 3.6$ mm, $T_{sub} = 313.45$ K, $P = 83500$ Pa and $H_t = 0.7$ mm. For more on experiment please refer to section 2.3.

parabolic flight. The drop VP140PF12 was only in constant contact area mode between time duration $t = 3.96$ s to 5.4 s i.e merely 1.8 s, after $t = 5.4$ s sessile drop starts spreading and sliding towards the south west corner of the substrate (please refer to movie of fig. 2.4). However, we can compare sessile drop numerical simulation with experiment at the given time for the number of the instability cells (N_{inst}), sub cooling $\Delta T = T_{apex} - T_{sub}$ and sessile drop eye radius R_{sc} (for more details refer to section 2.4). From the comparison in figures 4.27 a , b & c we could mention that the number of instability cells for numerical simulation is $N_{inst} = 25 \pm 2$ as compared to experimental one which is 27 ± 1. Similarly, for sub cooling is approximately $\Delta T = 2 \pm 0.15$ K for the both, where sessile drop eye radius is equal to $R_{sc} = 1.41$ mm and 1.2 mm for numerical and experiment drop, respectively. For

	$T_{sub} = 313\,\text{K}$	$T_{sub} = 328\,\text{K}$	$T_{sub} = 343\,\text{K}$
Evaporation rate ($E_{vw,exp}$), μLs^{-1} terrestrial gravity (Sáenz et al. [58])	0.0144	0.0340	0.0698
θ_{cirt}, (deg.) from exp. [58]	24 ± 2 (at $t = 580\,\text{s}$)	22 ± 3 (at $t = 248\,\text{s}$)	26 ± 3 (at $t = 125\,\text{s}$)
Evaporation rate ($E_{vw,num}$), μLs^{-1} microgravity (numerical)	0.0131	0.0282	0.0572
θ_{cirt}, (deg.)	$24°$ ($t = 635\,\text{s}$)	$22°$ ($t = 301\,\text{s}$)	$26°$ ($t = 142\,\text{s}$)
$(E_{vw,exp} - (E_{vw,num}))/\ E_{vw,exp}$ (%)	8.85	17.23	18.14

Table 4.3: Water sessile drops evaporation rate under microgravity (numerical) and terrestrial gravity (experiment) on heated substrate.

the given Ethanol sessile drop radius, contact angle, pressure and substrate temperature, numerical results show good comparison with the experiment.

4.5.3   *Evaporation of Water sessile drop under microgravity and terrestrial gravity conditions.*

The thermo-physical properties considered for Water are presented in table B.1. The evaporation of Water drops on a heated substrate is presented for $T_{sub} = 313.15\,, 328.15$, and $343.15\,\text{K}$. The initial volume, drop base radius and contact angle were $V_0 = 10.46\mu L$, $R = 1.86$ mm and $\theta_0 = 80°$, respectively. This led to drops whose initial height $H_0 = 1.56$ mm. Whereas ambient gas is nitrogen at pressure $105400\,\text{Pa}$. For simulation, sessile drop's initial geometrical parameter, substrate and ambient conditions corresponding to experiment performed under gravity by Sáenz et al. [58]. For the given T_{sub} and R, the sessile drop depinned at $\theta = 22 \pm 3°$ and $26 \pm 3°$ for $T_{sub} = 328.15$, and $343.15\,\text{K}$, respectively. However, for $T_{sub} = 313.15$ combined mode of evaporation start around $\theta = 24 \pm 2°$ before the first contact-line jump at $\theta = 10 \pm 2°$ [58]. However, in microgavity we may expected depinning earlier than gravity conditions [76]. So, for comparison, we consider the evaporation rate up to contact angle $\theta = 25°$ for all the case of Water. Nonetheless, we set the stopped conditions for the simulation at $\theta = 10°$ mainly just to observer if any secondary instability appearance in Water.

Movie for Fig. 4.28

In figure D.8 depicted the evolution of the evaporation rate and avg. interface temperature with contact angle under microgravity conditions over range of substrate temperature. In figure 4.28, presented the comparison of the instantaneous evolution of volume and contact angle (θ_t) from numerical simulation (microgravity) and experiment (terrestrial gravity) and results are summarize in table 4.3. Figure 4.28

(a)

(b)
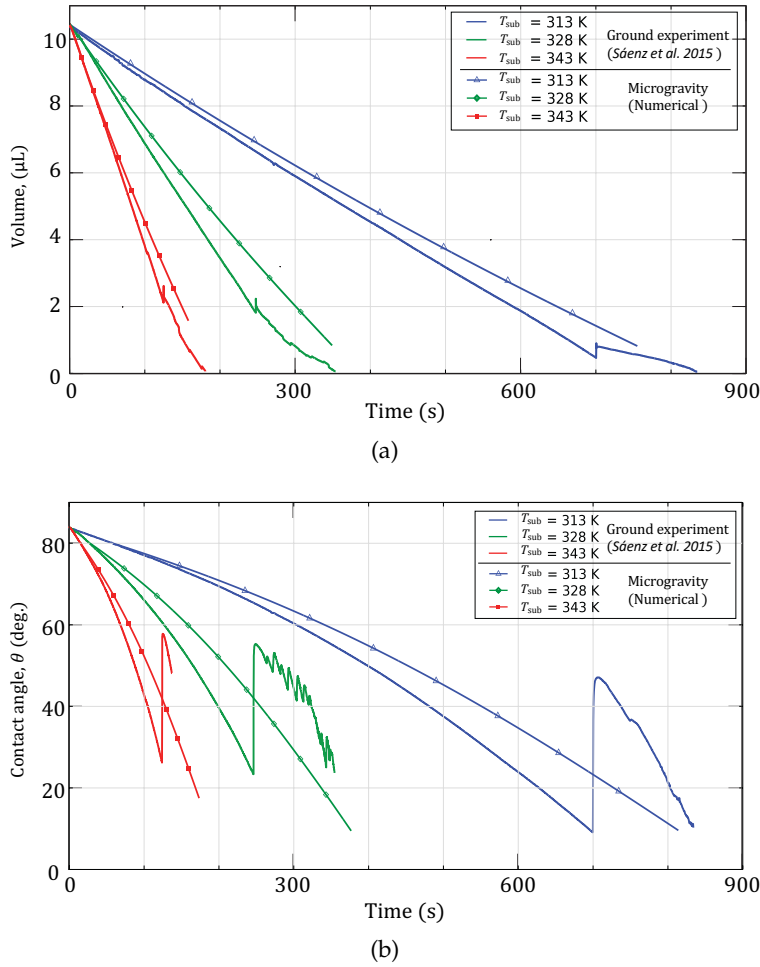
Figure 4.28: **Comparison of instantaneous evolution the Water sessile drops evaporation into N_2 under microgravity (numerical) and terrestrial gravity (experiment) at substrate temperatures $T_{sub} = 313.15$, 328.15, and 343.15 K. (a)** Volume evolution with time; **(b)** Contact angle with respect to time. Experiment performed under gravity by Sáenz et al. [58]. Supplementary movie for the numerical simulation of sessile drop at substrate temperature $T_{sub} = 328.15$ K is included. ▶ play or scan QR.

shows that both in microgravity and terrestrial gravity instantaneous volume evolution is considerably linear for any substrate temperature concurrently contact angle (θ_t) decreases at a progressively increasing rate. The comparison of the average of the evaporation rate in table 4.3 up to θ_{cirt} shows that at substrate temperature $T = 313$ K, evaporation rate under microgravity is 8.85% lower than the under terrestrial gravity condition but difference increase further up to 18.14% at $T = 343$ K. As expected evaporation under microgravity is lower than terrestrial gravity [76, 97] and the deviation continue to increase with the substrate temperature as observed in the case of Ethanol [97].
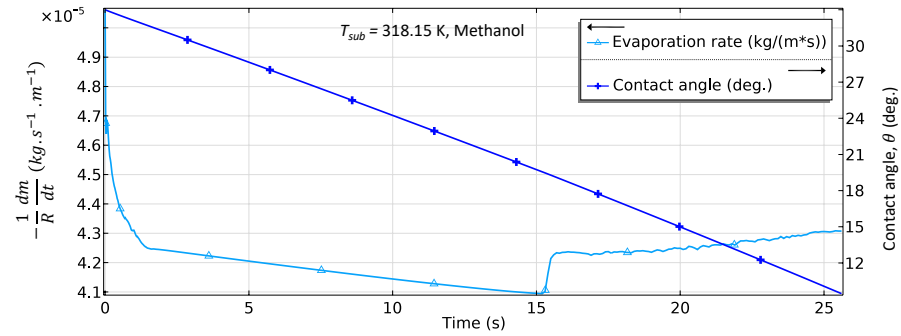
Figure 4.29: **Evaporation rate and contact angle of Methanol sessile drop with respect to time on heated substrate under microgravity.**

4.5.4 *Comparison of Ethanol and Methanol sessile drop evaporation under same conditions.*

Simulation for Methanol sessile drop's with initial geometrical parameter, substrate and ambient conditions corresponding to the similar conditions of Ethanol drop (S.No 7 of table 4.2) which are as follows: the drop base radius $R = 2$ mm and initial contact angle $\theta_0 = 33°$, whereas ambient gas is nitrogen at pressure $p = 0.835$ bar and substrate temperature $T_{\text{sub}} = 318.15$ K (see table 4.2 and for Ethanol case refer to 4.4.3). The thermo-physical properties considered for Methanol are presented in table B.1.
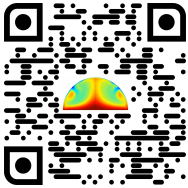
Movie for Fig.4.30 & 4.29

In figure 4.29, presented the evaporation rate and contact angle of Methanol drop with respect to time. The avg. global evaporation rate and avg. interface temperature are $E_v = 4 \pm 0.1 \times 10^{-5}$ kg $\cdot$ (s $\cdot$ m)$^{-1}$ (0.11 µL $\cdot$ s) and $T_{avg,\Gamma} = 315 \pm 0.5$ K for up to $\theta = 9.4°$ (refer to table 4.2). Figure 4.30, presented the comparison of Ethanol and Methanol sessile drop with respect to contact angle shows that Methanol sessile drop evaporation rate E_v nearly 70% higher at any given contact angle even though the average interface temperature $T_{avg,\Gamma}$ is lower by 1.5 K than Ethanol due the difference in thermo physical properties.

Interestingly, for both sessile drops secondary instability cells appears nearly at the same contact angle $\theta_{crit} = 19°$ even though critical Thermal Marangoni number are different however critical aspect ratios are same (see table 4.2). Similar trend was seen under different pressure for Ethanol sessile drops (refer to section 4.4.2.3), where we have variation of values E_v, $T_{avg,\Gamma}$, and $\text{Ma}_{\text{T,crit}}$ but secondary instability cells appears approximately at the same critical contact angle. It is expected as the thermal diffusion coefficient of surface tension for Ethanol and methanol are the nearly same. So it can be confirmed that the occurrence of the secondary instability is mainly influenced by the substrate temperature T_{sub}, surface tension γ and geometrical aspect ratio AR of the sessile drop.
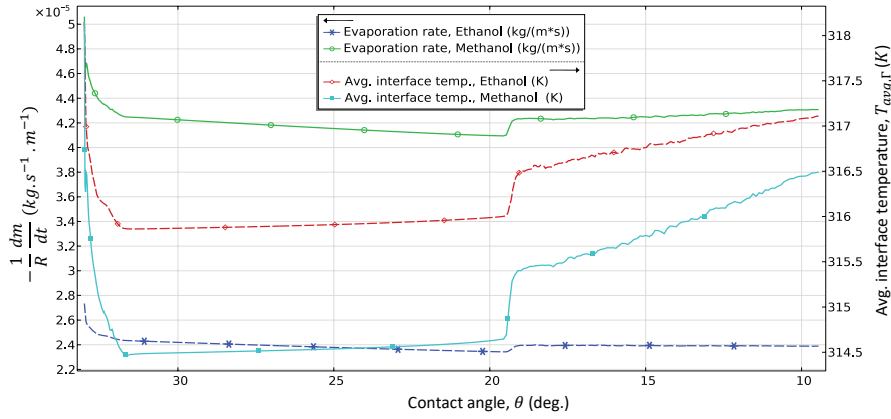
Figure 4.30: **Comparison of the Ethanol and Methanol sessile drop evaporation rate and average interface temperature under same conditions with respect to the contact angle.** For the comparison of surface temperature and velocity with time refer to movie (▶ play or Scan QR).

4.6 SYNOPSIS

In the aim to quantify the evaporation rate and internal flow structure of pinned sessile drop of a pure fluid on heated, an isothermal substrate under microgravity conditions a model is proposed. It has been validated with liquid HFE7100 sessile drop from a sounding rocket experiment. The quantitative comparison of evaporation rate with Ethanol sessile drop over the range of substrate temperature is performed and it confirmed that evaporation rate increases following a power law with substrate temperature. The numerical simulations further extended to the higher contact angles θ_t, which show the average interface temperature $T_{avg,\gamma}$ is independent of θ_t, within the primary instability phase. So, a correlation between T_{sub} and $T_{avg,\Gamma}$ is provided to calculate the evaporation rate. Afterwards, to show the influence of Marangoni convection on evaporation, simulations with FHDM and HDM are compared between contact angle from $\theta_0 = 90°$ to $10°$. In the same study, we analysed the secondary instability role on evaporation rate and interface temperature. Despite primary instability has a strong effect on sessile drop evaporation rate, secondary instability does not influence the evaporation rate heavily, even though the evaporation rate and average interface temperature displaying some trend change with its occurrence. The secondary instability only increases the evaporation rate of Ethanol sessile drop by approximately $2 - 3\%$. Then, a parametric study is undertaken with Ethanol sessile drop to broaden our analysis. Thermal Marangoni number linearly decreases for all the drops with the drop aspect ratio during the primary instability phase. Then, it fluctuates with the occurrence of secondary instability and critical thermal Marangoni number follows a power relation with critical aspect ratio.

Internal flow structure is especially explored for Ethanol sessile drop. Its seen that the local distribution pattern of evaporation rate is following the thermal field over the interface whereas the heat flux from the substrate follows the velocity field at the interface. Sessile drop evaporation started with axisymmetric torus roll (primary instability) and with time as a critical aspect ratio approach. The occurrence of secondary instability cells begins with the break of the axisymmetric torus roll. Instability cells are moving in the opposite direction of the main flow, starting from substrate to sessile drop interface while moving towards contact lines, having approximately 1 K higher temperature than surrounding liquid. The occurrence of secondary instability also induces the azimuthal velocity in the flow.

With the above, some other simulations are also performed as follows: i) Computations for actual sessile drop ($7DP\mu$g drop) from the ARLES experiments until complete evaporation time to assist in the future ARLES experiment by computing the critical volume and critical aspect ratio for the transition from primary to secondary instability; ii) The experiment and numerical comparison of secondary instability structure for Ethanol sessile drop at a given time are presented. However, it requires further investigation; iii) Comparison of the evaporation rate of Water sessile drop under microgravity (numerical) and terrestrial gravity (experiment) conditions. The comparison is as expected, evaporation under microgravity is lower than terrestrial gravity and the deviation continues to increase with the substrate temperature similar to previously observed in the case of Ethanol.

Finally, the comparison of Ethanol and Methanol sessile drop evaporation under microgravity also confirmed that the occurrence of the secondary instability is mainly influenced by the substrate temperature T_{sub}, surface tension γ and geometrical aspect ratio AR of the sessile drop.

The simulation cost is higher after the appearance of secondary instability which is further increased for high substrate temperature and volatile fluids. In the case of a study where secondary instability is not of interest, simulations can be performed only for the primary instability phase (higher contact angle) by keeping the stop condition at θ_{crit}.

CONCLUSIONS AND PERSPECTIVES

The use of parabolic flights has confirmed the observations of the previous experiments on the effect of natural convection on sessile drop evaporation. However, parabolic flights are still insufficient in terms of duration to conduct quantifiable measurements for the whole lifetime of sessile drop. Similar results from the ground and sounding rocket experiments also support the observations that convection in vapor phase plays an important role in the evaporation of sessile drops under gravity. The evaporation rate in microgravity conditions is nearly half of that under the Earth conditions for HFE7100. The experimental results also demonstrate the secondary instability appearance at a critical height of the sessile drop interface and it is slightly higher under microgravity than in gravity. The secondary instability strongly changes the fluid flow structure but does not significantly influence the evaporation rate in both Earth or microgravity conditions. Also, through the application of different combinations of body forces (electric field and gravity), experiments demonstrate the role of gravity on the shape of the sessile drop interface and its influence on the de-pinning of sessile drops.

In microgravity conditions, the driving instability takes place in the liquid phase, therefore we have developed a one-sided model to account for the gas phase in the simple manner, thanks to ad-hoc boundary conditions. Despite the fully coupled fluid flow-heat transfer problem inside the domain and at the interface we successfully managed to accommodate the effect of vapor in microgravity. The model has been implemented in the COMSOL Multiphysics software and computational optimizations were performed in order to capture the whole lifetime dynamics of sessile drop evaporation.

Quantitative validation of our model is performed by comparing it with the experimental results. Both, the numerical and the parabolic flight results over the range of substrate temperature for Ethanol sessile drop show that evaporation rate increases following a power law with substrate temperature. So, a correlation is proposed for evaporation rate which is valid for Ethanol pinned sessile drop of spherical shape under microgravity conditions (or saturation vapour density) on a heated substrate for any given pressure, with a neglecting effect of secondary instabilityfor the lower contact angle.

Now, the three relevant questions related to the dynamics of sessile drop evaporation that have been addressed are as following: i) Global

and local evolution of evaporation rate and temperature. ii) Instability structure and its occurrence. iii) Secondary instability and its influence on evaporation.

The evaporation rate starts to first decrease with the contact angle, then it suddenly increases approximately by $2-3\%$ with the occurrence of the secondary Marangoni instability at the critical height, however, then it becomes constant for Ethanol drop but for HFE7100 it starts decreasing again. The important contribution of Marangoni convection is transport of energy from substrate to interface thus elevating interface temperature and evaporation rate. This elevated interface temperature remains nearly constant and is approximately independent of the contact angle until the secondary instability occurs. Thus, the evaporation rate reduces with contact angle due to the reduction of the evaporating surface area. It is also noticed that evaporating cooling effect is approximately the same irrespective of the drop radius for the given substrate temperature. The local distribution pattern of evaporation rate is following the temperature pattern whereas the heat flux from the substrate is following the velocity field over the interface. The normalisation of observable quantities collapses into a single linear monotonically decreasing line with time for all the configurations of sessile drops. It can also be added that in reporting the evaporation rate one should express it in versus with initial and final contact angles instead of time.

Evaporation starts with a Marangoni convection (primary instability) that results in an axisymmetric torus roll, with the lowest temperature and accordingly the lowest evaporation rate around the apex, which increases along the radial position towards the contact line. The velocity magnitude is the highest along with the free surface surrounding the apex and then flow dives toward the substrate close to the symmetry axis. This torus roll appears as soon as it exists temperature gradient over the liquid drop surface.

Then, a transition to a secondary instability occurs once a critical thermal Marangoni is overcome and a fully $3D$ unsteady fluid flow is developed. The axisymmetric torus roll of the primary instability breaks into cells, core cells get too bigger, and split in turn. Then dynamic multicellular thermo-convective flower-like patterns emerge. Viscosity dissipation imposes cells to have an aspect ratio roughly close to unity. If cell flow doesn't satisfy this condition the flow structure splits into pieces. The secondary instability cells have an intrinsic wavelength that roughly depends on the local liquid thickness along the radial direction of the sessile drop. The secondary instability cells wavelength decreases along with the aspect ratio. The wave number strongly depends on the aspect ratio, substrate temperature and volatility of the fluid. Thermal Marangoni number linearly decreases

with the drop aspect ratio during the primary instability phase and starts fluctuating with the occurrence of secondary instability. The critical thermal Marangoni number follows a power law with respect to the critical aspect ratio. The radially outward moving instability cells create an illusion of the main flow moving from apex to contact line, however, velocity vectors confirm that instability cells are moving in the opposite direction of the main thermo-convective flow. Despite primary instability has a strong effect on sessile drop evaporation rate, secondary instability does not influence the evaporation rate heavily, even though the evaporation rate and average interface temperature trend change with its occurrence. Similar results related to the secondary instability are observed for HFE7100 experiments, both on the ground as well as in microgravity experiments.

The foremost requirement for future work is to have sufficient experimental accurate data for the sessile drop whole life evaporation under microgravity, for various parameters. Extensive validation of the developed numerical model should be undertaken, along with the validation of the bifurcation diagram for instability transition. Even though secondary instability doesn't play a crucial role in evaporation, however, secondary instability structure could be interesting. Indeed, it can be explored under gravity and microgravity with a high-resolution IR camera like we used it in parabolic flight and compared it for one case with numerical simulation. However, an extensive experimental and numerical investigation is required for a better understanding of its structure that could facilitate studies of particle deposition on the substrate.

If one wants to use the present model in a gravity field, then the model should be further extended towards a two-way coupling to account for the nonlinear coupling between the vapour phase and the liquid one. Indeed in the gravity field, one has to account for the convection in the gas phase induce by thermal-solutal gradients. The validation of saturated vapor pressure boundary condition under microgravity is an opportunity for reconsideration of vapor pressure influence on interface under gravity conditions.

The experiments for microgravity conditions remain a challenging task due to limited access to microgravity platforms and parabolic flights are not the best suitable means for sessile drop experiments. Although sounding rockets provide better stability, control over the injected volumes is still required.

BIBLIOGRAPHY

[1] J. G. Leidenfrost. *De aquae communis nonnullis qualitatibus tractatus*. Ovenius, 1756.

[2] T. Young. "III. An essay on the cohesion of fluids." In: *Philosophical Transactions of the Royal Society of London* 95 (Dec. 1805), pp. 65–87. DOI: 10.1098/rstl.1805.0005.

[3] N. A. Fuchs. *Evaporation and Droplet Growth in Gaseous Media*. Elsevier, 1959. DOI: 10.1016/c2013-0-08145-5.

[4] R. D. Deegan, O. Bakajin, T. F. Dupont, G. Huber, S. R. Nagel, and T. A. Witten. "Capillary flow as the cause of ring stains from dried liquid drops." In: *Nature* 389.6653 (Sept. 1997), pp. 827–829. DOI: 10.1038/39827.

[5] S. H. Ko, J. Chung, N. Hotz, K. H. Nam, and C. P. Grigoropoulos. "Metal nanoparticle direct inkjet printing for low-temperature 3D micro metal structure fabrication." In: *Journal of Micromechanics and Microengineering* 20.12 (2010), p. 125010.

[6] N. C. Schirmer, S. Ströhle, M. K. Tiwari, and D. Poulikakos. "On the Principles of Printing Sub-micrometer 3D Structures from Dielectric-Liquid-Based Colloids." In: *Advanced Functional Materials* 21.2 (Nov. 2010), pp. 388–395. DOI: 10.1002/adfm.201001426.

[7] M. Salyani. "Droplet Size Effect on Spray Deposition Efficiency of Citrus Leaves." In: *Transactions of the ASAE* 31.6 (1988), pp. 1680–1684. DOI: 10.13031/2013.30919.

[8] B. Sobac and D. Brutin. "Desiccation of a sessile drop of blood: Cracks, folds formation and delamination." In: *Colloids and Surfaces A: Physicochemical and Engineering Aspects* 448 (Apr. 2014), pp. 34–44. DOI: 10.1016/j.colsurfa.2014.01.076.

[9] F. Smith and D. Brutin. "Wetting and spreading of human blood: Recent advances and applications." In: *Current Opinion in Colloid & Interface Science* 36 (July 2018), pp. 78–83. DOI: 10.1016/j.cocis.2018.01.013.

[10] R. S. Bradley, M. G. Evans, and R. Whytlaw-Gray. "The rate of evaporation of droplets. Evaporation and diffusion coefficients, and vapour pressures of dibutyl phthalate and butyl stearate." In: *Proceedings of the Royal Society of London. Series A. Mathematical and Physical Sciences* 186.1006 (Sept. 1946), pp. 368–390. DOI: 10.1098/rspa.1946.0050.

[11] J. Wimp. "Special Functions and Their Applications (N. N. Lebedev)." In: *SIAM Review* 7.4 (Sept. 1965), pp. 577–580. DOI: 10.1137/1007133.

[12] R. Picknett and R Bexon. "The evaporation of sessile or pendant drops in still air." In: *Journal of Colloid and Interface Science* 61.2 (Sept. 1977), pp. 336–350. DOI: 10.1016/0021-9797(77)90396-4.

[13] C. Bourges-Monnier and M. E. R. Shanahan. "Influence of Evaporation on Contact Angle." In: *Langmuir* 11.7 (July 1995), pp. 2820–2829. DOI: 10.1021/la00007a076.

[14] S. M. Rowan, M. I. Newton, and G. McHale. "Evaporation of Microdroplets and the Wetting of Solid Surfaces." In: *The Journal of Physical Chemistry* 99.35 (Aug. 1995), pp. 13268–13271. DOI: 10.1021/j100035a034.

[15] K. Birdi and D. Vu. "Wettability and the evaporation rates of fluids from solid surfaces." In: *Journal of Adhesion Science and Technology* 7.6 (Jan. 1993), pp. 485–493. DOI: 10.1163/156856193x00808.

[16] H. Y. Erbil and R. A. Meric. "Evaporation of Sessile Drops on Polymer Surfaces: Ellipsoidal Cap Geometry." In: *The Journal of Physical Chemistry B* 101.35 (Aug. 1997), pp. 6867–6873. DOI: 10.1021/jp970328n.

[17] H. Hu and R. G. Larson. "Evaporation of a Sessile Droplet on a Substrate." In: *The Journal of Physical Chemistry B* 106.6 (Feb. 2002), pp. 1334–1344. DOI: 10.1021/jp0118322.

[18] G. Dunn, S. Wilson, B. Duffy, S. David, and K. Sefiane. "A mathematical model for the evaporation of a thin sessile liquid droplet: Comparison between experiment and theory." In: *Colloids and Surfaces A: Physicochemical and Engineering Aspects* 323.1-3 (June 2008), pp. 50–55. DOI: 10.1016/j.colsurfa.2007.09.031.

[19] É. Guyon, J.-P. Hulin, and L. Petit. *Hydrodynamique physique*. EDP Sciences, Nov. 2020. DOI: 10.1051/978-2-7598-0893-9.

[20] F. Carle and D. Brutin. "Convection." In: *Droplet Wetting and Evaporation*. Elsevier, 2015, pp. 115–128. DOI: 10.1016/b978-0-12-800722-8.00009-6.

[21] D. Zang, S. Tarafdar, Y. Y. Tarasevich, M. D. Choudhury, and T. Dutta. "Evaporation of a Droplet: From physics to applications." In: *Physics Reports* 804 (Apr. 2019), pp. 1–56. DOI: 10.1016/j.physrep.2019.01.008.

[22] *Droplet Wetting and Evaporation*. Elsevier, 2015. DOI: 10.1016/c2013-0-18955-6.

[23] D. Brutin and V. Starov. "Recent advances in droplet wetting and evaporation." In: *Chemical Society Reviews* 47.2 (2018), pp. 558–585. DOI: 10.1039/c6cs00902f.

[24] F. Carle. "Flow Motion in Sessile Droplets: Evaporation and Nanoparticles Assembly (Ph. D. thesis)." In: *Aix-Marseille University* (2014).

[25] S. David, K. Sefiane, and L. Tadrist. "Experimental investigation of the effect of thermal properties of the substrate in the wetting and evaporation of sessile drops." In: *Colloids and Surfaces A: Physicochemical and Engineering Aspects* 298.1-2 (Apr. 2007), pp. 108–114. DOI: 10.1016/j.colsurfa.2006.12.018.

[26] P. Kelly-Zion, C. Pursell, N. Hasbamrer, B. Cardozo, K. Gaughan, and K. Nickels. "Vapor distribution above an evaporating sessile drop." In: *International Journal of Heat and Mass Transfer* 65 (Sept. 2013), pp. 165–172. DOI: 10.1016/j.ijheatmasstransfer.2013.06.003.

[27] Z. Pan, S. Dash, J. A. Weibel, and S. V. Garimella. "Assessment of Water Droplet Evaporation Mechanisms on Hydrophobic and Superhydrophobic Substrates." In: *Langmuir* 29.51 (Dec. 2013), pp. 15831–15841. DOI: 10.1021/la4045286.

[28] M. A. Saada, S. Chikh, and L. Tadrist. "Evaporation of a sessile drop with pinned or receding contact line on a substrate with different thermophysical properties." In: *International Journal of Heat and Mass Transfer* 58.1-2 (Mar. 2013), pp. 197–208. DOI: 10.1016/j.ijheatmasstransfer.2012.11.026.

[29] B. Abramzon and W. Sirignano. "Droplet vaporization model for spray combustion calculations." In: *International Journal of Heat and Mass Transfer* 32.9 (Sept. 1989), pp. 1605–1618. DOI: 10.1016/0017-9310(89)90043-4.

[30] C. Bertoli and M. Migliaccio. "A finite conductivity model for diesel spray evaporation computations." In: *International Journal of Heat and Fluid Flow* 20.5 (Sept. 1999), pp. 552–561. DOI: 10.1016/s0142-727x(99)00044-2.

[31] S. S. Sazhin. "Advanced models of fuel droplet heating and evaporation." In: *Progress in Energy and Combustion Science* 32.2 (Jan. 2006), pp. 162–214. DOI: 10.1016/j.pecs.2005.11.001.

[32] L. Bin, R. Bennacer, and A. Bouvet. "Evaporation of methanol droplet on the Teflon surface under different air velocities." In: *Applied Thermal Engineering* 31.17-18 (Dec. 2011), pp. 3792–3798. DOI: 10.1016/j.applthermaleng.2011.07.018.

[33] A.-L. Ljung and T. S. Lundström. "Evaporation of a sessile water droplet subjected to forced convection in humid environment." In: *Drying Technology* 37.1 (Mar. 2018), pp. 129–138. DOI: 10.1080/07373937.2018.1441866.

[34] H. Navaz, E. Chan, and B. Markicevic. "Convective evaporation model of sessile droplets in a turbulent flow—comparison with wind tunnel data." In: *International Journal of Thermal Sciences* 47.8 (Aug. 2008), pp. 963–971. DOI: 10.1016/j.ijthermalsci.2007.08.004.

[35] V. Vancauwenberghe, P. D. Marco, and D. Brutin. "Wetting and evaporation of a sessile drop under an external electrical field: A review." In: *Colloids and Surfaces A: Physicochemical and Engineering Aspects* 432 (Sept. 2013), pp. 50–56. DOI: 10.1016/j.colsurfa.2013.04.067.

[36] R. G. Larson. "Transport and deposition patterns in drying sessile droplets." In: *AIChE Journal* 60.5 (Feb. 2014), pp. 1538–1571. DOI: 10.1002/aic.14338.

[37] M. Kumar and R. Bhardwaj. "A combined computational and experimental investigation on evaporation of a sessile water droplet on a heated hydrophilic substrate." In: *International Journal of Heat and Mass Transfer* 122 (July 2018), pp. 1223–1238. DOI: 10.1016/j.ijheatmasstransfer.2018.02.065.

[38] P. Gurrala, P. Katre, S. Balusamy, S. Banerjee, and K. C. Sahu. "Evaporation of ethanol-water sessile droplet of different compositions at an elevated substrate temperature." In: *International Journal of Heat and Mass Transfer* 145 (Dec. 2019), p. 118770. DOI: 10.1016/j.ijheatmasstransfer.2019.118770.

[39] T. Josyula, P. S. Mahapatra, and A. Pattamatta. "Insights into the evolution of the thermal field in evaporating sessile pure water drops." In: *Colloids and Surfaces A: Physicochemical and Engineering Aspects* 611 (Feb. 2021), p. 125855. DOI: 10.1016/j.colsurfa.2020.125855.

[40]   N. Shahidzadeh-bonn, S. Rafaï, A. Azouni, and D. Bonn. "Evaporating droplets." In: *Journal of Fluid Mechanics* 549.-1 (Feb. 2006), p. 307. DOI: 10.1017/s0022112005008190.

[41]   P. Kelly-Zion, C. Pursell, S. Vaidya, and J. Batra. "Evaporation of sessile drops under combined diffusion and natural convection." In: *Colloids and Surfaces A: Physicochemical and Engineering Aspects* 381.1-3 (May 2011), pp. 31–36. DOI: 10.1016/j.colsurfa.2011.03.020.

[42]   T. A. H. Nguyen, S. R. Biggs, and A. V. Nguyen. "Analytical Model for Diffusive Evaporation of Sessile Droplets Coupled with Interfacial Cooling Effect." In: *Langmuir* 34.23 (May 2018), pp. 6955–6962. DOI: 10.1021/acs.langmuir.7b03862.

[43]   X. Xu and L. Ma. "Analysis of the effects of evaporative cooling on the evaporation of liquid droplets using a combined field approach." In: *Scientific Reports* 5.1 (Feb. 2015). DOI: 10.1038/srep08614.

[44]   K. Gleason and S. A. Putnam. "Microdroplet Evaporation with a Forced Pinned Contact Line." In: *Langmuir* 30.34 (Aug. 2014), pp. 10548–10555. DOI: 10.1021/la501770g.

[45]   S. Semenov, V. M. Starov, R. G. Rubio, and M. G. Velarde. "Computer Simulations of Evaporation of Pinned Sessile Droplets: Influence of Kinetic Effects." In: *Langmuir* 28.43 (Sept. 2012), pp. 15203–15211. DOI: 10.1021/la303916u.

[46]   F. Girard, M. Antoni, S. Faure, and A. Steinchen. "Evaporation and Marangoni Driven Convection in Small Heated Water Droplets." In: *Langmuir* 22.26 (Dec. 2006), pp. 11085–11091. DOI: 10.1021/la061572l.

[47]   S. Ye, L. Zhang, C.-M. Wu, Y.-R. Li, and Q.-S. Liu. "Experimental investigation on evaporation dynamics of sessile ethanol droplets on a heated substrate." In: *International Journal of Heat and Mass Transfer* 162 (Dec. 2020), p. 120352. DOI: 10.1016/j.ijheatmasstransfer.2020.120352.

[48]   Y. Zhang, L. Zhang, D.-M. Mo, C.-M. Wu, and Y.-R. Li. "Numerical investigation on flow instability of sessile ethanol droplets evaporating in its pure vapor at low pressure." In: *International Journal of Heat and Mass Transfer* 156 (Aug. 2020), p. 119893. DOI: 10.1016/j.ijheatmasstransfer.2020.119893.

[49]   K. Sefiane, J. R. Moffat, O. K. Matar, and R. V. Craster. "Self-excited hydrothermal waves in evaporating sessile drops." In: *Applied Physics Letters* 93.7 (Aug. 2008), p. 074103. DOI: 10.1063/1.2969072.

[50]   D. Mamalis, V. Koutsos, and K. Sefiane. "Nonisothermal Spreading Dynamics of Self-Rewetting Droplets." In: *Langmuir* 34.5 (Jan. 2018), pp. 1916–1931. DOI: 10.1021/acs.langmuir.7b04045.

[51]   P. Chen, S. Harmand, S. Ouenzerfi, and J. Schiffler. "Marangoni Flow Induced Evaporation Enhancement on Binary Sessile Drops." In: *The Journal of Physical Chemistry B* 121.23 (June 2017), pp. 5824–5834. DOI: 10.1021/acs.jpcb.7b02766.

[52]   M. A. Mahmud and B. D. MacDonald. "Experimental investigation of interfacial energy transport in an evaporating sessile droplet for evaporative cooling applications." In: *Physical Review E* 95.1 (Jan. 2017). DOI: 10.1103/physreve.95.012609.

[53] H. Ghasemi and C. A. Ward. "Energy Transport by Thermocapillary Convection during Sessile-Water-Droplet Evaporation." In: *Physical Review Letters* 105.13 (Sept. 2010). DOI: 10.1103/physrevlett.105.136102.

[54] M. A. Kadhim, N. Kapur, J. L. Summers, and H. Thompson. "Experimental and Theoretical Investigation of Droplet Evaporation on Heated Hydrophilic and Hydrophobic Surfaces." In: *Langmuir* 35.19 (Apr. 2019), pp. 6256–6266. DOI: 10.1021/acs.langmuir.8b03601.

[55] O. A. Kabov, E. Y. Gatapova, A. A. Semenov, M. S. Jutley, V. V. Ajaev, E. O. Kirichenko, D. V. Feoktistov, G. V. Kuznetsov, and D. V. Zaitsev. "Experimental and numerical studies of evaporation of a sessile water drop on a heated conductive substrate." In: *Interfacial Phenomena and Heat Transfer* 6.4 (2018), pp. 421–435. DOI: 10.1615/interfacphenomheattransfer.2019030862.

[56] K. Sefiane, L. Tadrist, and M. Douglas. "Experimental study of evaporating water–ethanol mixture sessile drop: influence of concentration." In: *International Journal of Heat and Mass Transfer* 46.23 (Nov. 2003), pp. 4527–4534. DOI: 10.1016/s0017-9310(03)00267-9.

[57] P. J. Sáenz, A. W. Wray, Z. Che, O. K. Matar, P. Valluri, J. Kim, and K. Sefiane. "Dynamics and universal scaling law in geometrically-controlled sessile drop evaporation." In: *Nature Communications* 8.1 (Mar. 2017). DOI: 10.1038/ncomms14783.

[58] P. J. Sáenz, K. Sefiane, J. Kim, O. K. Matar, and P. Valluri. "Evaporation of sessile drops: a three-dimensional approach." In: *Journal of Fluid Mechanics* 772 (May 2015), pp. 705–739. DOI: 10.1017/jfm.2015.224.

[59] P. Innocenzi, L. Malfatti, S. Costacurta, T. Kidchob, M. Piccinini, and A. Marcelli. "Evaporation of Ethanol and Ethanol-Water Mixtures Studied by Time-Resolved Infrared Spectroscopy." In: *The Journal of Physical Chemistry A* 112.29 (June 2008), pp. 6512–6516. DOI: 10.1021/jp7111395.

[60] D. Brutin, B. Sobac, F. Rigollet, and C. L. Niliot. "Infrared visualization of thermal motion inside a sessile drop deposited onto a heated surface." In: *Experimental Thermal and Fluid Science* 35.3 (Apr. 2011), pp. 521–530. DOI: 10.1016/j.expthermflusci.2010.12.004.

[61] T.-S. Wang and W.-Y. Shi. "Transition of Marangoni convection instability patterns during evaporation of sessile droplet at constant contact line mode." In: *International Journal of Heat and Mass Transfer* 148 (Feb. 2020), p. 119138. DOI: 10.1016/j.ijheatmasstransfer.2019.119138.

[62] W.-Y. Shi, K.-Y. Tang, J.-N. Ma, Y.-W. Jia, H.-M. Li, and L. Feng. "Marangoni convection instability in a sessile droplet with low volatility on heated substrate." In: *International Journal of Thermal Sciences* 117 (July 2017), pp. 274–286. DOI: 10.1016/j.ijthermalsci.2017.04.007.

[63] B. Sobac and D. Brutin. "Thermocapillary instabilities in an evaporating drop deposited onto a heated substrate." In: *Physics of Fluids* 24.3 (Mar. 2012), p. 032103. DOI: 10.1063/1.3692267.

[64] S. Semenov, F. Carle, M. Medale, and D. Brutin. "3D unsteady computations of evaporative instabilities in a sessile drop of ethanol on a heated substrate." In: *Applied Physics Letters* 111.24 (Dec. 2017), p. 241602. DOI: 10.1063/1.5006707.

[65] J.-L. Zhu, W.-Y. Shi, and L. Feng. "Bénard-Marangoni instability in sessile droplet evaporating at constant contact angle mode on heated substrate." In: *International Journal of Heat and Mass Transfer* 134 (May 2019), pp. 784–795. DOI: 10.1016/j.ijheatmasstransfer.2019.01.082.

[66] A. A. Gavrilina and L. Y. Barash. "Modeling Unsteady Bénard-Marangoni Instabilities in Drying Volatile Droplets on a Heated Substrate." In: *Journal of Experimental and Theoretical Physics* 132.2 (Feb. 2021), pp. 302–312. DOI: 10.1134/s1063776121020114.

[67] G. Karapetsas, O. K. Matar, P. Valluri, and K. Sefiane. "Convective Rolls and Hydrothermal Waves in Evaporating Sessile Drops." In: *Langmuir* 28.31 (July 2012), pp. 11433–11439. DOI: 10.1021/la3019088.

[68] S. Semenov, F. Carle, M. Medale, and D. Brutin. "Boundary conditions for a one-sided numerical model of evaporative instabilities in sessile drops of ethanol on heated substrates." In: *Physical Review E* 96.6 (Dec. 2017). DOI: 10.1103/physreve.96.063113.

[69] F. Carle, B. Sobac, and D. Brutin. "Experimental evidence of the atmospheric convective transport contribution to sessile droplet evaporation." In: *Applied Physics Letters* 102.6 (Feb. 2013), p. 061603. DOI: 10.1063/1.4792058.

[70] P. L. Kelly-Zion, C. J. Pursell, R. S. Booth, and A. N. VanTilburg. "Evaporation rates of pure hydrocarbon liquids under the influences of natural convection and diffusion." In: *International Journal of Heat and Mass Transfer* 52.13-14 (June 2009), pp. 3305–3313. DOI: 10.1016/j.ijheatmasstransfer.2009.01.015.

[71] K Sefiane, S. Wilson, S David, G. Dunn, and B. Duffy. "On the effect of the atmosphere on the evaporation of sessile droplets of water." In: *Physics of fluids* 21.6 (2009), p. 062101.

[72] S. Semenov, V. Starov, R. Rubio, H. Agogo, and M. Velarde. "Evaporation of sessile water droplets: Universal behaviour in presence of contact angle hysteresis." In: *Colloids and Surfaces A: Physicochemical and Engineering Aspects* 391.1-3 (Nov. 2011), pp. 135–144. DOI: 10.1016/j.colsurfa.2011.07.013.

[73] X. Chen, X. Wang, P. G. Chen, and Q. Liu. "Determination of Diffusion Coefficient in Droplet Evaporation Experiment Using Response Surface Method." In: *Microgravity Science and Technology* 30.5 (July 2018), pp. 675–682. DOI: 10.1007/s12217-018-9645-2.

[74] V. Baghel, B. S. Sikarwar, and K. Muralidhar. "Modeling of heat transfer through a liquid droplet." In: *Heat and Mass Transfer* 55.5 (Nov. 2018), pp. 1371–1385. DOI: 10.1007/s00231-018-2520-2.

[75] D. Hu, H. Wu, and Z. Liu. "Effect of liquid–vapor interface area on the evaporation rate of small sessile droplets." In: *International Journal of Thermal Sciences* 84 (Sept. 2014), pp. 300–308. DOI: 10.1016/j.ijthermalsci.2014.05.024.

[76]   S. Kumar, M. Medale, P. D. Marco, and D. Brutin. "Sessile volatile drop evaporation under microgravity." In: *npj Microgravity* 6.1 (Dec. 2020). DOI: 10.1038/s41526-020-00128-2.

[77]   E. N. Fuller, K. Ensley, and J. C. Giddings. "Diffusion of halogenated hydrocarbons in helium. The effect of structure on collision cross sections." In: *The Journal of Physical Chemistry* 73.11 (Nov. 1969), pp. 3679–3685. DOI: 10.1021/j100845a020.

[78]   M. Lapuerta, J. P. Hernández, and J. R. Agudelo. "An equation for the estimation of alcohol-air diffusion coefficients for modelling evaporation losses in fuel systems." In: *Applied Thermal Engineering* 73.1 (Dec. 2014), pp. 539–548. DOI: 10.1016/j.applthermaleng.2014.08.009.

[79]   J. H. Arnold. "Studies in Diffusion." In: *Industrial & Engineering Chemistry* 22.10 (Sept. 1930), pp. 1091–1095. DOI: 10.1021/ie50250a023.

[80]   E. R. Gilliland. "Diffusion Coefficients in Gaseous Systems." In: *Industrial & Engineering Chemistry* 26.6 (June 1934), pp. 681–685. DOI: 10.1021/ie50294a020.

[81]   E. N. Fuller, P. D. Schettler, and J. C. Giddings. "New method for prediction of binary gas-phase diffusion coefficients." In: *Industrial & Engineering Chemistry* 58.5 (May 1966), pp. 18–27. DOI: 10.1021/ie50677a007.

[82]   Y. O. Popov. "Evaporative deposition patterns: Spatial dimensions of the deposit." In: *Physical Review E* 71.3 (Mar. 2005). DOI: 10.1103/physreve.71.036313.

[83]   C. Diddens, H. Tan, P. Lv, M. Versluis, J. G. M. Kuerten, X. Zhang, and D. Lohse. "Evaporating pure, binary and ternary droplets: thermal effects and axial symmetry breaking." In: *Journal of Fluid Mechanics* 823 (June 2017), pp. 470–497. DOI: 10.1017/jfm.2017.312.

[84]   S. Y. Misyura. "Evaporation of a sessile water drop and a drop of aqueous salt solution." In: *Scientific Reports* 7.1 (Nov. 2017). DOI: 10.1038/s41598-017-15175-1.

[85]   F. Carle and D. Brutin. "Convection." In: (2015), pp. 115–128. DOI: 10.1016/b978-0-12-800722-8.00009-6.

[86]   F. Girard, M. Antoni, S. Faure, and A. Steinchen. "Influence of heating temperature and relative humidity in the evaporation of pinned droplets." In: *Colloids and Surfaces A: Physicochemical and Engineering Aspects* 323.1-3 (June 2008), pp. 36–49. DOI: 10.1016/j.colsurfa.2007.12.022.

[87]   K. Sefiane and R. Bennacer. "An expression for droplet evaporation incorporating thermal effects." In: *Journal of Fluid Mechanics* 667 (Jan. 2011), pp. 260–271. DOI: 10.1017/s0022112010005446.

[88]   B. Sobac and D. Brutin. "Triple-Line Behavior and Wettability Controlled by Nanocoated Substrates: Influence on Sessile Drop Evaporation." In: *Langmuir* 27.24 (Dec. 2011), pp. 14999–15007. DOI: 10.1021/la203681j.

[89]   A Beutel. "NASA laser communication system sets record with data transmissions to and from moon." In: (2013).

[90] C. P. McGuckin, N. Forraz, M.-O. Baradez, S. Navran, J. Zhao, R. Urban, R. Tilton, and L. Denner. "Production of stem cells with embryonic characteristics from human umbilical cord blood." In: *Cell Proliferation* 38.4 (Aug. 2005), pp. 245–255. DOI: 10.1111/j.1365-2184.2005.00346.x.

[91] R. Weidling, C. Güttler, and J. Blum. "Free collisions in a microgravity many-particle experiment. I. Dust aggregate sticking at low velocities." In: *Icarus* 218.1 (Mar. 2012), pp. 688–700. DOI: 10.1016/j.icarus.2011.10.002.

[92] J. Reimann, S.-A. Kuhlmann, and S. Will. "Investigations on Soot Formation in Heptane Jet Diffusion Flames by Optical Techniques." In: *Microgravity Science and Technology* 22.4 (May 2010), pp. 499–505. DOI: 10.1007/s12217-010-9204-y.

[93] S. Nakamura, T. Hibiya, K. Kakimoto, N. Imaishi, S. ichi Nishizawa, A. Hirata, K. Mukai, S. ichi Yoda, and T. S. Morita. "Temperature fluctuations of the Marangoni flow in a liquid bridge of molten silicon under microgravity on board the TR-IA-4 rocket." In: *Journal of Crystal Growth* 186.1-2 (Mar. 1998), pp. 85–94. DOI: 10.1016/s0022-0248(97)00440-5.

[94] P. G. Hofmeister, J. Blum, D. Heißelmann, M. Nakagawa, and S. Luding. "The Flow Of Granular Matter Under Reduced-Gravity Conditions." In: *AIP Conference Proceedings*. AIP, 2009. DOI: 10.1063/1.3180028.

[95] A. Diana, M. Castillo, D. Brutin, and T. Steinberg. "Sessile Drop Wettability in Normal and Reduced Gravity." In: *Microgravity Science and Technology* 24.3 (Jan. 2012), pp. 195–202. DOI: 10.1007/s12217-011-9295-0.

[96] *ESA website. http://www.esa.int/ESA.*

[97] F. Carle, B. Sobac, and D. Brutin. "Hydrothermal waves on ethanol droplets evaporating under terrestrial and reduced gravity levels." In: *Journal of Fluid Mechanics* 712 (Nov. 2012), pp. 614–623. DOI: 10.1017/jfm.2012.446.

[98] F. Carle, S. Semenov, M. Medale, and D. Brutin. "Contribution of convective transport to evaporation of sessile droplets: Empirical model." In: *International Journal of Thermal Sciences* 101 (Mar. 2016), pp. 35–47. DOI: 10.1016/j.ijthermalsci.2015.10.012.

[99] C.-T. Pham, F. Lequeux, and L. Limat. "Dynamics of a Complete Wetting Liquid Under Evaporation." In: (2013), pp. 275–283. DOI: 10.1007/978-3-642-34070-3_25.

[100] H. Almohammadi and A. Amirfazli. "Sessile drop evaporation under an electric field." In: *Colloids and Surfaces A: Physicochemical and Engineering Aspects* 555 (Sept. 2018), pp. 580–585. DOI: 10.1016/j.colsurfa.2018.07.022.

[101] C. Snow. "Potential problems and capacitance for a conductor bounded by two intersecting spheres." In: *Journal of Research of the National Bureau of Standards* 43.4 (Sept. 1949), p. 377. DOI: 10.6028/jres.043.033.

[102] "COMSOL Multiphysics® v. 5.5. www.comsol.com. COMSOL AB, Stockholm, Sweden." In: (2020).

[103] "Documentation, COMSOL Multiphysics® v. 5.5. COMSOL AB, Stockholm, Sweden." In: (2020).

[104] *Dortmund Data Bank, 2020, www.ddbst.com*.

[105] M. H. Rausch, L. Kretschmer, S. Will, A. Leipertz, and A. P. Fröba. "Density, Surface Tension, and Kinematic Viscosity of Hydrofluoroethers HFE-7000, HFE-7100, HFE-7200, HFE-7300, and HFE-7500." In: *Journal of Chemical & Engineering Data* 60.12 (Nov. 2015), pp. 3759–3765. DOI: 10.1021/acs.jced.5b00691.

[106] *http://multimedia.3m.com/mws/media/199818O/3m-novec-7100-engineered-fluid.pdf, http://multimedia.3m.com/mws/media/569860O/3mtm-thermal-management-fluids-for-military-aerospace-apps.pdf*.

[107] *CAMEO Chemical database, National Oceanic and Atmospheric Administration (NOAA) available online at http://cameochemicals.noaa.gov/*.

[108] S. Chatterjee, M. Kumar, J. S. Murallidharan, and R. Bhardwaj. "Evaporation of Initially Heated Sessile Droplets and the Resultant Dried Colloidal Deposits on Substrates Held at Ambient Temperature." In: *Langmuir* 36.29 (June 2020), pp. 8407–8421. DOI: 10.1021/acs.langmuir.0c00756.

[109] R. Tuckermann, S. Bauerecker, and H. K. Cammenga. "IR - Thermography of Evaporating Acoustically Levitated Drops." In: *International Journal of Thermophysics* 26.5 (Sept. 2005), pp. 1583–1594. DOI: 10.1007/s10765-005-8105-6.

Part I

APPENDIX

A

Article published in njp microgravity, Dec 2020: Sanjeev Kumar, Marc Medale, Paolo Di Marco and David Brutin. "Sessile volatile drop evaporation under microgravity." npj Microgravity 6.1, 37 (2020). https://doi.org/10.1038/s41526-020-00128-2"

ARTICLE　　OPEN

Check for updates

Sessile volatile drop evaporation under microgravity

Sanjeev Kumar [1 ✉], Marc Medale[1], Paolo Di Marco [2] and David Brutin [1,3 ✉]

The evaporation of sessile drops of various volatile and non-volatile liquids, and their internal flow patterns with or without instabilities have been the subject of many investigations. The current experiment is a preparatory one for a space experiment planned to be installed in the European Drawer Rack 2 (EDR-2) of the International Space Station (ISS), to investigate drop evaporation in weightlessness. In this work, we concentrate on preliminary experimental results for the evaporation of hydrofluoroether (HFE-7100) sessile drops in a sounding rocket that has been performed in the frame of the MASER-14 Sounding Rocket Campaign, providing the science team with the opportunity to test the module and perform the experiment in microgravity for six consecutive minutes. The focus is on the evaporation rate, experimentally observed thermo-capillary instabilities, and the de-pinning process. The experimental results provide evidence for the relationship between thermo-capillary instabilities and the measured critical height of the sessile drop interface. There is also evidence of the effects of microgravity and Earth conditions on the sessile drop evaporation rate, and the shape of the sessile drop interface and its influence on the de-pinning process.

INTRODUCTION

Drops have been fascinating researchers for centuries[1–3]. Topics of interest include water falling onto a hot cooking plate, which is a typical example of Leidenfrost drops[1], the evaporation of sessile drops with nanoparticle deposition in coffee rings[4], inkjet printing[5,6], pesticides sprayed onto leaves[7], and blood analysis[8,9]. Although sessile drops are simple in geometry, the physics involved in the evaporation process is complex due to the numerous intricate interactions with the substrate and ambient environment, and the fluid nature of the sessile drop itself. An accurate quantitative model of the evaporation process can lead to greater understanding of the evaporation rate and control over the pattern formation or the deposition of particles after the evaporation of a sessile drop. This knowledge can then enhance the efficiency of several applications. The physically rich and complex evaporation of sessile drops is thus of interest to both the academic and industry communities.

Parabolic flight experiments on drops of various fluids have been performed multiple times by The National Centre for Space Studies (CNES), France, and The European Space Agency (ESA) parabolic flight campaigns[10–15]. The existence of thermo-capillary instabilities[14,16] and the effect of the reduced gravity environment on evaporation[11,17] and the drop interface[10,18,19] have already been demonstrated. Parabolic flights have enabled these observations, but such flights are not sufficient in terms of duration or residual acceleration for accurate measurements to be taken. Furthermore, the drop interface is highly sensitive to aircraft vibrations. A better level of microgravity and a longer evaporation time are therefore needed.

The Advanced Research on Liquid Evaporation in Space (ARLES) experiment module (see Figs. 1 and 2) was designed to support the investigation of the evaporation process in a controlled environment. ARLES was part of the payload in a SubOrbital Express rocket (MASER 14) and it successfully took place on Monday, 24 June 2019 from the Esrange Space Center in northern Sweden under the collaboration of the ESA and Swedish Space Corporation (SSC). The ARLES experiment was conducted as a

preparation for an experiment that is to be performed in the near future at the European Drawer Rack 2 of the International Space Station under the EVAPORATION project of the ESA. The intent is to study evaporating drops of pure fluids as well as drops of fluids that contain a low concentration of metallic nanoparticles. The influence of an electric field is also of interest. The application of an external electrostatic field induces electric stress at the vapor–liquid interface, deforming it and altering the contact angle. The resulting electric forces press the drop against the surface and elongate it in the vertical direction; in addition, electroconvection is induced in the liquid and in the surrounding vapor atmosphere, resulting in a possible enhancement of evaporation rate, which may result useful when gravity-driven convection is suppressed. The scientific objectives include dealing with the flow motion and the thermo-capillary instabilities occurring in the drop, at the drop interface, and in the vapor phase, and investigating the pattern formation on the substrate after the evaporation phase.

ARLES was a collaborative experiment among various teams. Each team focused on different aspects of the experiment to contribute to the overall scientific objectives of the experiment, such as flow motion and thermo-capillary instabilities occurring in the drop, at the drop interface, and in the vapor phase, the pattern formation on the substrate after evaporation of the volatile phase, the deposition of nanoparticles, and the eventual heat transfer enhancement. Our team primarily focused on the analysis of the flow motion and thermo-capillary instabilities occurring in the drop using data from the infrared (IR) (top view) camera and on the evaporation rate and interface evolution of the sessile drop using data from the side-view camera. The experimental results presented here address the effect of microgravity and Earth conditions on the evaporation, thermo-capillary instabilities, drop interface, and de-pinning of a forced sessile drop of hydrofluoroether (HFE-7100) liquid on a heated substrate. The experimental results allow for a comparison of data from both ground and space experiments, thereby providing firm conclusions.

[1]Aix-Marseille Universite, CNRS, IUSTI UMR 7343, Marseille 13013, France. [2]DESTEC, University of Pisa, Largo Lazzarino 1, Pisa 56122, Italy. [3]Institut Universitaire de France, Paris 75231, France. ✉email: sanjeev.kumar@univ-amu.fr; david.brutin@univ-amu.fr
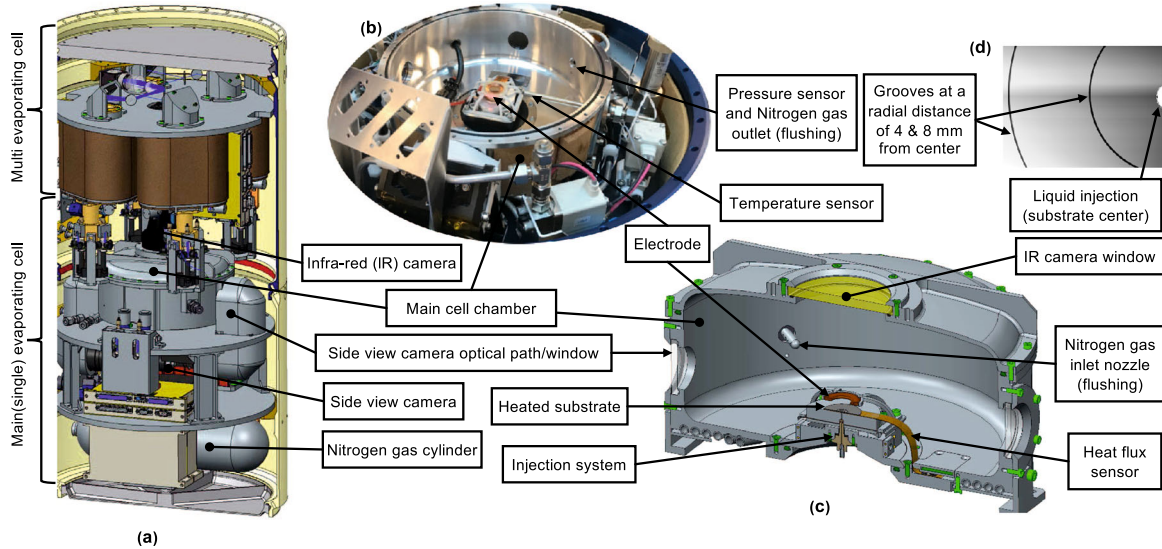
Fig. 1 Overview of the ARLES experimental setup. a Experiment module on-board the MASER 14 rocket, divided into two parts: the main evaporating and multi-evaporating cells. **b, c** Main evaporating cell (MEC) with a detailed schematic. **d** Platinum layered surface crystal silicon wafer substrate (top view) with grooves. Images **a**, **b**, and **c** are credited to the European Space Agency (ESA) and Swedish Space Corporation (SSC).
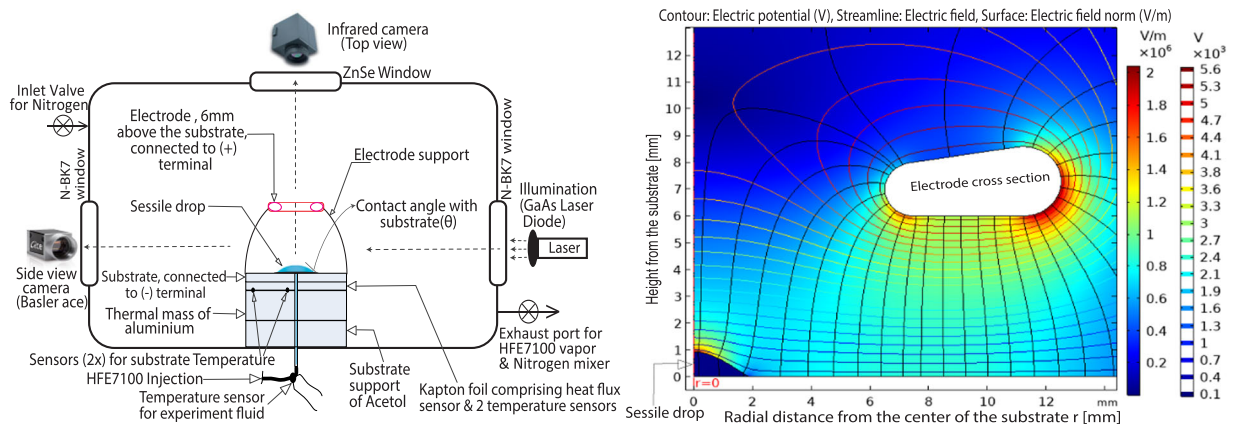

Fig. 2 Schematic of the main evaporating cell (MEC) of the ARLES experiment (left). Axisymmetric electric field around sessile drop (right). Readers are advised to refer to web version of this figure for better display.

RESULTS

Experimental setup and conditions

In Fig. 1a, a complete setup of the ALRES experiment has been shown. It consists of two parts, namely the main evaporating cell (MEC; bottom) and multi-evaporating cells (top). Our current focus is on the MEC experiment. The detailed schematic of the MEC is presented in the Fig. 2 (left) along with its chamber shown in Fig. 1b (top view) and 1c (cut view) with injection system, substrate, and electric field electrode (substrate is connected to the negative (−) terminal and the electrode to the positive (+) terminal). Figure 2 (right) shows the electric field distribution around the sessile drop for the axisymmetric case. For more details, please refer to MEC schematic in Fig. 2.

The ideal experimental conditions for the MEC are as follows: target theoretical nominal parameters for microgravity and Earth conditions were set to be similar for the purposes of comparison. The injection velocity of liquid HFE-7100 for sessile drop creation on the heated substrate was $4\,\mu L\,s^{-1}$ and the nominal volume of each sessile drop was set at $6\,\mu L$. However, multiple ground experiments have shown that it is difficult to precisely control the

injection liquid volume with the current injection system and hardware. Even though the actual injected volume of the drops during the ground experiment is lower than the target theoretical nominal value but the actual injected volume of the drops during the microgravity conditions is higher than the target nominal one (see Fig. 3). The temperature of the main test cell was set at 26 °C and the temperature of the substrate was set at 28 °C with an imposed electric field 8 kV for all drops with electric field, except for drop 8DPμgEF under microgravity, for which the field was set at 5.7 kV. Due to the grooves on the substrate, the base diameter of all the sessile drops remained constant (4 mm) during evaporation until the drops de-pinned.

Experimental results

For Earth gravity, the experimental data from the sensor are as follows: the main cell pressure (inside chamber) P_{amb}, ambient temperature (inside chamber) T_{amb}, and substrate center temperature T_{sc}, and the difference between the substrate center and ambient temperatures $(T_{sc} - T_{amb})$ were in the ranges 1053–1058 mbar, 26.16–25.87 °C, 27.93–28.00 °C, and
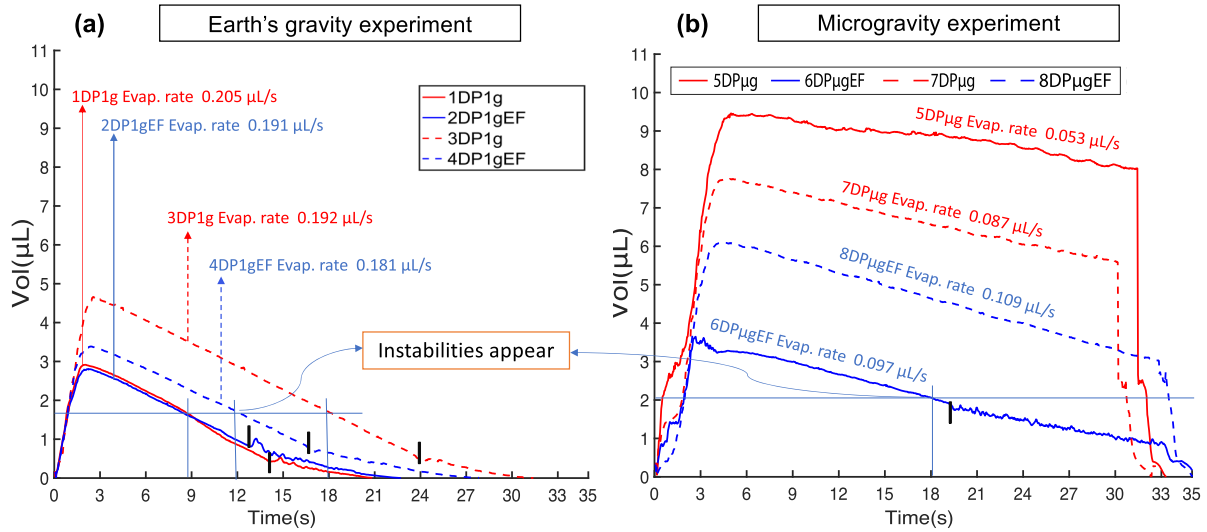
Fig. 3 Volume of sessile drops on the heated substrate vs. time. a Earth's gravity. **b** Microgravity conditions. The bar **I** denotes the de-pinning stage of the sessile drops. For the better interpretation, please also refer Table 1 along with figure. Readers are advised to refer to the web version of the figure.

1.84–2.14 °C, respectively, for all drops. Furthermore, the substrate edge temperature T_{se} was in the range 28.11–28.24 °C. Thus, $(T_{se} - T_{sc})$ was in the range 0.16–0.22 °C and $(T_{se} - T_{amb})$ was in the range 2.04–2.31 °C for all drops.

Similarly, for the microgravity experiment, the sensor data are as follows: the main cell pressure (inside chamber) P_{amb}, ambient temperature (inside chamber) T_{amb}, and substrate center temperature T_{sc}, and the difference between the substrate center and ambient temperatures $(T_{sc} - T_{amb})$ were in the range 1050–1057 mbar, 25.65–25.21 °C, 27.95–28.08 °C, and 2.39–2.79 °C, respectively, for all drops. The substrate edge temperature T_{se} was in the range 28.13–28.18 °C. Thus, $(T_{se} - T_{sc})$ was in the range 0.15–0.21 °C and $(T_{se} - T_{amb})$ was in the range 2.58–2.99 °C for all drops. The data and results from the Earth gravity and microgravity experiment are summarized in Table 1.

A comparison of the sessile drop volume with respect to time during evaporation is presented in Fig. 3. We can see that in the Earth's gravity experiment, all drops evaporated from the heated substrate before flushing started, whereas in the microgravity experiment flushing started before evaporation was complete (see the sudden fall in the drop volume). In the latter, only drop 6DPµgEF de-pinned, conversely to Earth's gravity experiment, where all drops did.

To compare the evaporation rates of sessile drops measured in microgravity experiment, one can refer to the analytical model for evaporation limited by diffusion, first derived by Picknett and Bexon[20] for a constant contact area (up to de-pinning) and a spherical cap shape. In our experiments, the wetted area between the liquid HFE-7100 and heated substrate was constant with a base diameter of 4 mm (owing to the groove in the substrate). The analytical evaporation rate is thus:

$$\frac{dV}{dt} = 2\pi D_{eff} C_{sat} L F(\theta) \tag{1}$$

$$C_{sat} = \frac{P_{sat} M_l}{R_{gas} T_{amb}} \tag{2}$$

$$F(\theta) = (8.957 \; 10^{-5} + 0.633 \; \theta + 0.116 \; \theta^2 - 0.08878 \; \theta^3$$
$$+ \; 0.01033 \; \theta^4) / \sin \theta \quad \text{for} \quad \pi/18 \le \theta \le \pi, \tag{3}$$

where L is the drop base radius, C_{sat} is the saturated vapor concentration, T_{amb} is the ambient temperature in Kelvin, R_{gas} is the universal gas constant, P_{sat} is the saturation pressure based on the

ambient temperature T_{amb} in the MEC, M_l is the molecular weight of the liquid (HFE-7100), and D_{eff} is the diffusion coefficient of HFE-7100 in a nitrogen gas environment. The diffusion coefficient D_{eff} was calculated according to the Fuller–Schettler–Giddings equation[21] and $F(\theta)$ is a function of the contact angle of the sessile drop, derived by Picknett and Bexon[20].

A comparison of experimental and theoretical evaporation rates is presented in Fig. 4 for drop 7DPµg under microgravity conditions at time $t = 30$ s (see Figs. 3 and 5b for a side view). The parameters for the analytical calculation are the base radius $L = 2$ mm, contact angle $\theta = 45.6°$, $D_{eff} = 5.4 \times 10^{-6}$ m^2 s^{-1}, $P_{sat} = 27{,}268$ Pa, $M_l = 0.25$ Kg mol^{-1}, $P_{amb} = 105{,}100$ Pa, and $T_{amb} = 25.36$ °C. The calculated theoretical value of the diffusion-limited evaporation rate for this drop (7DPµg) under microgravity conditions at time $t = 30$ s is 0.095 µL s^{-1}. The experimental value for the time evolution of the sessile drop volume is calculated from post-processing the side view of the drop shape (see Fig. 5e). The experimental values under Earth and microgravity conditions without electric field are 0.198 and 0.087 µL s^{-1}, respectively. This technique is more accurate in the constant contact area evaporation mode with an uncertainty maximum up to ±0.05 µL for the volume and of ±0.015 µL for the evaporation rate.

Drop shapes result from body forces equilibrium during the evaporation process. Fig. 5 shows the comparison of the sessile drop under gravity only (see Fig. 5a), microgravity only (see Fig 5b), both gravity and electric field (see Fig. 5c), and finally microgravity and electric field (see Fig. 5d). The combination of body forces results in changes of interface curvature, contact angle, and thus in the de-pining stage. Figure 5e is only intended to show the comparison between raw images from experiments (top) and clean ones (bottom) after post-processing. The cleaned images have been later used to calculate the time evolution of drop volumes reported in Fig. 3.

To better understand the overall evaporation process, it could be interesting to address the related coupled fluid-flow problem that is induced. For that purpose, Fig. 6 displays top view IR and side-view images of drop 6DPµgEF in the microgravity experiment and drop 4DP1gEF in the ground experiment subjected to an 8 kV electric field, as these were the only two drops of similar initial volume (see Fig. 3). The drop evaporation time series is divided in five sections, starting the sequence from the liquid injection to flushing. Next to the injection phase, surface temperature was almost uniform in both experiments, until

Table 1. Summary of experiments with internal notation.

Drops no.	Drops code	Injected volume (µL)	Evaporation rate during constant contact area (µL s⁻¹)			Instabilities appeared at volume (µL)	At de-pinning		Volumetric force condition
			Evaporation rate	Uncertainty (plus)	Uncertainty (minus)		Volume (µL)	θ (deg.)	
1	1DP1g	2.91 at $t = 2$ s	0.205	0.011	0.013	1.6	0.43	7.6	Gravity
2	2DP1gEF	2.81 at $t = 2.2$ s	0.191	0.005	0.007	1.59	0.81	14.6	Gravity with electric field
3	3DP1g	4.67 at $t = 2.6$ s	0.192	0.006	0.004	1.54	0.43	8.6	Gravity
4	4DP1gEF	3.88 at $t = 2.4$ s	0.181	0.012	0.005	1.67	0.76	13.4	Gravity with electric field
5	5DPµg	9.45 at $t = 5$ s	0.053	0.003	0.003	NA	NA	NA	Microgravity
6	6DPµgEF	3.28 at $t = 4.8$ s	0.097	0.014	0.001	2.01	1.83	18.7	Microgravity with electric field
7	7DPµg	7.75 at $t = 4.6$ s	0.087	0.007	0.006	NA	NA	NA	Microgravity
8	8DPµgEF	6.10 at $t = 4.5$ s	0.109	0.009	0.005	NA	NA	NA	Microgravity with electric field
9	9DPµg	6	0.095	NA	NA	NA	NA	NA	Microgravity without electric field (Analytical)
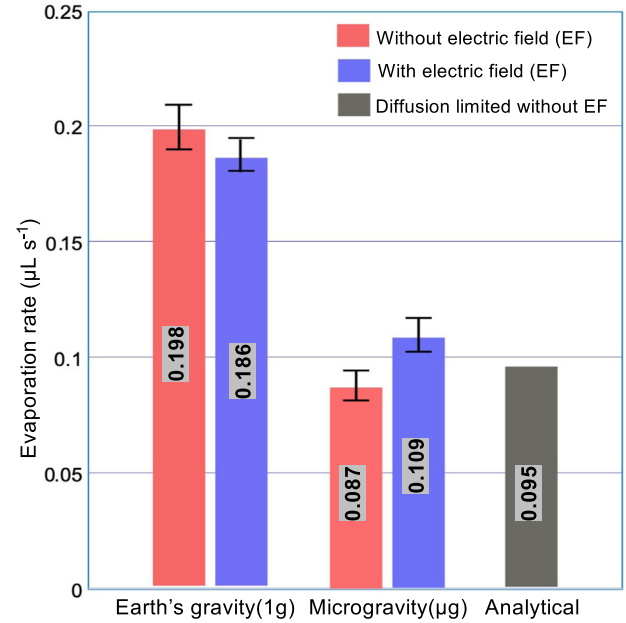
Fig. 4 Evaporation rates over the constant contact angle mode. Earth conditions: average evaporation rates of sessile drops 1DP1g and 3DP1g (without an electric field), and 2DP1gEF and 4DP1gEF (with an electric field). Microgravity conditions: evaporation rates of sessile drops 7DPµg (without an electric field) and 8DPµgEF (with an electric field). The parameters of sessile drop 7DPµg were used for the calculation of the analytical diffusion-limited evaporation rate without an electric field[20]. Error bars are calculated estimating the minimum and maximum evaporation rate experimentally measured.

thermo-capillary instabilities take place for drop 6DPµgEF at $t = 18.3$ s in the microgravity experiment and drop 4DP1gEF at $t = 12$ s in the ground experiment. The pattern of thermo-capillary instabilities shows several cells coming from bottom to surface of sessile drop and then moving toward the contact line. It clearly appears that these thermo-capillary instabilities only occur once the drop volume gets below a critical value (see horizontal lines in Fig. 3 and detailed values in Table 1). It is noteworthy from Fig. 3 that these thermo-convective instabilities do not significantly modify the evaporation rates, whatever been under Earth or microgravity conditions. The last two sections of Fig. 6 display the initiation stage of de-pinning and that of flushing, respectively.

DISCUSSION
Owing to unrepeatable injection drop volumes, one was faced with very different initial evaporation conditions between Earth and microgravity experiments (see Fig. 3). Moreover, the time plot for drop 5DPµg under microgravity conditions (see Fig. 3) exhibits some oscillations until de-pinning occurs. The detailed reasons for this strange behavior are under investigations, but the oscillations in volume may be related to higher mechanical coupling to the rocket vibrations due to its initial volume being larger than that of the other drops (see Table 1). It might also have resulted from the release of gas bubbles inside the drop during evaporation, as can be observed from the side-view images of the drop. The global evaporation rate of drop 5DPµg (microgravity) is thus excluded in the subsequent analysis.

The effect of gravity on the evaporation rate clearly appears in Fig. 4: its value is roughly halved under microgravity conditions as compared to Earth conditions; this is in agreement with
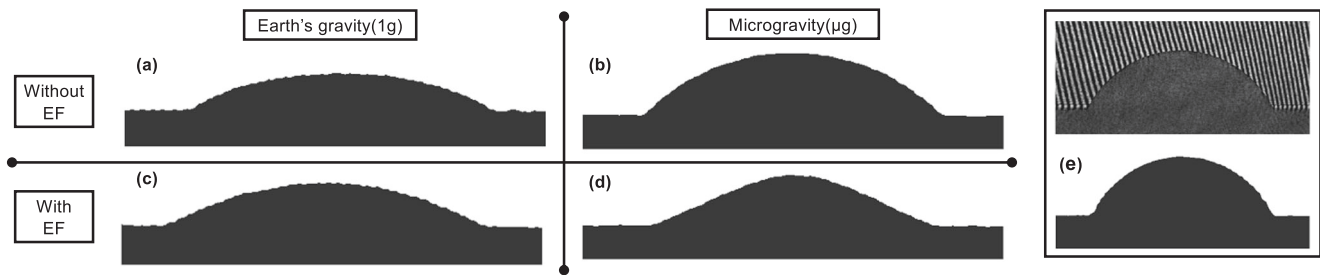
Fig. 5   Comparison of the sessile drop interface under the effect of gravitational and electrical field forces. a Drop 1DP1g on the ground at $t = 2.3$ s. **b** Drop 7DPμg under microgravity at $t = 30$ s. **c** Drop 2DP1gEF on the ground with an electric field at $t = 2.4$ s. **d** Drop 6DPμgEF under microgravity with an electric field at $t = 6.8$ s. **e** Image from a side-view camera with interferometry lines (top) and after cleaning (bottom). The cleaned images are used to measure volume over the time (see Fig. 3).
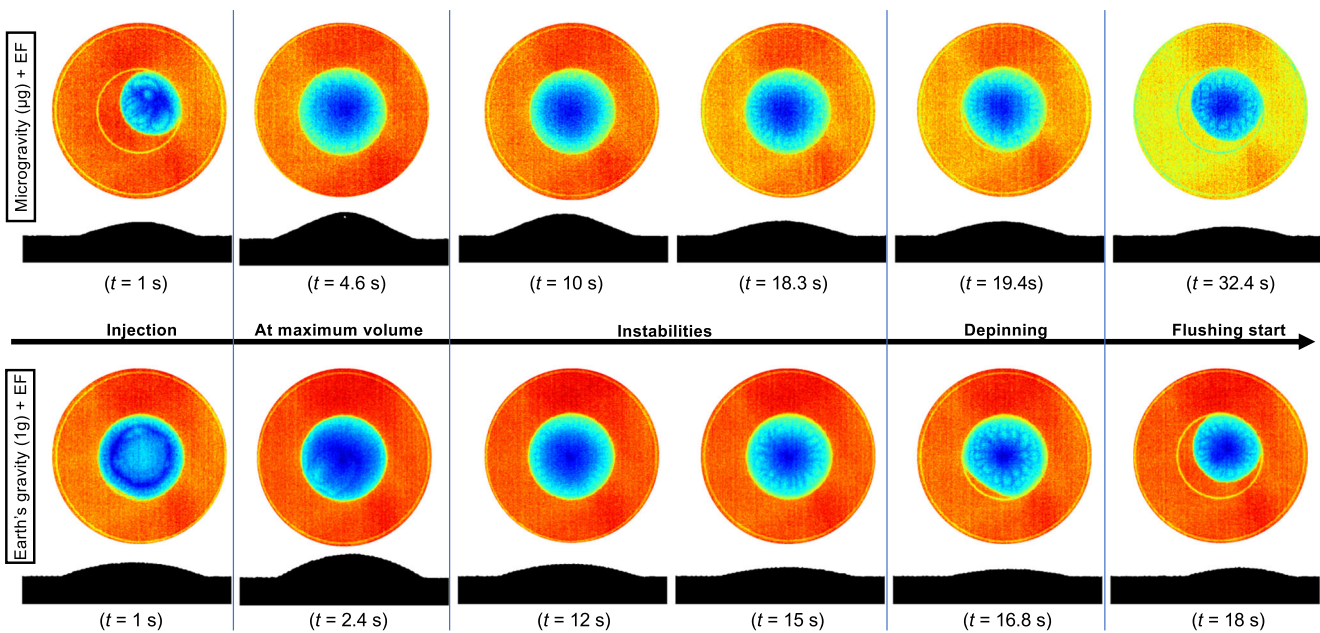
Fig. 6   Time series of infrared images (top view) during the evaporation of liquid HFE-7100 sessile drops on a heated substrate under microgravity and Earth conditions with electric field (EF). The frames illustrate the injection, instability pattern, and de-pinning stages, respectively, for drops 6DPμgEF and 4DP1gEF under microgravity (top) and Earth's gravitational conditions (bottom) (see Table 1 and refer to the Supplementary Materials for complete movies).

previous works[11,17,22]. Indeed, the average evaporation rate of the sessile drops of HFE-7100 under microgravity is 56% and 45% lower than that under Earth conditions without and with the electric field, respectively. Interestingly, the analytical diffusion-limited evaporation rate enables us to conclude that the average evaporation rate of HFE-7100 sessile drops under microgravity conditions in the absence of an electric field seems to be mainly controlled by diffusion. Furthermore, note that the average evaporation rate under Earth conditions with an electric field is 6% lower than the average rate without one, whereas the average evaporation rate under microgravity conditions with an electric field is 19% higher than the average rate without one. That is to say, the effect of an electric field on the evaporation rate of HFE-7100 is opposite under microgravity and Earth conditions, as it is for liquid water drops[22].

Figure 5 shows side views of the sessile drops under the four considered conditions. For a fair comparison, compare Fig. 5a with Fig. 5c and Fig. 5d with Fig. 6 (drop 4DP1gEF), as these drops were of comparable volumes (see Table 1). Also, it is noteworthy that no drop in microgravity without an electric field had a lower initial injected volume (see Fig. 3b). Therefore, the minimum volume for drop 7DPμg under microgravity at $t = 30$ s can be used for comparison of the

interface. The interface shape of the sessile drops resulted from body and surface forces acting on them. As it clearly appears in Fig. 5a, b, the shape of a sessile drop under microgravity is exactly spherical in comparison to that in Fig. 5a. In contrast, sessile drops exhibit clear cone formation under microgravity conditions with an electric field (see Figs. 5d, c and 6). Along with the influence on the interface (see Fig. 5), which is in agreement with other experiments[10,12,18,22,23], the de-pinning process is also associated with the gravitational and electrical forces individually or in combination. Based on these comparisons, we can see the correlation between the body and surface force conditions and the volumes (see Fig. 3) and contact angles (contact angles were measured by using the ImageJ software plugin known as DropSnake, which is based on B-spline snakes (active contours)) during de-pinning irrespective of the shape of the sessile drop interface shape. The fact that de-pinning is anticipated in the presence of an electric field can be attributed to the fact that the radial electric force is directed inwards, causing striction of the interface[12]. Accordingly, the order of de-pinning based on the volume and contact angle and body and surface force conditions was as follows: drop 6DPμgEF with an electric field (under microgravity conditions) at volume $= 1.83$ μL and contact angle $\theta = 18.7°$ de-pinned at the highest volume and contact angle and did so earlier

than drop 2DP1gEF with an electric field (under Earth conditions), which de-pinned at volume = 0.81 μL and contact angle $\theta = 14.6°$, and drop 4DP1gEF with electric field (under Earth conditions), which de-pinned at volume 0.76 μL and contact angle $\theta = 13.4°$. Drop 3DP1g without an electric field (under Earth conditions) at volume = 0.43 μL and contact angle $\theta = 8.6°$ and drop 1DP1g without an electric field (under Earth conditions) at volume = 0.43 μL and contact angle $\theta = 7.6°$ de-pinned with the smallest volumes and contact angles. According to the above correlations, it can be predicted that for sessile drops 5DPμg and 7DPμg (under microgravity without an electric field), the volume (and contact angle) should have been either equal to or higher than the volume (and contact angle) of drops 2DP1gEF and 2DP1gEF (under Earth conditions with an electric field) at de-pinning. The influence of the substrate grooves in the de-pinning dynamics could itself be a subject of investigation[24].

The IR images in Fig. 6 reveal some characteristic patterns associated with the thermo-capillary instabilities that occurred for drop 6DPμgEF in microgravity conditions at time $t = 18.3$ s, which corresponds to a volume of 2.01 μL, calculated using the side-view image (refer Fig. 6) in which the maximum sessile drop height is 0.41 mm. The thermo-capillary instabilities first appeared near the periphery of the sessile drop during evaporation and before de-pinning, and they remained visible up to complete evaporation (see Fig. 6). In the ground experiment, however, there were instability patterns for drop 4DP1gEF stating at time $t = 15$ s and volume = 1.67 μL (maximum interface height of 0.24 mm); the patterns began to appear at time $t = 12$ s and volume = 1.10 μL. Similarly, instability patterns appeared in all the sessile drops in the ground reference experiment (see Fig. 3), for which volume and time are reported in Fig. 3. The thermo-capillary instabilities appeared as soon as the maximum drop height was below a critical value of approximately between 0.2 and 0.3 mm for Earth conditions and around 0.4 mm for the microgravity conditions, which is associated with thermo-capillary instabilities referred to as Marangoni instabilities. Interestingly, the above critical thickness for HFE-7100 under Earth conditions fully agrees with Chauvet et al.[25]. Therefore, as the injected volume of most of the microgravity drops exceeded that of the drops in the Earth reference experiment, longer evaporation times would have been required for the former to reach the critical height at which thermo-capillary instabilities are observed. As a result, flushing of the largest microgravity sessile drops was unfortunately performed before instability patterns could be observed.

In conclusion, it is worth mentioning that it was very difficult to carry out repeatable injection of prescribed sessile drop volume both under Earth and microgravity conditions. The exact reasons for the formation of oversized sessile drops under microgravity conditions are still under investigation. In future microgravity experiments, it would therefore be preferable to perform sessile drop volume injection with real-time feedback control. Under our experimental conditions, the results provide evidence for the effect of microgravity conditions on the sessile drop evaporation rate, indicating that the rate under microgravity conditions is nearly half that under Earth conditions for HFE-7100. Furthermore, the effect of an electric field on the evaporation rate is opposite under microgravity and Earth conditions. The experimental results also demonstrate the relationship between thermo-capillary instabilities and the measured critical height of the sessile drop interface. For temperature differences between substrate and ambient in the range of 2–3 °C with a base diameter of 4 mm, the measured critical height for the appearance of thermo-capillary instabilities is approximately between 0.2 and 0.3 mm for Earth conditions and around 0.4 mm for the microgravity conditions for HFE-7100. It is also noteworthy that meanwhile they strongly change the fluid-flow structure in the sessile drop, these thermo-capillary instabilities do not significantly influence the evaporation

rates. Through the application of different combinations of volumetric forces (an electric field and gravity), we also demonstrate the role of gravity on the shape of the sessile drop interface and its influence on the de-pinning of sessile drops. To concrete the above evidence, module will re-fly again (as a baseline, in 2022). One of the main objectives of the reflight is to better control the actual injected volumes so as to ensure a better data comparison among the different testing conditions.

METHODS

Fluid property measurements
In all cases, the liquid used was 99.9% pure HFE-7100 (3M™ Novec™ 7100 Engineered Fluid, a hydrofluoroether also known as methoxy-nonafluorobutane (C4F9OCH3)). It was chosen for its volatility, semi-transparency in the IR wavelengths, perfect wetting, non-toxicity, and being non-flammable. For more on the properties of HFE-7100, please refer to https://multimedia.3m.com/mws/media/199818O/3m-novec-7100-engineered-fluid.pdf and https://multimedia.3m.com/mws/media/569860O/3mtm-thermal-management-fluids-for-military-aerospace-apps.pdf.

Hardware description
The ARLES experiment module was designed and manufactured by the SSC under the guidance of the ESA and Science team proposition based on the required scientific objectives. The overall design of the experiment module is subdivided into two parts (see Fig. 1a): the main evaporation cell (MEC), which is for single-drop experiment systems and the multi-drop cell, which is for multi-drop experiment systems to be executed in parallel. For safety reasons, a neutral gas nitrogen (N_2) atmosphere was used.

Main evaporation cell. The chamber volume of the main evaporation cell (MEC) is 4 l. It is sized to maintain a low vapor concentration throughout the whole experiment even if the N_2 evacuation fails during the flight. The cell thickness was chosen to withstand the expected pressure differences during the filling and emptying of the gas (N_2). Figures 1 and 2 shows the main cell used to perform sessile drop evaporation of a pure fluid on a heated substrate with and without an electric field. The substrate was a thin single-crystal silicon wafer coated with a 50 nm-thick platinum layer, whose surface roughness was less than 1 micron RMS, deposited by atomic layer deposition. The substrate had 50×50 μm grooves with 4 ± 0.1 mm in diameter to force the pinning of a sessile drop with a diameter of 4 mm (see Fig. 1d). The central hole for the fluid injection was 0.7 mm in diameter. The substrates were manufactured at MICAS TU Leuwen. An IR camera was mounted on the lid of the main evaporation cell, where a ZnSe window served as the passage for IR wavelengths. The interferometry camera observed the single-drop evaporation process through the side observation windows of the MEC.

Multi-drop cell. The multi-drop experiment system is for the analysis of different fluids with nanoparticle suspensions, and the related pattern formation on the substrates after the evaporation process, and its consequent functionalisation. As such, it is not part of our analysis.

Heat flux, temperature, and pressure measurements. Two T-type thermo-couples monitored the substrate temperature. One thermocouple was placed close to the center hole and the other one close to the edge of the substrate. These sensors were incorporated in the heat flux sensor by the CAPTEC manufacturer. The heat flux sensor with integrated thermocouples determined the heat flux to the drops and substrate temperature with a sensitivity of 2 μV W^{-1} m^2. Along with the substrate temperature, we used a set of PT-100 sensors to monitor the cell wall temperature and the ambient temperature inside the MEC (see Fig. 1 for the position). The temperature measurement rate was 30.4 Hz, with an uncertainty of ±2.1 K from the true temperature in the worst case. The passband of the filter was 4.56 Hz. A dedicated μ-TC interface board performed the readout of the heat flux sensor and the thermocouples. The pressure sensor measured pressure in the range of 0–1.6 bar with an accuracy of ±0.2% inside the MEC throughout the experiment.

Heater. The heaters were custom made and manufactured by NEL Technologies Ltd. They are capton patch heaters with an etched resistive

pattern. For the MEC, the heater was designed to provide 5 W of uniform heating power at 24 V. The heater was driven from 24 V pulse width modulation (PWM).

Electrode. The positive high voltage potential was connected to a conical shape electrode, which was located above the substrate, concentric with the substrate grooves and the drop injection inlet hole, at a distance of 6 mm from the substrate (see Fig. 2). On the other hand, the substrate is connected to negative voltage potential.

Image acquisition and analysis

To perform fluid-flow visualization of the drops, high-resolution IR images were captured by a commercial off-the-shelf bolometric (non-cooled) Xenics, Gobi 640 camera. The images are 640×480 pixels (H × V) with a noise-equivalent temperature difference of 50 mK at 30 °C and an IR wavelength region of 8–12 μm. The images were recorded via an IR optical path consisting of an AR-coated ZnSe window (75×6 mm). The depth-of-field of the IR camera with an image pixel density of 17 μm is 0.7 mm at 9 cycles mm^{-1}. To visualize and track the evolution of the interface of the sessile drops, we used images from the side-view camera of the interferometer. The interferometer images have a field-of-view of 15×15 mm with an image pixel density of 10.78 μm pixels^{-1} (11.2 μm pixels^{-1} for microgravity conditions). The interferometry fringes were removed from the raw images with the help of the ImageJ software. The cleaned images without fringes were used for the analysis (see Fig. 5e). The image acquisition rate for all the images was 25 Hz.

Experimental procedure

The SubOrbital Express rocket (MASER 14) launch took place successfully on Monday, 24 June 2019, from the Esrange Space Center in northern Sweden. The atmospheric replacement was executed 60 s after the launch by feeding in the N_2 while the experimental cells were connected to an exhaust port in the outer structure. At the start of the microgravity phase (100 km level) $t = 70.4$ s, the experiment liquid was injected to create the first drop of HFE-7100 upon the heated substrate. After a delay corresponding to the estimated drop evaporation time, the atmosphere in the chamber was flushed. After the flushing sequence, another drop was injected, and the evaporation cycle with diagnostics was repeated. The outside pressure was 0 bar during the microgravity period. At the bottom of the ARLES experiment module is an N_2 pressure vessel for flushing the single-drop cell after each consecutive drop. Flushing was performed to prevent the evaporated liquid from condensing in the experiment cell. The ground test experiment were executed in the same way as during the flight. The only difference was the membrane vacuum pump, which was connected to the exhaust of the module.

Reporting summary

Further information on research design is available in the Nature Research Reporting Summary linked to this article.

DATA AVAILABILITY

The data collected during this study is available from the corresponding authors upon reasonable request.

REFERENCES

1. Leidenfrost, J. G. *De aquae communis nonnullis qualitatibus tractatus* (Ovenius, 1756).
2. Young, T. III. An essay on the cohesion of fluids. *Philos. Trans. R. Soc. Lond.* **95**, 65–87 (1805).
3. Fuchs, N. A. *Evaporation and Droplet Growth in Gaseous Media* (Pergamon, 1959).
4. Deegan, R. D. et al. Capillary flow as the cause of ring stains from dried liquid drops. *Nature* **389**, 827–829 (1997).
5. Ko, S. H., Chung, J., Hotz, N., Nam, K. H. & Grigoropoulos, C. P. Metal nanoparticle direct inkjet printing for low-temperature 3d micro metal structure fabrication. *J. Micromech. Microeng.* **20**, 125010 (2010).
6. Schirmer, N. C., Ströhle, S., Tiwari, M. K. & Poulikakos, D. On the principles of printing sub-micrometer 3d structures from dielectric-liquid-based colloids. *Adv. Funct. Mater.* **21**, 388–395 (2010).
7. Salyani, M. Droplet size effect on spray deposition efficiency of citrus leaves. *Trans. ASAE* **31**, 1680–1684 (1988).
8. Sobac, B. & Brutin, D. Desiccation of a sessile drop of blood: Cracks, folds formation and delamination. *Colloids Surf. A Physicochem. Eng. Asp.* **448**, 34–44 (2014).
9. Smith, F. & Brutin, D. Wetting and spreading of human blood: Recent advances and applications. *Curr. Opin. Colloid Interface Sci.* **36**, 78–83 (2018).
10. Brutin, D. et al. Sessile drop in microgravity: creation, contact angle and interface. *Microgravity Sci. Technol.* **21**, 67–76 (2009).
11. Carle, F., Semenov, S., Medale, M. & Brutin, D. Contribution of convective transport to evaporation of sessile droplets: empirical model. *Int. J. Therm. Sci.* **101**, 35–47 (2016).
12. Saccone, G. Effects of Force Fields on Interface Dynamics in view of Two-Phase Heat Transfer Enhancement and Phase Management in Space Applications. (University of Pisa, 2018).
13. Carle, F., Sobac, B. & Brutin, D. Hydrothermal waves on ethanol droplets evaporating under terrestrial and reduced gravity levels. *J. Fluid Mech.* **712**, 614–623 (2012).
14. Sobac, B. & Brutin, D. Thermocapillary instabilities in an evaporating drop deposited onto a heated substrate. *Phys. Fluids* **24**, 032103 (2012).
15. Dehaeck, S., Rednikov, A. & Colinet, P. Vapor-based interferometric measurement of local evaporation rate and interfacial temperature of evaporating droplets. *Langmuir* **30**, 2002–2008 (2014).
16. Sefiane, K., Moffat, J. R., Matar, O. K. & Craster, R. V. Self-excited hydrothermal waves in evaporating sessile drops. *Appl. Phys. Lett.* **93**, 074103 (2008).
17. Carle, F., Sobac, B. & Brutin, D. Experimental evidence of the atmospheric convective transport contribution to sessile droplet evaporation. *Appl. Phys. Lett.* **102**, 061603 (2013).
18. Kabov, O. A. & Zaitsev, D. V. The effect of wetting hysteresis on drop spreading under gravity. *Dokl. Phys.* **58**, 292–295 (2013).
19. Diana, A., Castillo, M., Brutin, D. & Steinberg, T. Sessile drop wettability in normal and reduced gravity. *Microgravity Sci. Technol.* **24**, 195–202 (2012).
20. Picknett, R. & Bexon, R. The evaporation of sessile or pendant drops in still air. *J. Colloid Interface Sci.* **61**, 336–350 (1977).
21. Fuller, E. N., Ensley, K. & Giddings, J. C. Diffusion of halogenated hydrocarbons in helium. the effect of structure on collision cross sections. *J. Phys. Chem.* **73**, 3679–3685 (1969).
22. Almohammadi, H. & Amirfazli, A. Sessile drop evaporation under an electric field. *Colloids Surf. A Physicochem. Eng. Asp.* **555**, 580–585 (2018).
23. Abdella, K., Rasmussen, H. & Inculet, I. Interfacial deformation of liquid drops by electric fields at zero gravity. *Comput. Math. Appl.* **31**, 67–82 (1996).
24. Grishaev, V., Amirfazli, A., Chikov, S., Lyulin, Y. & Kabov, O. Study of edge effect to stop liquid spillage for microgravity application. *Microgravity Sci. Technol.* **25**, 27–33 (2012).
25. Chauvet, F., Dehaeck, S. & Colinet, P. Threshold of bénard-marangoni instability in drying liquid films. *Europhys. Lett.* **99**, 34001 (2012).

ACKNOWLEDGEMENTS

AUTHOR CONTRIBUTIONS

COMPETING INTERESTS

The authors declare no competing interests.

ADDITIONAL INFORMATION

Supplementary information is available for this paper at https://doi.org/10.1038/s41526-020-00128-2. A supplementary movie for Fig. 6 is available online.

Correspondence and requests for materials should be addressed to S.K. or D.B.

Reprints and permission information is available at http://www.nature.com/reprints

Publisher's note Springer Nature remains neutral with regard to jurisdictional claims in published maps and institutional affiliations.

B

Fluid properties used as temperature function:

1. Ethanol [104, 107]

   - Density, $\rho \left(\text{kg} \cdot \text{m}^{-3} \right)$, $273.15 < T < 343$

     $475.02 + 4.7 * T - 0.018 * T^2 + 1.84 \cdot 10^{-5} * T^3$

   - Dynamic viscosity, $\mu (\text{Pa} \cdot \text{s})$, $273.15 < T < 343$

     $0.074 - 6.17 \cdot 10^{-4} * T + 1.7 \cdot 10^{-6} * T^2 - 1.67 \cdot 10^{-9} * T^3$

   - Specific heat capacity, $C_\text{p} \left(\text{J} \cdot \text{kg}^{-1} \cdot \text{K}^{-1} \right)$, $273.15 < T < 343$

     $4012.28 - 18.7 * T + 0.045 * T^2$

   - Thermal conductivity, $K \left(\text{W} \cdot \text{m}^{-1} \cdot \text{K}^{-1} \right)$, $273.15 < T < 343.15$

     $0.219 - 1.22 \cdot 10^{-4} * T - 1.79 \cdot 10^{-7} * T^2$

   - Surface tension, $\gamma \left(\text{N} \cdot \text{m}^{-1} \right)$, $273.15 < T < 343.15$

     $0.001 * (24.05 - 0.0832 * ((T - 273.15[K])))$

2. Hydrofluoroether HFE7100 [105, 106]

   - Density, $\rho \left(\text{kg} \cdot \text{m}^{-3} \right)$, $273.15 < T < 363.15$

     $-0.0982 * T^2 - 11.751 * T + 1590.6$

   - Dynamic viscosity, $\mu \left(\text{Pa} \cdot \text{s} \right)$, $273.15 < T < 373.15$

     $(85.44 * exp((\frac{-1859.59}{T}) - 0.009152 * T + \frac{332097}{T^2}))$

     $* (-0.0982 * T^2 - 11.751 * T + 1590.6)$

   - Specific heat capacity, $C_\text{p} \left(\text{J} \cdot \text{kg}^{-1} \cdot \text{K}^{-1} \right)$, $273.15 < T < 343$

     $2.00 * (T - 273.15) + 1133$

   - Thermal conductivity, $K \left(\text{W} \cdot \text{m}^{-1} \cdot \text{K}^{-1} \right)$, $273.15 < T < 343$

     $-1.9548 \cdot 10^{-4} * (T - 273.15) + 0.073714$

   - Surface tension, $\gamma \left(\text{N} \cdot \text{m}^{-1} \right)$, $273.15 < T < 373.15$

     $49.351 \left((1 - (\frac{T}{468.45[\text{ K}]}))^{1.26} \right) * \left(\left(1 - 0.0527 * \left((1 - (\frac{T}{468.45[\text{ K}]}))^{0.5} \right) \right) \right)$

	Water [104]	Methanol [104]
Density, ρ $\left(\text{kg}\cdot\text{m}^{-3}\right)$	997	786.08
Dynamic viscosity, $\mu(\text{mPa}\cdot\text{s})$	0.890	0.543
Molar mass, $M_l(\text{Kg}\cdot\text{mol}^{-1})$	0.018015	0.03204
Atomic diffusion volume, v_l	12.7	31.25
Latent heat of vaporization , H_{evap} $\left(\text{kJ}\cdot\text{kg}^{-1}\right)$	2449	1155
Specific heat capacity, C_{p} $\left(\text{J}\cdot\text{kg}^{-1}\cdot\text{K}^{-1}\right)$	4180	2535.6
Thermal conductivity, K $\left(\text{W}\cdot\text{m}^{-1}\cdot\text{K}^{-1}\right)$	0.606	0.2
Capillary length, $L_{\text{c}}(\text{mm})$	2.73	1.69
Thermal expansion coefficient, β $\left(\text{K}^{-1}\right)$	2.56×10^{-4}	3.98×10^{-4}
Surface tension, $\gamma(\text{mN}\cdot\text{m}^{-1})$	71.92	22.13
Surface tension temperature coefficient, γ_{T} $\left(\text{N}\cdot\text{m}^{-1}\cdot\text{K}^{-1}\right)$	-1.68×10^{-4}	-0.835×10^{-4}
Emissivity, $\varepsilon(-)$	0.96[109]	-
Absorption coefficient, k_{SW} mm^{-1}	15.3 [60]	3.02 [60]
Boiling point ($^\circ$C)	100	65

Table B.1: Physical properties of water and methanol at 298.15 K and 1 atm.

MESH CONVERGENCE AND SENSITIVITY ANALYSIS
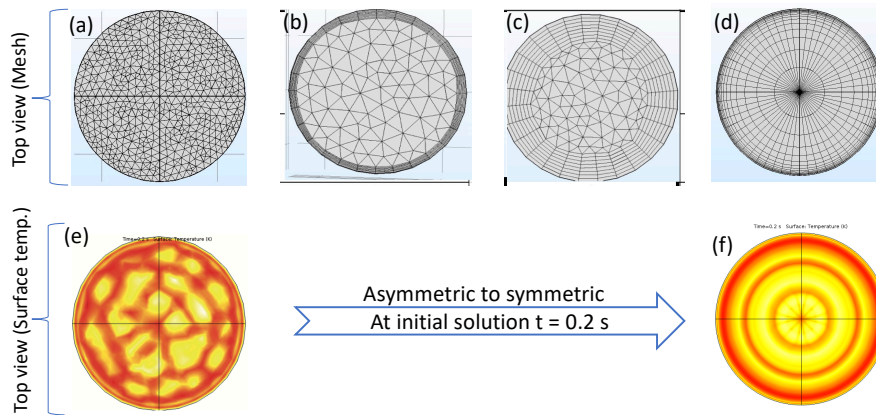
Figure C.1: Influence of the structure of the mesh on the solution.

In figure C.1 we show the top view of different mesh structure tested for our modeling, from unstructured tetrahedral mesh element (fig. C.1a) to semi-structured (fig. C.1b & c are with boundary layers), then almost structured C.1d. The effect of the mesh structure is presented in the figure C.1e & f, it shows at $t = 0.2$ s appearance of non-uniform instabilities compared to torus shaped uniform primary instability that would later break with time into non-symmetric instability. The mesh structure that shown in figure C.1d is finally selected for all our numerical simulation with number of elements adjusted based on the numerical parameters.

C.0.1 *Space discretization for low substrate temperature*

In figures C.2 and C.3 presented the Ethanol sessile drop evaporation rate with respect to the contact angle for parametric study of space discretization at substrate temperature $T_{sub} = 293.15$ and 298.15 K. Table C.1 with summary of numerical simulation. In figure C.2a & b the evaporation rate remains comparatively same for the lowest and highest total number of elements for both temperatures. However computation cost increases nearly by 25 times. However the influence of the contact angle and number of the elements can be notice in the figure C.3.
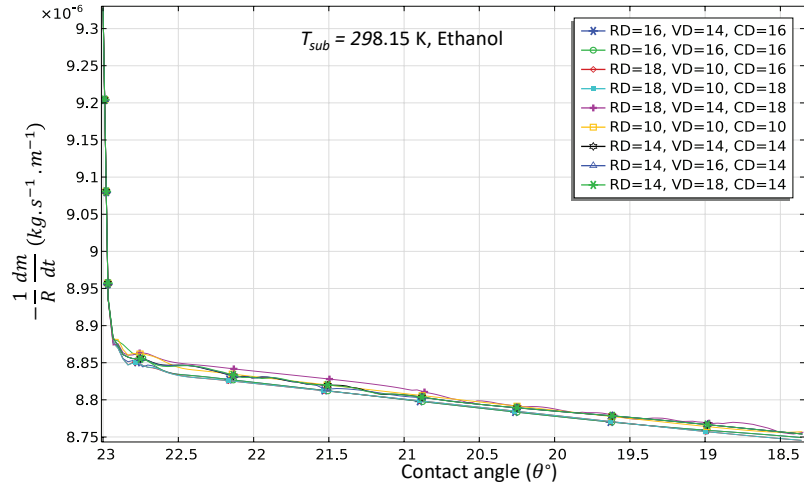
(a)
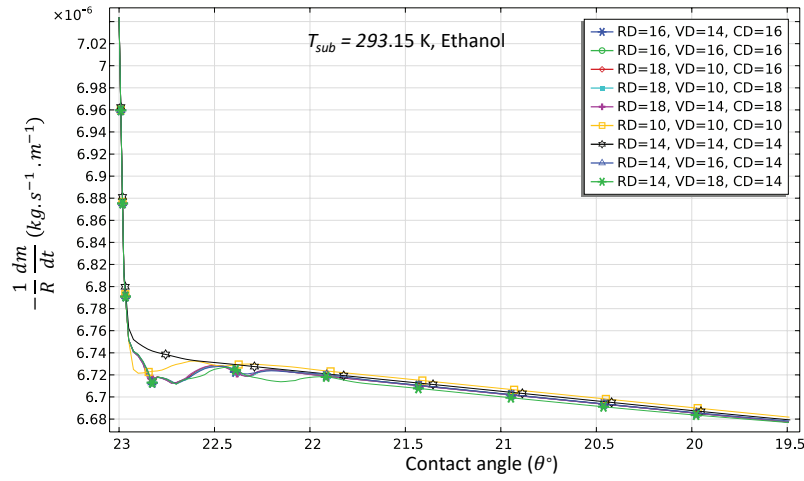
(b)

Figure C.2: Parametric study of Space discretization for ethanol sessile drop
(a) Substrate temperature $T_{sub} = 298.15$ K; (b) Substrate temperature $T_{sub} = 293.15$ K.

S.No	RD	VD	CD	Total elements	Degree of freedom (DOF)	Computational time for $T_{sub} = 298.15$ K	E_v (kg · (s · m)$^{-1}$) at $T_{sub} = 298.15$ K, & $\theta = 22°$	Computational time for $T_{sub} = 293.15$ K	E_v (kg · (s · m)$^{-1}$) at $T_{sub} = 293.15$ K & $\theta = 22°$
1	16	14	16	13440	921205	12h, 10min	8.82E-06	12h, 28min	6.72E-06
2	16	16	16	15360	1044483	18h, 6min	8.82E-06	17h, 11min	6.72E-06
3	18	10	16	10880	756121	8h, 0min	8.82E-06	8h, 52min	6.72E-06
4	18	10	18	12240	849729	9h, 4min	8.82E-06	10h, 4min	6.72E-06
5	18	14	18	17136	1161053	49h, 2min	8.84E-06	19h, 18min	6.72E-06
6	10	10	10	3600	270561	1h, 48min	8.82E-06	1h, 33min	6.73E-06
7	14	14	14	10192	709101	15h, 40min	8.82E-06	6h, 0min	6.72E-06
8	14	16	14	11648	803771	19h, 37min	8.82E-06	11h, 34min	6.72E-06
9	14	18	14	13104	898441	24h, 50min	8.82E-06	17h, 30min	6.72E-06

Table C.1: Summary of the numerical simulations of Ethanol sessile drops.
Computational time mention for the $t = 14$ s. Mesh elements
distribution presented as radial direction (RD), vertical direction
(VD) and circumferential direction (CD).

(a)

(b)
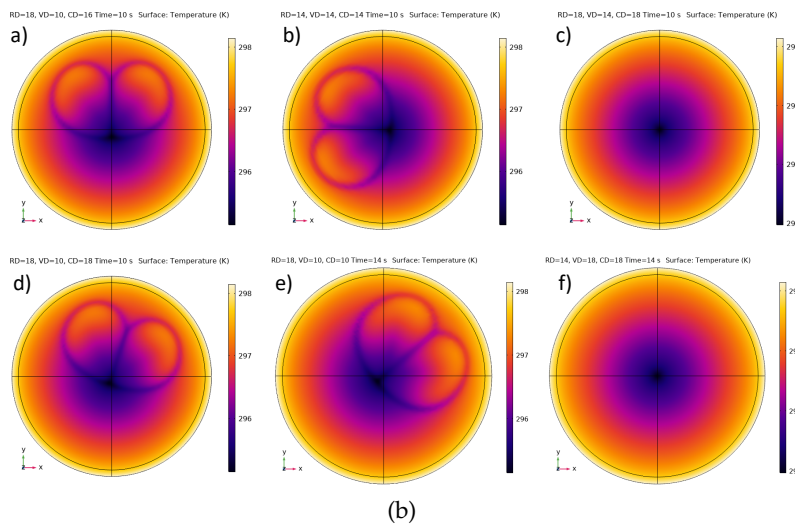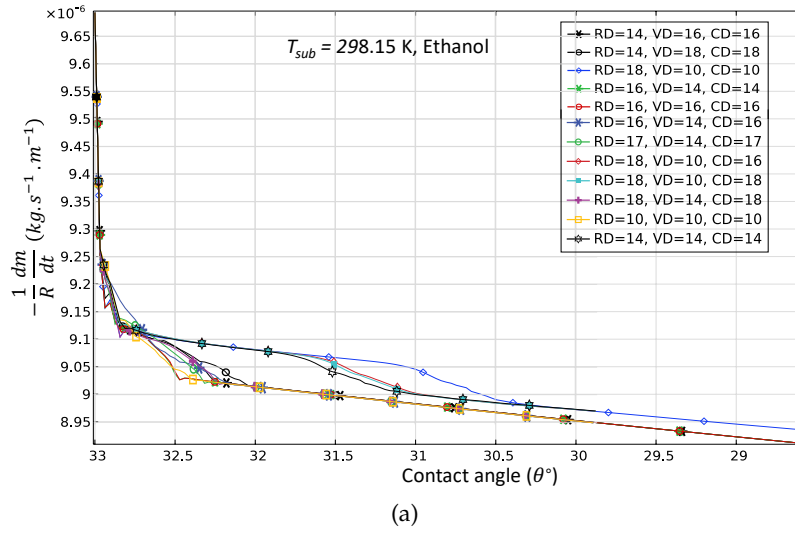
Figure C.3: Parametric study of Space discretization for ethanol sessile drop at Substrate temperature $T_{sub} = 298.15$ K. **(a)** Evaporation rate **(b)** Top view surface temperature with representing influence of the space discretization.

C.0.2   *Space discretization for high substrate temperature conditions*
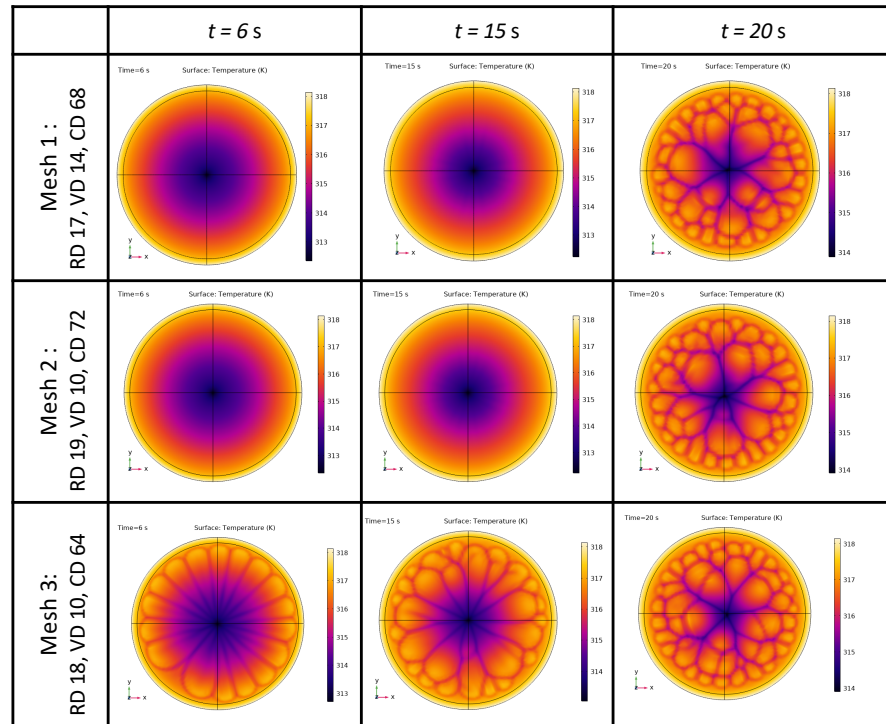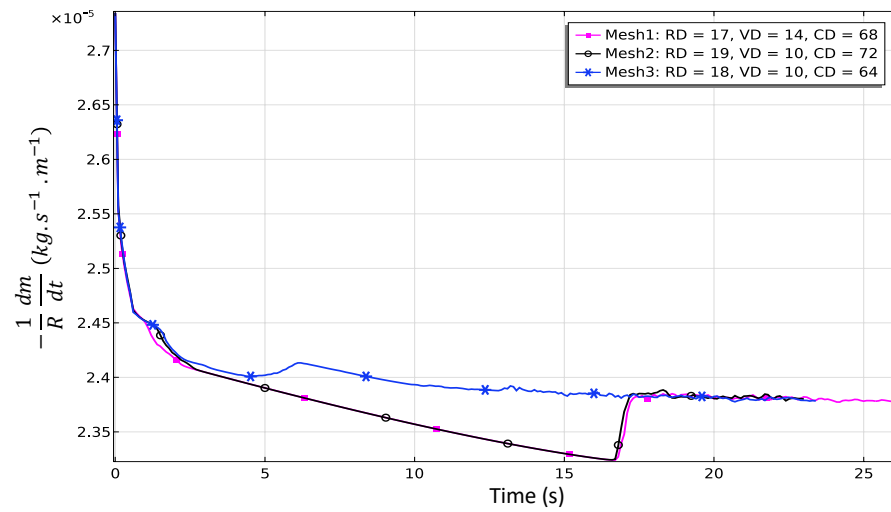
Figure C.4: Comparison of evaporation rate and instabilities pattern for heated substrate for different meshes.

In figure C.4 shown the comparison of three mesh (mesh structure similar to figure C.1d) for Ethanol sessile drop at substrate temperature $T_{sub} = 318.15\,\text{K}$, pressure $P = 0.835\,\text{bar}$, initial contact angle $\theta = 33°$ and radius $R = 1.5\,\text{mm}$. The first case Mesh1 consist with number of the element in the RD 18 with ER 3, No. of the elements for the CD 16 in one-quarter of sessile drop with ER 1, and No. of elements in the VD 10 with ER 4 that correspond to 756121 total degrees of freedom are solved in 3 days and 10 hours on 4 x Intel(R) Xeon(R)

CPU $E5 - 4610$ v2 at 2.30 GHz. Whereas, Mesh2 consists of 17 number of elements in the RD with ER 3, 17 no. of elements for the CD in one-quarter of sessile drop with ER 1, and 14 no. of elements in the VD with ER 4. Total no. of degree of freedom solved is 1037661 in 6 days and 11 hours on 2 x Intel(R) Xeon(R) Gold 6142 CPU at 2.60 GHz, using 2 sockets with 32 cores in total.

The total computational cost increases nearly by twice by increasing 37% total degree of freedom from Mesh1 to Mesh2 of figure C.4 and error in total evaporation volume in 23 s is 0.043% with respect to Mesh2 evaporation volume (total evaporation volume for Mesh2 in 23 s is 1.039 μL)
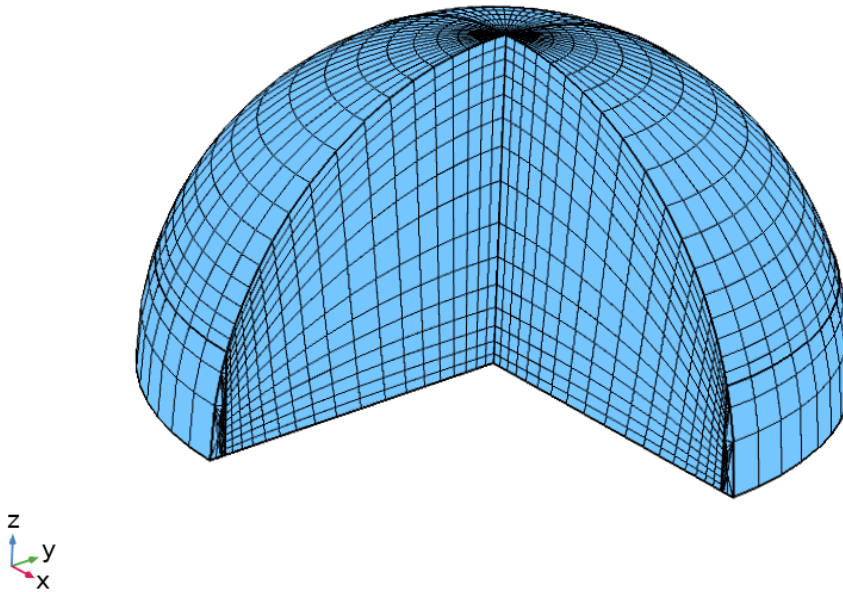
Figure C.5: Structure of the mesh for initial contact angle $\theta_0 = 90°$.

For the sessile drop of ethanol with initial contact angle $\theta_0 = 90°$, base radius $R = 2$ mm, ambient pressure 0.835 bar, and substrate temperature $T_{sub} = 323.15$ K. We use 18 number of elements in the RD with ER 3, 64 number of elements for the CD with ER 1, and 15 number of the elements in the VD with ER 4 which lead to generate total 21312 number of Mesh elements (see fig. C.5). Among the elements: 16320 are the Hexahedra elements, 4600 are the Quads element, 4992 are the Prisms elements and rest are the Triangles, Edges elements and Vertex element.

In table C.2, we present Ethanol numerical simulation computation data in detail for the reference. Similarly in table C.3 for the liquid HFE7100 sessile drops.

S.No	R (mm)	T_{sub} (K)	CPU Power	No. of degrees of freedom (DOF) solved	Phyical time t (s)	Wall-clock time	Method	For θ (Deg.)
1	1.5	318.15	(1 Nodes) Running on 2 x AMD EPYC 7302 16-Core Processor. Using 2 sockets with 32 cores in total Available memory: 257.15 GB.	709388	143.6	Solution time: 15032 s. (4 hours, 10 minutes, 32 seconds) Physical memory: 44.11 GB	HDM	90 to 9.45
2	1.5	323.15	(1 Nodes) Running on 2 x AMD EPYC 7302 16-Core Processor. Using 2 sockets with 32 cores in total Available memory: 257.15 GB.	709388	119.6	Solution time: 12172 s. (3 hours, 22 minutes, 52 seconds) Physical memory: 43.6 GB	HDM	90 to 9.45
3	1.5	318.15	(1 Nodes) Running on 2 x AMD EPYC 7302 16-Core Processor. Using 2 sockets with 32 cores in total Available memory: 257.15 GB.	1250371	106.89	Solution time: 147852 s. (1 day, 17 hours, 4 minutes, 12 seconds) Physical memory: 162.06 GB	FHDM	90 to 27
4	1.5	318.15	(2 nodes) Running on 2 x Intel(R) Xeon(R) Gold 6142 CPU at 2.60 GHz. Using 4 sockets with 64 cores in total Available memory: 191.85 GB (each node)	1037661	26.08	Solution time: 560244 s. (6 days, 11 hours, 37 minutes, 24 seconds) Physical memory: 76.63 GB	FHDM	33 to 9.45
5	1.5	323.15	(1 Nodes) Running on 2 x AMD EPYC 7302 16-Core Processor. Using 2 sockets with 32 cores in total Available memory: 257.15 GB.	1250371	84.94	Solution time: 169665 s. (1 day, 23 hours, 7 minutes, 45 seconds) Physical memory: 161 GB	FHDM	90 to 27
6	1.5	323.15	(2 nodes) Running on 2 x Intel(R) Xeon(R) Gold 6142 CPU at 2.60 GHz. Using 4 sockets with 64 cores in total Available memory: 191.85 GB (each node).	1037661	20.641	Solution time: 772329 s. (8 days, 22 hours, 32 minutes, 9 seconds) Physical memory: 62.78 GB	FHDM	33 to 9.45
7	1.5	313.15	(2 nodes) Running on 2 x Intel(R) Xeon(R) Gold 6142 CPU at 2.60 GHz. Using 4 sockets with 64 cores in total. Available memory: 191.85 GB (each node)	895513	33.19	Solution time: 340043 s. (3 days, 22 hours, 27 minutes, 23 seconds) Physical memory: 63.28 GB	FHDM	33 to 9.45
8	1.5	308.15	(1 nodes) Running on 4 x Intel(R) Xeon(R) CPU E7-4850 v2 at 2.30 GHz. Using 4 sockets with 48 cores in total Available memory: 515.76 GB.	895513	42.61	Solution time: 323488 s. (3 days, 17 hours, 51 minutes, 28 seconds) Physical memory: 112.08 GB	FHDM	33 to 9.45
9	3m	318.15	(2 nodes) Running on 2 x AMD EPYC 7302 16-Core Processor. Using 4 sockets with 64 cores in total Available memory: 257.15 GB (each node).	869920	102.61	Solution time: 2293390 s. (26 days, 13 hours, 3 minutes, 10 seconds) Physical memory: 107.81 GB	FHDM	33 to 9.45
10	2m	318.15	(2 nodes) Running on 2 x AMD EPYC 7302 16-Core Processor. Using 4 sockets with 64 cores in total Available memory: 257.15 GB (each node).	895513	46.03	Solution time: 905467 s. (10 days, 11 hours, 31 minutes, 7 seconds) Physical memory: 118.75 GB	FHDM	33 to 9.45

Table C.2: Summary of the numerical simulations of Ethanol sessile drops. Using Quadratic shape order for all the above simulation.

S.No	R (mm)	T_{sub} (K)	CPU Power	No. of degrees of freedom (DOF) solved	Phyical time t (s)	Wall-clock time	Method	For θ (Deg.)
1	2	301.15	(1 Nodes) on 4 x Intel(R) Xeon(R) CPU E7-4850 v2 at 2.30 GHz. Using 4 sockets with 48 cores in total Available memory: 515.76 GB.	1240906	75.3	Solution time: 70 days, 17 hours physical memory 180.04 GB (virtual memory 202.64 GB)	FHDM	60 to 9.4
2	2	301.15	(1 Nodes) Running on 2 x AMD EPYC 7302 16-Core Processor. Using 2 sockets with 32 cores in total Available memory: 257.15 GB.	756530	86.6	Solution time: 22 hours, 40 minutes, Physical memory: 45.24 GB GB and virtual memory 58.96 GB	HDM	60 to 9.4

Table C.3: Summary of numerical simulation for liquid HFE7100 sessile drops numerical simulation.

SUPPORTING RESULTS
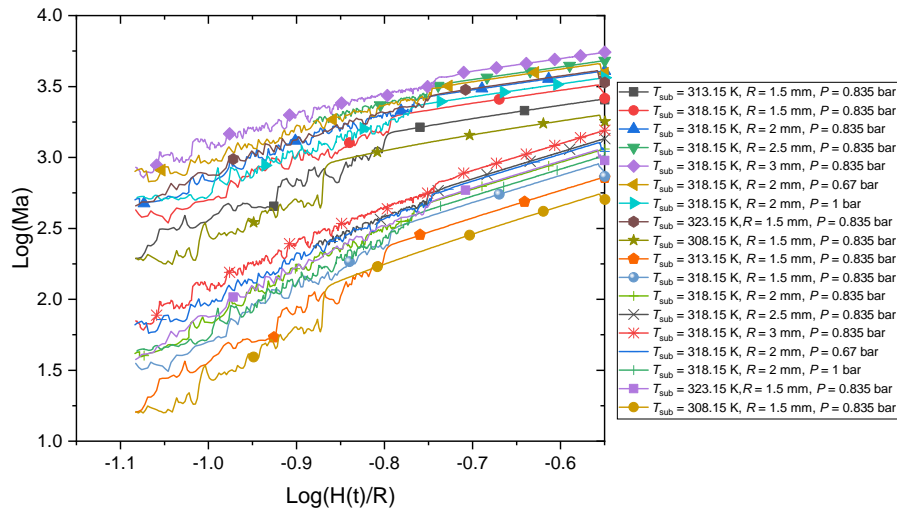
Figure D.1: Log-log plot for thermal Marangoni number (Ma_T) and sessile drop Marangoni number (Ma_{SD}).
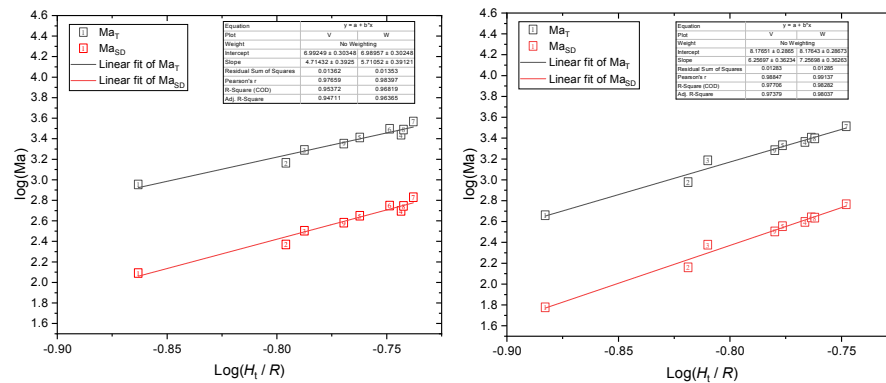
Figure D.2: Fitting for critical thermal Marangoni number ($Ma_{T,crit}$) and critical sessile drop Marangoni number ($Ma_{SD,crit}$) critical value at transition begins (left) and transition completed (right).
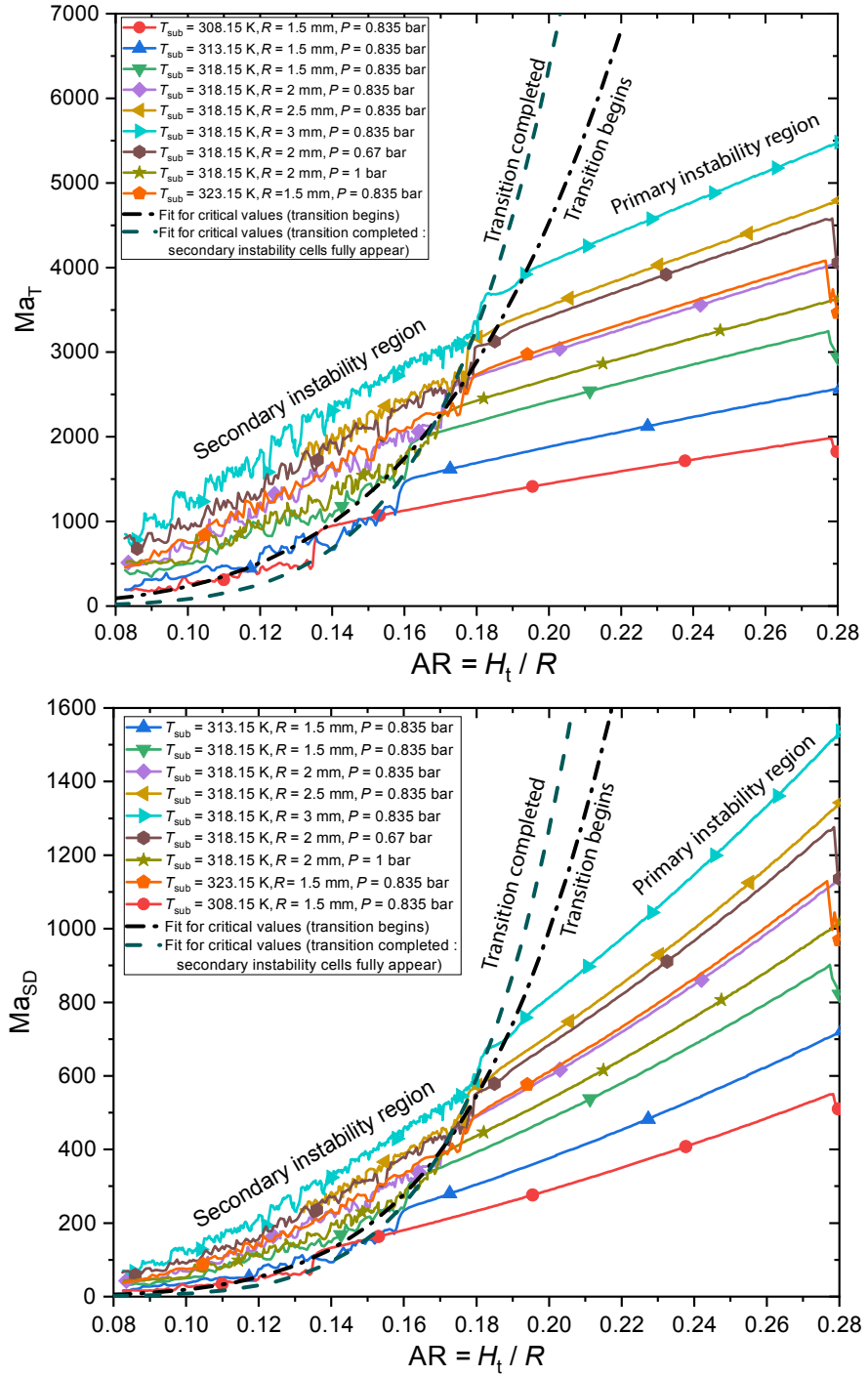
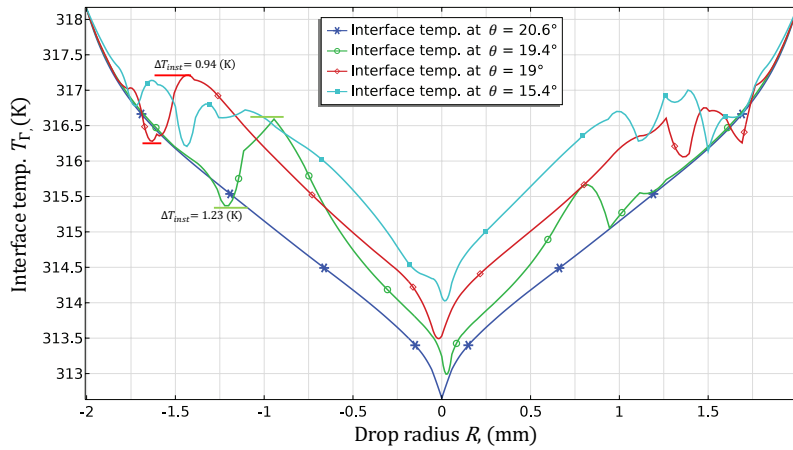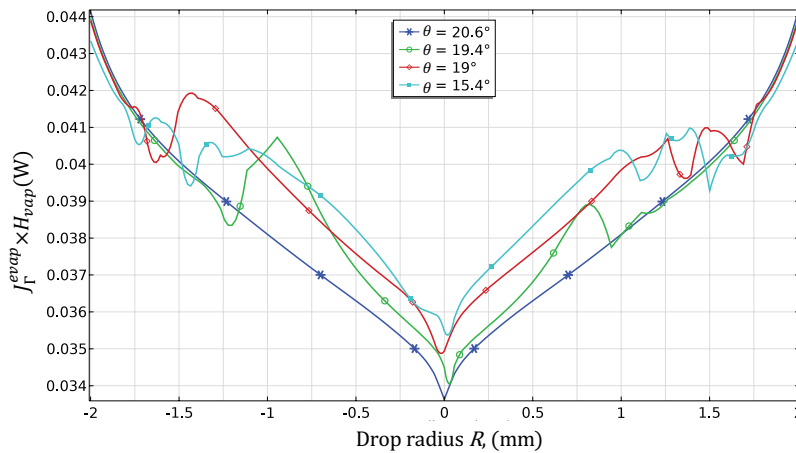Figure D.3: Thermal Marangoni number (Ma_T) and sessile drop Marangoni number (Ma_{SD}) with instability region and critical values fittings.

Figure D.4: Comparison of interface temperature T_Γ along the radial position of sessile drop interface at different contact angle. For more details please refer to Fig. D.4. Numerical parameters are same as Fig. D.4 & Fig. 4.17.

(a)
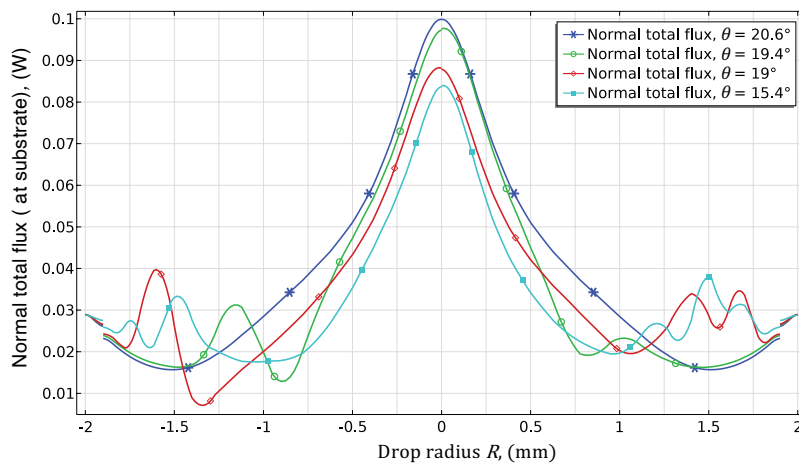
(b)

Figure D.5: Comparison of heat flux along the radial position of the sessile drop at the different contact angle. **(a)** Heat flux profile along the interface; **(b)** Normal total flux profile along the substrate. Numerical parameters are same as Fig. 4.17.
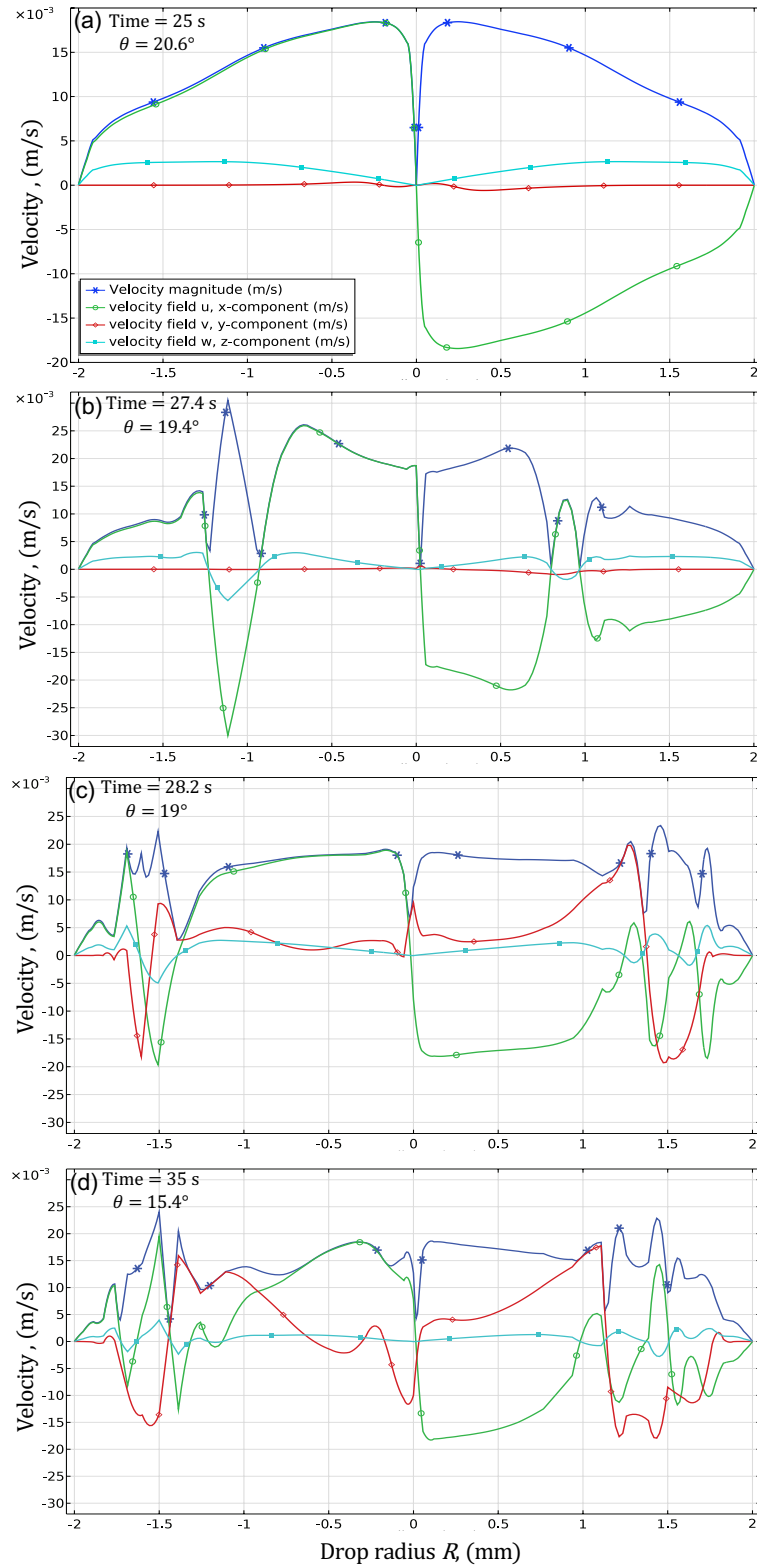
Figure D.6: Velocity magnitude and velocity field component along the radial position of the sessile drop. **(a)** at $\theta = 20.6°$ at the primary instability phase; **(b)** $\theta = 19.4°$, starting of the secondary instability cells; **(c)** $\theta = 19°$ fully developed stage of the secondary instability with flower like pattern; **(d)** $\theta = 15.4°$ secondary instability core cells are getting bigger. Numerical parameters are same as Fig. 4.17. Supplementary for the figure 4.21 & 4.17. For movie ▶ play or Scan QR.
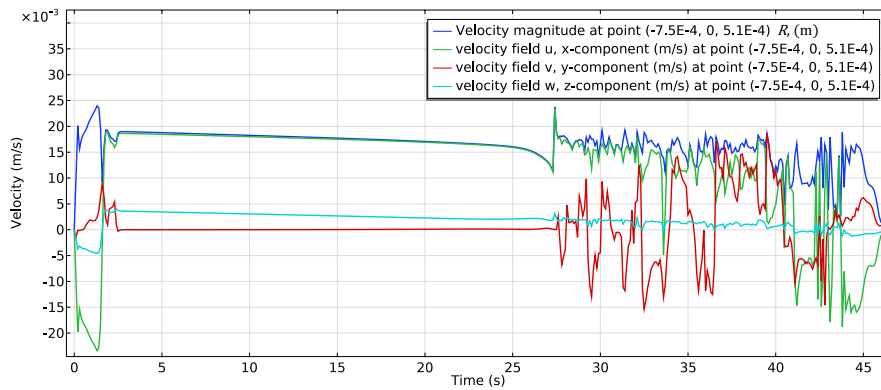
Figure D.7: Velocity magnitude and velocity field component at a probe point on the interface of the sessile drop. Numerical parameters are same as Fig. 4.17. Supplementary for the figure 4.21 & 4.17. For movie ▶ play or Scan QR.
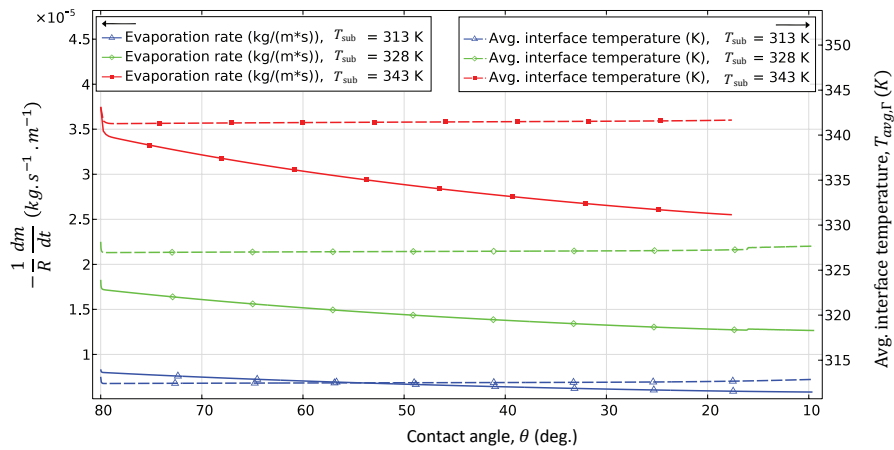
Figure D.8: Evaporation rate and average interface temperature with respect to contact angle of water sessile drop on heated substrate under microgravity. Supplementary for the figure 4.28.

MOVIES LIST

1. Top view of sessile drop surface temperature (IR) and drop shape under microgravity from parabolic fight VP140. Reference Fig. 2.8 & 2.9. ▶ play or Scan QR.
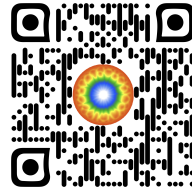
2. Top view of sessile drops surface temperature (IR) under microgravity from parabolic fight VP140. Reference Fig. 2.10. ▶ play or Scan QR.
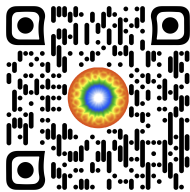
3. Evolution of infrared (top view) and drop shapes during the evaporation of liquid HFE-7100 sessile drops on a heated substrate under microgravity and Earth conditions with electric field (EF). Reference Fig. 6 of section A. ▶ Play or Scan QR.
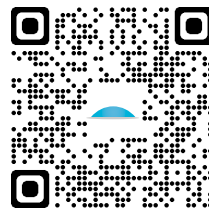
4. Top view comparison of sessile drop surface temperature and velocity at different substrate temperatures under microgravity. Reference Fig. 4.10. ▶ play or Scan QR.
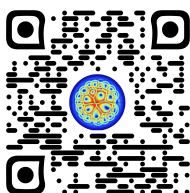
5. Top view comparison of sessile drops surface temperature and velocity at different base radius at constant substrate temperature and ambient pressure under microgravity. Reference Fig. 4.12. ▶ play or Scan QR.
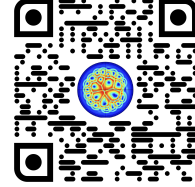
6. Top view comparison of sessile drops surface temperature and velocity at different ambient pressure at constant substrate temperature and base radius under microgravity. Reference Fig. 4.14. ▶ play or Scan QR.
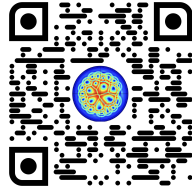
7. Evolution of the sessile drop interface surface temperature, top view (IR), local evaporation rate, surface velocity and local normal total flux (at substrate) on heated substrate under microgravity. Reference Fig. 4.17. ▶ play or Scan QR.
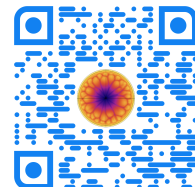
8. Streamline and velocity vector of ethanol sessile drops at substrate temperature $T_{sub} = 318.15\,\text{K}$, pressure $P = 0.835\,\text{bar}$ and radius $R = 2\,\text{mm}$ under microgravity. Reference Fig. 4.18. ▶ play or Scan QR.

9. Vorticity field vector on the surface of Ethanol sessile drop on heated substrate. Numerical simulation and subplot conditions are same as fig 4.18. Reference Fig. 4.19. ▶ play or Scan QR.
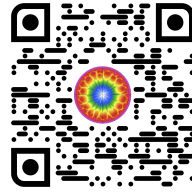
10. Temperature (top) and velocity vector (middle) and velocity magnitude (bottom) at the cut plane (half), inside the domain of ethanol sessile drops. Numerical simulation and subplot conditions are same as fig. 4.18 Reference Fig. 4.20. ▶ play or Scan QR.
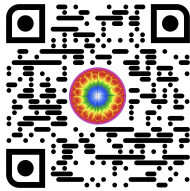
11. Instantaneous evoluation of Ethanol sessile drop evaporation rate, temperature and velocity along the radial position of sessile drop interface . Reference Fig. 4.21, D.4 & D.6. ▶ play or Scan QR.
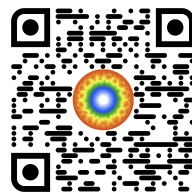
12. Local evaporation rate and temperature at the probe point at initial location ($x = 0.75\,\text{mm}, y = 0\,\text{mm}, z = 0.51\,\text{mm}$) on the sessile drop interface. The probe point is moving with sessile drop interface. Numerical simulation conditions are same as Fig 4.17. Reference Fig. 4.4 4.17, D.7 & 4.22. ▶ play or Scan QR.
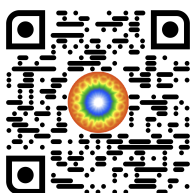
13. Experiment and numerical comparison of liquid HFE7100 sessile drop evaporation on heated substrate. Reference Fig. 4.4, 4.24, 4.25 & 4.26. ▶ play or Scan QR.
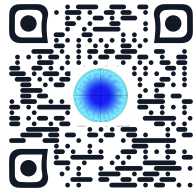
14. Water sessile drops evaporation into N_2 under microgravity (numerical) at substrate temperatures $T_{sub} = 328.15$ K. Reference Fig. 4.28 & table 4.3. ▶ play or Scan QR.
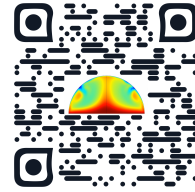
15. Comparison of the Ethanol and Methanol sessile drop temperature and velocity at interface under same conditions. Reference Fig. 4.30. ▶ play or Scan QR.

F
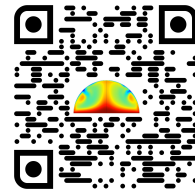
GRAVITY EFFECT ON LIQUID DOMAIN ONLY

Experimental comparison from the ground and microgravity show the difference in evaporation with higher in gravity [76]. And is consistent with the previous observations on the convective transport in vapour influencing the evaporation [34, 40, 69, 70]. In the support of the demonstration in figure F.1 we compare with our model the numerical simulation from 0g with 1g as body force with surface tension. The comparison clearly shows that adding the body force in the liquid domain doesn't influence the evaporation rate of microgravity. So it can be inferred that experimentally observed elevated evaporation rate under gravity is the result of crucial influences from vapour dynamic around the sessile drop. It can be concluded that gravity has its dominant effects are actually located in the vapor phase via vapour density gradient induces thermal-solutal convection. To capture the thermal-solutal convection influences on sessile drop two-way coupled model is required, unlike the current model that is sufficient for microgravity conditions.
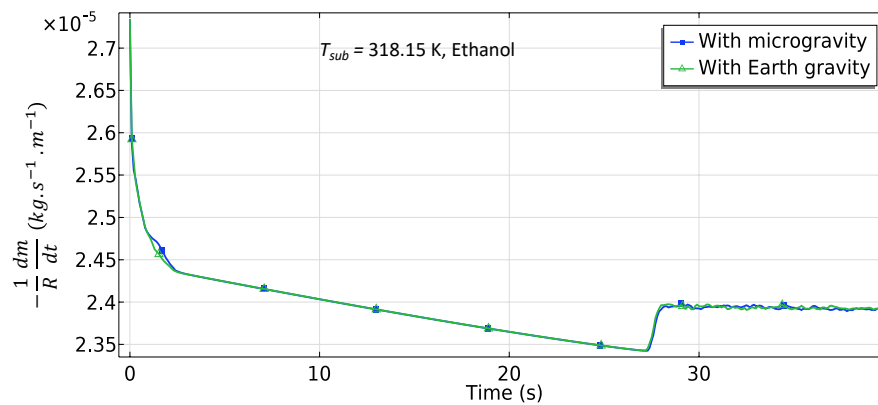

Figure F.1: Comparison of the evaporation rate of sessile drop under Earth gravity and microgravity with our one-way coupled model. Numerical simulation parameters are same as in Fig. 4.17.

G

BRIEF REPORT ON POST-FLIGHT ANALYSIS AND RECOMMENDATIONS FOR ARLES

INTRODUCTION: The ARLES experiment aimed to investigate the sessile drop evaporation of the Novec^{TM} HFE7100. Among the various studies and data acquisition during the microgravity phase of the main evaporation cell, we, AMU-IUSTI team focused on the study of flow instabilities occurring in the sessile drop. We use the following data/instruments information for our study:

- IR Images for observing the flow instabilities patterns in the sessile drop.

- Heat flux-sensor with integrated thermocouples for determining the heat flux of the drop and the temperature of the substrate.

- Interferometry Images as the side-view to calculate the volume, contact angle and evaporation rate.

- Other temperature and pressure instruments.

G.1 ISSUES CONFRONT DURING THE ANALYSIS:

IR IMAGES: As it has been already mentioned in the lambda-x report $ARLES - TN - LX - 007 - A/0$ that is:

1. A non-uniform background pattern appears over the course of the experiment.

2. The flight images seem blurrier than the images recorded during the science validation campaign.

INTERFEROMETRY IMAGES: No issue.
HEAT FLUX-SENSOR: No issue.
PRESSURE INSTRUMENTS: Only one pressure sensor (P1) is used for the measurement of the pressure inside the main cell. In the ENG-18 Design Report ARLES, Document ID $MASER-1429217191-159$ Version: 3.41 Pages 47, Figure $3.4-22$ "Shared GN2 system for Main evaporation and multi-drop cells", it has been shown that pressure sensors (P6) at the vacuum vent on the structure will also be used, however, no instrumentation has been used so no data is available but had it been there, it could have played a crucial role in the numerical simulation of flushing.

G.2   REMARKS:

IR IMAGES: To resolve the issue Lambda-x provided the re-calibration and cleaning for the IR images. In figure G.1 we can see the comparison of the IR images before and after the cleaning. We can clearly see the removal of the non-uniform background pattern but there is not much improvement in the visibility of the instability patterns. The drop shown in the Lambda-x report is the drop between the actual drop no.4 and drop no.5 (with nanoparticle) which has been created due to unwanted injection. It can be clearly seen that the drop of the figure G.1 is the drop after the time of depinning. Figure G.2, is the side view of the figure G.1, in which it can be seen that the current height of the sessile drop is 24 pixel (i.e 0.025 mm) with the secondary instability cells.
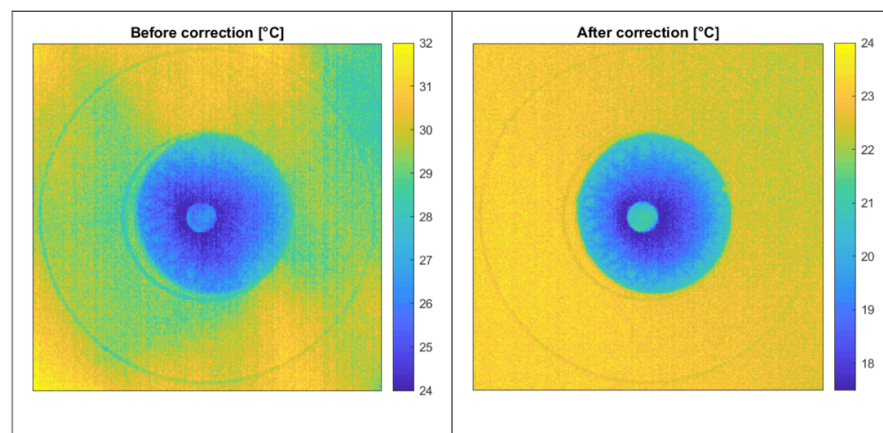

Figure G.1: Droplet: before and after background correction (frame no 18698) from Lambda-x report.

Figure G.2: Droplet side view of the frame no 18698 (of figure G.1).

It can be stated as a fact that the root cause of the problem lies in the size of the droplets themselves. The IR camera used for the IR images should have Depth-of-Field (DoF) of 1 mm for 5.7 cycles/mm according to it specification but for the current resolution the DoF is 0.7 mm at 9 cycles/mm. In figure G.3, we see the height comparison of the sessile droplets under microgravity. Almost all the droplets have a starting height higher than 0.7 mm. For the drop2, with electric volt, the secondary instability cells start appearing during the evaporation near the periphery of drop before the depinning remained visible until the end of the complete evaporation(see figure G.3) which is in agreement with the science validation test. This can also be seen in figure G.4, as the height of the sessile droplets when the secondary

instability cells appear is between 0.3 to 0.2 mm (refer to the markings in the figure G.4). However, the flight images seem blurrier than the images recorded during the science validation campaign, for which factors other than the Depth-of-Field (DoF) are responsible for causing the blurring of the IR images.
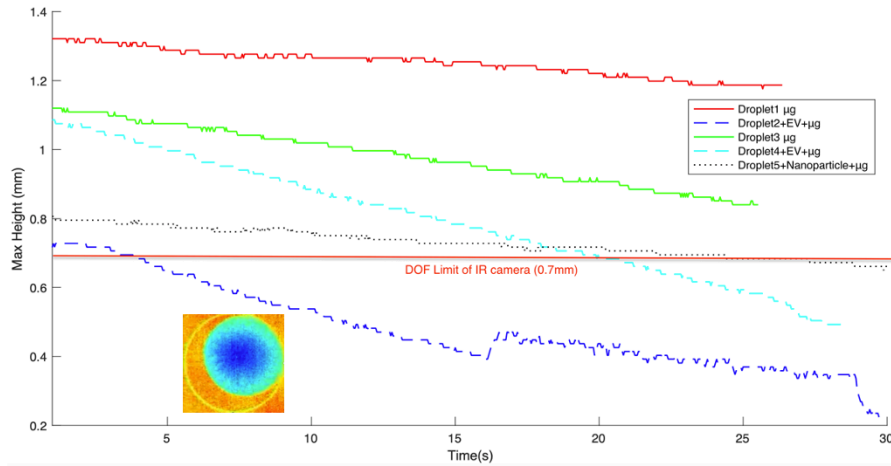

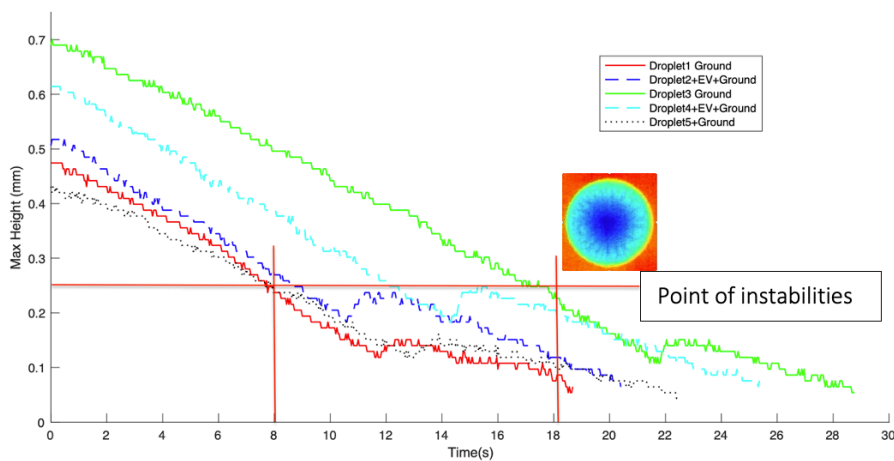Figure G.3: Heights of the sessile drop under microgravity with to respect time.

Figure G.4: Heights of the sessile drop with respect time during science validation test.

The blurring of the IR images may possibly arise due to multiple reasons such as:

1. Vapour cloud near the substrate after the insufficient flushing of the main cell.

2. Focusing issues of the IR camera due to oversize of the drop.

3. Rise in the temperature of the IR camera sensor.

To check the possibility of the first point, we did the numerical simulation of the main evaporating cell for one flushing cycle with the

assumption that the constant pressure at the inlet is 1055 mbar. The varying time-dependent pressure at the outlet has been shown in the figure G.5 at the right hand side.
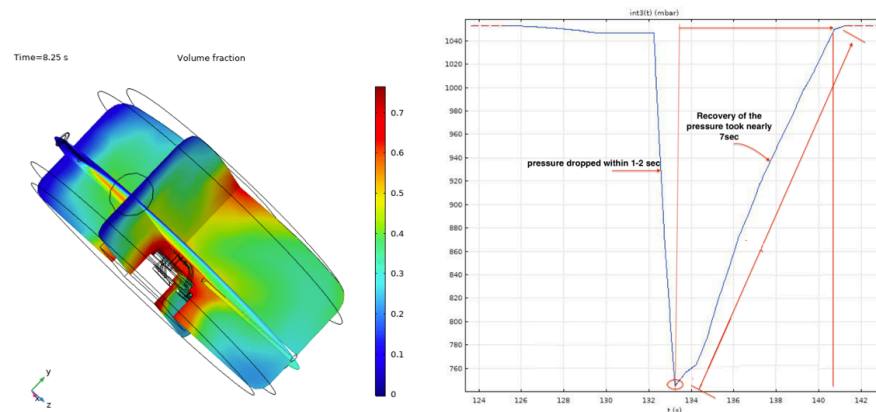

Figure G.5: Volume fraction at time 8.25 s with 1 mark for fully HFE7100 and 0 for fully nitrogen in main cell (left-hand) and outlet pressure of main cell with respect to time (right-hand).

In figure G.5, at the left hand side, we can see that before starting of the nitrogen top up in the main evaporating cell at the time 8.25 s, it still has the HFE7100 vapour cloud around the substrate and near the glass opening for the IR camera. Due to the absence of natural convection in microgravity,the main evaporating cell design also needs to focuses on the vapour accumulated during the evaporation between the substrate and electrode for the efficient flushing and also, on the vapor in front of the IR camera window.

G.3   RECOMMENDATIONS FOR FUTURE ARLES EXPERIMENT:

Below recommendations originate based on the experience from the ARLES experiment and simulation analysis which further deepen the understanding of the sessile drop evaporation process under microgravity.

FOR VOLUME INJECTION SYSTEM: The recommended max injection volume of HFE7100 liquid should be between 3 to 3.5 μL as the secondary instability cells appear between 1.5 μL and 2 μL.

IR IMAGES QUALITY: Size of the drop in the IR images, in comparison to the whole 640×480 pixels size, for the drop it is only 165 pixels for 4 mm diameter in each direction which is equal to only 9% of the total IR image information. In figure G.6, are the IR images recorded during the ARLES (left-hand) with pixel size of $17\,\mu \cdot \text{pixel}^{-1}$ and ESA (right-hand) funded parabolic flight companion VP140 with pixel size of $21\,\mu \cdot \text{pixel}^{-1}$ (fluid: Ethanol, frame size 640×480 pixels) has been provided for the understanding. With this comparison, it is recommended to use micro lens for zooming.
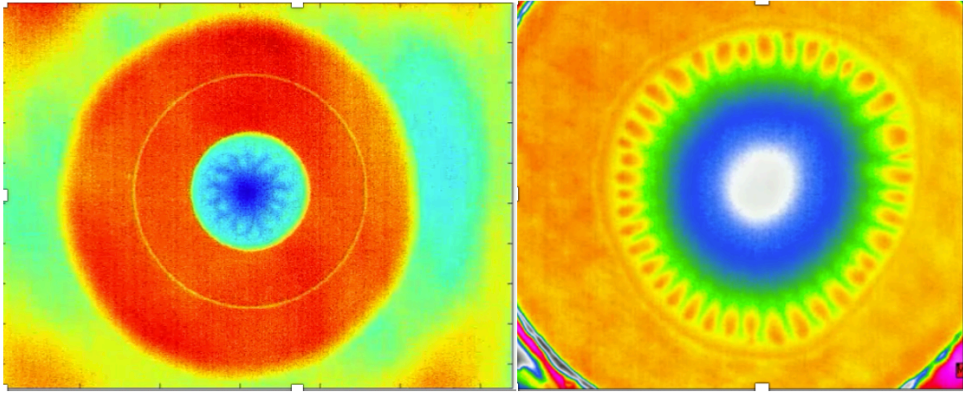
Figure G.6: Comparison of the IR Images from ARLES (Left hand) and Parabolic flight VP140 (Right hand) with both pixel size of the 640×480.

It is preferable not to clean the Images as it may lead to the loss of the information or alter the information which may further lead to wrong interpretation. However, control of IR Camera sensor temperature is advised.
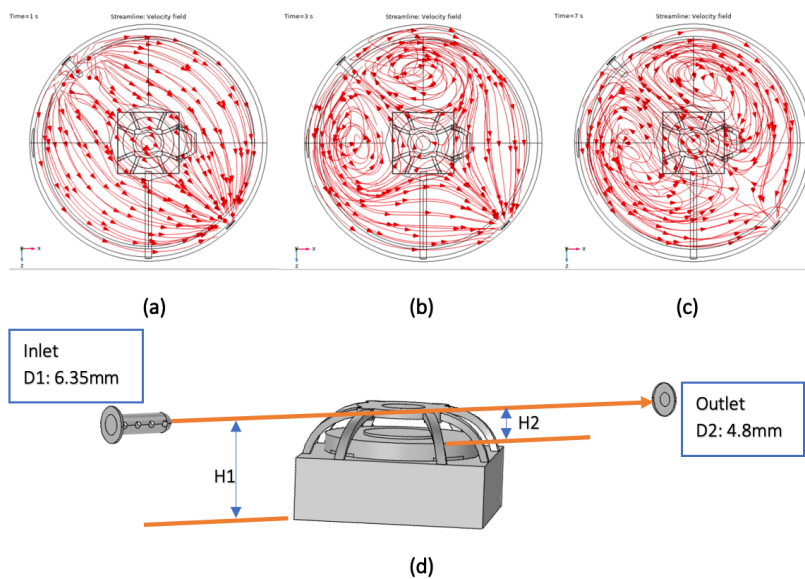

Figure G.7: Velocity field streamlines at the time t : **(a)** 1 s; **(b)** 3 s; **(c)** 7 s; **(d)** shows the positioning of the flushing inlet and outlet with substrate cell.

FOR FLUSHING: To avoid the possibility of having vapour cloud between the substrate and electrode even after the flushing. In Figure no. G.7a, G.7b, and G.7c is shown the numerical simulation for main evaporating cell with the evolution of the velocity field with respect to time. It shows the development of circulation inside the main cell during the flushing. It is also noticed that the velocity magnitude near the vertical side wall is significantly higher in comparison to that at

the center of the main cell. The possibility of improving the flushing is either by increasing the time duration of flushing or by modifying the main cell design. To achieve efficient main cell design, the preliminary suggestions include modifications such as changing the inlet nozzle design (example: orientation, holes locations and sizes), increasing the outlet diameter (D2) equal or larger than the inlet diameter D1 (recommended), and bringing the inlet nozzle height (H) equal to the substrate height or lower i.e. the $H = H1 - H2$.

PRESSURE INSTRUMENT: It is convenient to have pressure reading from the proposed pressure sensor (P6) at the outer vent line for the numerical simulation.

FLUID PROPERTY: The necessary thermophysical properties of the Novec^{TM} HFE7100 are not included in the design manual. The thermophysical properties available online are varying from reference to reference. So, thermophysical property data from Novec^{TM} HFE7100 supplier should be included in the design manual.

The Parabolic flight campaign could be used to test the experiment system before the rocket launch. It would help to check the performance and rectify the unknown issues that may be encountered during microgravity conditions at the preliminary stage.